Fundamental controls on triple oxygen-isotope ratios in Antarctic precipitation and ice cores

Spruce William Schoenemann

A dissertation
submitted in partial fulfillment of the
requirements for the degree of

Doctor of Philosophy

University of Washington
2014

Reading Committee:
Eric Steig, Chair
Becky Alexander Suess
Cecilia Bitz

Program Authorized to Offer Degree:
Earth and Space Sciences

© Copyright 2014
Spruce William Schoenemann

University of Washington

Abstract

Fundamental controls on triple oxygen-isotope ratios in Antarctic precipitation and ice cores

by Spruce William Schoenemann

Chair of the Supervisory committee:
Professor Eric J. Steig
Department of Earth and Space Sciences

Stable isotope ratios of water (δD and δ^{18}O) in polar precipitation and ice cores have long been used to study past climate variations and the hydrological cycle. Recently-developed methods permit the precise measurement of δ^{17}O and the ^{17}O excess, relative to the δ^{17}O *vs*. δ^{18}O meteoric water line. The novel isotope parameter "$^{17}O_{excess}$" provides an additional tool for investigating the global hydrological cycle.

Early experimental and modeling studies showed that $^{17}O_{excess}$ in atmospheric water vapor is sensitive to relative humidity during evaporation from the ocean surface, and suggested that there was little fractionation during condensation. It was therefore expected that $^{17}O_{excess}$ in polar snow could be used as an indicator for humidity in the ocean source regions where polar moisture originates. Later work shows that the magnitude of $^{17}O_{excess}$ change between the last glacial period and the Holocene warm period, measured in Antarctic ice cores, increases from the Antarctic coast towards the interior, suggested significant fractionation during transport. Full interpretation of these conflicting results has been challenging, hindered in part by the labor-

intensive nature of making $^{17}O_{excess}$ measurements and by the lack of an accepted standard for reporting $^{17}O_{excess}$ values.

This thesis provides a new, comprehensive assessment of the $^{17}O_{excess}$ of Antarctic precipitation and ice core data. The contributions from this work also include improvements to $^{17}O_{excess}$ measurement techniques, using both isotope-ratio mass spectrometry and collaborative developments in laser spectroscopy, and a formal calibration of international water standards for $^{17}O_{excess}$. It further addresses both the spatial and temporal variations observed in Antarctic $^{17}O_{excess}$ values, providing a coherent explanation for both.

New Antarctic $^{17}O_{excess}$ measurements from this work show that there is a strong negative spatial gradient of $^{17}O_{excess}$ in snowfall towards the interior of Antarctica, a similar spatial pattern to the glacial-interglacial change in $^{17}O_{excess}$, and a smaller-amplitude seasonal cycle in West Antarctica than in the interior of East Antarctica. These measurements, when combined with earlier published work, provide the most complete view of the spatial distribution and temporal variability of $^{17}O_{excess}$ to date.

Model studies, using both an intermediate complexity isotope model (ICM) and an isotope-enabled general circulation model (GCM), have permitted a thorough investigation of the most relevant and important processes affecting $^{17}O_{excess}$ in Antarctica. The model simulations show that changes in source relative humidity have only a modest effect on $^{17}O_{excess}$ in polar precipitation, and can not account for the full seasonal cycle amplitude, nor the large glacial-interglacial $^{17}O_{excess}$ changes observed in Antarctic ice cores. The spatial gradient of $^{17}O_{excess}$ in modern precipitation, along with the large amplitude seasonal cycle in East Antarctica and the greater magnitude of $^{17}O_{excess}$ change for interior sites between glacial and interglacial periods, can be explained by kinetic isotope fractionation during snow formation under supersaturated

conditions. The model experiments further show that the influence of moisture recharge is important to the evolution of $^{17}O_{excess}$ in poleward-moving air masses. The seasonal presence of sea ice is also a significant factor affecting $^{17}O_{excess}$. Greater sea ice concentration or extent reduces evaporative recharge and increases the spatial area over which kinetic fractionation processes are important; both these factors tend to lower $^{17}O_{excess}$.

Table of Contents

ACKNOWLEDGEMENTS

I would like to thank my advisor, Dr. Eric Steig, for his guidance, confidence, and support that he provided me over the past five years. Eric has been a steadfast mentor, and a true friend. I have enjoyed working *together* with Eric, as he as treated me as a peer, and as a team we have accomplished much, both in the lab, on mountain glaciers, and on the powdered slopes. I would also like to thank Andrew Schauer, Δ*IsoLab Manager and isotope guru. His technological savvy and aptitude to solve any and all problems in the lab saved me many hours. I greatly value the time and support Andy offered me, and especially the productive conversations regarding all things, isotopic or otherwise. I am grateful for his mentorship and owe much of my successes to his help. Much of the GCM modeling would not have been possible without the help of Qinghua Ding and Dr. Cecilia Bitz, and I really appreciate the many model runs that they carried out.

I would also like to thank my committee members, Dr. Paul Quay, Dr. Cecilia Bitz, and Dr. Becky Alexander, for their fruitful discussions and helpful suggestions, along with their valuable editorial comments. I would also like to acknowledge the assistance of Kyle Samek, Beth Vanden Heuvel, Rebecca Teel, Rebecca Smith and Morgan Shusterman on the isotopic measurements that made much of this work possible. I also appreciate the long-distance conversations with Renato Winkler and Amaelle Landais in helping to sort out interlaboratory calibration differences.

Finally, I would like to acknowledge the many graduates students in the Dept. of Earth and Space Sciences and the Program on Climate Change who offered their camaraderie and support. I would like to especially thank Peter Neff, Bradley Markle, Perry Spector, and Kat Huybers for their steadfast friendship, guidance, and adventuresome spirit. Most importantly, I would like to

thank Mary Schoenemann, my wife, for her continual support over this five-year endeavor, during which she has listened to my incessant isotope jargon and has always believed in me.

Chapter 1.

Introduction

A recent innovation in ice core paleoclimate research is the analysis of the oxygen isotope ratio $\delta^{17}O$, complementing traditional measurements of δD and $\delta^{18}O$. New techniques to measure the $^{17}O/^{16}O$ ratio precisely has allowed the parameter $^{17}O_{excess} = \ln(\delta^{17}O + 1) - 0.528 \ln(\delta^{18}O + 1)$ to be added to the ice-core isotope toolbox [*Baker et al.*, 2002; *Barkan and Luz*, 2005]. Unlike the better-known deuterium excess, $d_{excess} = \delta D - 8 \times (\delta^{18}O)$, $^{17}O_{excess}$ is insensitive to ocean surface temperature during evaporation. The theoretical advantage of $^{17}O_{excess}$ is that it is considerably less sensitive than d_{excess} to equilibrium fractionation processes during condensation; however, both $^{17}O_{excess}$ and d_{excess} are sensitive to kinetic fractionation during the formation of snow and ice particles. The use of $^{17}O_{excess}$, in combination with $\delta^{18}O$ and d_{excess}, provides a potential means to unravel the fractionation effects during evaporation at the moisture source, along the transport path, and in the condensation of precipitation. Beyond its usefulness in ice core research, applications of $^{17}O_{excess}$ are expanding into the studies of terrestrial and biologic systems, offering an additional constraint on geochemical processes.

The research presented here has focused on investigating the fundamental controls on the ratios of triple oxygen isotopes (^{16}O, ^{17}O, ^{18}O) in Antarctic precipitation and ice cores over large spatial scales, and over both glacial-interglacial and seasonal time scales. Much of the work evolved from the initial task of developing and interpreting the first $^{17}O_{excess}$ ice core record from West Antarctica, which required the development of a water fluorination line, optimization and refinement of an Isotope Ratio Mass Spectrometer for precise measurement, accurate and reproducible normalization techniques for data reporting, and the implementation of $\delta^{17}O$ into isotope models for advancement of understanding the observed natural variations in $^{17}O_{excess}$.

The interpretation of past changes in $^{17}O_{excess}$ is difficult without a solid understanding of the controls on modern $^{17}O_{excess}$ precipitation. The challenge, in the case of $^{17}O_{excess}$, has been the dearth of present-day $^{17}O_{excess}$ measurements over the oceans and ice sheets. The current state of knowledge of $^{17}O_{excess}$ in the hydrological cycle is based on a small number of studies that include a limited amount of data (typically fewer than 50 analyses each): measurements of seawater (*Luz and Barkan*, [2010]), a Southern Ocean transect of water vapor (*Uemura et al.* [2010], meteoric waters from mostly low-to-mid latitudes (*Luz and Barkan*, [2010]), a transect of Antarctic surface snow data (*Landais et al.* [2008]), seasonal samples from Greenland and Vostok (*Landais et al.* [2012a; 2012b]), and three low-resolution ice core records of the penultimate glacial-interglacial transition (*Landais et al*. [2008], *Winkler et al*. [2012]). These studies comprise the most noteworthy data that, over the past six years, have contributed the essential results for understanding $^{17}O_{excess}$ in the hydrological cycle, from ocean source regions to polar precipitation.

In this work, I present three new ice core records, two from West Antarctica and one from coastal East Antarctica, that cover the Last Glacial Maximum (LGM), Early Holocene (EH), and modern periods. These new $^{17}O_{excess}$ ice core measurements, published in *Schoenemann et al.* [2014], in combination with the studies of *Landais et al*. [2008] and *Winkler et al.* [2012], provide evidence that the LGM to EH change in $^{17}O_{excess}$ was much larger for sites in the Antarctic interior than at sites closer to the Antarctic coast. I also present the first application of laser spectroscopic methods to the measurement of natural variations in $^{17}O_{excess}$, from a seasonally-resolved West Antarctic firn core. This preliminary work, using an instrument jointly

developed with Picarro, Inc. the instrument manufacturer and *Steig et al*. [2014], shows that cavity ring-down spectroscopy (CRDS) can be an efficient and precise tool for simultaneous measurements of the triple water isotope ratios in Antarctic ice and snow. Future ice core measurements should now be possible at much greater temporal resolution than was possible using the conventional Isotope Ratio Mass Spectrometry (IRMS) technique.

Motivation

Beyond understanding the behavior of $^{17}O_{excess}$ in polar regions, this work has broader significance across multiple disciplines. Although measurement of $^{17}O_{excess}$ is analytically time-intensive, it is clear that $^{17}O_{excess}$ is quickly becoming one of the "standard measurements" in the ice core/glaciology research community. As improvements in the routine measurement of $^{17}O_{excess}$ on water develop (particularly with laser spectroscopic techniques), the use of $^{17}O_{excess}$ can be extended to a variety of other applications, ranging from hydrology, oceanography, geology, biology, and atmospheric sciences. An example of one such application is the measurement of $^{17}O_{excess}$ on atmospheric water vapor, where the use of water isotopes can be used to improve understanding of atmospheric convection, moisture transport, and condensation. Current developments in the use of the triple oxygen isotope ratios as hydrological indicators include: transpiration during leaf evaporation, precipitation of carbonates in soils, and seasonal exchange of water in the biosphere with tropospheric CO_2.

Background

Measurements of the stable isotope ratios of water (δD and δ^{18}O) in polar precipitation have long been used in paleoclimate ice core studies [*Dansgaard*, 1964; *Merlivat and Jouzel*, 1979; *Jouzel and Merlivat*, 1982; *Dansgaard et al.*, 1993; *Jouzel et al.*, 2003; *Masson-Delmotte et al.*, 2004]. Although the underlying physics have been well understood for many decades, continual innovations have kept this a stimulating area of research. The latest major innovation is the development of methods for obtaining precise measurements of a third water isotope ratio, δ^{17}O [*Baker et al.*, 2002; *Barkan and Luz*, 2005]. Combined measurements of δ^{18}O and δ^{17}O can be expressed with the parameter $^{17}O_{excess}$. The $^{17}O_{excess}$ is defined as: $^{17}O_{excess} = \ln(\delta^{17}O+1) - 0.528 \times \ln(\delta^{18}O+1)$, where δ^{18}O and δ^{17}O are unitless ratios; i.e. $\ln(\delta^{17}O+1) = \ln[(^{17}O/^{16}O)_{sample}/(^{17}O/^{16}O)_{std})]$. The slope of 0.528 is determined from measurements of meteoric waters and is referred to as the Global Meteoric Water Line [*Barkan and Luz*, 2007; *Luz and Barkan*, 2010]. Deviations from the GMWL result from the combined effects of liquid-vapor equilibrium fractionation and diffusive fractionation during evaporation [*Angert et al.*, 2004; *Barkan and Luz*, 2007; *Landais et al.*, 2008; *Risi et al.*, 2010]. Variations in $^{17}O_{excess}$ are generally several orders of magnitude smaller than variations in δ^{18}O and are conventionally expressed in per meg (10^6) or ppm. The parameter deuterium excess ($d_{excess} = \delta D - 8\ (\delta^{18}O)$) is commonly used as a proxy for moisture source conditions, but its interpretation is problematic because d_{excess} is sensitive to both temperature and humidity at the oceanic source site, and it is strongly affected by equilibrium fractionation during transport [*Jouzel and Merlivat*, 1984; *Cuffey and Vimeux*, 2001; *Vimeux et al.*, 2001; *Kavanaugh and Cuffey*, 2002; 2003]. In contrast, $^{17}O_{excess}$ is nearly insensitive to evaporation temperature [*Barkan and Luz*, 2007; *Risi et al.*, 2010]. It was originally thought to be less sensitive than d_{excess} to fractionation processes during transport and precipitation; this is true at relatively warm temperatures, but like d_{excess}, $^{17}O_{excess}$ is sensitive to ice-vapor kinetic fractionation during snow formation.

Both theory and experimental results show that an excess of ^{17}O in meteoric water originates

from evaporation of ocean water into under-saturated air and that the $^{17}O_{excess}$ value is negatively correlated with relative humidity [*Angert et al.*, 2004; *Barkan and Luz*, 2007; *Luz and Barkan*, 2010]. Variations of $\delta^{17}O$ and $\delta^{18}O$ stem from the difference in saturation vapor pressures between the light and heavy isotopologues, resulting in liquid-vapor equilibrium fractionation at the ocean surface, expressed as $\theta_{eq} = \ln(^{17}\alpha_{eq})/\ln(^{18}\alpha_{eq})$ where ($\theta_{eq} = 0.529$), and α is the fractionation factor (given as greater than 1). The greater diffusivity of the light isotopologue with respect to the heavy isotopologue leads to kinetic fractionation during vapor diffusion into under-saturated air, where $\theta_{diff} = \ln(^{17}\alpha_{diff})/\ln(^{18}\alpha_{diff}) = 0.518$ [*Barkan and Luz*, 2007].

The equilibrium isotopic fractionations discussed reflect differences in the masses of different isotopologues (i.e., molecules with the same chemistry but different molecular masses), which result in differences in chemical and physical properties (e.g., reaction rates, diffusion rates, heat capacity, vapor pressure) and impact the rotational, translational, and vibrational energy states of the molecule. Of the three modes of motion available to a molecule, the vibrational motion plays the most important role in isotopic fractionation. The vibrational energy is dependent on temperature, and from quantum theory, can occur only at discrete energy levels, their values dependent on mass. Even at absolute zero, atoms will vibrate at a ground frequency ν_o, and this ground energy state is referred to as the *Zero Point Energy* (ZPE). The energy of the system is given by $(½+n)h\nu_o$, where *h* is Planck's constant and n = energy level (n = 0 for ZPE). The ZPE depends on the masses of the atoms involved, and therefore the energy levels will be different for different isotopologues. For a given quantum number, a bond involving a heavier isotope of an element will have a lower vibrational energy level. In general, the energy of a system will be minimized when the heavy isotope occupies the site with the stronger bond. At equilibrium, bonds involving the lighter isotopes are weaker and more readily dissociated, and therefore the lighter isotopes of an element are more likely to partake in a given reaction. Isotopic equilibrium is achieved when the isotopic composition of each of the reacting compounds is no longer changing over time.

In the case of water molecules, the bonds between $H_2{}^{16}O$ are weaker than $H_2{}^{18}O$, and thus at equilibrium the tendency of $H_2{}^{16}O$ to be in the vapor phase is greater than that for $H_2{}^{18}O$. At equilibrium, the isotopic equilibrium constant (K_{eq}) describes the ratio of the abundances of each molecule as follows: $K_{eq} = (AX^*)(BX)/(AX)(BX^*)$, where AX and BX are two compounds and * denotes the heavier isotope of element X. This expression can be simplified to $K_{eq} = (X^*/X)_A/(X^*/X)_B$, which represents the isotope ratio of compound A divided by the isotope ratio of compound B. The isotopic fractionation factor that results from this equilibrium process is typically expressed as α, where $\alpha = K_{eq}$.

The term "kinetic fractionation" refers to the degree of fractionation in non-reversible or incomplete reactions. For example, the different molecular diffusion rates of isotopologues yield isotopic fractionation effects that will be different, in general, from the equilibrium values. The velocity of a molecule depends on its kinetic energy (KE) = ½ mv^2, and thus $v = \sqrt{(2\times KE)/m}$. Since the diffusion rate of the molecule is related to its mean velocity (v), the molecular diffusion rate depends inversely on its mass (e.g., molecular $H_2{}^{16}O$ diffuses slightly faster than $H_2{}^{18}O$). The kinetic isotope effect (α) is described by the ratio of reaction rates for heavy (*K) and light (K) isotopologues, where $\alpha = {}^*K/K$.

Theoretically, kinetic isotopic fractionation from diffusive transport of water vapor in air (θ_{diff}) should dominate the mean $^{17}O_{excess}$ in water vapor at the ocean surface [*Gat*, 1996; *Angert et al.*, 2004; *Barkan and Luz*, 2005; 2007; *Uemura et al.*, 2010]. As expected, an excess of ^{17}O (positive $^{17}O_{excess}$) has been measured in meteoric waters, marine vapor, polar snow, and ice

cores [*Barkan and Luz*, 2007; *Landais et al.*, 2008; *Luz and Barkan*, 2010; *Uemura et al.*, 2010; *Winkler et al.*, 2012; *Landais et al.*, 2012b]. Measurements of $\delta^{17}O$ and $\delta^{18}O$ in meteoric waters show an average $^{17}O_{excess}$ of 33 per meg with respect to Vienna Standard Mean Ocean Water (VSMOW), normalized to Standard Light Antarctic Precipitation (SLAP), while seawater has an average $^{17}O_{excess}$ of –5 per meg (also on the VSMOW-SLAP scale), with more negative values in regions of high evaporation [*Luz and Barkan*, 2010]. Using a simple Rayleigh distillation model coupled to a Single Column Model, *Risi et al.* [2010] showed that the normalized relative humidity (hereafter rh_n) immediately above the ocean surface is the main factor controlling $^{17}O_{excess}$ in the marine boundary layer. The rh_n is defined as the relative humidity in the free air divided by the saturated vapor pressure at ocean surface temperature [*Barkan and Luz*, 2007; *Risi et al.*, 2010; *Uemura et al.*, 2010]. The process of condensation is not expected to alter the initial $^{17}O_{excess}$ gained in atmospheric vapor above the ocean, as the subsequent rainout occurs with a slope at or near 0.528, indicating the combined influences of equilibrium fractionation (θ_{eq} = 0.529) and a relatively small proportion of kinetic fractionation (θ_{diff} = 0.518) [*Barkan and Luz*, 2007]. Early work suggested $^{17}O_{excess}$ to be only weakly influenced by kinetic fractionation during precipitation over the ice sheet unlike d_{excess}, and it was therefore expected that $^{17}O_{excess}$ could be used as a proxy for humidity at the ocean surface [*Barkan and Luz*, 2007; *Landais et al.*, 2008; *Risi et al.*, 2010]. My modeling results and observational data suggest a larger role for kinetic fractionation during snow and ice deposition in the extremely cold interior regions of Antarctica.

The use of $^{17}O_{excess}$ in ice core research is still in the early stages of application. Previous to the research reported here, there were only three published ice core records of glacial-interglacial change, and the few measurements of the spatial distribution of $^{17}O_{excess}$ in polar precipitation were limited to East Antarctica [*Landais et al.*, 2008; *Winkler et al.*, 2012]. Nor has $^{17}O_{excess}$ been routinely incorporated, much less validated, in tracer-enabled GCMs; rather, modeling of $^{17}O_{excess}$ has been done using relatively simple Rayleigh distillation models like the Mixed Cloud Isotopic Model of *Ciais and Jouzel*, [1994] or combined with a Single Column Model that accounts for mixing within the marine boundary layer [*Risi et al.*, 2010]. Recently, the first $^{17}O_{excess}$ isotope-enabled GCM results were published by *Risi et al*. [2013] and although significant advances are presented, the main conclusion was that current state-of-the-art modeling is still unable to reproduce the observational data, emphasizing the need for further model development, and additional data for model assessment. A large part of the apparent model-data discrepancy is an artifact of inconsistent normalization techniques; this is addressed through adoption of an agreed upon value for $\delta^{17}O$ of SLAP, as recommended in *Schoenemann et al.* [2013].

Organization

This dissertation is organized into seven chapters, beginning with the Introduction and ending with an Outlook of future research topics. The middle five chapters include three published papers, one chapter of supplementary information, and a fourth paper that is nearing submission. These papers all focus on understanding the fundamental controls of the triple water-isotope ratios (δD, $\delta^{18}O$, and $\delta^{17}O$) in the hydrological cycle. A synopsis of each paper is given on the first page of the chapter along with a short description of my contribution to the work.

Chapter 2

Measurement of SLAP2 and GISP $\delta^{17}O$ and proposed VSMOW-SLAP normalization for $\delta^{17}O$ and $^{17}O_{excess}$

Originally published in Rapid Communications in Mass Spectrometry
http://onlinelibrary.wiley.com/doi/10.1002/rcm.6486/full

This paper is focused on the importance of consistent normalization techniques for reporting $^{17}O_{excess}$ values. The paper was a culmination of the $^{17}O_{excess}$ method development, refinement and optimization of the isotope-ratio mass spectrometry methods, and calibration to internal and International Atomic Energy Agency (IAEA) reference standards. This was an essential component of establishing the $^{17}O_{excess}$ water fluorination technique at the UW Δ*IsoLab for the production of the West Antarctic Ice Sheet Divide $^{17}O_{excess}$ record. New measurements of $\delta^{17}O$ of Standard Light Antarctic Precipitation 2 (SLAP2) and GISP (water sampled from the Greenland Ice Sheet Project location) are presented, along with Δ*IsoLab reference waters, which independently verified the proposed Global Meteoric Water Line slope originally presented by *Barkan and Luz* [2005]. In comparing our results with other published studies, we found that the $^{17}O_{excess}$ value of SLAP and GISP waters varied significantly between labs, and that a large part of the discrepancy was due to the lack of an agreed-upon $\delta^{17}O$ value and to inconsistent normalization methods for correcting $\delta^{17}O$ to the VSMOW-SLAP scale.

We proposed that the accepted $\delta^{17}O$ value of SLAP be defined in terms of $\delta^{18}O \equiv -55.5$ ‰ and $^{17}O_{excess} = 0$, yielding a $\delta^{17}O$ value of approximately –29.6986 ‰. Using this new definition for the $\delta^{17}O$ of SLAP and a recommended linear normalization procedure, the $\delta^{17}O$ value of GISP is –13.112 ‰ and the $^{17}O_{excess}$ value of GISP is 28 ± 4 per meg. We also calculated a weighted average of GISP based on measurements from the three most precise labs at the time of publication ([*Barkan and Luz*, 2005; *Kusakabe and Matsuhisa*, 2008; *Schoenemann et al.*, 2013]), which resulted in a $\delta^{17}O$ value of –13.16 ± 0.05 ‰ and a $^{17}O_{excess}$ value of 22 ± 11 per meg for GISP. More recently, IRMS and laser-spectroscopy based measurements from *Berman et al.* [2013] and Chapter 5 (published in *Steig et al.* [2014]) validated our GISP $\delta^{17}O$ and $^{17}O_{excess}$ results.

My contributions to this work included refining and optimizing the IRMS, developing the water fluorination line, producing the $^{17}O_{excess}$ measurements, analyzing and normalizing the data, writing the manuscript, and making all the figures and tables. Andrew Schauer assisted with the VSMOW and VSMOW-SLAP calibration methods, and Eric Steig produced the Newton error-analysis for estimating the sensitivity of $^{17}O_{excess}$ to measurement variations in $\delta^{17}O$ and $\delta^{18}O$. Eric Steig and Andrew Schauer both contributed significant guidance on the IRMS work, and editorial improvements to the manuscript.

Research Article

Rapid Communications in Mass Spectrometry

Received: 12 October 2012 Revised: 1 December 2012 Accepted: 6 December 2012 Published online in Wiley Online Library

Rapid Commun. Mass Spectrom. **2013**, *27*, 582–590
(wileyonlinelibrary.com) DOI: 10.1002/rcm.6486

Measurement of SLAP2 and GISP $\delta^{17}O$ and proposed VSMOW-SLAP normalization for $\delta^{17}O$ and $^{17}O_{excess}$

Spruce W. Schoenemann[1]*, Andrew J. Schauer[1] and Eric J. Steig[1,2]

[1]Isolab, Department of Earth and Space Sciences, University of Washington, Seattle, WA 98195, USA
[2]Quaternary Research Center, University of Washington, Seattle, WA 98195, USA

RATIONALE: The absence of an agreed-upon $\delta^{17}O$ value for the primary reference water SLAP leads to significant discrepancies in the reported values of $\delta^{17}O$ and the parameter $^{17}O_{excess}$. The accuracy of $\delta^{17}O$ and $^{17}O_{excess}$ values is significantly improved if the measurements are normalized using a two-point calibration, following the convention for $\delta^{2}H$ and $\delta^{18}O$ values.

METHODS: New measurements of the $\delta^{17}O$ values of SLAP2 and GISP are presented and compared with published data. Water samples were fluorinated with CoF_3. Helium carried the O_2 product to a 5A (4.2 to 4.4 Å) molecular sieve trap submerged in liquid nitrogen. The O_2 sample was introduced into a dual-inlet ThermoFinnigan MAT 253 isotope ratio mass spectrometer for measurement of *m/z* 32, 33, and 34. The $\delta^{18}O$ and $\delta^{17}O$ values were calculated after 90 comparisons with an O_2 reference gas.

RESULTS: We propose that the accepted $\delta^{17}O$ value of SLAP be defined in terms of $\delta^{18}O = -55.5$ ‰ and $^{17}O_{excess} = 0$, yielding a $\delta^{17}O$ value of approximately −29.6968 ‰. Using this definition for SLAP and the recommended normalization procedure, the $\delta^{17}O$ value of GISP is -13.16 ± 0.05 ‰ and the $^{17}O_{excess}$ value of GISP is 22 ± 11 per meg. Correcting previous published values of GISP $\delta^{17}O$ to both VSMOW and SLAP improves the inter-laboratory precision by about 10 per meg.

CONCLUSIONS: The data generated here and compiled from previous studies provide a substantial volume of evidence to evaluate the various normalization techniques currently used for triple oxygen isotope measurements. We recommend that reported $\delta^{17}O$ and $^{17}O_{excess}$ values be normalized to the VSMOW-SLAP scale, using a definition of SLAP such that its $^{17}O_{excess}$ is exactly zero. Copyright © 2013 John Wiley & Sons, Ltd.

The stable isotope ratios of water and ice are powerful tracers of the global hydrological system.[1,2] Recently, the development of a high-precision analytical method for the analysis of the triple oxygen isotopes of water has provided a new hydrological tracer: $^{17}O_{excess}$.[3,4] The stable isotope ratios of water are expressed in δ notation, where $\delta^{18}O$ and $\delta^{17}O$ are defined as $R/R_{VSMOW} - 1$, where $R(^{18}O/^{16}O)$ and $R(^{17}O/^{16}O)$ are determinations of $N(^{18}O)/N(^{16}O)$ and $N(^{17}O)/N(^{16}O)$, respectively; abbreviated herein as $(^{18}O/^{16}O)$ and $(^{17}O/^{16}O)$. VSMOW is Vienna Standard Mean Ocean Water, which was distributed between 1969 and approximately 2004 by the International Atomic Energy Agency (IAEA, Vienna, Austria). Combined measurements of $^{17}O/^{16}O$ and $^{18}O/^{16}O$ can be expressed with the parameter $^{17}O_{excess}$:

$$^{17}O_{excess} = \ln(\delta^{17}O + 1) - 0.528 \times \ln(\delta^{18}O + 1) \quad (1)$$

where $\delta^{18}O$ and $\delta^{17}O$ are unitless ratios. Variations in $^{17}O_{excess}$ are generally several orders of magnitude smaller than variations in $\delta^{18}O$ values and are conventionally expressed in per meg (10^{-6}). While oxygen isotopic ratios of natural waters were historically reported relative to SMOW,[5] using a single standard fixes only the zero-point of the δ scale, and an additional standard is needed for normalization,[6–8] to account for inter-laboratory scaling differences.[9] The Consultants' Meeting on Stable Isotope Standards and Intercalibration in Hydrology and in Geochemistry[10] recommended that oxygen isotope ratios be normalized on the VSMOW-SLAP scale, where the consensus value for $\delta^{18}O$ SLAP (Standard Light Antarctic Precipitation) is exactly −55.5 ‰ relative to VSMOW.[7] Due to the consumption of the original VSMOW and SLAP reference waters, two replacement reference waters, VSMOW2 and SLAP2, were developed. No significant difference between the original and replacement water $\delta^{18}O$ and $\delta^{17}O$ values has been detected[11] and hereafter we will treat VSMOW and SLAP as synonymous with VSMOW2 and SLAP2 when referring to the normalization of waters on the VSMOW-SLAP scale.[12] When discussing results of measured waters we explicitly label them as VSMOW, VSMOW2, SLAP, or SLAP2.

IAEA recommended that the reference waters VSMOW and SLAP be measured for both $^{18}O/^{16}O$ and $^{17}O/^{16}O$ isotopic ratios.[13] Since that recommendation, only a few published values for $\delta^{17}O$ of SLAP have been published,[3,14–16] and there is still no agreed-upon SLAP $\delta^{17}O$ value. Consequently, it has been routine to report $^{17}O_{excess}$ and $\delta^{17}O$ values without normalization (e.g.[3,17,18]) to SLAP. This has led to discrepancies between laboratories carrying out such measurements. A

* *Correspondence to:* S. W. Schoenemann, Department of Earth and Space Sciences, University of Washington, Johnson Hall Rm-070, Box 351310, Seattle, WA 98195–1310, USA.
E-mail: schoes@uw.edu

 Copyright © 2013 John Wiley & Sons, Ltd.

similar issue was recognized in the 1980s with the normalization of hydrogen isotopes, where the measured difference between two standards was found to vary among different isotope ratio mass spectrometers; when VSMOW and SLAP normalization was used, inter-laboratory differences were significantly reduced.[8,19] In this paper we show that inter-laboratory differences for $^{17}O_{excess}$ and $\delta^{17}O$ values are similarly reduced when a $\delta^{17}O$ value for SLAP is adopted. We present recommendations for normalizing $\delta^{17}O$ SLAP values based on high-precision $^{17}O_{excess}$ measurements of VSMOW2, SLAP2, and GISP (Greenland Ice Sheet Precipitation).

Throughout the paper, when we report values relative to VSMOW and SLAP, we adopt a notation similar to that of Kaiser[6] where all normalized δ values are clearly stated to be on the VSMOW-SLAP scale, using the form $\delta^{18}O^{normalized}_{s/VSMOW\text{-}SLAP}$, where the right superscript denotes 'measured', 'assigned', or 'normalized' and the right subscript denotes sample (s) normalized to VSMOW-SLAP ($_{s/VSMOW\text{-}SLAP}$). We use the form $\delta^{18}O_{s/VSMOW}$ for a sample that is referenced to VSMOW but has not been normalized on the VSMOW-SLAP scale. We use the term 'instrument slope' to refer to the quotient of $\delta^{18}O^{assigned}_{SLAP/VSMOW}$ to $\delta^{18}O^{measured}_{SLAP/VSMOW}$ occurring within an individual isotope ratio mass spectrometer. Here, 'measured' refers solely to the isotope ratio produced directly from the mass spectrometer and corrected only to VSMOW, without SLAP normalization. Throughout the paper, all equations are formatted as simple quantity equations without the commonly used extraneous factor of 10^3 or 10^6, as recommended by the 8th SI Brochure.[20]

EXPERIMENTAL

Measurement methods

Water was fluorinated to produce O_2 as previously described[3,4,21] and the O_2 was collected as in Abe.[22] Briefly, 2 μL of water was injected into a 370 °C 15 cm long nickel column containing 7 g CoF_3 converting H_2O into O_2 and creating HF and CoF_2 as byproducts. Helium carried O_2 at 30 mL min^{-1} through a trap submerged in liquid nitrogen to collect HF, which was later vented to a fume hood; the NaF trap originally recommended by Baker *et al.*[4] was not used. The O_2 sample was collected in a trap for 20 min, and then transferred to a 14 cm stainless steel cold finger. Both the trap and cold finger contained approximately 40 mg of 5A (4.2 to 4.4 Å) molecular sieve and were submerged in liquid nitrogen. To minimize memory effects, following Barkan and Luz,[3] we injected and discarded a minimum of four injections when switching between waters with a difference in $\delta^{18}O$ value of greater than 5.0 ‰. The cold fingers were sealed using a bellows valve (SS-4BKT or SS4H; Swagelok, Cleveland, OH, USA).

The O_2 samples were warmed to 60 °C and expanded for 10 min into the sample bellows through a custom multiport on a dual-inlet ThermoFinnigan MAT 253 isotope ratio mass spectrometer (Thermo Electron, Bremen, Germany) with Faraday cup amplifiers for *m/z* 32, 33, and 34 of 1×10^9 Ω, 1×10^{12} Ω, and 1×10^{11} Ω, respectively. The custom-designed multiport used air-actuated bellows valves (Swagelok SS-4BKT), air pressure control originally intended for a stock microvolume, and modified ISL scripts. The O_2 sample was analyzed for *m/z* 32, 33, and 34 abundance ratios to determine $\delta^{18}O$ and $\delta^{17}O$ values with reference to O_2 gas ($\delta^{17}O^{measured}_{s/VSMOW} = -4.319\text{‰} \pm 0.009$, $\delta^{18}O^{measured}_{s/VSMOW} = -8.255\text{‰} \pm 0.002$). Each mass spectrometric measurement comprised 90 sample-to-reference comparisons. Each of these comparisons consisted of 26 s of integration and 15 s of idle time. After every 30 comparisons, the *m/z* 32 signals of the sample and reference gases were balanced to 10 V and the mass spectrometer was peak-centered on *m/z* 33. The reference bellows was automatically refilled before each sample to a pressure that was equal to that of the sample. Over the course of these measurements the mass spectrometer exhibited an internal reproducibility of 0.002 ‰, 0.004 ‰, and 0.0037 ‰ (3.7 per meg) for $\delta^{17}O$, $\delta^{18}O$, and $^{17}O_{excess}$ values, respectively, where the internal reproducibility was calculated as the standard error of the mean ($\sigma/\sqrt{n-1}$, n = 90). The sample reproducibility associated with each reference water was given by the standard error (1σ) (Table 1) and the $\delta^{18}O$ precision was of the order of 0.1 ‰. The waters measured in this study included the CIAAW (Commission on Isotopic Abundances and Atomic Weights) primary reference waters (VSMOW2 IAEA No. 284 and SLAP2 IAEA No. 280) and the secondary reference water (GISP IAEA No. 1756), as well as four in-house reference waters (Penn, Seattle, WAIS, Vostok) and two reference waters (D57, TALOS) from the Laboratoire des Sciences du Climat et l'Environnement (LSCE, Gif –Sur-Yvette, France) (see Table 1).

Normalization methods

Normalization of meteoric waters to both VSMOW and SLAP has been recommended to eliminate instrumental bias.[7,23] When we report values relative to VSMOW without normalization to SLAP, we follow the correction technique given by Brand[24]:

$$\delta_{s/VSMOW} = \delta_{s/WG} + \delta_{WG/VSMOW} + (\delta_{s/WG})(\delta_{WG/VSMOW}) \quad (2)$$

where we measure VSMOW water converted into O_2 relative to our working gas ($\delta_{VSMOW/WG}$) and then determine the working gas with respect to VSMOW using:

$$\delta_{WG/VSMOW} = (\delta_{VSMOW/WG} + 1)^{-1} - 1 \quad (3)$$

for both $\delta^{17}O$ and $\delta^{18}O$ values.

Normalization to the VSMOW-SLAP scale is as follows:

$$\delta^{18}O^{normalized}_{s/VSMOW\text{-}SLAP} = \delta^{18}O^{measured}_{s/VSMOW}\frac{\left(\delta^{18}O^{assigned}_{SLAP/VSMOW}\right)}{\left(\delta^{18}O^{measured}_{SLAP/VSMOW}\right)} \quad (4)$$

where $\delta^{18}O^{assigned}_{SLAP/VSMOW} = -55.5\text{‰}$. We refer to this as the 'traditional linear' method. We propose normalization of $\delta^{17}O^{measured}_{s/VSMOW}$ values to $\delta^{17}O^{assigned}_{SLAP/VSMOW}$, using the same 'traditional linear' method as in Eqn. (4):

$$\delta^{17}O^{normalized(Schoenemann)}_{s/VSMOW\text{-}SLAP} = \delta^{17}O^{measured}_{s/VSMOW}\frac{\left(\delta^{17}O^{assigned}_{SLAP/VSMOW}\right)}{\left(\delta^{17}O^{measured}_{SLAP/VSMOW}\right)} \quad (5)$$

where the $\delta^{17}O^{assigned}_{SLAP/VSMOW}$ value is not yet agreed upon.

 Copyright © 2013 John Wiley & Sons, Ltd.

Table 1. University of Washington-IsoLab measurements of $\delta^{17}O$ and $\delta^{18}O$ isotope values of reference waters on the VSMOW-SLAP scale. Stated uncertainties are 1σ standard error of the mean of each sample including chemical preparation for $\delta^{17}O$ and $\delta^{18}O$, and 1σ standard deviation for $^{17}O_{excess}$. n = number of samples. 'Kaiser' $\delta^{17}O_{\text{VSMOW-SLAP}}$ values are normalized to $\delta^{18}O^{assigned}_{SLAP/VSMOW} = -55.5$ ‰ by Eqn. (8), identical to Eqn. (37) in Kaiser.[6] 'Schoenemann' $\delta^{17}O_{\text{VSMOW-SLAP}}$ values are normalized to $\delta^{18}O^{assigned}_{SLAP/VSMOW} = -55.5$ ‰ and $^{17}O_{excess} = 0$ by Eqn. (5) with the $\delta^{17}O^{assigned}_{SLAP/VSMOW}$ calculated using Eqn. (9). Note that we present our $\delta^{17}O^{measured}_{s/VSMOW}$ and $\delta^{18}O^{measured}_{s/VSMOW}$ data to the third decimal place (following e.g. Luz and Barkan[26]) in order to reduce rounding errors and reproducibility of $^{17}O_{excess}$ calculations in this paper.

Sample waters	n	$\delta^{17}O^{measured}_{VSMOW}$ (‰)	± 1σ	$\delta^{18}O^{measured}_{VSMOW}$ (‰)	± 1σ	$^{17}O_{excess\ VSMOW}$ (per meg) Measured	± 1σ	$\delta^{17}O^{normalized}_{VSMOW\text{-}SLAP}$ (‰) Kaiser	$\delta^{17}O^{normalized}_{VSMOW\text{-}SLAP}$ (‰) Schoenemann	$\delta^{18}O^{normalized}_{VSMOW\text{-}SLAP}$ (‰) *trad. linear*	$^{17}O_{excess\ VSMOW\text{-}SLAP}$ (per meg) *trad. linear*	± 1σ
VSMOW2	20	0.000	± 0.06	0.000	± 0.10	0	0	0.000	0.000	0.000	0	0
SLAP2	19	−28.822	± 0.04	−53.874	± 0.08	−6	± 8	−29.704	−29.699	−55.50	0	0
GISP	20	−12.725	± 0.04	−24.014	± 0.08	27	± 4	−13.115	−13.112	−24.739	28	± 4
WAIS	20	−17.421	± 0.04	−32.783	± 0.07	26	± 8	−17.954	−17.950	−33.773	27	± 8
Vostok	9	−29.659	± 0.07	−55.424	± 0.14	−2	± 8	−30.567	−30.561	−57.097	5	± 8
Seattle	16	−5.578	± 0.03	−10.602	± 0.06	34	± 5	−5.749	−5.748	−10.922	34	± 5
Penn	12	−3.573	± 0.03	−6.814	± 0.06	31	± 5	−3.682	−3.682	−7.020	31	± 5
LSCE D57	2	−16.990	± 0.06	−31.964	± 0.11	16	± 3	−17.510	−17.506	−32.928	17	± 3
LSCE Talos	4	−20.897	± 0.04	−39.123	± 0.07	−46	± 3	−21.536	−21.532	−40.304	−46	± 3

An alternative normalization of $\delta^{17}O^{measured}_{s/VSMOW}$ using $\left(\delta^{18}O^{assigned}_{SLAP/VSMOW}\right)/\left(\delta^{18}O^{measured}_{SLAP/VSMOW}\right)$ in place of the right-hand fraction in Eqn. (5) is only appropriate if the instrument slope (the quotient of assigned to measured values) can be demonstrated to be the same for $\delta^{18}O$ values as for $\delta^{17}O$ values. We refer to this linear normalization as the '$\delta^{18}O$ Approximation' method and do not recommend its usage; we include it here in the interest of completeness.

Three other normalization approaches have been used, and, while the differences among them are unimportant for $\delta^{18}O$ values, they lead to significantly different $^{17}O_{excess}$ values. Jabeen and Kusakabe[14] used a linear approach similar to Eqn (5), but where $\delta^{17}O^{measured}_{SLAP/VSMOW}$ is assumed to be $0.52 \times \delta^{18}O^{assigned}_{SLAP/VSMOW}$:

$$\delta^{17}O^{normalized}_{s/VSMOW\text{-}SLAP} = \delta^{17}O^{measured}_{s/VSMOW} \frac{\left(0.52 \times \delta^{18}O^{assigned}_{SLAP/VSMOW}\right)}{\left(\delta^{17}O^{measured}_{SLAP/VSMOW}\right)} \tag{6}$$

We refer to this as the '$\delta^{17}O$ Approximation' method. Another normalization approach, introduced by Kusakabe and Matsuhisa,[15] uses a linear correction that includes the natural log of $\delta^{17}O^{measured}_{s/VSMOW}$, $\delta^{18}O^{measured}_{SLAP/VSMOW}$, and $\delta^{18}O^{assigned}_{SLAP/VSMOW}$ for the VSMOW-SLAP normalization, as follows:

$$\delta^{17}O^{normalized(Kusakabe)}_{s/VSMOW\text{-}SLAP} = \exp\left(\frac{\ln\left(\delta^{17}O^{measured}_{s/VSMOW}+1\right)}{\ln\left(\delta^{18}O^{measured}_{SLAP/VSMOW}+1\right)}\ln\left(\delta^{18}O^{assigned}_{SLAP/VSMOW}+1\right)\right) - 1 \tag{7}$$

We refer to this logarithmic method as 'Kusakabe' normalization.

Finally, Kaiser[6] proposed to normalize $\delta^{17}O$ values to VSMOW-SLAP as:

$$\delta^{17}O^{normalized(Kaiser)}_{s/VSMOW\text{-}SLAP} = \frac{\left(\delta^{17}O^{measured}_{s/VSMOW}\right)}{\left(\delta^{18}O^{measured}_{SLAP/VSMOW}+1\right)^{0.528}}\left(\delta^{18}O^{assigned}_{SLAP/VSMOW}+1\right)^{0.528} - 1 \tag{8}$$

In this case, (s/VSMOW) is the measured $\delta^{17}O$ value of SLAP versus VSMOW.[7,8] Note that the left-hand side of the above equation has been labeled as $\delta^{17}O^{normalized(Kaiser)}_{s/VSMOW\text{-}SLAP}$ rather than $\delta^{17}O^{normalized}_{s/VSMOW}$ as in Kaiser[6] to unambiguously indicate normalization on the VSMOW-SLAP scale. Equation (8) reduces to Eqn. (5) when $\ln(\delta^{17}O+1) = 0.528 \times \ln(\delta^{18}O+1)$, as is implicitly assumed in Kaiser[6] and other work.[25] This implies a $^{17}O_{excess}$ value equal to zero and therefore an 'expected' SLAP $\delta^{17}O$ value of approximately −29.6986 ‰. As we will show, zero is an appropriate choice for $^{17}O_{excess}$ of SLAP.

wileyonlinelibrary.com/journal/rcm Copyright © 2013 John Wiley & Sons, Ltd.

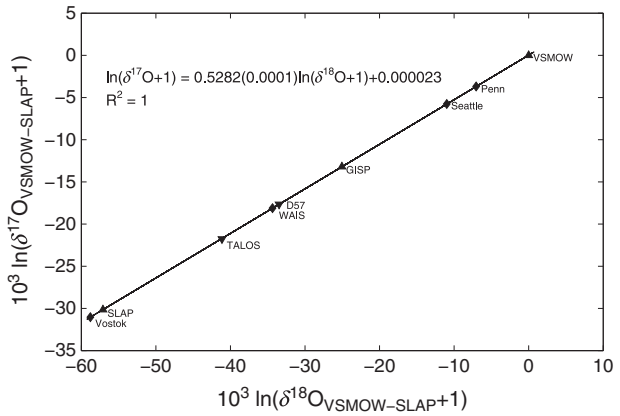

Figure 1. Plot of $\ln(\delta^{17}O + 1)$ vs. $\ln(\delta^{18}O + 1)$ showing the isotopic composition of all meteoric waters measured and the slope of the Global Meteoric Water Line (GMWL). $\ln(\delta^{17}O + 1) = 0.5282\ (\pm\ 0.0001) \times \ln(\delta^{18}O + 1) + 0.000023$ ($R^2 = 1.00000$, standard error at 95 % confidence limit). Talos is not included in the calculation of the GMWL. The error bars are smaller than the size of the symbols. All values are VSMOW-SLAP normalized using the *'traditional linear'* method by Eqns. (4) and (5).

RESULTS

Table 1 summarizes paired $\delta^{17}O$ and $\delta^{18}O$ measurements made at the University of Washington-Isolab (UW) with and without normalization to VSMOW and VSMOW-SLAP, and using the various normalization methods discussed above. Figure 1 shows $\delta^{17}O^{normalized}_{VSMOW\text{-}SLAP}$ and $\delta^{18}O^{normalized}_{VSMOW\text{-}SLAP}$ results from all UW-analyzed reference waters in Table 1, using 'traditional linear' normalization (Eqn. (5)) with $^{17}O_{excess}$ value of SLAP = 0; the best fit line is $\ln(\delta^{17}O + 1) = (0.5282 \pm 0.0001) \times \ln(\delta^{18}O + 1) + 0.000023$ (95 % confidence intervals). The intercept represents the average $^{17}O_{excess}$ value of meteoric (Antarctic and North American) waters with respect to VSMOW and SLAP (Fig. 2). These results are indistinguishable from independent estimates of the global meteoric water line slope by Luz and Barkan[26] (0.528 ± 0.0001), Meijer and Li[27] (0.5281 ± 0.0015) and Kusakabe and Matsuhisa[15] (0.5282 ± 0.001), confirming that the definition of $^{17}O_{excess}$ using a slope of 0.528 is appropriate.

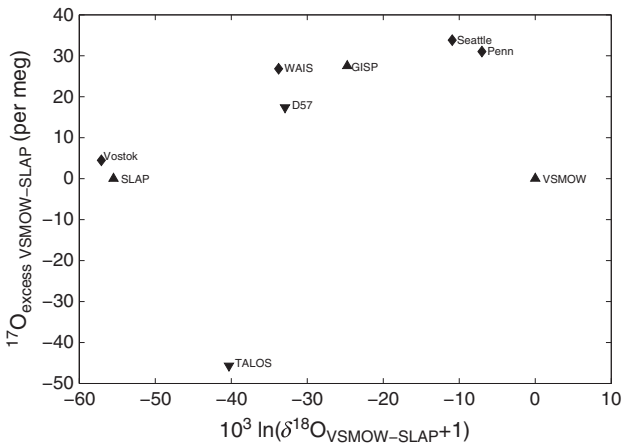

Figure 2. Mean values of $^{17}O_{excess\ VSMOW\text{-}SLAP}$ for meteoric (Antarctic and North American) waters with respect to $\delta^{18}O_{VSMOW\text{-}SLAP}$ values normalized by Eqns. (4) and (5).

All data from Table 1, along with all published $\delta^{17}O$ and $\delta^{18}O$ values of SLAP and GISP, are summarized in Table 2. Here we limit the review to dual-inlet isotope ratio mass spectrometry (IRMS), except for one continuous-flow IRMS study[16] that has comparable precision. We compare the various normalization methods (Eqns. (3), (4), (5) and (8)). In columns 4 through 7 of Table 2, we report the published values of $\delta^{17}O^{measured}_{s/VSMOW}$ and $\delta^{18}O^{measured}_{s/VSMOW}$, and the standard error of the mean based on number of samples measured. In column 8, we normalize the $\delta^{17}O$ values to the VSMOW-SLAP scale using the 'Kaiser' (Eqn. (8)) normalization, while we use the 'traditional linear' method (Eqn. (4)) to normalize the $\delta^{18}O$ values in column 10, where we define $\delta^{17}O^{assigned}_{SLAP/VSMOW}$ such that SLAP $^{17}O_{excess} = 0$.

The 'Kaiser' normalization is useful for comparison among the published $SLAP_{(s/VSMOW)}$ results in Table 2. After normalization by Eqn. (8), the inter-laboratory agreement in SLAP $\delta^{17}O$ and $\delta^{18}O$ values was significantly improved compared with the original reported (s/VSMOW) values (SLAP $\delta^{17}O$ standard deviation decreased from 0.43 to 0.03 ‰). The $\delta^{17}O^{normalized(Kaiser)}_{SLAP2/VSMOW\text{-}SLAP}$ values measured in our lab were −29.70 ‰, in excellent agreement with the 'Kaiser'-normalized values for $\delta^{17}O$ SLAP reported in various previous studies: –29.73 ‰,[6,16] –29.64 ‰,[6,14] –29.69 ‰,[3,6] –29.67 ‰,[15] –29.67 ‰,[11] and SLAP2 –29.68 ‰.[11] The average $\delta^{17}O^{normalized(Kaiser)}_{SLAP/VSMOW\text{-}SLAP}$ value for SLAP from all studies was -29.68 ± 0.03 ‰ (1σ). Inter-laboratory agreement was also improved for GISP: the 'Kaiser' normalization reduced the standard deviation for $\delta^{17}O$ from 0.24 ‰ for raw measured values to 0.06 ‰. The 'traditional linear' method produced a comparable improvement, resulting in average GISP values of $\delta^{17}O^{normalized(Schoenemann)}_{GISP/VSMOW\text{-}SLAP} = -13.12 \pm 0.06$ ‰ and $\delta^{18}O^{normalized(Schoenemann)}_{GISP/VSMOW\text{-}SLAP} = -24.79 \pm 0.08$ ‰, in excellent agreement with the IAEA $\delta^{18}O$ value (-24.78 ± 0.075 ‰).

In Table 3, we show $^{17}O_{excess}$ values calculated from all the data in Table 2. For our 'measured' SLAP2 reference water we determined a $^{17}O_{excess\ VSMOW}$ value of -6 ± 8 per meg. Averaging of all the 'measured' SLAP $^{17}O_{excess\ VSMOW}$ values yielded a mean of 15 ± 28 per meg. The calculated SLAP $^{17}O_{excess\ VSMOW\text{-}SLAP}$ values using the 'Kaiser'-normalized values ($\delta^{17}O^{normalized(Kaiser)}_{s/VSMOW\text{-}SLAP}$ and $\delta^{18}O^{normalized(Kaiser)}_{s/VSMOW\text{-}SLAP}$) spanned from −28 to 60 per meg, similar in range to the '$\delta^{18}O$ Approximation' and the 'Kusakabe' VSMOW-SLAP normalized values. An advantage of the Kaiser[6] method is that is preserves the original measured $^{17}O_{excess}$ from $\delta^{17}O_{s/VSMOW}$ and $\delta^{18}O_{s/VSMOW}$, while adjusting the $\delta^{17}O_{s/VSMOW}$ values to the accepted $\delta^{18}O_{SLAP/VSMOW}$ (−55.5 ‰). This is apparent in the comparison of 'measured' $^{17}O_{excess\ VSMOW}$ versus 'Kaiser' $^{17}O_{excess\ VSMOW\text{-}SLAP}$ in Table 3. In the last column of Table 3, the calculated GISP $^{17}O_{excess\ VSMOW\text{-}SLAP}$ values using the 'Schoenemann'-normalized technique yield an average of 48 ± 34 per meg. Note, however, that most previous work did not report $^{17}O_{excess}$, and in most cases there was insufficient data shown to calculate it accurately. To determine a best estimate for the $^{17}O_{excess\ VSMOW\text{-}SLAP}$ of GISP, we therefore used the three $\delta^{17}O$ and $\delta^{18}O$ datasets [3,15, this study] that have the best reported precision and the largest number of measurements to date. The weighted average values are GISP $\delta^{17}O = -13.16 \pm 0.05$ ‰ and $^{17}O_{excess} = 22 \pm 11$ per meg, as reported in Tables 2 and 3.

 Copyright © 2013 John Wiley & Sons, Ltd.

Table 2. Summary of $\delta^{17}O$ and $\delta^{18}O$ isotopic compositions of SLAP and GISP relative to VSMOW and VSMOW-SLAP for all studies reviewed. Stated uncertainties are 1σ standard deviations of the distribution of analyses and 1σ standard error of the mean. n = number of samples in each study. SLAP $\delta^{17}O^{normalized}_{VSMOW\text{-}SLAP}$ values normalized to $\delta^{18}O^{assigned}_{SLAP/VSMOW} = -55.5$ ‰ by Eqn. (8), and Eqn. (5). GISP $\delta^{17}O^{normalized}_{VSMOW\text{-}SLAP}$ values normalized to $\delta^{17}O^{assigned}_{SLAP/VSMOW} \approx -29.6986$ ‰ by Eqn. (5). Italics represent additional significant figures carried beyond 2 decimal places for this study's data, included to avoid rounding errors when calculating $^{17}O_{excess}$ to the per meg level.

Sample Waters	References	n	$\delta^{17}O^{measured}_{VSMOW}$ (‰)	1σ SE (‰)	$\delta^{18}O^{measured}_{VSMOW}$ (‰)	1σ SE (‰)	$\delta^{17}O^{normalized}_{VSMOW\text{-}SLAP}$ (‰) Kaiser	$\delta^{17}O^{normalized}_{VSMOW\text{-}SLAP}$ (‰) Schoenemann	$\delta^{18}O^{normalized}_{VSMOW\text{-}SLAP}$ (‰) *trad. linear*
SLAP	Li *et al.*[16] (BrF_5)	13	−29.90	± 0.04	−55.82	± 0.02	−29.73	≈ −29.6986	−55.5
	Jabeen and Kusakabe[14] (BrF_5)	6	−28.58	± 0.05	−53.54	± 0.06	−29.64	≈ −29.6986	−55.5
							−28.86[a]		−55.5
	Barkan and Luz[3] (CoF_3)	20	−29.48	± 0.02	−55.11	± 0.03	−29.69	≈ −29.6986	−55.5
	Kusakabe and Matsuhisa[15] (BrF_5)	5	−29.21	± 0.03	−54.65	± 0.03	−29.67	≈ −29.6986	−55.5
	Lin *et al.*[11] (BrF_5)	4	−29.06	± 0.04	−54.38	± 0.06	−29.67	≈ −29.6986	−55.5
SLAP2	Lin *et al.*[11] (BrF_5)	2	−29.19	± 0.10	−54.59	± 0.17	−29.68	≈ −29.6986	−55.5
	This study (CoF_3)	19	−28.822	± 0.05	−53.874	± 0.08	−29.704	≈ −29.6986	−55.5
	Average ± Stdev (1σ)		**−29.18 ± 0.43**		**−54.57 ± 0.76**		**−29.68 ± 0.03**	**≈ −29.6986**	**−55.5**
	IAEA				**−55.45 ± 0.17**		[c]	[c]	**−55.5**
GISP	Li *et al.*[16] (BrF_5)	16	−13.14	± 0.03	−24.83	± 0.03	−13.06	−13.05	−24.69[b]
	Jabeen and Kusakabe[14] (BrF_5)	6	−12.59	± 0.04	−23.94	± 0.05	−13.06	−13.08	−24.82[b]
							−12.71[a]		−24.83[a]
	Barkan and Luz[3] (CoF_3)	20	−13.12	± 0.01	−24.73	± 0.01	−13.21	−13.22	−24.91[b]
	Kusakabe and Matsuhisa[15] (BrF_5)	6	−12.91	± 0.03	−24.41	± 0.03	−13.11	−13.13	−24.79[b]
	This Study (CoF_3)	20	−12.726	± 0.04	−24.014	± 0.06	−13.115	−13.112	−24.739[b]
	Average ± Stdev (1σ)		**−12.90 ± 0.24**		**−24.38 ± 0.40**		**−13.11 ± 0.06**	**−13.12 ± 0.06**	**−24.79 ± 0.08**
	Barkan, Kusakabe, Schoenemann Weighted Avg ± Stdev (1σ)		**−12.92 ± 0.19**		**−24.38 ± 0.34**		**−13.16 ± 0.05**	**−13.16 ± 0.05**	**−24.82 ± 0.08**
	IAEA				**−24.78 ± 0.075**		[c]	[c]	**−24.78**[b]

[a]Original published values, where $\delta^{17}O^{assigned}_{SLAP/VSMOW}$ obtained when $\delta^{18}O^{assigned}_{SLAP/VSMOW}$ is multiplied by 0.52.

[b]traditional linear correction, where $\delta^{18}O^{normalized}_{s/VSMOW\text{-}SLAP} = \delta^{18}O^{measured}_{s/VSMOW} \times (-55.5\text{ ‰}/\delta^{18}O^{measured}_{SLAP/VSMOW})$.

[c]IAEA has not assigned an accepted value for $\delta^{17}O$ of SLAP or GISP.

Copyright © 2013 John Wiley & Sons, Ltd.

Table 3. Comparison of calculated $^{17}O_{excess}$ values using '$\delta^{18}O$ Approx.', 'Kusakabe', 'Kaiser', and 'Schoenemann'. $^{17}O_{excess}$ is the offset from the GMWL (calculated using Eqn. (1) according to Luz and Barkan[26]) with a slope of 0.5280. Our proposed normalization method ('traditional linear', SLAP $^{17}O_{excess} = 0$) provides the best inter-laboratory agreement (see GISP standard deviation). $\delta^{17}O_{VSMOW\text{-}SLAP}$ values are normalized to $\delta^{18}O^{assigned}_{SLAP/VSMOW} = -55.5$ ‰ using the normalization techniques discussed in the text, starting with a linear approximation scaling (Eqn. (6)), logarithmic linear scaling (Eqn. (7)), exponential scaling (Eqn. (8)), and lastly This Study's recommended traditional linear scaling (Eqns. (4) and (5)) with $^{17}O_{excess}$ of SLAP = 0 (Eqn. (9)). Note that $\delta^{17}O$ and $\delta^{18}O$ values are reported to only two decimal places in Table 2; these $^{17}O_{excess}$ values could change if the $\delta^{17}O$ and $\delta^{18}O$ values were reported to a third decimal place. $^{17}O_{excess}$ precision values are not reported due to only two decimal places reported by other studies

Sample Waters	References	n	$^{17}O_{excess\ VSMOW}$ (per meg) Measured	$^{17}O_{excess\ VSMOW\text{-}SLAP}$ (per meg) $\delta^{18}O$ Approx. *linear*	$^{17}O_{excess\ VSMOW\text{-}SLAP}$ (per meg) Kusakabe *logarithmic*	$^{17}O_{excess\ VSMOW\text{-}SLAP}$ (per meg) Kaiser *exponential*	$^{17}O_{excess\ VSMOW\text{-}SLAP}$ (per meg) Schoenemann *trad. linear*
SLAP	Li *et al.*[16]	13	−29	−31	−29	−28	0
	Jabeen and Kusakabe[14]	6	58	75	60	60	0
	Barkan and Luz[3]	20	7[a]	10	7	7	0
	Kusakabe and Matsuhisa[15]	5	28[b]	35	29	29	0
	Lin *et al.*[11]	4	32	41	33	33	0
SLAP2	Lin *et al.*[11]	2	16	23	16	16	0
	This study	19	−6	6	−6	−6	0
	Average ± Stdev (1σ)		**15 ± 28**	**23 ± 33**	**16 ± 29**	**16 ± 29**	**0**
GISP	Li *et al.*[16]	16	49	48	48	49	61
	Jabeen and Kusakabe[14]	6	124	132	129	125	99
	Barkan and Luz[3]	20	15	15	13	14	11
	Kusakabe and Matsuhisa[15]	6	54[b]	56	52	54	41
	This study	20	27	30	22	25	28
	Average ± Stdev (1σ)		**54 ± 42**	**56 ± 45**	**53 ± 46**	**53 ± 43**	**48 ± 34**
	Barkan, Kusakabe, Schoenemann Weighted Avg ± Stdev (1σ)		**25 ± 13**	**27 ± 13**	**22 ± 12**	**24 ± 13**	**22 ± 11**

[a]Reported with no VSMOW-SLAP scaling.
[b]VSMOW-SLAP normalization by Eqn. (7). Note that Kusakabe and Matsuhisa[15] calculated $^{17}O_{excess}$ values of 40 and 70 per meg, for SLAP and GISP, respectively, using slope = 0.5282.

Copyright © 2013 John Wiley & Sons, Ltd.

DISCUSSION

Two important findings can be drawn from the data compiled in Tables 1–3. First, neither our data, nor any other published results, suggest a $^{17}O_{excess\ VSMOW}$ value for SLAP that is distinguishable from zero. This is true regardless of the normalization procedure used. Second, normalization to the VSMOW-SLAP scale significantly reduces the inter-laboratory differences in the measurement of the $\delta^{17}O$ value of SLAP. The average $\delta^{17}O$ value for all 'Kaiser'-normalized measurements (-29.68 ± 0.03 ‰) is well within the measurement error of the value obtained when SLAP $^{17}O_{excess}$ is defined to be identically zero. Note, however, that 'Kaiser' normalization did not greatly improve inter-laboratory differences in measurements of the $^{17}O_{excess}$ of GISP (Table 3). Here, the lack of a definition of $^{17}O_{excess}$ for SLAP becomes apparent.

Based on these results, we propose that a new procedure for calculating $^{17}O_{excess}$ be adopted. We recommend normalization to the VSMOW-SLAP scale using the 'traditional linear' method, using an assigned $\delta^{17}O_{SLAP/VSMOW}$ value based on the accepted $\delta^{18}O_{SLAP/VSMOW}$ of −55.5 ‰ and $^{17}O_{excess} = 0$. This requires using the following equation to solve for the assigned $\delta^{17}O_{SLAP/VSMOW}$:

$$\delta^{17}O^{normalized}_{SLAP/VSMOW} = \exp\left(^{17}O^{assigned}_{excess} + 0.528 \times \ln\left(\delta^{18}O^{assigned}_{SLAP/VSMOW} + 1\right)\right) - 1 \quad (9)$$

where $^{17}O^{assigned}_{excess} = 0$. This yields $\delta^{17}O^{assigned}_{SLAP/VSMOW} = -29.6986$ ‰ approximated to four decimal places. As noted above, the 'Kaiser' normalization (Eqn. (8)) becomes identical to the 'traditional linear' formulation of Eqn. (5), using this definition of $\delta^{17}O^{assigned}_{SLAP/VSMOW}$.

In contrast, the linear scaling using the log transform of the $\delta^{17}O$ and $\delta^{18}O$ values as recommended in Kusakabe and Matsuhisa[15] alters the currently accepted $\delta^{18}O$ values for all international standards, and is unnecessary as long as the log definition of $^{17}O_{excess}$ is maintained (i.e. $^{17}O_{excess} = \ln(\delta^{17}O + 1) - 0.528 \times \ln(\delta^{18}O + 1)$).

A major advantage of our recommended approach for normalization of $\delta^{17}O$ values is that it is straightforward, and is the same approach that most laboratories currently use for $\delta^{18}O$ values. Furthermore, the resulting inter-laboratory differences in $\delta^{18}O$ and $^{17}O_{excess}$ values for all other reference waters are reduced. This is illustrated by the results for GISP in Tables 2 and 3. As expected, the precision of the $\delta^{18}O$ value of GISP among the published studies is improved from 0.40 ‰ to 0.08 ‰ when normalization to the VSMOW-SLAP scale is used. Similarly, when our proposed method of $\delta^{17}O$ normalization is employed, the precision of $^{17}O_{excess\ VSMOW\text{-}SLAP}$ of GISP is improved by ~10 per meg (Table 3).

We note that because there has been no defined value for the $\delta^{17}O$ of SLAP, some recent studies[17,18] have used the $\delta^{17}O_{s/VSMOW}$ SLAP values reported by Barkan and Luz,[3] which were based on the assumption of identical instrument slopes for both $\delta^{17}O$ and $\delta^{18}O$, as well as a value for $\delta^{18}O$ SLAP of −55.11 ‰, which differs from the recommended IAEA accepted value of −55.5 ‰. This complicates comparison of published $^{17}O_{excess}$ measurements, and also may create confusion about reported $\delta^{18}O$ values. Using our recommended normalization approach, the instrument slope in our laboratory for $\delta^{17}O$ is −29.6986/−28.822 = 1.0304. This is very similar to the instrument slope for $\delta^{18}O$ (−55.5/−53.874 = 1.0302), but it is not identical. Defining both $\delta^{17}O$ and $\delta^{18}O$ SLAP values makes assumptions about the instrument slope unnecessary.

Our results also show that the individual precision of the $\delta^{18}O$ and $\delta^{17}O$ values need not be as high as implied in some previous work (e.g. Barkan and Luz[3]). As noted by Barkan and Luz,[21] the errors in $\delta^{18}O$ and $\delta^{17}O$ values are covarying; therefore, very precise and accurate $^{17}O_{excess}$ measurements can be made even when the individual $\delta^{18}O$ and $\delta^{17}O$ errors are relatively large (e.g. a few tenths of a per mil). There are several possible sources of correlated error in $\delta^{18}O$ and δ^{17} O values: during sample preparation these include fractionation occurring during equilibrium phase changes, diffusive fractionation of water, fractionation of O_2 during the freezing of O_2; in the mass spectrometer, fractionation or preferential ionization may occur in the mass spectrometer source. In all cases, the relationship between the errors in $\delta^{18}O$ and $\delta^{17}O$ values will follow a slope of about 0.52.[28] It can be shown that the error in $^{17}O_{excess}$ then depends primarily on the difference between the actual slope of the correlated errors and the slope of the definition of $^{17}O_{excess}$: 0.528. For example, in the case where the relationship between errors in $\ln(\delta^{18}O + 1)$ and $\ln(\delta^{17}O + 1)$ is 0.54, the error in $^{17}O_{excess}$ assuming no independent (uncorrelated) errors, is simply given by:

$$\sigma^2_{xs} = ((0.54 - 0.528) \times \ln(\sigma_{18} + 1))^2 \quad (10)$$

where, for example, if the measured $\delta^{18}O$ error $\sigma_{18} = 0.36$ ‰, the resulting $^{17}O_{excess}$ error is only $\sigma_{xs} = 4.3$ per meg. This is comparable with our measurement reproducibity for SLAP2 and GISP. In contrast, with uncorrelated errors, the relevant equation would be $\sigma^2_{xs} = (\ln(\sigma_{17} + 1))^2 + \left(0.528 \times (\ln(\sigma_{18} + 1))\right)^2$ and assuming $\sigma_{18} = 0.36$ ‰ and $\sigma_{17} = \sigma_{18}/2$, we would obtain σ_{xs} = 269 per meg, which is obviously well outside the range of our measured standard sample reproducibility.

CONCLUSIONS

We have measured the triple oxygen isotopic ratios of meteoric waters, including VSMOW2, SLAP2, and GISP, using the established methods of Barkan and Luz,[3] with the modification suggested by Abe,[22] where the final O_2 collection uses molecular sieve/liquid nitrogen rather than liquid helium. We obtain a meteoric water line with a slope of 0.5282 ± 0.0001 (standard error at 95 % confidence limit), indistinguishable from that of Luz and Barkan,[26] supporting the use of the slope 0.528 in the definition of $^{17}O_{excess}$.

The increasingly common use of $^{17}O_{excess}$ in applications using water isotopes makes it important that there be no ambiguity in the definition of measurement standards and normalization procedures among different laboratories. How one chooses to normalize oxygen isotopic measurements to the VSMOW-SLAP scale has a significant effect on $^{17}O_{excess}$. Published $^{17}O_{excess}$ values vary by as much as 33 per meg depending on the practice of normalization. We recommend using the conventional method of linear scaling for $\delta^{17}O$ values that is already commonly used for $\delta^{18}O$ values (Eqn. (5)):

Copyright © 2013 John Wiley & Sons, Ltd.

$$\delta^{17}O^{\text{normalized(Schoenemann)}}_{\text{s/VSMOW-SLAP}} = \delta^{17}O^{\text{normalized}}_{\text{s/VSMOW}} \frac{\left(\delta^{17}O^{\text{assigned}}_{\text{SLAP/VSMOW}}\right)}{\left(\delta^{17}O^{\text{measured}}_{\text{SLAP/VSMOW}}\right)}$$

where $\delta^{17}O^{\text{assigned}}_{\text{SLAP/VSMOW}}$ is defined in terms of the $^{17}O_{\text{excess}}$ of SLAP, which is assigned to be identically 0. The $\delta^{17}O^{\text{assigned}}_{\text{SLAP/VSMOW}}$ is then defined precisely as:

$$\delta^{17}O^{\text{assigned}}_{\text{SLAP/VSMOW}} = \exp(0.528 \times \ln(-0.0555 + 1)) - 1 \quad (11)$$

This results in an approximate value of $\delta^{17}O^{\text{assigned}}_{\text{SLAP/VSMOW}} = -29.6986$ ‰, but we emphasize $\delta^{17}O^{\text{assigned}}_{\text{SLAP/VSMOW}}$ be defined only in terms of its assigned $\delta^{18}O$ and $^{17}O_{\text{excess}}$ values. We note that, in general, reporting $\delta^{17}O$ and $\delta^{18}O$ values only to their individual measurement precision (typically, to two decimal places) is not adequate for $^{17}O_{\text{excess}}$ calculations. Because $^{17}O_{\text{excess}}$ can be measured to significantly greater precision than either $\delta^{17}O$ and $\delta^{18}O$ values, we recommend that $^{17}O_{\text{excess}}$ values of measured samples always be reported when available, rather than reporting only $\delta^{17}O$ and $\delta^{18}O$ values.

The normalization and reporting procedure that we recommend has several advantages over previous approaches. First, because it defines a value for the $\delta^{17}O$ of SLAP, inter-laboratory differences in both $\delta^{17}O$ and $^{17}O_{\text{excess}}$ measurements are reduced. This is consistent with the original adoption of $\delta^{18}O$ of SLAP = −55.5 ‰, and the recommendation that all $\delta^{18}O$ values be normalized to the VSMOW-SLAP scale.[8,29] Second, the adoption of $^{17}O_{\text{excess}}$ of SLAP to be defined as zero is consistent with all previous results, which cannot distinguish the $^{17}O_{\text{excess}}$ of SLAP (or SLAP2) from zero. Finally, several published values for the $\delta^{17}O$ of SLAP have assumed implicitly the $^{17}O_{\text{excess}}$ of SLAP to be zero (e.g. Kaiser[6] and Franz and Röckmann[25] state that the 'expected' SLAP $\delta^{17}O = 0.528 \times \ln(\delta^{18}O + 1)$).

Laboratories are encouraged to measure the reference water GISP to ensure proper calibration to the VSMOW-SLAP scale. When our proposed method of $\delta^{17}O$ normalization is employed, the inter-laboratory differences for both $\delta^{17}O$ and $^{17}O_{\text{excess}}$ values for GISP are reduced. Using the most precise $\delta^{17}O$ and $\delta^{18}O$ data from Table 2, we find that the weighted average value for GISP is $\delta^{17}O^{\text{normalized}}_{\text{VSMOW-SLAP}} = -13.16 \pm 0.05$‰ and $^{17}O_{\text{excess VSMOW-SLAP}} = 22 \pm 11$ per meg. We do not recommend adopting a $\delta^{17}O$ value for GISP but, based on the most precise and largest number of measurements available (Barkan and Luz,[3] Kusakabe and Matsuhisa,[15] and This Study), the GISP $^{17}O_{\text{excess VSMOW-SLAP}}$ value of 22 ± 11 per meg should be taken as the current best estimate.

Acknowledgements

We thank Kyle Samek and Beth Vanden Heuvel for assistance with the measurements, Becky Alexander for use of the MAT 253, and B. Luz, E. Barkan, and A. Landais for their advice on sample preparation and for sharing reference waters. This work was supported by grant OPP-ANT 0837990 from the U.S. National Science Foundation and by the University of Washington Quaternary Research Center. Constructive comments by two anonymous reviewers led to improvements in the manuscript.

REFERENCES

[1] W. Dansgaard. Stable isotopes in precipitation. *Tellus* **1964**, *16*, 436.
[2] L. Merlivat, J. Jouzel. Global climatic interpretation of the deuterium-oxygen 18 relationship for precipitation. *J. Geophys. Res.* **1979**, *84*, 5029.
[3] E. Barkan, B. Luz. High precision measurements of $^{17}O/^{16}O$ and $^{18}O/^{16}O$ ratios in H_2O. *Rapid Commun. Mass Spectrom.* **2005**, *19*, 3737.
[4] L. Baker, I. A. Franchi, J. Maynard, I. P. Wright, C. T. Pillinger. A technique for the determination of $^{18}O/^{16}O$ and $^{17}O/^{16}O$ isotopic ratios in water from small liquid and solid samples. *Anal. Chem.* **2002**, *74*, 1665.
[5] H. Craig. Standard for reporting concentrations of deuterium and oxygen-18 in natural waters. *Science* **1961**, *133*, 1833.
[6] J. Kaiser. Reformulated ^{17}O correction of mass spectrometric stable isotope measurements in carbon dioxide and a critical appraisal of historic 'absolute' carbon and oxygen isotope ratios. *Geochim. Cosmochim. Acta* **2008**, *72*, 1312.
[7] R. Gonfiantini. Standards for stable isotope measurements in natural compounds. *Nature* **1978**, *271*, 534.
[8] T. B. Coplen. Normalization of oxygen and hydrogen isotope data. *Chem. Geol.: Isot. Geosci.* **1988**, *72*, 293.
[9] H. A. J. Meijer, R. E. M. Neubert, G. H. Visser. Cross contamination in dual inlet isotope ratio mass spectrometers. *J. Mass Spectrom.* **2000**, *35*, 45.
[10] R. Gonfiantini, in *Consultants' Meeting on Stable Isotope Standards and Intercalibration in Hydrology and in Geochemistry*. IAEA, Vienna, Austria, **1977**.
[11] Y. Lin, R. Clayton, M. Gröning. Calibration of $\delta^{17}O$ and $\delta^{18}O$ of international measurement standards – VSMOW, VSMOW2, SLAP, and SLAP2. *Rapid Commun. Mass Spectrom.* **2010**, *24*, 773.
[12] P. Martin, M. Gröning. *Reference Sheet for International Measurement Standards VSMOW2 and SLAP2*. IAEA, Vienna, Austria, **2009**.
[13] R. Gonfiantini, W. Stichler, K. Rozanski, in *Reference and Intercomparison Materials for Stable Isotopes of Light Elements, Proceedings of a Consultant Meeting*, Vienna, 1–3 December 1993, TECDOC-825. IAEA, Vienna, Austria, **1995**, p. 13.
[14] I. Jabeen, M. Kusakabe. Determination of $\delta^{17}O$ values of reference water samples VSMOW and SLAP. *Chem. Geol.* **1997**, *143*, 115.
[15] M. Kusakabe, Y. Matsuhisa. Oxygen three-isotope ratios of silicate reference materials determined by direct comparison with VSMOW-oxygen. *Geochem. J.* **2008**, *42*, 309.
[16] W. Li, D. Jin, Q. Zhang. Comparison of the oxygen-17 abundance in three international standard waters. *Huaxue Tongbao* **1988**, *6*, 39.
[17] R. Winkler, A. Landais, H. Sodemann, L. Dümbgen, F. Prié, V. Masson-Delmotte, B. Stenni, J. Jouzel. Deglaciation records of ^{17}O-excess in East Antarctica: reliable reconstruction of oceanic relative humidity from coastal sites. *Climate of the Past* **2012**, *8*, 1.
[18] A. Landais, E. Barkan, B. Luz. Record of $\delta^{18}O$ and ^{17}O-excess in ice from Vostok Antarctica during the last 150 000 years. *Geophys. Res. Lett.* **2008**, *35*, L02709.
[19] W. A. Brand, T. B. Coplen. An interlaboratory study to test instrument performance of hydrogen dual-inlet isotope-ratio mass spectrometers. *Fresenius' J. Anal. Chem.* **2001**, *370*, 358.
[20] *The International System of Units (SI), 8th edition brochure (in English)*, BIPM, Sévres, France, **2006**.
[21] E. Barkan, B. Luz. Diffusivity fractionations of $H_2^{16}O/H_2^{17}O$ and $H_2^{16}O/H_2^{18}O$ in air and their implications for isotope hydrology. *Rapid Commun. Mass Spectrom.* **2007**, *21*, 2999.

 Copyright © 2013 John Wiley & Sons, Ltd.

[22] O. Abe. Isotope fractionation of molecular oxygen during adsorption/desorption by molecular sieve zeolite. *Rapid Commun. Mass Spectrom.* **2008**, *22*, 2510.
[23] D. Paul, G. Skrzypek, I. Fórizs. Normalization of measured stable isotopic compositions to isotope reference scales – a review. *Rapid Commun. Mass Spectrom.* **2007**, *21*, 3006.
[24] W. A. Brand, in *Handbook of Stable Isotope Analytical Techniques*, vol. *1*, (Ed: P. A. de Groot). Elsevier Science, Amsterdam, **2004**, p. 855.
[25] P. Franz, T. Röckmann. A new continuous flow isotope ratio mass spectrometry system for the analysis of δ^2H, δ^{17}O and δ^{18}O of small (120 µg) water samples in atmospheric applications. *Rapid Commun. Mass Spectrom.* **2004**, *18*, 1429.
[26] B. Luz, E. Barkan. Variations of ^{17}O/^{16}O and ^{18}O/^{16}O in meteoric waters. *Geochim. Cosmochim. Acta* **2010**, *74*, 6276.
[27] H. A. J. Meijer, W. J. Li. The use of electrolysis for accurate δ^{17}O and δ^{18}O isotope measurements in water. *Isot. Environ. Health Stud.* **1998**, *34*, 349.
[28] M. F. Miller. Isotopic fractionation and the quantification of ^{17}O anomalies in the oxygen three-isotope system: an appraisal and geochemical significance. *Geochim. Cosmochim. Acta* **2002**, *66*, 1881.
[29] R. Gonfiantini, in *Advisory Group Meeting on Stable Isotope Reference Samples for Geochemical and Hydrological Investigations*. IAEA, Vienna, Austria, **1984**, p. 77.

 Copyright © 2013 John Wiley & Sons, Ltd.

Chapter 3

Triple water-isotopologue record from WAIS Divide, Antarctica: controls on glacial-interglacial changes in $^{17}O_{excess}$ of precipitation

Originally Published in Journal of Geophysical Research: Atmospheres
http://onlinelibrary.wiley.com/doi/10.1002/2014JD021770/full

The main text of this paper is in Chapter 3 and the supplementary material makes up Chapter 4.

The primary objective of this work was to determine if the large glacial-interglacial change in $^{17}O_{excess}$ observed in the Vostok ice core (*Landais et al.* [2008]) was representative of the magnitude of $^{17}O_{excess}$ change for other regions of Antarctica, particularly West Antarctica because of its more marine-influenced climate. The major contribution of this paper was the first high-resolution West Antarctic $^{17}O_{excess}$ record, produced for the WAIS Divide (WD) Ice Core covering the past 25 kyr. The WAIS Divide $^{17}O_{excess}$ record is also the first ice core record to span the entire Holocene period. We also obtained $^{17}O_{excess}$ measurements from limited sections of the Siple Dome and Taylor Dome ice cores for the Holocene and glacial periods. These $^{17}O_{excess}$ results, combined with recent results from Talos Dome and Dome C (*Winkler et al.* [2012]) provide the most complete spatial and temporal view of $^{17}O_{excess}$ in Antarctica to date. Measurements were made using water fluorination techniques and dual-inlet Isotope Ratio Mass Spectrometry (IRMS) in the UW Δ*IsoLab.

Our results from the modern-day ice core samples and Antarctic snow demonstrate that there is a strong spatial gradient of decreasing $^{17}O_{excess}$ towards the interior of the continent. This finding was counter to the conventional view of the $^{17}O_{excess}$ spatial gradient based on the available measurements from Talos Dome, Dome C and Vostok. However, the isotopic data for the different ice cores had not been consistently calibrated between the various labs, and therefore, artificial differences due to discrepancies in normalization had produced an increasing $^{17}O_{excess}$ gradient from the coast (Talos) to the interior (Vostok). In this work, all original and published $\delta^{17}O$ and $\delta^{18}O$ data were normalized as recommended by *Schoenemann et al.* [2013], allowing consistent comparison of the data for the first time.

The work of *Winkler et al.* [2012] showed that there were different magnitudes of $^{17}O_{excess}$ change for the Last Glacial Maximum (LGM, 20-25 ka) to Early Holocene (EH, 9-12 ka) periods, and the authors attributed this to different moisture sources for each ice core site, each with its own change in the different source relative humdities. The additional results from WD, Siple Dome, and Taylor Dome showed that there is indeed a spatial pattern to the change in $^{17}O_{excess}$ between glacial and interglacial periods, with sites further inland showing a greater magnitude of change, while near-coastal sites indicate little or no change in $^{17}O_{excess}$. At WD, the LGM to EH change in $^{17}O_{excess}$ is 17 per meg, comparable to the large change of 22 per meg at Vostok.

To interpret the observed changes in $^{17}O_{excess}$ we used the ECHAM4.6 isotope-enabled atmospheric general circulation model (GCM) to simulate LGM and present-day Antarctic conditions. To do this we added $\delta^{17}O$ to the isotope module, which required updating equilibrium and kinetic fractionation factors and tuning the model to match present-day $^{17}O_{excess}$ observations. The model can qualitatively reproduce the observed spatial distribution of modern

$^{17}O_{excess}$ in Antarctic precipitation, but only when tuned with a higher sensitivity of supersaturation to temperature than is commonly used in the literature.

The LGM to EH model simulations show that kinetic isotope effects during snow formation under supersaturated conditions (e.g., very cold temperatures) are best able to explain the spatial pattern of LGM to Early Holocene change. Additional GCM experiments show that the expansion of sea ice reduces moisture recharge and increases the area over which kinetic fractionation can occur, amplifying the effect of colder temperatures, and thereby decreasing $^{17}O_{excess}$ en-route to Antarctica. We find there is no need to invoke changes in humidity over the ocean that are often required to explain d_{excess} and $^{17}O_{excess}$ data. Temperature and sea ice changes alone are sufficient to explain the observed glacial-interglacial increases in $^{17}O_{excess}$ across Antarctica.

This second paper represents the main body of my graduate research. Most of the WAIS Divide, Taylor Dome, and Siple Dome $^{17}O_{excess}$ measurements were made by myself, with additional help from K. Samek and B. Vanden Heuvel. I produced the compilation and normalization of the previously published datasets. Qinghua Ding carried out the GCM simulations in accordance with my suggestions for experimental design, boundary conditions, and fractionation factors. Andrew Schauer assisted in data analysis protocols to identify outliers and to calibrate the $^{17}O_{excess}$ measurements to VSMOW and SLAP over multiple measurement periods. Bradley Markle contributed on techniques to redefine d_{excess} to the logarithmic form (d_{ln}), and provided valuable comments on how to best demonstrate the $^{17}O_{excess}$ sensitivity to temperature. Eric Steig offered significant editorial and conceptual suggestions to improving the manuscript. I wrote the manuscript and supplement, interpreted the $^{17}O_{excess}$ records, analyzed all the GCM output, and produced all the figures and tables.

AGU PUBLICATIONS

JGR

Journal of Geophysical Research: Atmospheres

RESEARCH ARTICLE
10.1002/2014JD021770

Key Points:
- Ice core 17O-xs changes in West Antarctica are comparable to East Antarctica
- Antarctic snow formation under supersaturated conditions results in lower 17O-xs
- Sea ice changes, and lower temperature, explain glacial-Holocene 17O-xs changes

Supporting Information:
- Readme
- Figure S1
- Figure S2
- Figure S3
- Figure S4
- Figure S5
- Data S1
- Table S1
- Text S1

Correspondence to:
S. W. Schoenemann,
schoes@uw.edu

Citation:
Schoenemann, S. W., E. J. Steig, Q. Ding, B. R. Markle, and A. J. Schauer (2014), Triple water-isotopologue record from WAIS Divide, Antarctica: Controls on glacial-interglacial changes in $^{17}O_{excess}$ of precipitation, *J. Geophys. Res. Atmos.*, *119*, doi:10.1002/2014JD021770.

Received 14 MAR 2014
Accepted 13 JUN 2014
Accepted article online 18 JUN 2014
Published online 28 JUL 2014

Triple water-isotopologue record from WAIS Divide, Antarctica: Controls on glacial-interglacial changes in $^{17}O_{excess}$ of precipitation

Spruce W. Schoenemann[1], Eric J. Steig[1], Qinghua Ding[1], Bradley R. Markle[1], and Andrew J. Schauer[1]

[1]IsoLab, Department of Earth and Space Sciences, University of Washington, Seattle, USA

Abstract Measurements of the $^{17}O_{excess}$ of H_2O were obtained from ice cores in West and East Antarctica. Combined with previously published results from East Antarctica, the new data provide the most complete spatial and temporal view of Antarctic $^{17}O_{excess}$ to date. There is a steep spatial gradient of $^{17}O_{excess}$ in present-day precipitation across Antarctica, with higher values in marine-influenced regions and lower values in the East Antarctic interior. There is also a spatial pattern to the change in $^{17}O_{excess}$ between the Last Glacial Maximum (LGM) and Holocene periods. At coastal locations, there is no significant change in $^{17}O_{excess}$. At both the West Antarctic Ice Sheet Divide site and at Vostok, East Antarctica, the LGM to Early Holocene change in $^{17}O_{excess}$ is about 20 per meg. Atmospheric general circulation model (GCM) experiments show that both the observed spatial gradient of $^{17}O_{excess}$ in modern precipitation, and the spatial pattern of LGM to Early Holocene change, can be explained by kinetic isotope effects during snow formation under supersaturated conditions, requiring a high sensitivity of supersaturation to temperature. The results suggest that fractionation during snow formation is the primary control on $^{17}O_{excess}$ in Antarctic precipitation. Variations in moisture source relative humidity play a negligible role in determining the glacial-interglacial $^{17}O_{excess}$ changes observed in Antarctic ice cores. Additional GCM experiments show that sea ice expansion increases the area over which supersaturating conditions occur, amplifying the effect of colder temperatures. Temperature and sea ice changes alone are sufficient to explain the observed $^{17}O_{excess}$ glacial-interglacial changes across Antarctica.

1. Introduction

Measurements of the stable isotope ratios of water (δD and δ^{18}O) in polar precipitation have long been used in ice core studies [*Dansgaard*, 1964; *Merlivat and Jouzel*, 1979; *Gat*, 1996; *Jouzel et al.*, 2003]. A recent innovation is the development of methods for obtaining precise measurements of the third water isotope ratio, δ^{17}O [*Baker et al.*, 2002; *Barkan and Luz*, 2005], complementing traditional measurements of δD and δ^{18}O. Combined measurements of δ^{18}O and δ^{17}O can be expressed with the parameter $^{17}O_{excess}$:

$$^{17}O_{excess} = \ln\left(\delta^{17}O + 1\right) - 0.528 \times \ln\left(\delta^{18}O + 1\right) \quad (1)$$

where δ^{18}O and δ^{17}O are unitless ratios defined by $\delta^{i}O = {}^{i}R_{sample}/{}^{i}R_{VSMOW} - 1$, and ${}^{i}R$ is the ratio of isotopologue $H_2{}^{i}O$ to the common isotopologue $H_2{}^{16}O$. Variations in $^{17}O_{excess}$ are generally several orders of magnitude smaller than variations in δ^{18}O and are conventionally expressed in per meg (10^{-6}) or ppm.

Like the better known deuterium excess, $d_{excess} = \delta D - 8 \times \delta^{18}O$, $^{17}O_{excess}$ is sensitive to kinetic fractionation. The d_{excess} in precipitation has frequently been interpreted as a proxy for moisture source conditions because it is sensitive to both temperature and humidity during evaporation. However, this interpretation is complicated by the fact that d_{excess} is not a conservative tracer in the atmosphere, even under purely equilibrium conditions [*Jouzel and Merlivat*, 1984; *Petit et al.*, 1991; *Kavanaugh and Cuffey*, 2003; *Masson-Delmotte et al.*, 2008; *Uemura et al.*, 2012]. The theoretical advantage of $^{17}O_{excess}$ is that it is insensitive to evaporation temperature [*Barkan and Luz*, 2007; *Risi et al.*, 2010a] and is less sensitive than d_{excess} to equilibrium fractionation processes during the formation of snow. In combination with δ^{18}O and d_{excess}, $^{17}O_{excess}$ offers a potential means to disentangle the competing effects of fractionation during evaporation, in transport, and during the formation and deposition of precipitation.

Both theory and experimental results show that an excess of ^{17}O in meteoric water originates from evaporation of ocean water into undersaturated air and is negatively correlated with relative humidity [*Barkan and Luz*, 2007;

©2014. American Geophysical Union. All Rights Reserved.

Luz and Barkan, 2010; *Risi et al.*, 2010a]. Variations of $\delta^{17}O$ and $\delta^{18}O$ stem from the difference in saturation vapor pressures between the light and heavy isotopes, resulting in vapor liquid equilibrium fractionation expressed as $\theta = \ln(^{17}\alpha)/\ln(^{18}\alpha)$, where ($\theta_{eq} = 0.529$) and α is the fractionation factor [*Matsuhisa et al.*, 1978]. The greater diffusivity of light isotopes leads to kinetic fractionation, with $\theta_{diff} = 0.518$ [*Barkan and Luz*, 2007]. Theoretically, kinetic isotopic fractionation from diffusive transport of water vapor in air should dominate the mean $^{17}O_{excess}$ in water vapor at the ocean surface. As expected, elevated values of $^{17}O_{excess}$ are observed in marine vapor and in meteoric waters, including polar snow [*Gat*, 1996; *Barkan and Luz,* 2005, 2007; *Landais et al.*, 2008; *Uemura et al.*, 2010].

During snow formation in the polar regions, the condensation of water vapor to liquid or ice typically occurs above saturation (i.e., >100% relative humidity). In this environment, the vapor pressure surrounding a water droplet or ice crystal is greater than that of the saturated vapor pressure for the condensing surface, resulting in supersaturation. In Antarctica, the lack of ice nuclei onto which water vapor can condense results in highly supersaturated conditions. The strong gradient in vapor pressure between the supersaturated water vapor and the ice surface favors preferential removal of $H_2{}^{17}O$, leaving the remaining vapor enriched in $H_2{}^{18}O$ relative to the global meteoric water line (GMWL = 0.528). This kinetic fractionation process during ice crystal formation is due to the greater amount of molecular diffusion that occurs for the lighter isotopologue ($H_2{}^{17}O$). Note that relative to $H_2{}^{16}O$, both the heavy isotopologues ($H_2{}^{17}O$ and $H_2{}^{18}O$) are still preferentially removed through equilibrium fractionation and the vapor becomes more depleted in $\delta^{17}O$ and $\delta^{18}O$. Equilibrium fractionation alone would preferentially deplete $H_2{}^{18}O$ in the water vapor and therefore result in more positive $^{17}O_{excess}$ values. However, the competing influence of kinetic fractionation under stronger supersaturation conditions dominates the total effective fractionation. This results in progressively lower $^{17}O_{excess}$ as condensation proceeds (e.g., for snowfall forming from an air mass moving further into the Antarctic interior).

The normalized relative humidity (hereafter, rh_n) immediately above the ocean surface is the main factor controlling $^{17}O_{excess}$ in the marine boundary layer, though the degree of turbulence (i.e., the wind speed) affects the sensitivity [*Landais et al.*, 2008; *Risi et al.*, 2010a]. The rh_n is defined as the water vapor concentration in the free air divided by the saturated vapor concentration at the temperature of the ocean surface [*Gat*, 1996; *Barkan and Luz*, 2007; *Uemura et al.*, 2010; *Risi et al.*, 2010a]:

$$rh_n = rh_a \times \frac{q_{sat}(T_a)}{q_{sat}(T_s)} \tag{2}$$

Previous work suggested $^{17}O_{excess}$ to be only weakly influenced by fractionation during precipitation, and it was therefore expected that $^{17}O_{excess}$ in polar snow and ice could be used as a proxy for the humidity in the marine boundary layer over the moisture source areas where polar moisture originates [*Barkan and Luz,* 2005, 2007; *Landais et al.*, 2008; *Luz and Barkan*, 2010; *Risi et al.*, 2010a; *Winkler et al.*, 2012; *Landais et al.*, 2012a]. In particular, *Landais et al.* [2008] interpreted the 20 per meg $^{17}O_{excess}$ decrease between the Early Holocene (EH, 12–9 ka) and Last Glacial Maximum (25–20 ka) in the Vostok ice core to indicate a 20% rh_n increase over the average glacial ocean moisture source for East Antarctic precipitation. However, two additional $^{17}O_{excess}$ records from East Antarctica (European Project for Ice Coring in Antarctica (EPICA) Dome C and Talos Dome) show smaller degrees of Last Glacial Maximum (LGM) to EH change than at Vostok. *Winkler et al.* [2012] showed that this observation made the interpretation of $^{17}O_{excess}$ change at Vostok as a change in source region rh_n problematic. They proposed several mechanisms: different moisture source regions reflecting different rh_n and moisture trajectories and kinetic fractionation with a stronger supersaturation sensitivity to temperature, in order to explain the different $^{17}O_{excess}$ evolution between cores. It was suggested earlier by *Miller* [2008] that the relatively large magnitude of LGM to EH $^{17}O_{excess}$ change observed at Vostok may reflect the influence of stratospheric water vapor with a strong anomalous $^{17}O_{excess}$ signature. Interpretation of $^{17}O_{excess}$ in Antarctic ice cores thus remains ambiguous.

To date, all records of Antarctic $^{17}O_{excess}$ variability have come from East Antarctica. Here we contribute new $^{17}O_{excess}$ data from West Antarctica, including a ~25,000 year long record from an ice core at the central West Antarctic Ice Sheet divide (WAIS Divide). We also present new deuterium excess data from the WAIS Divide ice core. As recommended by *Uemura et al.* [2012] we adopt a natural log definition of

©2014. American Geophysical Union. All Rights Reserved.

d_{excess} (hereafter, d_{ln}). *Uemura et al.* [2012] calculated a second-order polynomial best fit to the natural log of the isotopic data from the Global Network of Isotopes in Precipitation and a compilation of Antarctic isotope data [*Masson-Delmotte et al.*, 2008]:

$$d_{ln} = \ln(\delta D + 1) - \left(-2.85 \times 10^{-2} \left(\ln\left(\delta^{18}O + 1\right)\right)^2 + 8.47 \left(\ln\left(\delta^{18}O + 1\right)\right)\right) \quad (3)$$

The use of d_{ln} better accounts for differences in temperature sensitivity of equilibrium fractionation between δD and δ^{18}O than does the traditional d_{excess}. The use of d_{ln} also reduces the impact of glacial-interglacial changes in the isotopic concentration of seawater, which requires a significant correction for d_{excess} [*Stenni et al.*, 2010b].

Together, the new data provide a more complete picture of the spatial distribution of $^{17}O_{excess}$ across Antarctica, and allow us to better assess the controls on $^{17}O_{excess}$ on glacial-interglacial timescales.

2. Methods

The WAIS Divide ice core (WDC) was drilled over a 5 year period, reaching a depth of 3405 m in 2011. The core was drilled at latitude 79°28.06'S and longitude 112°05.2'W, about 24 km west of the Ross-Amundsen ice flow divide and 160 km east of the Byrd Station ice core site. The elevation at the ice core site is 1766 m; the modern accumulation rate is 22 cm a^{-1} (ice equivalent) and the mean annual temperature is approximately −30°C. The age of the oldest recovered ice is ~68 ka [*WAIS Divide Project Members*, 2013].

We measured $^{17}O_{excess}$ on the WDC using methods developed by *Baker et al.* [2002] and *Barkan and Luz* [2005, 2007] and described in detail in *Schoenemann et al.* [2013]. Briefly, water is fluorinated with CoF_3 to produce O_2 [*Barkan and Luz*, 2005], which is then carried by helium to a molecular sieve trap as in *Abe* [2008]. The O_2 sample is analyzed for *m/z* 32, 33, and 34 abundance ratios on a dual-inlet ThermoFinnigan MAT 253 isotope ratio mass spectrometer (ThermoElectron, Bremen, Germany) to determine δ^{18}O and δ^{17}O values with reference to O_2 gas.

Samples from the WDC were measured every 20 and 10 m for Holocene age and glacial age samples, respectively. The measurements cover from ~25 ka to the present, spanning depths 2600 m to 0 m in the WDC. We used both an internal water standard (WAIS Water) and the Vienna Standard Mean Ocean Water (VSMOW) 2, Standard Light Antarctic Precipitation (SLAP)/SLAP2, and GISP standards from the International Atomic Energy Agency, measured after every 10–15 samples to calibrate and verify the performance of both the fluorination line and the mass spectrometer. All samples were reproduced in duplicate or greater. The measured δ^{18}O and δ^{17}O data were corrected to the VSMOW-SLAP scale using the normalization technique of *Schoenemann et al.* [2013]. The reproducibility associated with each sample is given by the population standard deviation (6 per meg) of the WAIS Water standard ($n = 31$). In addition to the WDC samples, we measured $^{17}O_{excess}$ on a limited number of Holocene age and glacial age ice core samples from the Taylor Dome and Siple Dome ice cores using the same methods. The δ^{18}O and δD on the WDC were measured at a resolution of 0.5 m with a Picarro L1102i using cavity ring down spectroscopy and then normalized to the VSMOW-SLAP scale [*WAIS Divide Project Members*, 2013]. The precision of δ^{18}O and δD are 0.09‰ and 0.59‰, respectively, and the propagated error for d_{excess} and d_{ln} values is 0.60‰.

To eliminate interlaboratory differences among published data resulting from different calibration methods, we normalized all previously reported δ^{17}O and δ^{18}O values to the VSMOW-SLAP scale using SLAP $\delta^{18}O = -55.5$‰ and $^{17}O_{excess} = 0$ per meg, following *Schoenemann et al.* [2013]. Note that after VSMOW-SLAP normalization, some values, particularly those far removed from VSMOW, will be different than reported in the original published work. We provide all original data and data normalized to VSMOW-SLAP in Data S1 in the supporting information. In the case of the Vostok record from East Antarctica, calibration discrepancies have been noted between the two laboratories that performed the measurements, Le Laboratoire des Sciences du Climat et l'Environnement (LSCE) and Institute of Earth Sciences (IES), Hebrew University of Jerusalem [*Winkler et al.*, 2012; *Landais et al.*, 2012b; *Risi et al.*, 2013]. Long-term repeated measurements show that surface snow at Vostok is ~3 per meg, about 24 per meg lower than at WAIS Divide [*Schoenemann et al.*, 2013]. In comparing the Vostok record of $^{17}O_{excess}$ with that from WDC and other ice cores, we therefore apply an offset of −24 per meg from the mean of the VSMOW-SLAP-normalized data from *Landais et al.* [2008]. This is consistent with measurements of precipitation samples at Vostok, performed at both LSCE and IES [*Landais et al.*, 2012a].

©2014. American Geophysical Union. All Rights Reserved.

2.1. Model Simulations

To aid interpretation of the $^{17}O_{excess}$ data, we use the European Center Hamburg atmospheric general circulation model, ECHAM4.6 [*Roeckner et al.*, 1996]. As used here, ECHAM4.6 has 19 vertical levels and a horizontal resolution of T42 (2.8° by 2.8°). We modified the water isotope module [*Hoffmann et al.,* 1998] for ECHAM4.6 by adding an implementation for $^{17}O_{excess}$ and by using the most up-to-date fractionation factors for the water isotopologues.

Equilibrium fractionation factors for deuterium ($^2\alpha_{eq} = (HD^{16}O)_l/(H_2{}^{16}O)_v$) and oxygen-18 ($^{18}\alpha_{eq} = (H_2{}^{18}O)_l/(H_2{}^{16}O)_v$) are calculated using the original temperature-dependent values from *Majoube* [1971] for $T > 273$ K, where l = liquid and v = vapor:

$$^2\alpha^{eq}_{l-v} = \exp\left(52.612\times10^{-3} - 76.248\ /T + 24844/T^2\right) \quad (4)$$

$$^{18}\alpha^{eq}_{l-v} = \exp\left(-2.0667\times10^{-3} - 0.4156/T + 1137/T^2\right) \quad (5)$$

The most important update is for ice/vapor equilibrium fractionation for temperatures between 233 K and 273 K from *Ellehøj et al.* [2013]:

$$^2\alpha^{eq}_{i-v} = \exp\left(0.2133 - 203.10/T + 48888/T^2\right) \quad (6)$$

$$^{18}\alpha^{eq}_{i-v} = \exp\left(0.0831 - 49.192/T + 8312.5/T^2\right) \quad (7)$$

$$^{17}\alpha^{eq}_{i-v} = \left(^{18}\alpha^{eq}_{i-v}\right)^{0.529} \quad (8)$$

For $(H_2{}^{17}O)_l/(H_2{}^{16}O)_v$, the equilibrium fractionation factors are calculated as $^{17}\alpha_{eq} = (^{18}\alpha_{eq})^{0.529}$ for temperatures both above and below 273 K [*Barkan and Luz*, 2005]. The kinetic fractionation factors for the molecular diffusivity of deuterium ($^2\alpha_{diff}$) include the temperature-dependent linear approximation from *Luz et al.* [2009] where the relationship between diffusive fractionations of hydrogen and oxygen is:

$$\varphi_{diff} = \left(^2\alpha_{diff} - 1\right)/\left(^{18}\alpha_{diff} - 1\right) \quad (9)$$

and the linear approximation of the temperature dependence of φ_{diff} is given by

$$\varphi_{diff(T)} = 1.25 - 0.02T\ (T\ \text{in}\ ^\circ\text{C}) \quad (10)$$

For the molecular diffusivity of $H_2{}^{18}O$ and $H_2{}^{17}O$, we use $^{18}\alpha_{diff} = D(H_2{}^{18}O)/D(H_2{}^{16}O) = 1.0096$ and $^{17}\alpha_{diff} = (^{18}\alpha_{diff})^{0.518}$ [*Barkan and Luz*, 2007; *Luz and Barkan*, 2010]. The value for $^{18}\alpha_{diff}$ was determined from water vapor samples collected over the open ocean, incorporating the influences of wind speed and molecular turbulence [*Uemura et al.*, 2010]. We note that this value is somewhat higher than values derived from experimental estimates by *Merlivat and Jouzel* [1979] ($^{18}\alpha_{diff} = 1.007$ for low wind speeds, 1.003–1.005 for rough regimes), which have frequently been used in earlier modeling work.

During snow formation, the kinetic fractionation between vapor and liquid water or ice is calculated as

$$\alpha_{kin} = \frac{S}{1 + \alpha_{eq}\left(\frac{D}{D^*}\right)(S-1)} \quad (11)$$

where S is the supersaturation parameter, following *Jouzel and Merlivat* [1984]. The effective fractionation factor is then given by $\alpha_{eff} = \alpha_{eq}\alpha_{kin}$. The supersaturation parameter, S, is assumed to be linearly related to cloud temperature (T). The diffusion constants D and D^* represent the diffusion constants for the light and heavy isotopologue, respectively. The supersaturation dependence on condensation temperature is defined by $S = a - bT$, with T in degrees Celsius and where a and b are empirical constants. We use $a = 1$ and vary b from 0.002 to 0.007, which covers the range of values used previously in both intermediate complexity isotope models and general circulation model (GCM) studies to capture observed Antarctic d_{excess} variability [*Kavanaugh and Cuffey*, 2003; *Schmidt et al.*, 2005; *Risi et al.*, 2010b; *Werner et al.*, 2011; *Landais et al.*, 2012b].

In the GCM experiments, the ocean surface water $\delta^{18}O$ and δD are set to 0‰, while $^{17}O_{excess}$ is set to −5 per meg. *Luz and Barkan* [2010] measured seawater $^{17}O_{excess}$ values ranging from −15 to 5 per meg; however, none of these measurements were made southward of 32°S, providing little constraint on seawater $^{17}O_{excess}$ for the Southern Ocean and midlatitude moisture sources. Initial conditions for atmospheric water vapor are set to 20 per meg, but results are insensitive to this value since the model water vapor quickly approaches

©2014. American Geophysical Union. All Rights Reserved.

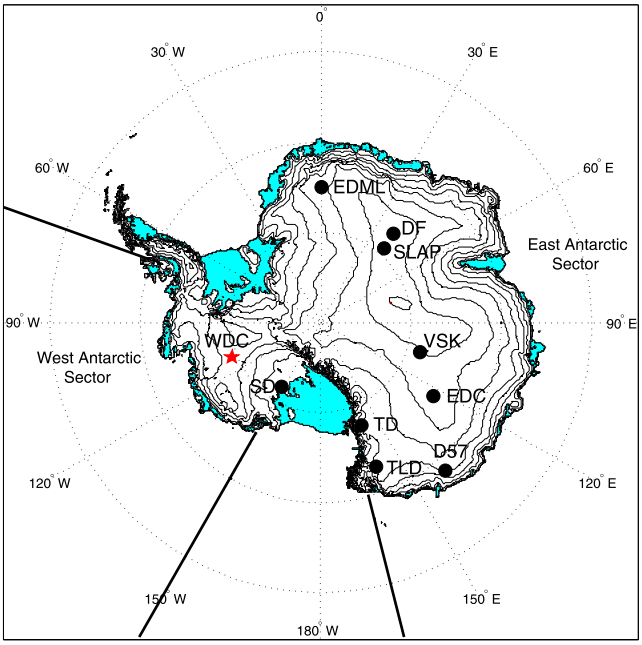

Figure 1. Map of Antarctic ice core locations and surface snow data. The West Antarctic Ice Sheet Divide ice core (WDC) is marked by the red star. The relevant sites discussed throughout the text include: Siple Dome (SD), Taylor Dome (TD), Talos Dome (TLD), European Project for Ice Coring in Antarctica (EPICA) Dome C (EDC), Vostok (VSK), Dome Fuji (DF), Plateau Station (SLAP water), EPICA Dronning Maud Land (EDML), and D57. The West Antarctic sector spans from 70°W to 150°W and the East Antarctic sector spans from 165°E to 70°W. All locations indicated above are the same throughout the following figures.

equilibrium with the ocean. *Uemura et al.* [2010] found $^{17}O_{excess}$ vapor measurements in the Southern Ocean near Antarctica (60–65°S) ranged from −8 to 19 per meg; the higher value is consistent with our GCM simulations.

To simulate present-day precipitation-weighted $\delta^{18}O$, d_{ln}, d_{excess}, and $^{17}O_{excess}$, we initialized the ECHAM4.6 atmospheric general circulation model with modern boundary conditions (preindustrial greenhouse gas concentrations, modern ice sheet topography, and orbital parameters). We prescribed a climatological seasonal sea surface temperature (SST) cycle to obtain the model's mean climate. A second control using an Atmospheric Model Intercomparison Project-style configuration (forced by historical ERA-Interim/ERA-40 SST data) for a 30 year period showed no significant difference in the mean. As noted above, a range of supersaturation sensitivities to temperature, as used in previously published model studies [*Schmidt et al.*, 2005; *Risi et al.*, 2010a; *Winkler et al.*, 2012; *Landais et al.*, 2012a; *Risi et al.*, 2013], was evaluated.

To simulate precipitation-weighted $\delta^{18}O$, d_{ln}, d_{excess}, and $^{17}O_{excess}$ for the Last Glacial Maximum (LGM, 21 ka), we prescribed boundary conditions following the Paleoclimate Modeling Intercomparison Project (PMIP II) [*Braconnot et al.*, 2007]: LGM ice sheet topography (Ice-5G) [*Peltier*, 2004], solar insolation [*Berger*, 1978], CO_2 concentration of 185 ppmv, and SST output data from an LGM experiment of the coupled ocean-atmosphere model CCSM3 [*Otto-Bliesner et al.*, 2006]. As for the modern simulations, we used a range of supersaturation sensitivities. Each experiment consisted of 30 year integrations where only the last 20 years are used. In addition to the "LGM" experiments, we performed "LGM-cold" simulations in which a uniform 4°C global decrease to the LGM sea surface temperature field is applied, in order to better match the high-latitude temperatures estimated from Antarctic ice core reconstructions.

To complement the LGM and LGM-cold experiments, in which the change in SST and sea ice boundary conditions is found to play a significant role in the resulting $\delta^{18}O$, d_{ln}, d_{excess}, and $^{17}O_{excess}$ fields, we performed another set of experiments (Extend-Ice) that use modern boundary conditions but with extended sea ice. We prescribe an amplified sea ice seasonality, as supported by *Collins et al.* [2012] for the LGM. In winter, the edge of sea ice is expanded ~10° north from the edge of the present-day model (July, August, and September, JAS) sea ice climatology, while in the summer (January, February, and March, JFM) the sea ice extent is equal to present-day. In the transition seasons (October, November, and December (OND) and April, May, and June (AMJ)), we extend the sea ice edge by ~5°.

To make comparisons of the isotopic records and model results, we account for the change in $\delta^{18}O$ and δD composition of the ocean during the glacial period resulting from the buildup of continental ice sheets. These seawater corrections have a considerable influence on the d_{excess} records and are therefore necessary in order to interpret the glacial-interglacial d_{excess} changes [*Jouzel et al.*, 2003; *Stenni et al.*, 2010b]. We find that the d_{ln} definition of d_{excess} (following *Uemura et al.* [2012]) reduces the large impact of the isotopic seawater correction

©2014. American Geophysical Union. All Rights Reserved.

Table 1. Present-Day (PD) δD, δ^{18}O, d_{excess}, d_{ln}, and $^{17}O_{excess}$ Isotopic Measurements From Snow or Ice Core Samples[a]

Ice Core	Sample Type	PD δD (‰)	PD δ^{18}O (‰)	PD d_{excess} (‰)	PD d_{ln} (‰)	EH $^{17}O_{excess}$ (per meg) VSMOW-SLAP	PD $^{17}O_{excess}$ (per meg) VSMOW-SLAP
WDC[e]	ice core	−264.35	−33.46	3.32	14.24	29	25
WW UW Isolab[f]	snow	−267.44	−33.82	2.64	13.29	––	27
Siple Dome[g]	ice core	−205.38	−26.16	3.89	14.63	––	21
Taylor Dome[h]	ice core	−315.03	−40.17	4.99	14.87	17	––
D57[i]	snow	−258.14	−32.63	2.90	13.76	––	20
SLAP (Plateau Sta.)[j]	snow	−428.00	−55.50	16.00	17.94	––	0
VW UW Isolab[j]	snow	−438.57	−56.56	13.91	12.50	––	3
Vostok[l]	ice core	−441.28	−57.09	15.44	14.28	6[c]	2[b], −8[c]
Dome C[m]	ice core	−396.66	−50.73	9.16	12.97	19[b]	23[c]
Talos Dome[n]	ice core	−285.62	−36.19	3.92	14.61	0[b]	––
Dome F[o]	ice core	−426.01	−55.04	14.32	15.65	––	−6[c]
EDML[p]	ice core	−353.89	−44.82	4.69	11.54	8[d]	––

[a]The present-day is defined as the past 2 kyr average, except for Dome C δ^{18}O, δD (2–1.2 ka), and Siple Dome $^{17}O_{excess}$ (2–1 ka) due to lack of available data. All $^{17}O_{excess}$ data normalized to VSMOW-SLAP scale as in *Schoenemann et al.* [2013], except EDML $^{17}O_{excess}$ (see supporting information). Note, that for snow, the present-day consists of multiple years of accumulation to provide the annual average reference water value (e.g., not 2 kyr). Early Holocene (EH = 12–9 ka), except for Taylor Dome $^{17}O_{excess}$ (6–2 ka) due to lack of available ice core data. The d_{ln} values are calculated using equation (3), as in *Uemura et al.* [2012, equation (A1)].
[b]$^{17}O_{excess}$ measurements performed at LSCE.
[c]$^{17}O_{excess}$ measurements performed at IES.
[d]$^{17}O_{excess}$ unpublished from *Risi et al.* [2013], not VSMOW-SLAP normalized.
[e]*WAIS Divide Project Members* [2013] and this study.
[f]Updated from *Schoenemann et al.* [2013] with more data.
[g]*Brook et al.* [2005] and this study.
[h]*Steig et al.* [1998b] and this study.
[i]This study (reference water from LSCE).
[j]*Schoenemann et al.* [2013].
[k]*Schoenemann et al.* [2013].
[l]*Vimeux et al.* [2001] and *Landais et al.* [2008, 2012a].
[m]*EPICA Community Members* [2004], *Stenni et al.* [2004], and *Winkler et al.* [2012].
[n]*Stenni et al.* [2010a], B. Stenni, (personal communication, 2013), Talos Dome (unpublished d_{excess} data), and *Winkler et al.* [2012].
[o]*Fujita and Abe* [2006], and *Luz and Barkan* [2010].
[p]*EPICA Community Members* [2006], *Stenni et al.* [2010b], *Winkler et al.* [2012], and *Risi et al.* [2013].

on d_{excess}. Seawater-corrected d_{ln} and d_{excess} ice core data are referred-to throughout as $d_{ln\ corr}$ and $d_{xs\ corr}$. The seawater correction for $^{17}O_{excess}$ results in a negligible change (<0.5 per meg), and therefore, we leave $^{17}O_{excess}$ uncorrected.

3. Results

3.1. Ice Core Data

Table 1 compares data from present-day surface snow and Holocene ice at WAIS Divide, Taylor Dome, and Siple Dome (Figure 1), with previously published data from ice core sites in East Antarctica [*Vimeux et al.*, 2001; *Landais et al.*, 2008; *Masson-Delmotte et al.*, 2008; *Stenni et al.*, 2010a; *Uemura et al.*, 2012; *Winkler et al.*, 2012]. For the ice core records, "present-day" is defined as the average value of the past 2 kyr except for $^{17}O_{excess}$ at Taylor Dome (6–2 ka) and EPICA Dome C (EDC) (2–1.2 ka) due to limited availability of samples.

In Figures 2, 3, and 4, we compare $^{17}O_{excess}$ and δ^{18}O for WAIS Divide with the results from Taylor Dome, Siple Dome, Vostok, Talos Dome, and EDC. The WDC $^{17}O_{excess}$ measurements cover from ~25 ka to the present. The WDC data provide the highest resolution available measurements of $^{17}O_{excess}$ from the LGM through the entire Holocene. The minimum resolution is four samples per thousand years. Both the individual measurements (sample mean) and 1σ standard deviation are shown for the WDC record, along with a Monte Carlo average cubic spline and 1σ (6 per meg) standard deviation envelope following the methods given in *Schmitt et al.* [2012]. In Figure 3, we show $^{17}O_{excess}$ measurements of Taylor Dome and Siple Dome for the LGM and some Holocene periods. Included are previously published δ^{18}O records of Taylor Dome and Siple Dome each on their published timescales [*Steig et al.*, 2000; *Brook et al.*, 2005]. For consistency with previous $^{17}O_{excess}$ studies [*Landais et al.*, 2008; *Winkler et al.*, 2012], we compare the records for LGM (25–20 ka) and Early Holocene (12–9 ka) time periods.

Our results show that, in general, present-day West Antarctic ice core $^{17}O_{excess}$ samples have elevated mean annual values compared to those of the East Antarctic interior. This pattern also appears to hold throughout

©2014. American Geophysical Union. All Rights Reserved.

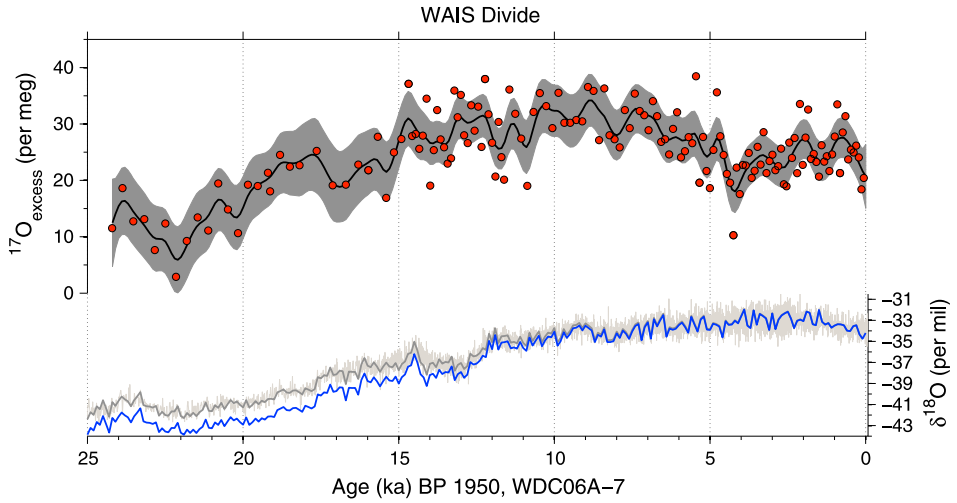

Figure 2. WDC record of $^{17}O_{excess}$ (black line = Monte Carlo Cubic Spline Average, gray band = 1σ standard deviation) and $\delta^{18}O$ (light gray = original data, dark gray = 200 year average, and blue = 200 year average seawater corrected) on the WDC06A-7 timescale. We follow the Monte Carlo Averaging (MCA) methods used by *Schmitt et al.* [2012]. The MCA is composed of 4000 randomly distributed iterations, with a 100 year resolution, and a cutoff period of 1000 years. All data are included in the 1σ envelope of 6 per meg [see *Schmitt et al.*, 2012].

the Holocene. The LGM to EH change in $^{17}O_{excess}$ at WAIS Divide is 17 per meg, very similar to that at Vostok (22 per meg) (Table 2). The $^{17}O_{excess}$ change between LGM and EH at WAIS Divide appears to occur in two steps, with a first increase beginning around 22 ka, and a second, marked increase at ~15 ka. There is a short decrease during the Antarctic Cold Reversal (14.5 to 11.9 ka), followed by a period (11.5–9.5 ka) of elevated

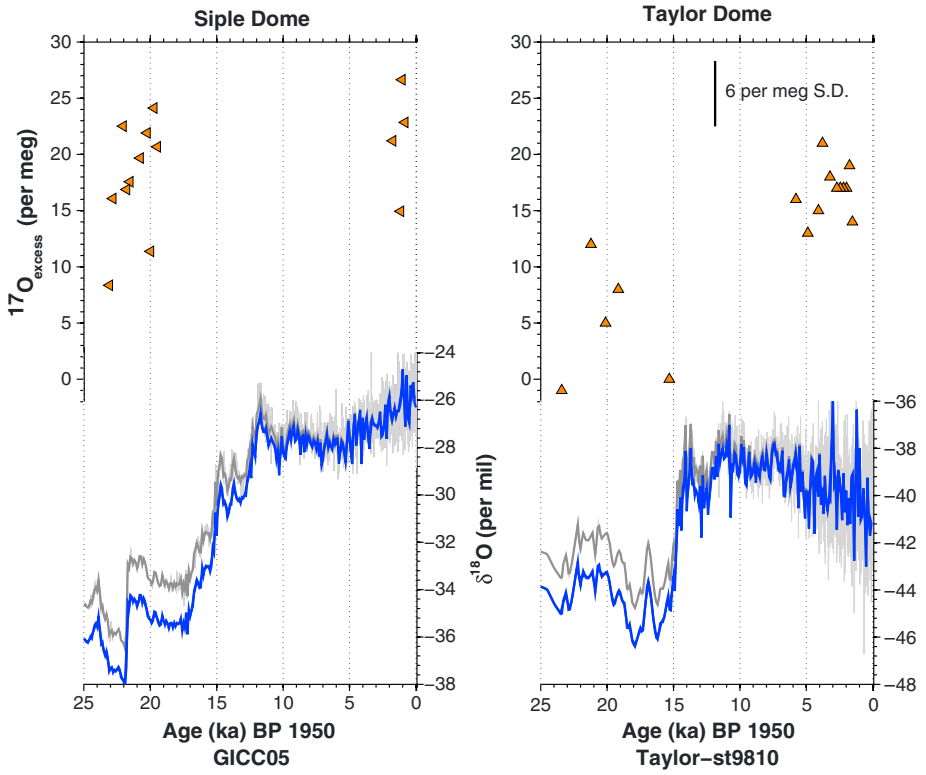

Figure 3. Record of $^{17}O_{excess}$ and $\delta^{18}O$ for Siple Dome for LGM and late Holocene (2–1 ka) on the GICC05 age scale [*Brook et al.*, 2005] and $^{17}O_{excess}$ and $\delta^{18}O$ for Taylor Dome for LGM and mid-Holocene (6–2 ka). Note that the Taylor Dome timescale used is *st9810,* which has large age errors in the LGM period [*Steig et al.*, 2000].

©2014. American Geophysical Union. All Rights Reserved.

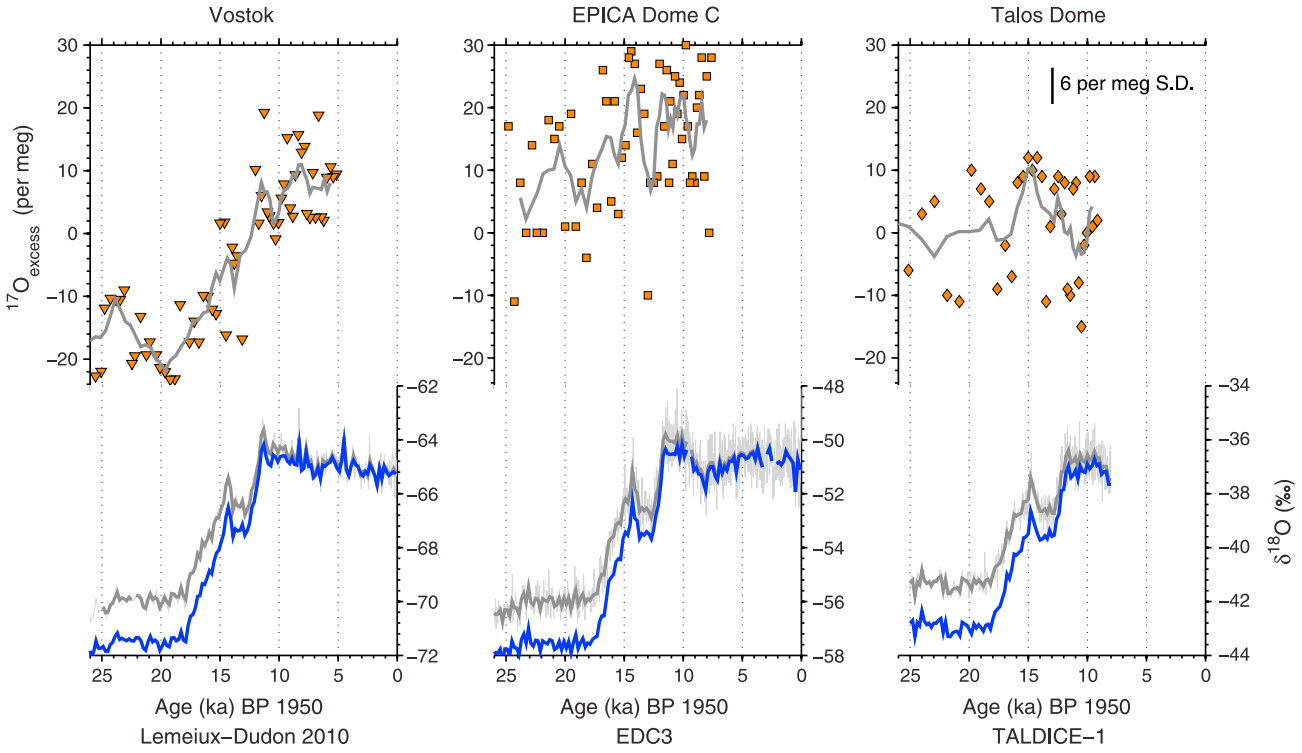

Figure 4. East Antarctic ice core records spanning the LGM (25–20 ka) to Early Holocene (12–9 ka) from Vostok, Dome C, and Talos Dome for $^{17}O_{excess}$ (orange, gray 5 point running mean) [*Landais et al.*, 2008; *Winkler et al.*, 2012], and $\delta^{18}O$ (light gray = original data, dark gray = 200-year average, and blue = 200 year average seawater corrected) normalized to the VSMOW-SLAP scale. Vostok $^{17}O_{excess}$ record has been shifted down based on UW IsoLab WW − VW difference of 24 per meg. The $^{17}O_{excess}$ data are presented on their originally published age scales: Dome C on EDC3, Talos Dome on TALDICE-1, and for Vostok, the $\delta^{18}O$ data have been transferred to the Lemiuex-Dudon 2010.

Table 2. Change in $\delta^{18}O$, δD, d_{excess}, and d_{ln} From the Last Glacial Maximum (LGM) to Early Holocene (EH) and Present-Day (PD) for Seawater Isotopic Corrected Ice Core Data ($_{corr}$)[a]

Ice Core Site	LGM-EH $\delta^{18}O_{corr}$ (‰)	LGM-PD $\delta^{18}O_{corr}$ (‰)	LGM-EH $d_{xs\ corr}$ (‰)	LGM-PD $d_{xs\ corr}$ (‰)	LGM-EH $d_{ln\ corr}$ (‰)	LGM-PD $d_{ln\ corr}$ (‰)	LGM $^{17}O_{excess}$ (per meg)	EH $^{17}O_{excess}$ (per meg)	LGM-EH $^{17}O_{excess}$ (per meg)
WDC[f]	−8.04	−9.44	−0.76	−0.67	−4.89	−5.16	12	29	−17
Siple Dome[g]	−8.27	−9.80	0.12	−1.05	−0.79	−2.24	18	21[e]	−3
Taylor Dome[h]	−5.23	−3.55	−2.65	−3.61	−7.06	−7.98	6	17[e]	−11
Vostok[i,c]	−6.96	−5.66	5.02	3.08	−5.67	−7.08	−16	6	−22
EPICA Dome C[j,b]	−6.95	−6.74	2.07	2.00	−7.77	−7.82	7	19	−12
Talos Dome[k,b]	−5.86	−6.84	−3.28	−3.67	−8.24	−9.24	−1.5	0	−1.5
Dome F[l]	−6.89	−6.20	4.86	4.58	−4.60	−4.19	––	––	––
EDML[m]	−6.89	−7.00	2.95	2.57	−3.13	−4.00	6[d]	8[d]	−2

[a]LGM (20–25 ka), EH (12–9 ka), and PD (2–0 ka), except for EDC $\delta^{18}O$, δD, and d_{excess} (2–1.2 ka). All $^{17}O_{excess}$ data normalized to VSMOW-SLAP scale as in *Schoenemann et al.* [2013], except EDML $^{17}O_{excess}$.
[b]$^{17}O_{excess}$ measurements performed at LSCE.
[c]$^{17}O_{excess}$ measurements performed at IES.
[d]$^{17}O_{excess}$ unpublished in *Risi et al.* [2013], from *Winkler et al.* [2012].
[e]Siple $^{17}O_{excess}$ PD = (2-1 ka), Taylor $^{17}O_{excess}$ EH = (6–2 ka).
[f]*WAIS Divide Project Members* [2013] and this study.
[g]*Brook et al.* [2005] and this study.
[h]*Steig et al.* [1998b] and this study.
[i]*Vimeux et al.* [2001], *Landais et al.* [2008, 2012a],and *Risi et al.* [2013].
[j]*EPICA Community Members* [2004], *Stenni et al.* [2004, 2010b], *Winkler et al.* [2012].
[k]*Stenni et al.* [2010a]; B. Stenni (personal communication , 2013), Talos Dome (unpublished d_{excess} data), and *Winkler et al.* [2012].
[l]*Fujita and Abe* [2006].
[m]*EPICA Community Members* [2006], *Stenni et al.* [2010b], *Winkler et al.* [2012], and *Risi et al.* [2013].

©2014. American Geophysical Union. All Rights Reserved.

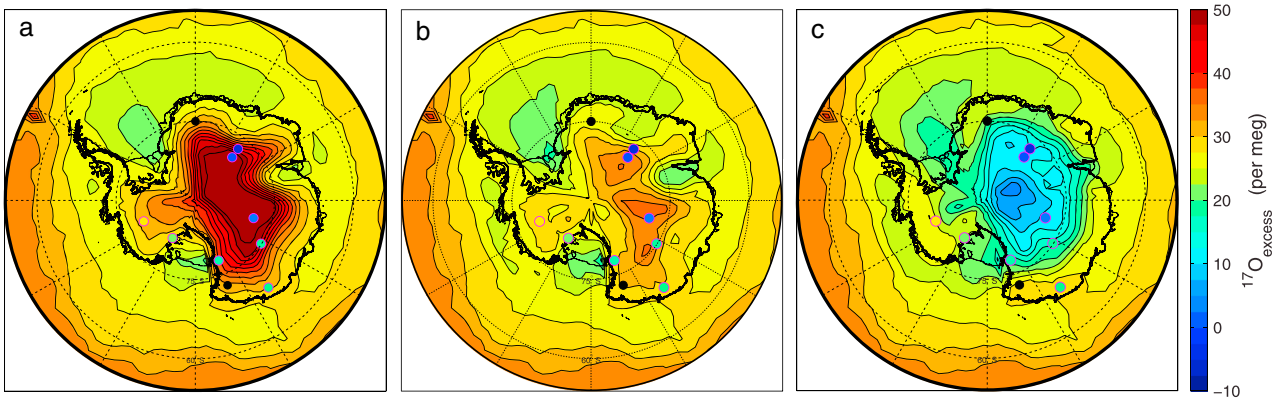

Figure 5. (a) Present-day spatial gradient of modeled $^{17}O_{excess}$ using supersaturation parameterization of $S = 1 - 0.002\,T$, (b) $S = 1 - 0.004\,T$, and (c) $S = 1 - 0.007\,T$ from ECHAM4.6, compared to the present-day $^{17}O_{excess}$ ice core data normalized to VSMOW-SLAP as in *Schoenemann et al.* [2013] from Table 1. Note, the model output for all three panels has been offset by +20 per meg for straightforward comparison with the ice core values.

values in the early Holocene. The early Holocene maximum is followed by a long-term $^{17}O_{excess}$ decrease toward the present (~1 per meg/ka); such a long-term decrease has not previously been identified in Antarctic ice cores, which generally have not included data more recent than the mid-Holocene.

Together, the multiple data sets show a clear spatial pattern to the change in $^{17}O_{excess}$ between LGM and Holocene periods, with more coastal sites showing very little change, and sites in the interior showing greater change. At the low elevation coastal site of Siple Dome, there is no measurable change in $^{17}O_{excess}$, similar to the lack of significant change at Talos Dome. At Taylor Dome, $^{17}O_{excess}$ increases by 11 per meg from LGM to the mid-Holocene, comparable to the change at Dome C.

3.2. Model-Data Comparison

3.2.1. Present-Day Conditions

Figure 5 compares the spatial distribution of present-day $^{17}O_{excess}$ measurements with the modeled spatial pattern, for different temperature-dependent parameterizations of the supersaturation value ($S = a - bT$;

Table 3. Site Characteristics of Ice Core Locations for the Present-Day Compared to ECHAM4.6 GCM Control Simulation[a]

	Site Observations						Model	
Location	Latitude (S)	Longitude	Elevation (m MSL)	Distance to Coast (km)	Current Accumulation Rate (mm w.e./yr)	Mean Annual Surface Temperature (°C)	ECHAM 4.6 Accumulation Rate (mm w.e./yr)	ECHAM4.6 Mean Annual Surface Temperature (°C)
WDC[b]	−79.47	−112.08	1766	585	220.0	−28.5	437.2	−23.0
Siple Dome[c]	−81.67	−148.82	621	470	106.1	−24.5	185.1	−25.2
Taylor Dome[d]	−77.79	158.72	2365	120	47.4 to 66.3	−37, −41	41.0	−35.5
D57[e]	−68.46	140.00	2000	200	––	––	521.4	−25.5
Plateau Station[f]	−79.25	40.55	3625	1100	25.4	−56.4	21.3	−50.0
Vostok[g]	−78.47	106.87	3488	1260	21.8	−57	15.2	−52.3
Dome C[h]	−75.1	123.35	3233	870	26.9	−54.5	15.7	−49.3
Talos Dome[i]	−72.81	159.18	2318	250	80.5	−41, −43	168.2	−27.1
Dome F[j]	−77.32	39.70	3810	1000	25 to 30	−54.8, −57.7	14.6	−50.0
EDML[k]	−75.00	0.07	2892	529	60.6	−43.2	51.0	−34.8

[a] Model output for the 2.8° × 2.8° grid surrounding the ice core latitude-longitude.
[b] *WAIS Divide Project Members* [2013] and *Orsi et al.* [2012].
[c] *Brook et al.* [2005].
[d] *Steig et al.* [1998b, 2000].
[e] *Legrand and Delmas* [1985].
[f] *Radok and Lile* [1977].
[g] *Petit et al.* [1999].
[h] *EPICA Community Members* [2004], *Stenni et al.* [2004], and *Jouzel et al.* [2007].
[i] *Frezzotti et al.* [2004] and *Stenni et al.* [2010a].
[j] *Watanabe et al.* [2003], *Motoyama et al.* [2005], and *Fujita and Abe* [2006].
[k] *EPICA Community Members* [2006].

©2014. American Geophysical Union. All Rights Reserved.

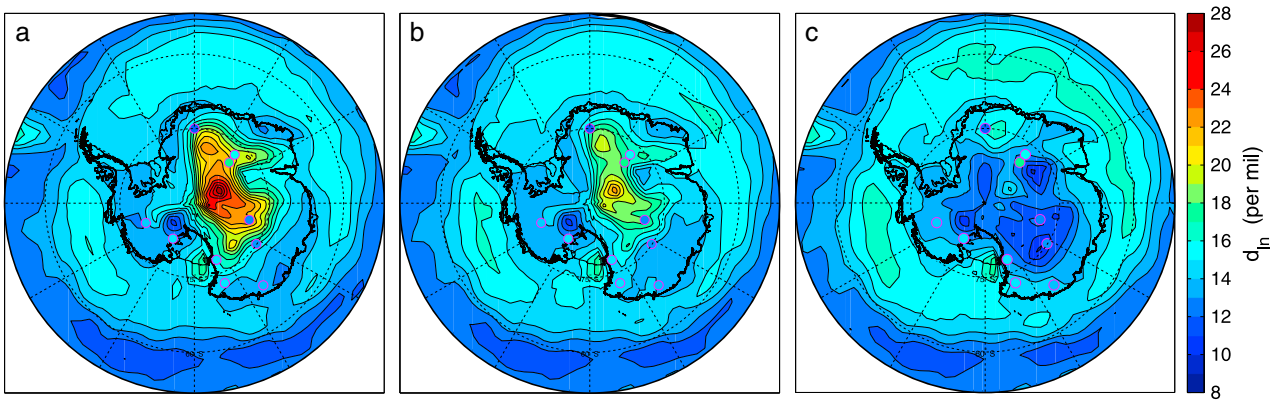

Figure 6. (a) Present-day spatial gradient of d_{ln} using supersaturation parameterization of $S = 1 - 0.002\,T$, (b) $S = 1 - 0.004\,T$, and (c) $S = 1 - 0.007\,T$ from ECHAM4.6, and present-day ice core d_{ln} data from Table 1.

$a = 1$; $b = 0.002$, 0.004, 0.007). To make straightforward comparisons between the spatial patterns in the data and modeling results, we offset the model output (+20 per meg, +4‰, and +3‰) such that the model WAIS Divide grid cell $^{17}O_{excess}$, d_{ln}, and d_{excess} values match the real WDC values (27 per meg, 13‰, and 3‰, respectively).

We find that the best fit for the $^{17}O_{excess}$ spatial pattern is obtained when using large values for *b,* reflecting a strong sensitivity of supersaturation to temperature. As shown in Figure 5, using $b = 0.007$, the modeled spatial pattern captures the higher $^{17}O_{excess}$ values found in West Antarctica (WAIS Divide and Siple Dome) and also shows relatively high $^{17}O_{excess}$ along the coastal margins of East Antarctica but low values in the central East Antarctic plateau. In contrast, using moderate and low sensitivity of supersaturation to temperature ($b = 0.004$ and 0.002) results in an overestimation of $^{17}O_{excess}$ values in East Antarctica and fails to reproduce the strong negative spatial gradient observed in present-day $^{17}O_{excess}$ between the coast and the East Antarctica interior. Indeed, even the $b = 0.007$ model experiments overestimate the $^{17}O_{excess}$ values found at Vostok, Plateau Station (SLAP), and Dome F, relative to those at WAIS Divide. This could suggest an even greater sensitivity of supersaturation to temperature; however, the magnitude of this difference is also a function of model resolution and the model bias that tends to produce temperatures over East Antarctica that are too warm (Table 3) [*Hoffmann et al.*, 1998; *Schmidt et al.*, 2005; *Helsen et al.*, 2007; *Werner et al.*, 2011].

Comparison of present-day d_{ln} data with the model results is shown in Figure 6. We find that, as for $^{17}O_{excess}$, the best overall agreement between d_{ln} data and model simulations occurs with a relatively high sensitivity of supersaturation to temperature (e.g., $b = 0.007$). We note that most previous model simulations of d_{excess} in Antarctica have used lower sensitivity ($b = 0.002$ to 0.0045) to match present-day data. However, most of this earlier work was based on fractionation factors for δD and $\delta^{18}O$ that were poorly constrained at low temperature. Our results show that, when the most up-to-date fractionation factors [*Luz et al.*, 2009; *Ellehøj et al.*, 2013] are used, the d_{ln} data are consistent with the greater sensitivity required by the $^{17}O_{excess}$ data. Lower sensitivities to supersaturation result in very high d_{ln} values in the East Antarctic interior, inconsistent with the data (Table 1 and Figures 6a and 6b).

3.2.2. LGM to Holocene Change

We now consider model-data comparison for the LGM period and for the magnitude of the LGM to Holocene transition. We use results from the present-day simulations as an approximation of early Holocene conditions. The limited data available suggest that Early Holocene (EH) $^{17}O_{excess}$ values are generally elevated relative to present, so that the model calculation of the LGM minus present-day may tend to underestimate the total isotopic LGM to EH change. Note that, taken at face value, the published data of *Landais et al.* [2008] compared with those of *Landais et al.* [2012a] imply a ~30 per meg decline in $^{17}O_{excess}$ since the Early Holocene. Given the calibration discrepancies noted above, and the small $^{17}O_{excess}$ difference between EH and present-day at both Dome C and WAIS Divide, we think this is unlikely. Indeed, assuming that Vostok is similar to Dome C in having only a modest difference between EH and present-day is consistent with the offset to the published Vostok

©2014. American Geophysical Union. All Rights Reserved.

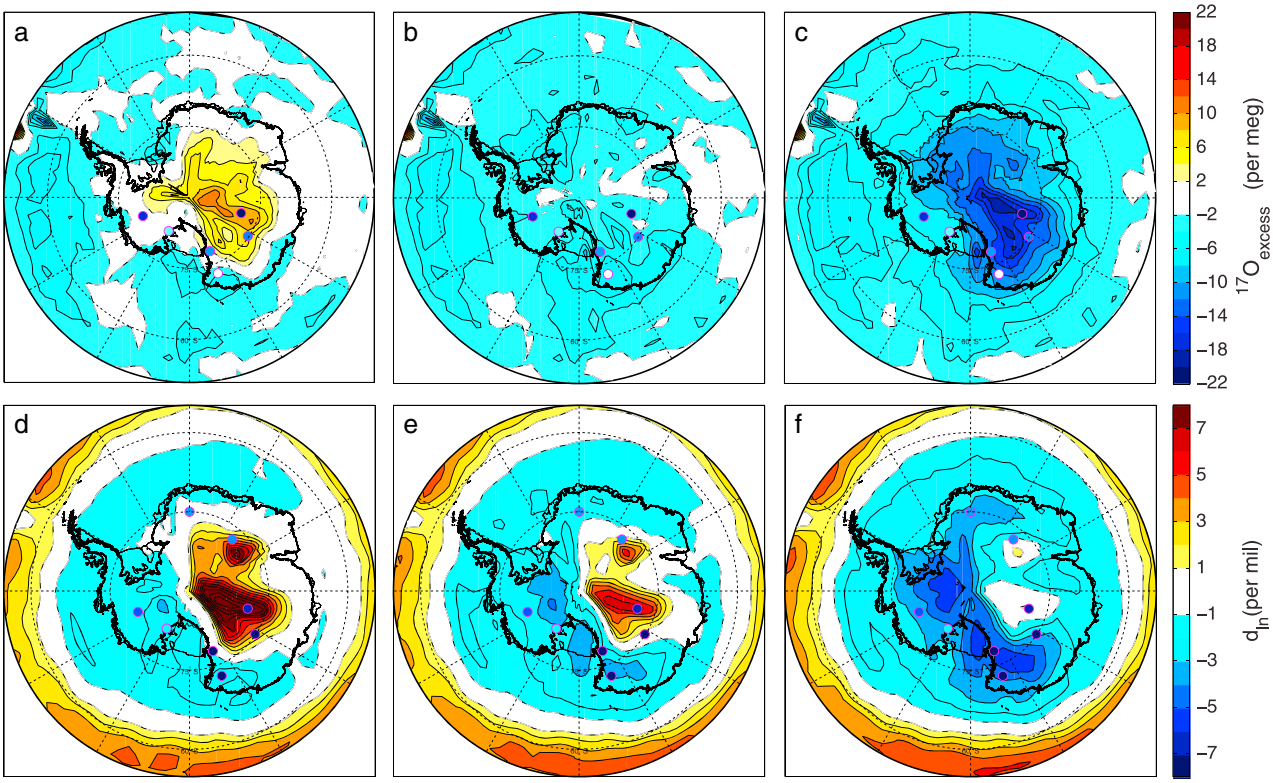

Figure 7. Model simulations for the LGM (21 ka) minus PD (0 ka) performed by ECHAM4.6 to determine (a–c) $^{17}O_{excess}$ and (d–f) d_{ln} sensitivity to all three supersaturation values ($S = 1 - 0.002\,T$ in Figures 7a and 7d, $S = 1 - 0.004\,T$ in Figures 7b and 7e, and $S = 1 - 0.007\,T$ in Figures 7c and 7f), compared with the LGM-EH change in $^{17}O_{excess}$ and $d_{ln\ corr}$ ice core data (Table 2). All experiments were run at T42 (2.8° by 2.8°) resolution.

data suggested by available interlaboratory comparisons. This assumption has no impact on the magnitude of the glacial-interglacial change.

All model comparisons hereafter are "Experiment" minus "Control" (e.g., LGM minus present-day). In Figure 7 we show the spatial pattern of $^{17}O_{excess}$ and d_{ln} change between LGM and present-day model simulations, for different supersaturation parameterizations. As for the modern spatial pattern, the best reproduction of the observed spatial pattern of LGM to EH $^{17}O_{excess}$ change is achieved with $b = 0.007$. Using this high sensitivity of supersaturation to temperature captures the large decrease (22 per meg) in $^{17}O_{excess}$ values at Vostok during the LGM, while also correctly simulating the smaller (~12 per meg) $^{17}O_{excess}$ decreases observed at Dome C and Taylor Dome. At WAIS Divide, the high-sensitivity LGM simulation underestimates the full magnitude of the glacial to interglacial $^{17}O_{excess}$ change but correctly predicts the sign. In contrast, lower values of b result in LGM $^{17}O_{excess}$ values that are of incorrect sign and higher than present in the East Antarctic interior (for example, an LGM minus EH change of +9 per meg at Vostok, opposite in sign to the observed −22 per meg change).

The same high-sensitivity value for supersaturation parameter b that best fits the $^{17}O_{excess}$ data also better captures the observed spatial pattern in $d_{ln\ corr}$ change between the LGM and present-day. The model pattern is characterized by greater, more negative d_{ln} changes in West Antarctica and coastal areas and relatively small, positive d_{ln} changes in the central East Antarctica interior. In contrast, LGM model simulations using low and moderate supersaturation sensitivities result in larger, positive d_{ln} changes in the East Antarctic interior, contrary to the negative $d_{ln\ corr}$ changes in the ice core data. The high-sensitivity ($b = 0.007$) model result shows a uniform decrease in d_{ln} values around the periphery of the continent during the LGM, which is supported by the $d_{ln\ corr}$ ice core data. The model result closely matches the magnitude of LGM to EH change at EDML and WDC, though it underestimates the LGM minus EH change in $d_{ln\ corr}$ at Vostok and Dome F.

©2014. American Geophysical Union. All Rights Reserved.

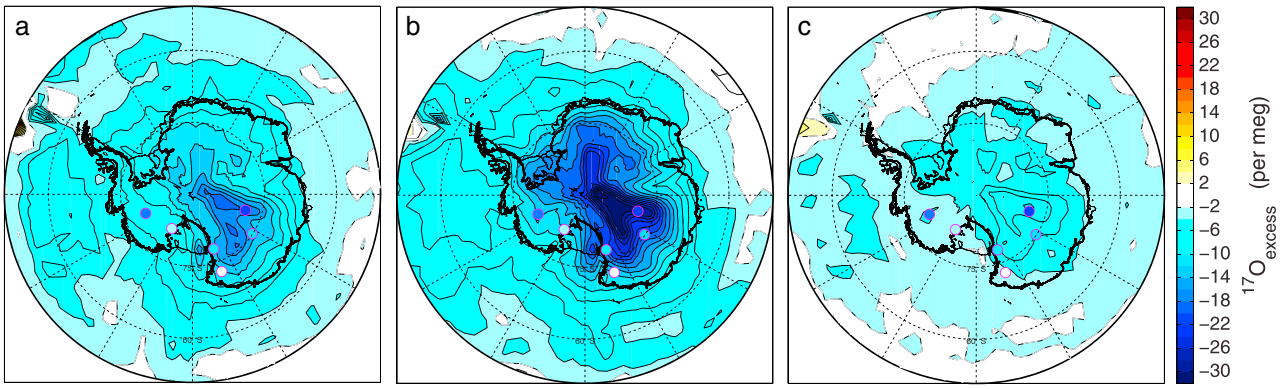

Figure 8. $^{17}O_{excess}$ spatial difference maps comparing model simulations for (a) LGM, (b) LGM-cold, and (c) Extend-Ice minus PD (0 ka), using ECHAM4.6 (GCM) with high sensitivity to supersaturation ($S = 1 - 0.007$ T). Note change in color bar scale of −32 to 32, from −22 to 22 in Figure 7.

For the case of $d_{xs\ corr}$, the low and moderate sensitivity LGM minus present-day experiments result in greatly overestimated change in $d_{xs\ corr}$ (by 4–6 ‰) in the central East Antarctic interior, while the high-sensitivity simulation achieves the spatial distribution of LGM to EH change in $d_{xs\ corr}$ most consistent with the data, characterized by lower LGM minus present-day $d_{xs\ corr}$ values in West Antarctica and coastal regions, and higher LGM minus present $d_{xs\ corr}$ values on the East Antarctic plateau (Figure S1). We emphasize that the seawater correction is such that the glacial-interglacial change of $d_{xs\ corr}$ in the East Antarctic interior is of opposite sign to that of d_{excess} [*Stenni et al.*, 2010b], and the magnitude of change is greatly reduced in West Antarctica (Figure S2). This potentially confusing change in sign is another reason why in general d_{ln} is a more useful parameter than d_{excess}.

3.2.3. Dependence on Model Boundary Conditions

The Modern and LGM model results both show that a relatively high sensitivity of supersaturation to temperature best reproduces the $^{17}O_{excess}$ data. The details of the $^{17}O_{excess}$ response depend on the model boundary conditions, particularly SST and sea ice cover. We performed two additional sets of experiments to examine the sensitivity of $^{17}O_{excess}$ to varying these boundary conditions. Here we use only $b = 0.007$, for comparison with the best results from the LGM and Modern experiments.

A recognized problem with GCMs is the difficulty in simulating cold-enough Antarctic temperatures, both in modern and LGM simulations [*Hoffmann et al.*, 2005; *Schmidt et al.*, 2005; *Masson-Delmotte et al.*, 2008; *Werner et al.*, 2011]. To assess the importance of this issue for simulating $^{17}O_{excess}$, we performed a set of "LGM-cold" model experiments, where we prescribed a global 4°C decrease to LGM SSTs. Unlike the LGM simulation, the LGM-cold model experiment produces Antarctic mean surface temperatures that are comparable to paleoclimate estimates from ice cores [*Jouzel et al.*, 2003]. The magnitude of LGM-cold minus present-day temperature change on the central East Antarctica plateau is more consistent with the ice core records at Dome F and Vostok (−8 to −12°C, respectively) than the LGM simulation but results in an unrealistically large $^{17}O_{excess}$ change in this region (Taylor Dome ~ 21, Dome C ~ 22 per meg, Vostok ~ 32 per meg) (Figure 8b). On the other hand, the LGM-cold experiment better reproduces the magnitude of LGM to Early Holocene change in $^{17}O_{excess}$ at WAIS Divide (~14 per meg).

Comparisons between the LGM-cold and LGM experiment show that in general, making the model colder produces the expected response of greater $^{17}O_{excess}$ changes in the interior resulting from even stronger kinetic fractionation due to colder temperatures. However, the pattern of $^{17}O_{excess}$ change does not directly follow the pattern of temperature change, showing that the spatial pattern of $^{17}O_{excess}$ change is not simply a linear function of temperature. An important aspect of the LGM-cold experiment is that the sea ice extent is overestimated by (~3 to 12° of latitude, as shown in Figure 9), relative to estimates of LGM sea ice extent from proxy reconstructions [*Gersonde et al.*, 2005; *Collins et al.*, 2012; *Roche et al.*, 2012]), and this may also affect the $^{17}O_{excess}$.

To examine the influence of sea ice extent on $^{17}O_{excess}$, we performed an additional experiment, "Extend-Ice," in which we use modern SST boundary conditions but prescribe amplified sea ice seasonality. In winter, we

©2014. American Geophysical Union. All Rights Reserved.

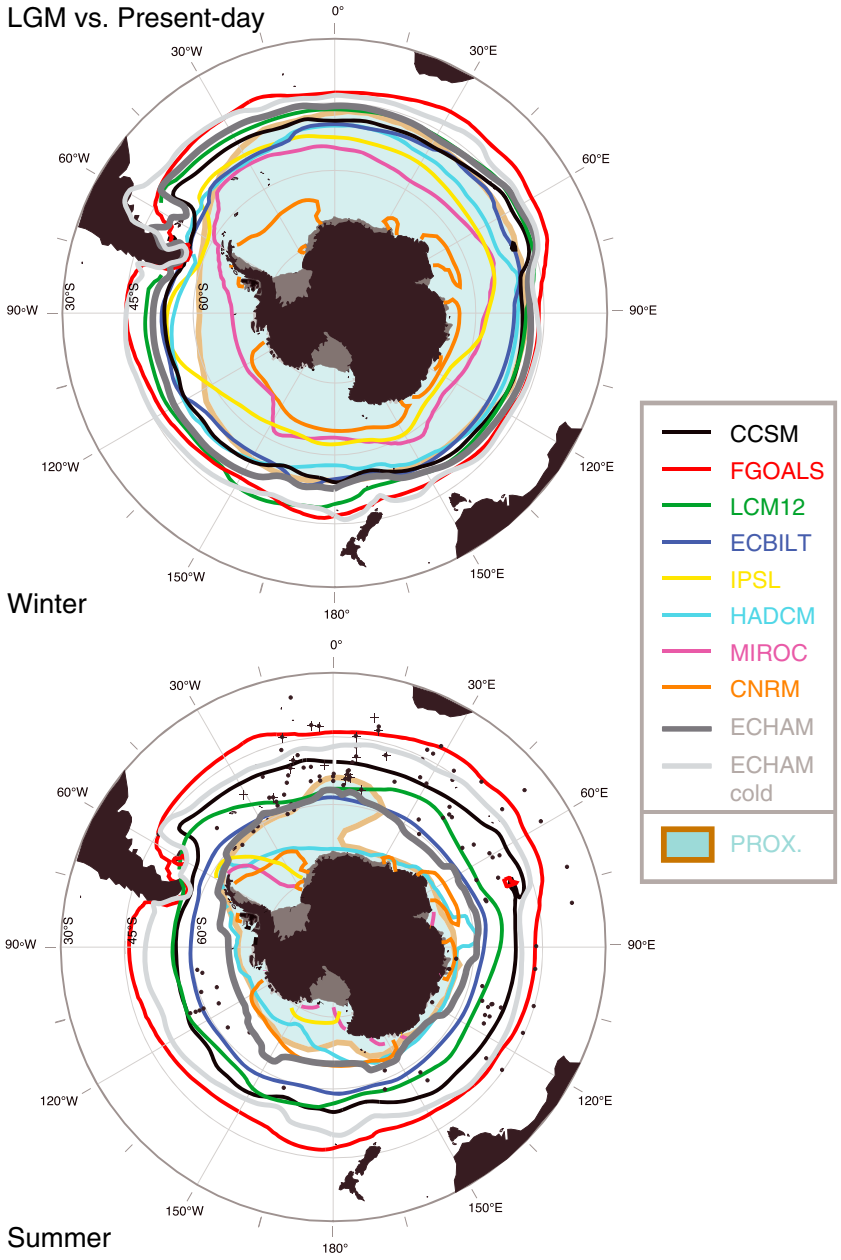

Figure 9. Comparison of LGM (dark gray) and LGM-cold (light gray) ECHAM4.6 winter and summer sea ice extent with multiple LGM GCM simulations adapted from *Roche et al.* [2012]. Maximum sea ice extent (>15 % sea ice concentration) for LGM (21 ka) compared with other GCM LGM simulations and proxy data [*Gersonde et al.*, 2005] for (top) winter and (bottom) summer.

extend the model sea ice climatology by ~10°N but keep summer sea ice extent unchanged. Between summer and winter the sea ice is prescribed to change linearly, extending ~5°N on average for both fall and spring seasons (Figure 10). Annual average results show that the extended sea ice margin results in a decrease of $^{17}O_{excess}$ over the entire Antarctic continent, with decreases of 8 to 12 per meg in the Antarctic interior over Vostok and Dome C, and a decrease at WAIS Divide of ~5 per meg, roughly half the response of the LGM simulation (Figure 8). The Extend-Ice simulations show a particularly strong decrease in $^{17}O_{excess}$ over West (~9 per meg) and East Antarctica (~14 per meg) during winter (JAS), as expected due to the prescribed winter sea ice expansion.

©2014. American Geophysical Union. All Rights Reserved.

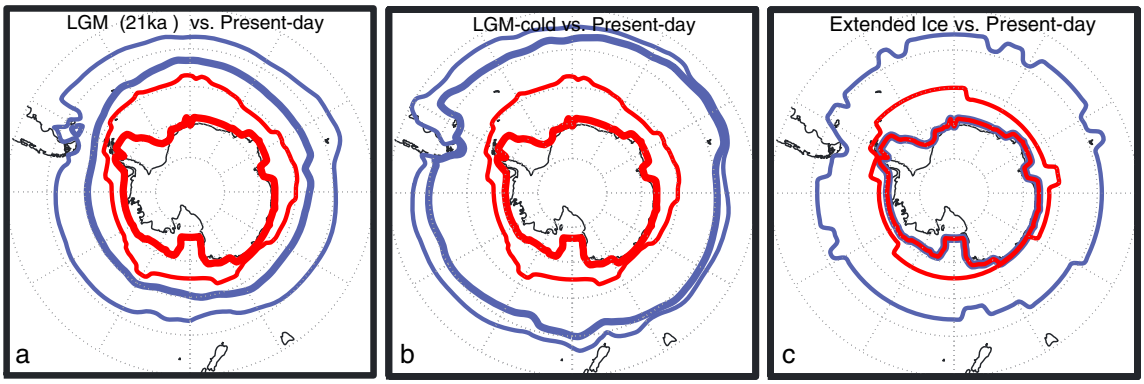

Figure 10. (a) Comparison of winter (thin) and summer (bold) sea ice extent for LGM (21 ka) (blue) versus present-day (red) in ECHAM4.6. (b) LGM-cold (21 ka minus 4°C) versus present-day. (c) Extended sea ice (modern day boundary conditions and 10°N expansion of winter-time sea ice) versus present-day. Winter and summer sea ice calculated as JAS and JFM mean.

4. Discussion

4.1. Controls on the $^{17}O_{excess}$ in Antarctic Precipitation

Interpretation of $^{17}O_{excess}$ in Antarctic ice cores has been challenging due to limited and inconsistently-calibrated data. Our findings show that there is a clear present-day spatial gradient of $^{17}O_{excess}$ across Antarctica, with higher values in the coastal and marine-influenced regions and lower values in the central East Antarctic interior. There is a similar spatial pattern to the change in $^{17}O_{excess}$ between the Last Glacial Maximum (LGM) and Early Holocene (EH) periods, with near-coastal sites showing little or no change in $^{17}O_{excess}$, while sites further inland—in both East and West Antarctica—indicate a greater magnitude of change. In the following paragraphs we discuss the implications of these results, with a focus on what matters to $^{17}O_{excess}$ in terms of climate boundary conditions. Sea ice extent emerges as a particularly important factor.

To illustrate the sensitivity of $^{17}O_{excess}$ to different model boundary conditions, we calculate the zonal annual average response of $^{17}O_{excess}$ (for $b = 0.007$), sea ice fraction, surface temperature, and rh_n versus latitude for all the model experiments (Modern, LGM, LGM-cold, and Extend-Ice). We display the West and East Antarctic sectors separately to allow for regional differences in sea ice concentration and extent (Figures 11 and 12). The gray bars highlight the latitude of maximum sea ice extent for each model experiment.

Figures 11 and 12 show that for both modern snowfall and for the LGM-EH change, the influence of supersaturation largely determines how $^{17}O_{excess}$ varies with latitude on the ice sheet. As already noted, the values used for tuning the sensitivity of supersaturation to temperature spans the range typically used in most previous work [*Hoffmann et al.*, 1998; *Schmidt et al.*, 2005; *Risi et al.*, 2010b; *Landais et al.*, 2012b], and a value of $b = 0.007$ in the standard linear parameterization provides a significantly better match to the data than lower values. That reasonably good model agreement with d_{ln} data during the present-day and LGM is also achieved with $b = 0.007$ provides further support for a strong sensitivity of supersaturation to temperature.

In contrast with the supersaturation effect, ocean surface relative humidity has a limited role in explaining the $^{17}O_{excess}$ of Antarctic precipitation. Normalized relative humidity does determine the initial $^{17}O_{excess}$ value in the marine boundary layer, and as the model results in Figures 11 and 12 illustrate, $^{17}O_{excess}$ in precipitation roughly tracks rh_n in midlatitudes, beginning to decrease as rh_n increases (when going from the equator towards the poles). However, the humidity-$^{17}O_{excess}$ relationship is decoupled at higher latitudes, as the strong dependence of $^{17}O_{excess}$ on kinetic fractionation increases in importance as colder temperatures are encountered. Indeed, the present-day latitudinal distribution of $^{17}O_{excess}$ is contrary to that expected if oceanic moisture source regions control present-day Antarctic $^{17}O_{excess}$ values. In the case of Vostok, Dome C, and Dome Fuji, for example, the dominant moisture sources are estimated to be from subtropical to midlatitude oceans [*Sodemann and Stohl*, 2009], which corresponds with lower rh_n and should therefore result in higher $^{17}O_{excess}$, whereas lower $^{17}O_{excess}$ is observed. In West Antarctica and coastal

©2014. American Geophysical Union. All Rights Reserved.

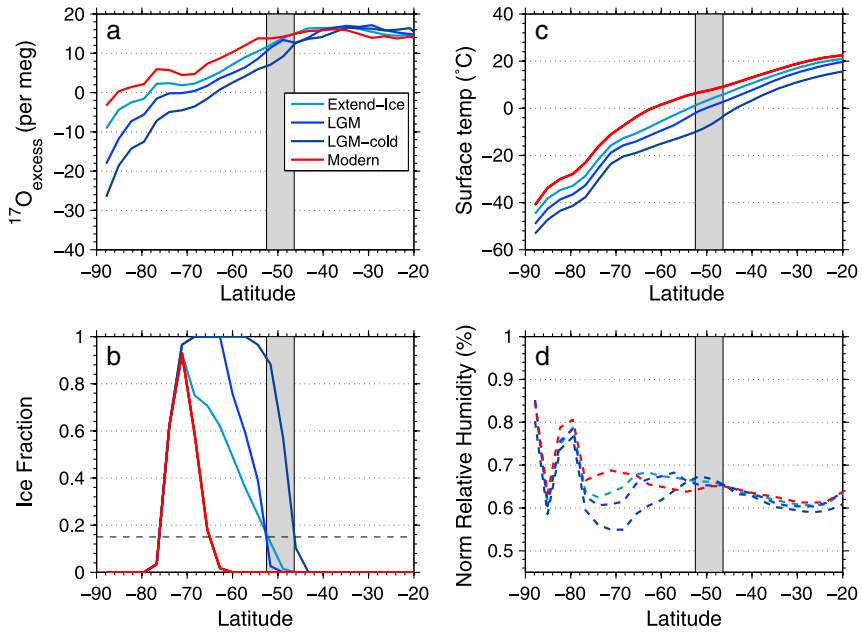

Figure 11. Modern, Extend-Ice, LGM, and LGM-cold GCM simulations for West Antarctica (70°W to 170°W) annual average using high supersaturation ($S = 1 - 0.007\,T$). (a) $^{17}O_{excess}$ versus latitude, gray band marks the range of latitude of maximum sea ice extent using a minimum threshold of 0.15 ice fraction. (b) Ice fraction for all simulations versus latitude. (c) Surface temp versus latitude for all three simulations. (d) Normalized relative humidity (rh_n %) versus latitude. Note that the few percent (2–3%) change in rh_n over the midlatitude is insufficient to explain the magnitude of $^{17}O_{excess}$ changes based on ~ −1 per meg/% rh_n from *Risi et al.* [2010a].

sites in East Antarctica, which tend to receive greater moisture from mid- to high-latitude source regions with greater rh_n, elevated $^{17}O_{excess}$ values are observed, opposite to that expected if rh_n were the determining factor.

It has been argued that observed glacial to interglacial $^{17}O_{excess}$ differences between ice core locations is due to different oceanic moisture source regions, controlled by their respective surface humidity [*Landais et al.*, 2008; *Risi et al.*, 2010a; *Winkler et al.*, 2012]. Yet our simulations show that fractionation under supersaturated conditions alone is sufficient to account for the magnitude of glacial-interglacial change, provided a relatively strong sensitivity of supersaturation to temperature. In the same simulations, rh_n increases only a few percent over the Southern Ocean moisture source regions (20 to 55°S), too little to account for the simulated $^{17}O_{excess}$ changes, the magnitude of which is clearly determined by the degree of fractionation in transport. Larger changes (~10%) in rh_n do occur over the sea ice region but are of the wrong sign (i.e., $^{17}O_{excess}$ on the continent decreases when rh_n decreases). In any case, moisture fluxes from the sea ice region are small and do not contribute a significant fraction of moisture to the continent.

The simple parameterization of supersaturation in terms of temperature does not fully capture all the ice core observations. Indeed, depending on the supersaturation sensitivity, the modeled LGM versus present-day $^{17}O_{excess}$ change may be underestimated in some locations and overestimated in others. Comparison of the different model experiments suggests that prescribed sea ice boundary conditions play an important role. Referring to the gray bars in Figures 11 and 12, which illustrate the maximum latitude of sea ice extent, we note that there is a marked change in the latitudinal gradient in $^{17}O_{excess}$ that occurs approximately at the latitude of the sea ice margin. In each of the LGM, LGM-cold, and Extend-Ice experiments, compared with the Modern experiment, there is correspondence between the location of the maximum sea ice extent and change in slope of the $^{17}O_{excess}$ gradient.

Although it is difficult to separate the influence of sea ice from the influence of temperature (because the two are highly correlated), the change in $^{17}O_{excess}$ between each progressively colder model experiment does not

©2014. American Geophysical Union. All Rights Reserved.

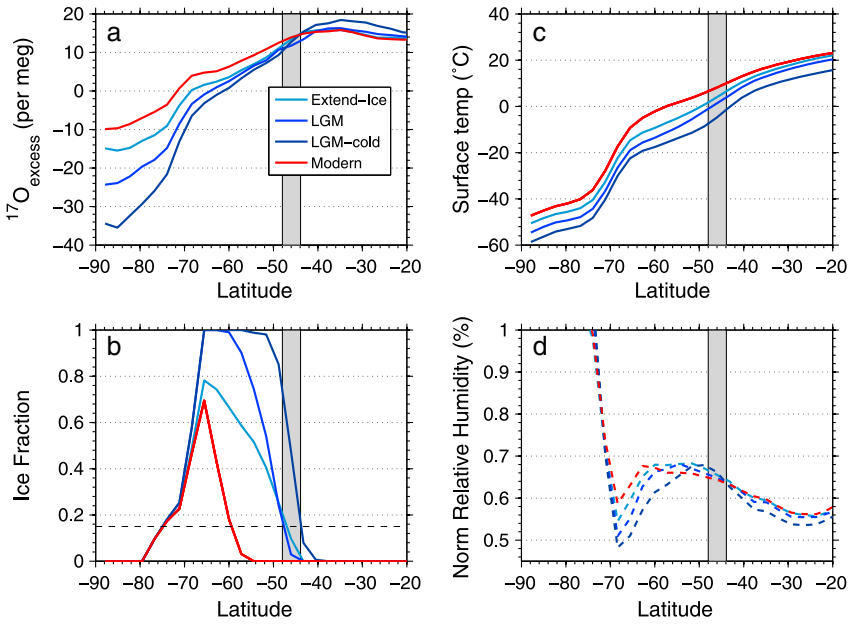

Figure 12. Modern, Extend-Ice, LGM, and LGM-cold GCM simulations for East Antarctica (290°E to 160°E) annual average using high supersaturation ($S = 1 - 0.007\,T$). (a) $^{17}O_{excess}$ for all simulations versus latitude, gray band same as in Figure 11. (b) Ice fraction versus latitude. (c) Surface temperature versus latitude. (d) Normalized relative humidity (rh_n %) versus latitude.

scale directly with the lower temperatures. Rather, the $^{17}O_{excess}$ gradient steepens for the same respective change in temperature in each model experiment. For example, in the Modern simulation the zonal average slope in $^{17}O_{excess}$ is −0.53 per meg/°C for temperatures between −20°C and − 45°C; this increases in magnitude to −0.63, −0.70, and −0.87 per meg/°C for Extend-Ice, LGM, and LGM-cold, respectively (Figure S3). Note that the increasing $^{17}O_{excess}$/temperature gradient also tracks the pattern of greater sea ice fraction for each colder model simulation. Furthermore, in the Extend-Ice simulation, the strongest response in $^{17}O_{excess}$ occurs during austral fall and winter, the periods of greatest sea ice expansion and maximum ice extent, while there is no change in $^{17}O_{excess}$ during austral summer (JFM), despite cooler temperatures relative to the Modern simulation.

These results suggest that $^{17}O_{excess}$ is sensitive to sea ice boundary conditions. The expansion of sea ice in these experiments influences $^{17}O_{excess}$ in at least two ways. First, expanded sea ice cover increases the meridional temperature gradient, with the result that poleward traveling air masses reach cold conditions sooner, resulting in stronger supersaturation and greater kinetic fractionation; this effect largely explains the change in slope of $^{17}O_{excess}$ approximately at the sea ice margin. Second, greater sea ice cover reduces the availability of local (high-latitude) moisture recharge of relatively enriched $^{17}O_{excess}$ water vapor into the atmosphere. In our model setup, sea ice concentration is binary (grids are either "on" or "off") and may not produce realistic estimates of sea ice concentration change, which would influence the degree to which the moisture-recharge effect is important. In general, though, both of these influences tend to lower $^{17}O_{excess}$ over the Antarctic continent. As the process of isotope fractionation acts as an integrator of the entire moisture transport path, changes in both ice fraction and extent would be expected to have a cumulative impact on the $^{17}O_{excess}$ in precipitation.

4.2. Interpretation of Individual Antarctic $^{17}O_{excess}$ Records

We conclude that the sign and magnitude of LGM to EH $^{17}O_{excess}$ changes apparent in the ice core time series can be explained by a common process: strong sensitivity of supersaturation to temperature during kinetic fractionation. One important implication of this result is that it is unnecessary to invoke the contribution of stratospheric moisture as an explanation for the Vostok $^{17}O_{excess}$ record. *Miller* [2008] suggested that, due to the low annual accumulation and high elevation of the East Antarctic plateau, the large glacial-interglacial $^{17}O_{excess}$ change at Vostok could reflect input from high-$^{17}O_{excess}$ water vapor with a

©2014. American Geophysical Union. All Rights Reserved.

stratospheric source. Yet the LGM to Early Holocene change in $^{17}O_{excess}$ at WAIS Divide is similar to that at Vostok. Based on present-day downward fluxes [*Stohl and Sodemann*, 2010; *Winkler et al.*, 2013], stratospheric water vapor contributes ~10^{-5} of the 22 cm a^{-1} annual mean ice accumulation rate at WAIS Divide, an order of magnitude less than the 0.014% calculated for Vostok by *Winkler et al.* [2013]. Even if the contribution of stratospheric input were 10 times greater for WAIS Divide, assuming a stratospheric $^{17}O_{excess}$ signature of ~3000 per meg [*Zahn et al.*, 2006; *Winkler et al.*, 2013], it would change the $^{17}O_{excess}$ by less than 0.12 per meg.

Our model results additionally show that sea ice extent plays an important role in determining the magnitude of $^{17}O_{excess}$ changes on glacial-interglacial timescales. In general, greater sea ice extent amplifies the $^{17}O_{excess}$ response to temperature. In this context, differences among the different ice core sites that are not fully captured by the model results discussed above are informative.

Taylor Dome and Talos Dome share similar elevations (~2300 m) and mean annual temperature (~40°C) and are in close proximity to one another. These sites are often referred to as "coastal," since they are both within less than 300 km from periodically open water. However, their moisture sources are quite different. Back trajectory modeling shows that Taylor Dome receives more than 60% of its total precipitation from the Pacific, along a trajectory that crosses over West Antarctica [*Scarchilli et al.*, 2010]; thus, the majority of the trajectories cross over the ice sheet. Talos Dome receives nearly twice the accumulation of Taylor Dome and about half of its total precipitation originates from the Indian Ocean; about one third originates from the Ross Sea [*Scarchilli et al.*, 2010].

At Talos Dome, the model versus data discrepancy is relatively large: the ice core observations show no change between the LGM and EH, while the model, using $b = 0.007$ which best fits most other locations, including Taylor Dome, simulates a change of ~12 per meg for LGM boundary conditions. Based on the similar LGM-EH $\delta^{18}O$ change (~5.5‰) at both Taylor Dome and Talos Dome, we can assume that the temperature changes were comparable; temperature-driven changes in supersaturation effects on $^{17}O_{excess}$ should also have been similar. This implies that either the air mass trajectory changes affected Talos Dome and Taylor Dome differently or that regional boundary conditions were different or both. Note that Talos Dome is situated upwind of Terra Nova Bay and the Ross Sea Polynya in the western Ross Sea. In winter, the Ross Sea Polynya contributes significantly to mesocyclonic activity, which favors the advection of moist maritime air into the interior. Local changes to features like this—which are not captured in the relatively coarse grid of our GCM simulations—could explain differences between these sites. For example, expansion of the Ross Sea ice shelf to form the Ross Sea Ice Sheet during the LGM [e.g., *Hall et al.*, 2000]; expanded sea ice north of the ice sheet margin would have cut off local moisture sources and would perhaps have had a larger impact on the isotopic composition of precipitation at Talos Dome than Taylor Dome.

The importance of local boundary conditions is also illustrated by comparing the model results for both Taylor Dome and Talos Dome with those for Siple Dome. The LGM model simulation ($b = 0.007$) produces a ~12 per meg decrease in $^{17}O_{excess}$ at Taylor Dome and Talos Dome, relative to present-day, but little to no change at Siple Dome. In the LGM simulation there is a significant increase in sea ice in the western Ross Sea but no change in the eastern Ross Sea (adjacent to Siple Dome). In the model simulations, local moisture sources near Siple Dome change little; since this low elevation (600 m), truly coastal site is relatively warm and not subject to significant supersaturation effects, and since rh_n does not change significantly between the two simulations, there is no resulting change of $^{17}O_{excess}$. This is consistent with the suggestion of *Winkler et al.* [2012] that warmer, more coastal sites should be less influenced by the effects of supersaturation and therefore more faithfully record changes of rh_n (or in this case, lack thereof), than more interior sites. In the actual ice core measurements, there is no evidence of a glacial-interglacial change in $^{17}O_{excess}$ at Siple Dome, supporting this understanding. Nevertheless, these comparisons also suggest that using $^{17}O_{excess}$ from coastal sites to infer moisture source changes is likely to be problematic. In general, such sites are more likely to be influenced by local peculiarities in ocean surface conditions than more interior sites, and therefore, despite the reduced sensitivity to supersaturation, coastal cores may not provide representative information. When interpreting $^{17}O_{excess}$ data in detail as additional higher-resolution records are obtained, it will be important to consider regional details such as air mass trajectories and sea ice concentration.

Finally, some unique features of the WAIS Divide ice core record are noted. As discussed in *WAIS Divide Project Members* [2013], the WDC $\delta^{18}O$ record shows an early deglacial warming, beginning between 22 and 20 ka.

©2014. American Geophysical Union. All Rights Reserved.

East Antarctic ice core $\delta^{18}O$ records show little change until a relatively abrupt $\delta^{18}O$ increase at ~18 ka. Model experiments using a symmetric sea ice reduction suggest that the earlier warming at WAIS Divide could reflect the greater sensitivity of this site to sea ice change [*WAIS Divide Project Members*, 2013]. Consistent with this, the WDC $^{17}O_{excess}$ record shows an inflection point occurring at ~22 ka, while $^{17}O_{excess}$ at both Vostok and Dome C begins to increase between ~ 18.5 ka and 17.5 ka. Based on the model experiments discussed above, we propose that the early increase in $^{17}O_{excess}$ at ~22 ka in WDC results from early decreasing sea ice extent resulting in a reduced influence of kinetic fractionation on $^{17}O_{excess}$, owing both to warmer temperatures, greater local moisture recharge, and less transit distance over sea ice. The difference between LGM and LGM-cold model experiments show that the response of sea ice can be asymmetric. Expressions of early deglacial changes in SST and sea ice extent have been identified in other high-latitude Southern Hemisphere records and are suggestive of greater changes in the Pacific sector than elsewhere [*Kanfoush*, 2000; *Lamy et al.*, 2007; *Collins et al.*, 2012], which would contribute to the different timing signature observed in $^{17}O_{excess}$ between East and West Antarctica.

Another notable feature of the WDC $^{17}O_{excess}$ record is the unambiguous rise in $^{17}O_{excess}$ beginning at ~15 ka. WDC $^{17}O_{excess}$ increases by ~10 per meg over the ~400 year period prior to the Antarctic Isotope Maximum (AIM) 1 peak in $\delta^{18}O$, which in turn is near-coincident with the rapid increase in $\delta^{18}O$ in Greenland ice cores and the abrupt rise in methane at ~14.7 ka B.P. that defines the beginning of the Bølling-Allerød warm interval [*WAIS Divide Project Members*, 2013]. Relative to the background variability in $^{17}O_{excess}$, the magnitude of the $^{17}O_{excess}$ rise is much larger than seen in the d_{ln} (or d_{excess}) record in WDC, suggesting a significant change in boundary conditions. We speculate that this reflects a decrease in sea ice concentration preceding the isotope maximum, as indicated for example by ocean model simulations of AIM events [*Knorr and Lohmann*, 2003]. We note that there is a small but significant decrease in the ssNa concentration during this interval, also consistent with decreasing sea ice [*Wolff et al.*, 2006; *WAIS Divide Project Members*, 2013].

During the Holocene (12 to 0 ka) interval, $^{17}O_{excess}$ in WDC varies little compared to the magnitude of glacial-interglacial change. However, it exhibits a long-term negative trend beginning at ~9 ka. We note that a similar long-term decrease has been observed in other Southern Hemisphere and SST proxy records [*Lamy et al.*, 2002; *Nielsen et al.*, 2004; *Lamy et al.*, 2007], which has been suggested to result from decreasing austral spring orbital forcing and increasing sea ice extent and/or concentration [*Steig et al.*, 1998a; *Hodell et al.*, 2001; *Renssen et al.*, 2005]. This is again consistent with our finding that sea ice exerts a significant control on $^{17}O_{excess}$.

4.3. Implications for Modeling $^{17}O_{excess}$

The development of $^{17}O_{excess}$ ice core records covering the last glacial-to-interglacial transition, in combination with d_{ln}, provides an important new constraint for water isotope-enabled GCM simulations. The amount of kinetic fractionation in the model, parameterized by a temperature-dependent supersaturation function, has a strong influence on the magnitude and sign of the $^{17}O_{excess}$ spatial gradient. As we have shown, capturing the spatial pattern of glacial-interglacial change in $^{17}O_{excess}$ using the standard linear parameterization of supersaturation requires greater kinetic fractionation during ice formation than has typically been used in the literature [*Hoffmann et al.*, 1998; *Werner and Heimann*, 2002; *Schmidt et al.*, 2005; *Masson-Delmotte et al.*, 2008; *Werner et al.*, 2011]. However, the linear parameterization for supersaturation as a simple function of temperature, as used in most work (including that presented here) was developed over 35 years ago, and the choice of a linear dependence on temperature is somewhat arbitrary. Indeed, *Jouzel and Merlivat* [1984] also proposed exponential and power law dependencies. The increasing availability of $^{17}O_{excess}$ data should inspire reevaluation of the treatment of supersaturation in GCMs. The routine inclusion of $^{17}O_{excess}$ within GCMs also has the potential to help improve other aspects of the model hydrological cycle beyond those related to ice core research, such as the partitioning of water vapor versus ice in clouds, rain reevaporation during convective downdrafts, and surface evaporative processes [*Risi et al.*, 2008; *Landais et al.*, 2010; *Risi et al.*, 2010b].

As already noted, all of our model simulations underestimate the mean $^{17}O_{excess}$ over Antarctica. This may largely reflect uncertainty in the mean seawater $^{17}O_{excess}$ value but may also reflect biases in the model climatology. In particular, the relatively low model resolution means that the steepness of the Antarctic

©2014. American Geophysical Union. All Rights Reserved.

continental margin is underestimated, which may allow greater penetration of marine air mass intrusion into Antarctica, making the Antarctic interior more influenced by marine sources than it actually is [*Noone and Simmonds*, 2004; *Ding et al.*, 2011]. Indeed, we find that the modeled annual precipitation at WAIS Divide is ~50 % higher than observed. Analysis of different model resolutions in ECHAM5 by *Werner et al.* [2011] showed that, in general, higher-resolution simulations produced better agreement with observational data sets. In particular, the relationship between d_{excess} and δD is in much better agreement with the *Masson-Delmotte et al.* [2008] Antarctic isotope database in the ECHAM5 T159 simulation.

Although the ECHAM4.6 model qualitatively reproduces both the present-day spatial gradient and the magnitude of LGM-EH change in $^{17}O_{excess}$, inconsistencies between the ice core observations and model experiments highlight the additional work needed. We identify a number of important factors relevant to accurately simulating $^{17}O_{excess}$, d_{ln}, and d_{excess}.

First, additional measurements of $\delta^{18}O$, d_{excess}, and $^{17}O_{excess}$ in laboratory experiments at subzero temperatures are needed to refine the relationship of temperature-dependent equilibrium fractionation between all isotope species, which can provide a more solid foundation from which to investigate kinetic fractionation effects on d_{excess} (and d_{ln}). The benchmark for isotope-enabled GCM validation in polar regions has been the reproduction of the observed d_{excess} spatial gradient, in conjunction with the highly depleted δD or $\delta^{18}O$ values. There has been difficulty simulating realistic values of d_{excess} in the East Antarctic interior, which typically have too steep a spatial gradient in the simulations. In ECHAM4.6, the inclusion of a temperature-dependent diffusion fractionation factor for δD [*Luz et al.*, 2009], as well the most up-to-date equilibrium fractionation factors for δD and $\delta^{18}O$ below freezing [*Ellehøj et al.*, 2013] have reduced the steep spatial gradient, in better agreement with d_{excess} observations.

Second, a key goal should be to improve the relatively simple kinetic fractionation parameterizations used in both simple 1-D isotope models and intermediate complexity isotope models, as well as in most GCMs. In particular, the increased computational capacity available for GCMs permits moving beyond the fairly simple supersaturation parameterization to explicitly determine supersaturation, dependent on detailed cloud microphysics (e.g., types of condensation nuclei). The subgrid scale at which phase changes occur require kinetic fractionation to still be parameterized; however, more advanced parameterizations of kinetic fractionation are being implemented that better account for convective cloud processes in the tropical regions [*Risi et al.*, 2008; *Blossey et al.*, 2010; *Landais et al.*, 2010]. Similarly, more sophisticated parameterizations that incorporate surface kinetic fractionation effects due to differences in water droplet size, ice crystal morphology (e.g., columnar versus dendritic) are needed. These surface kinetic fractionation effects may vary greatly between regions where dry deposition of tiny ice crystals (diamond dust) prevail, like the East Antarctic plateau, compared to wet deposition sites in coastal regions [*Nelson*, 2011]. The sensitivity of $^{17}O_{excess}$ to kinetic fractionation makes it an ideal indicator for testing such aspects of the model physics.

The importance of supersaturation in determining the behavior of $^{17}O_{excess}$ and d_{ln} (or d_{excess}) also suggests that further work must be done to characterize the kinetic fractionation effects during ice crystal formation on a microscopic level, both with additional empirical lab studies and in situ low temperature/high altitude measurements. The early study by *Jouzel and Merlivat* [1984] on kinetic isotope fractionation during snow formation was performed on the frost grown onto a cooling plate (−20°C) from room temperature (20°C) without conditions that controlled the supersaturation ratio, resulting in an overestimated supersaturation ration of 2.00 [*Uemura et al.*, 2005]. Recent work by *Uemura et al.* [2005] produced experimental conditions that mimicked those of mixed clouds in which both vapor and supercooled water droplets coexist due to the realistic temperature range (−12 to −15°C). Their results produced lower supersaturation ratios than *Jouzel and Merlivat* [1984], but the range of supersaturation ratios (S = 1.165 to 1.221) at −15°C are consistent with a higher sensitivity of supersaturation where $b > 0.007$. Measurements performed at colder temperatures ranging from −20 to −50°C would be invaluable.

Finally, to improve the interpretation of Antarctic $^{17}O_{excess}$, more measurements on surface snow and ice cores from both coastal and interior sites are needed. Acquiring additional $^{17}O_{excess}$ measurements on transects that span coastal to interior sites, like those obtained by *Landais et al.* [2008], would provide higher spatial resolution, important for examining the sensitivity of $^{17}O_{excess}$ to regional details such as coastal moisture sources (e.g., leads and polynyas) and orographic features.

©2014. American Geophysical Union. All Rights Reserved.

5. Conclusions

Our ice core measurements, in combination with those from *Landais et al.* [2008] and *Winkler et al.* [2012] show that there is a strong spatial gradient of $^{17}O_{excess}$ across Antarctica, with elevated values in the coastal and marine-influenced regions and lower values in the central East Antarctic plateau. The modern spatial gradient in $^{17}O_{excess}$ is best captured with a strong sensitivity of supersaturation to temperature. The data also show that there are large changes in the inland regions of both East and West Antarctica, but little change in the coastal regions over the last deglaciation (LGM to Early Holocene). An atmospheric GCM forced with LGM boundary conditions, and the same strong sensitivity of supersaturation to temperature that best matches the modern data, reproduces the observed sign, magnitude, and spatial pattern of LGM to Early Holocene change in $^{17}O_{excess}$. We conclude that kinetic isotope effects result from supersaturation of water vapor over ice dominate the spatial pattern of modern $^{17}O_{excess}$ in Antarctic precipitation as well as the pattern of change through the last deglaciation. These results imply a limited role of changes in relative humidity in determining the glacial-interglacial $^{17}O_{excess}$ in Antarctic precipitation and show that the influence of stratospheric water vapor inputs is probably negligible.

In the GCM experiments, there is correspondence between the latitude of maximum sea ice extent and a change in $^{17}O_{excess}$ gradient, indicating that the sea ice boundary conditions play a role in controlling $^{17}O_{excess}$. A principal control on the amount of kinetic fractionation is the temperature gradient between moisture source and precipitation site, and in our GCM experiments, an effective way to increase the temperature gradient is by expansion of sea ice. The expansion of sea ice causes poleward traveling moisture to encounter colder conditions earlier, resulting in the onset of supersaturation conditions, and initiating a decrease in $^{17}O_{excess}$. A secondary result of sea ice cover is the reduction of evaporative moisture recharge to the overlying air mass, which limits the addition of relatively enriched $^{17}O_{excess}$ water vapor from the high-latitude ocean surface.

Most previous studies have relied on changes in normalized relative humidity at the moisture origin to explain the observed glacial-interglacial changes in $^{17}O_{excess}$. Despite the ~10° northward expansion of sea ice in both the LGM and present-day Extend-Ice experiments, we simulate only minor changes in the relative humidity at the ocean surface. Furthermore, $^{17}O_{excess}$ over Antarctica does not respond as would be expected if surface relative humidity were the main driver. Sea ice changes and the associated temperature changes alone—with no significant change in moisture source humidity—are sufficient to explain the observed $^{17}O_{excess}$ glacial-interglacial changes at most locations in Antarctica where observations exist.

Due to the few $^{17}O_{excess}$ ice core measurements and inconsistently normalized data, interpretation of $^{17}O_{excess}$ in Antarctic ice cores has been challenging. The measurements from the WDC record provide the first complete $^{17}O_{excess}$ record through the LGM to the present-day, indicating an early deglacial change in $^{17}O_{excess}$ around 22 ka, an early Holocene optimum from 11.5 to 9.5 ka, and a post EH optimum period of $^{17}O_{excess}$ decline. We propose that expansion of sea ice during the LGM and post EH optimum led to the lowering of $^{17}O_{excess}$ during these periods. The response of $^{17}O_{excess}$ at 22 ka, which predates changes in both $^{17}O_{excess}$ and $\delta^{18}O$ in Dome C and Vostok by approximately 4000 years, suggests an early retreat of sea ice in the southern Pacific Ocean, and supports the findings of *WAIS Divide Project Members* [2013] that changes in sea ice extent may explain the early $\delta^{18}O$ increases in WDC at 22 and 20 ka.

Even with strong supersaturation sensitivity and expanded sea ice boundary conditions, we find that our GCM simulations generally underestimate the magnitude of LGM-EH change in $^{17}O_{excess}$ in the WDC record. We speculate that reflects a combination of modeled modern temperatures and modeled LGM temperatures that are too warm; the "LGM-cold" experiment with temperature reduced an additional 4°C supports this view. Preliminary estimates of the glacial-interglacial temperature change at WAIS Divide from borehole temperature reconstructions indicate a larger temperature change than simulated in our experiments (K. Cuffey, personal communication, 2013). This suggests that $^{17}O_{excess}$ could provide an independent constraint on the magnitude of glacial-interglacial temperature change. However, site-specific differences between the observed and modeled ice core $^{17}O_{excess}$ data suggest that the climate interpretation of $^{17}O_{excess}$ at particular locations will require assessment of regional circulation patterns, sea ice concentration, and local meteorological conditions.

©2014. American Geophysical Union. All Rights Reserved.

Acknowledgments
This work was supported by National Science Foundation (NSF) OPP grants 0837990 and 1043092 to E.J.S. We thank K. Samek, B. Vanden Heuvel, and R. Teel for their assistance with the isotope measurements. We also thank J. Pedro for discussions, J. Schmitt for use of the Monte Carlo Averaging code, B. Stenni for providing the unpublished Talos Dome $\delta^{18}O$ and δD data, and D. Roche for figure permissions. The authors appreciate the support of the WAIS Divide Science Coordination Office (K. Taylor, M. Twickler, and J. Souney) for the collection and distribution of the WAIS Divide ice core; Ice Drilling and Design and Operations for drilling; and the National Ice Core Laboratory for curating the core. Many thanks to two anonymous reviewers for valuable comments and suggestions. Data from this paper are available from the National Snow and Ice Data Center (www.nsidc.org).

References

Abe, O. (2008), Isotope fractionation of molecular oxygen during adsorption/desorption by molecular sieve zeolite, *Rapid Commun. Mass Spectrom.*, *22*(16), 2510–2514.

Baker, L., I. Franchi, J. Maynard, I. Wright, and C. Pillinger (2002), A technique for the determination of $^{18}O/^{16}O$ and $^{17}O/^{16}O$ isotopic ratios in water from small liquid and solid samples, *Anal. Chem.*, *74*(7), 1665–1673.

Barkan, E., and B. Luz (2005), High precision measurements of $^{17}O/^{16}O$ and $^{18}O/^{16}O$ ratios in H_2O, *Rapid Commun. Mass Spectrom.*, *19*(24), 3737–3742.

Barkan, E., and B. Luz (2007), Diffusivity fractionations of $H_2{}^{16}O/H_2{}^{17}O$ and $H_2{}^{16}O/H_2{}^{18}O$ in air and their implications for isotope hydrology, *Rapid Commun. Mass Spectrom.*, *21*, 2999–3005.

Berger, A. (1978), Long-term variations of caloric insolation resulting from the Earth's orbital elements, *Quatern. Res.*, *9*(2), 139–167, doi:10.1016/0033-5894(78)90064-9.

Blossey, P. N., Z. Kuang, and D. M. Romps (2010), Isotopic composition of water in the tropical tropopause layer in cloud-resolving simulations of an idealized tropical circulation, *J. Geophys. Res.*, *115*, D24309, doi:10.1029/2010JD014554.

Braconnot, P., B. Otto-Bliesner, S. Harrison, S. Joussaume, J. Y. Peterchmitt, A. Abe-Ouchi, M. Crucifix, E. Driesschaert, T. Fichefet, and C. D. Hewitt (2007), Results of PMIP2 coupled simulations of the mid-Holocene and Last Glacial Maximum–Part 1: Experiments and large-scale features, *Clim. Past*, *3*(2), 261–277.

Brook, E. J., J. W. C. White, A. S. M. Schilla, M. L. Bender, B. Barnett, J. P. Severinghaus, K. C. Taylor, R. B. Alley, and E. J. Steig (2005), Timing of millennial-scale climate change at Siple Dome, West Antarctica, during the last glacial period, *Quaternary Sci. Rev.*, *24*(12-13), 1333–1343, doi:10.1016/j.quascirev.2005.02.002.

Collins, L. G., J. Pike, C. S. Allen, and D. A. Hodgson (2012), High-resolution reconstruction of southwest Atlantic sea-ice and its role in the carbon cycle during marine isotope stages 3 and 2, *Paleoceanography*, *27*, PA3217, doi:10.1029/2011PA002264.

Dansgaard, W. (1964), Stable isotopes in precipitation, *Tellus*, *16*, 436–468.

Ding, Q., E. J. Steig, D. S. Battisti, and M. Küttel (2011), Winter warming in West Antarctica caused by central tropical Pacific warming, *Nat. Geosci.*, *4*(6), 398–403, doi:10.1038/ngeo1129.

Ellehøj, M. D., H. C. Steen-Larsen, S. J. Johnsen, and M. B. Madsen (2013), Ice-vapor equilibrium fractionation factor of hydrogen and oxygen isotopes: Experimental investigations and implications for stable water isotope studies, *Rapid Commun. Mass Spectrom.*, *27*(19), 2149–2158, doi:10.1002/rcm.6668.

EPICA Community Members (2004), Eight glacial cycles from an Antarctic ice core, *Nature*, *429*(6992), 623–628, doi:10.1038/nature02599.

EPICA Community Members (2006), One-to-one coupling of glacial climate variability in Greenland and Antarctica, *Nature*, *444*(7116), 195–198, doi:10.1038/nature05301.

Frezzotti, M., G. Bitelli, and P. de Michelis (2004), Geophysical survey at Talos Dome, East Antarctica: The search for a new deep-drilling site, *Ann. Glaciol.*, *39*(1), 423–432.

Fujita, K., and O. Abe (2006), Stable isotopes in daily precipitation at Dome Fuji, East Antarctica, *Geophys. Res. Lett.*, *33*, L18503, doi:10.1029/2006GL026936.

Gat, J. (1996), Oxygen and hydrogen isotopes in the hydrologic cycle, *Annu. Rev. Earth Planet. Sci.*, *24*, 225–262.

Gersonde, R., X. Crosta, A. Abelmann, and L. Armand (2005), Sea-surface temperature and sea ice distribution of the Southern Ocean at the EPILOG Last Glacial Maximum—A circum-Antarctic view based on siliceous microfossil records, *Quaternary Sci. Rev.*, *24*(7–9), 869–896, doi:10.1016/j.quascirev.2004.07.015.

Hall, B. L., G. H. Denton, and C. H. Hendy (2000), Evidence from Taylor Valley for a grounded ice sheet in the Ross Sea, Antarctica, *Geogr. Ann. A.*, *82*(2–3), 275–303.

Helsen, M. M., R. S. W. van de Wal, and M. R. van den Broeke (2007), The isotopic composition of present-day Antarctic snow in a Lagrangian atmospheric simulation*, *J. Clim.*, *20*(4), 739–756, doi:10.1175/JCLI4027.1.

Hodell, D. A., S. L. Kanfoush, A. Shemesh, X. Crosta, C. D. Charles, and T. P. Guilderson (2001), Abrupt cooling of Antarctic surface waters and sea ice expansion in the south Atlantic sector of the southern ocean at 5000 cal yr B.P, *Quatern. Res.*, *56*(2), 191–198, doi:10.1006/qres.2001.2252.

Hoffmann, G., M. Werner, and M. Heimann (1998), Water isotope module of the ECHAM atmospheric general circulation model: A study on timescales from days to several years, *J. Geophys. Res.*, *103*(D14), 16,871–16,896, doi:10.1029/98JD00423.

Hoffmann, G., M. Cuntz, J. Jouzel, and M. Werner (2005), A systematic comparison between the IAEA/GNIP isotope network and the ECHAM 4 atmospheric general circulation model, in *Isotopes in the Water Cycle: Past, Present and Future of a Developing Science*, pp. 303–320, Springer, Netherlands.

Jouzel, J., and L. Merlivat (1984), Deuterium and oxygen 18 in precipitation: Modeling of the isotopic effects during snow formation, *J. Geophys. Res.*, *89*, 11,749–11,757, doi:10.1029/JD089iD07p11749.

Jouzel, J., F. Vimeux, N. Caillon, G. Delaygue, G. Hoffmann, V. Masson-Delmotte, and F. Parrenin (2003), Magnitude of isotope/temperature scaling for interpretation of central Antarctic ice cores, *J. Geophys. Res.*, *108*(D12), 4361, doi:10.1029/2002JD002677.

Jouzel, J., et al. (2007), Orbital and millennial antarctic climate variability over the past 800,000 years, *Science*, *317*(5839), 793–796, doi:10.1126/science.1141038.

Kanfoush, S. L. (2000), Millennial-scale instability of the antarctic Ice sheet during the Last Glaciation, *Science*, *288*(5472), 1815–1819, doi:10.1126/science.288.5472.1815.

Kavanaugh, J. L., and K. M. Cuffey (2003), Space and time variation of $\delta^{18}O$ and δD in Antarctic precipitation revisited, *Global Biogeochem. Cycles*, *17*(1), 1017, doi:10.1029/2002GB001910.

Knorr, G., and G. Lohmann (2003), Southern Ocean origin for the resumption of Atlantic thermohaline circulation during deglaciation, *Nature*, *424*(6948), 532–536, doi:10.1038/nature01855.

Lamy, F., C. Rühlemann, D. Hebbeln, and G. Wefer (2002), High- and low-latitude climate control on the position of the southern Peru-Chile Current during the Holocene, *Paleoceanography*, *17*(2), 1028, doi:10.1029/2001PA000727.

Lamy, F., J. Kaiser, H. W. Arz, D. Hebbeln, U. Ninnemann, O. Timm, A. Timmermann, and J. R. Toggweiler (2007), Modulation of the bipolar seesaw in the Southeast Pacific during Termination 1, *Earth Planet. Sci. Lett.*, *259*(3-4), 400–413, doi:10.1016/j.epsl.2007.04.040.

Landais, A., E. Barkan, and B. Luz (2008), Record of $\delta^{18}O$ and ^{17}O-excess in ice from Vostok Antarctica during the last 150,000 years, *Geophys. Res. Lett.*, *35*, L02709, doi:10.1029/2007GL032096.

Landais, A., C. Risi, S. Bony, F. Vimeux, L. Descroix, S. Falourd, and A. Bouygues (2010), Combined measurements of ^{17}O-excess and d-excess in African monsoon precipitation: Implications for evaluating convective parameterizations, *Earth Planet. Sci. Lett.*, *298*(1), 104–112.

Landais, A., A. Ekaykin, E. Barkan, R. Winkler, and B. Luz (2012a), Seasonal variations of ^{17}O-excess and d-excess in snow precipitation at Vostok station, East Antarctica, *J. Glaciol.*, *58*(210), 725–733, doi:10.3189/2012JoG11J237.

©2014. American Geophysical Union. All Rights Reserved.

Landais, A., H. C. Steen-Larsen, M. Guillevic, V. Masson-Delmotte, B. Vinther, and R. Winkler (2012b), Triple isotopic composition of oxygen in surface snow and water vapor at NEEM (Greenland), *Geochim. Cosmochim. Acta*, *77*, 304–316, doi:10.1016/j.gca.2011.11.022.

Legrand, M., and R. J. Delmas (1985), Spatial and temporal variations of snow chemistry in Terre Adelie (East Antarctica), *Ann. Glaciol.*, *7*, 20–25.

Luz, B., and E. Barkan (2010), Variations of $^{17}O/^{16}O$ and $^{18}O/^{16}O$ in meteoric waters, *Geochim. Cosmochim. Acta*, *74*(22), 6276–6286, doi:10.1016/j.gca.2010.08.016.

Luz, B., E. Barkan, R. Yam, and A. Shemesh (2009), Fractionation of oxygen and hydrogen isotopes in evaporating water, *Geochim. Cosmochim. Acta*, *73*(22), 6697–6703.

Majoube, M. (1971), Oxygen-18 and deuterium fractionation between water and steam, *J. Chim. Phys. Phys. Chim. Biol.*, *68*(10), 1423–1436.

Masson-Delmotte, V., et al. (2008), A review of Antarctic surface snow isotopic composition: Observations, atmospheric circulation, and isotopic modeling, *J. Clim.*, *21*(13), 3359–3387, doi:10.1175/2007JCLI2139.1.

Matsuhisa, Y., J. R. Goldsmith, and R. N. Clayton (1978), Mechanisms of hydrothermal crystallization of quartz at 250°C and 15 kbar, *Geochim. Cosmochim. Acta*, *42*(2), 173–182, doi:10.1016/0016-7037(78)90130-8.

Merlivat, L., and J. Jouzel (1979), Global climatic interpretation of the deuterium-oxygen 18 relationship for precipitation, *J. Geophys. Res.*, *84*(C8), 5029–5033, doi:10.1029/JC084iC08p05029.

Miller, M. F. (2008), Comment on "Record of $\delta^{18}O$ and ^{17}O-excess in ice from Vostok Antarctica during the last 150,000 years" by Amaelle Landais et al, *Geophys. Res. Lett.*, *35*, L23708, doi:10.1029/2008GL034505.

Motoyama, H., N. Hirasawa, K. Satow, and O. Watanabe (2005), Seasonal variations in oxygen isotope ratios of daily collected precipitation and wind drift samples and in the final snow cover at Dome Fuji Station, Antarctica, *J. Geophys. Res.*, *110*, D11106, doi:10.1029/2004JD004953.

Nelson, J. (2011), Theory of isotopic fractionation on facetted ice crystals, *Atmos. Chem. Phys.*, *11*(22), 11,351–11,360, doi:10.5194/acp-11-11351-2011.

Nielsen, S. H. H., N. Koç, and X. Crosta (2004), Holocene climate in the Atlantic sector of the Southern Ocean: Controlled by insolation or oceanic circulation?, *Geology*, *32*(4), 317, doi:10.1130/G20334.1.

Noone, D., and I. Simmonds (2004), Sea ice control of water isotope transport to Antarctica and implications for ice core interpretation, *J. Geophys. Res.*, *109*, D07105, doi:10.1029/2003JD004228.

Orsi, A. J., B. D. Cornuelle, and J. P. Severinghaus (2012), Little Ice Age cold interval in West Antarctica: Evidence from borehole temperature at the West Antarctic Ice Sheet (WAIS) Divide, *Geophys. Res. Lett.*, *39*, L09710, doi:10.1029/2012GL051260.

Otto-Bliesner, B. L., E. C. Brady, G. Clauzet, R. Tomas, S. Levis, and Z. Kothavala (2006), Last glacial maximum and Holocene climate in CCSM3, *J. Clim.*, *19*(11), 2526–2544, doi:10.1175/JCLI3748.1.

Peltier, W. R. (2004), Global glacial isostasy and the surface of the ice-age Earth: The ICE-5G (VM2) model and GRACE, *Annu. Rev. Earth Planet. Sci.*, *32*, 111–149, doi:10.1146/annurev.earth.32.082503.144359.

Petit, J. R., J. White, N. W. Young, J. Jouzel, and Y. S. Korotkevich (1991), Deuterium excess in recent Antarctic Snow, *J. Geophys. Res.*, *96*(D3), 5113–5122, doi:10.1029/90JD02232.

Petit, J. R., et al. (1999), Climate and atmospheric history of the past 420,000 years from the Vostok ice core, Antarctica, *Nature*, *399*(6735), 429–436, doi:10.1038/20859.

Radok, U., and R. C. Lile (1977), A year of snow accumulation at Plateau Station, *Antarct. Res.*, *25*, 17–26.

Renssen, H., H. Goosse, T. Fichefet, V. Masson-Delmotte, and N. Koç (2005), Holocene climate evolution in the high-latitude Southern Hemisphere simulated by a coupled atmosphere-sea ice-ocean-vegetation model, *Holocene*, *15*(7), 951–964, doi:10.1191/0959683605hl869ra.

Risi, C., S. Bony, and F. Vimeux (2008), Influence of convective processes on the isotopic composition ($\delta^{18}O$ and δD) of precipitation and water vapor in the tropics: 2. Physical interpretation of the amount effect, *J. Geophys. Res.*, *113*, D19306, doi:10.1029/2008JD009943.

Risi, C., A. Landais, S. Bony, J. Jouzel, V. Masson-Delmotte, and F. Vimeux (2010a), Understanding the ^{17}O-excess glacial-interglacial variations in Vostok precipitation, *J. Geophys. Res.*, *115*, D10112, doi:10.1029/2008JD011535.

Risi, C., S. Bony, F. Vimeux, and J. Jouzel (2010b), Water-stable isotopes in the LMDZ4 general circulation model: Model evaluation for present-day and past climates and applications to climatic interpretations of tropical isotopic records, *J. Geophys. Res.*, *115*, D12118, doi:10.1029/2009JD013255.

Risi, C., A. Landais, R. Winkler, and F. Vimeux (2013), Can we determine what controls the spatio-temporal distribution of d-excess and ^{17}O-excess in precipitation using the LMDZ general circulation model?, *Clim. Past*, *9*(5), 2173–2193, doi:10.5194/cp-9-2173-2013.

Roche, D. M., X. Crosta, and H. Renssen (2012), Evaluating Southern Ocean sea-ice for the Last Glacial Maximum and pre-industrial climates: PMIP-2 models and data evidence, *Quaternary Sci. Rev.*, *56*, 99–106, doi:10.1016/j.quascirev.2012.09.020.

Roeckner, E., K. Arpe, and L. Bengtsson (1996), The atmospheric general circulation model ECHAM-4: Model description and simulation of present-day climate, *Max-Planck-Institut für Meteorologie Rep.*, *218*, 90.

Scarchilli, C., M. Frezzotti, and P. M. Ruti (2010), Snow precipitation at four ice core sites in East Antarctica: Provenance, seasonality and blocking factors, *Clim. Dyn.*, *37*(9–10), 2107–2125, doi:10.1007/s00382-010-0946-4.

Schmidt, G. A., G. Hoffmann, D. T. Shindell, and Y. Hu (2005), Modeling atmospheric stable water isotopes and the potential for constraining cloud processes and stratosphere-troposphere water exchange, *J. Geophys. Res.*, *110*, D21314, doi:10.1029/2005JD005790.

Schmitt, J., et al. (2012), Carbon isotope constraints on the deglacial CO2 rise from ice cores, *Science*, *336*(6082), 711–714, doi:10.1126/science.1217161.

Schoenemann, S. W., A. J. Schauer, and E. Steig (2013), Measurement of SLAP2 and GISP $\delta^{17}O$ and proposed VSMOW-SLAP normalization for $\delta^{17}O$ and $^{17}O_{excess}$, *Rapid Commun. Mass Spectrom.*, *27*, 582–590, doi:10.1002/rcm.6486.

Sodemann, H., and A. Stohl (2009), Asymmetries in the moisture origin of Antarctic precipitation, *Geophys. Res. Lett.*, *36*, L22803, doi:10.1029/2009GL040242.

Steig, E. J., C. P. Hart, J. W. C. White, W. L. Cunningham, M. D. Davis, and E. S. Saltzman (1998a), Changes in climate, ocean and ice-sheet conditions in the Ross embayment, Antarctica, at 6 ka, *Ann. Glaciol.*, *27*, 305–310.

Steig, E. J., E. J. Brook, J. White, C. M. Sucher, M. L. Bender, S. J. Lehman, D. L. Morse, E. D. Waddington, and G. D. Clow (1998b), Synchronous climate changes in Antarctica and the North Atlantic, *Science*, *282*(5386), 92–95.

Steig, E. J., D. L. Morse, E. D. Waddington, M. Stuiver, P. M. Grootes, P. A. Mayewski, M. S. Twickler, and S. I. Whitlow (2000), Wisconsinan and Holocene climate history from an ice core at Taylor Dome, western Ross Embayment, Antarctica, *Geogr. Ann. A*, *82*(2–3), 213–235.

Stenni, B., J. Jouzel, V. Masson-Delmotte, R. Rothlisberger, E. Castellano, O. Cattani, S. Falourd, S. J. Johnsen, A. Longinelli, and J. P. Sachs (2004), A late-glacial high-resolution site and source temperature record derived from the EPICA Dome C isotope records (East Antarctica), *Earth Planet. Sci. Lett.*, *217*(1-2), 183–195, doi:10.1016/S0012-821X(03)00574-0.

Stenni, B., et al. (2010a), Expression of the bipolar see-saw in Antarctic climate records during the last deglaciation, *Nat. Geosci.*, *4*(1), 46–49, doi:10.1038/ngeo1026.

©2014. American Geophysical Union. All Rights Reserved.

Stenni, B., V. Masson-Delmotte, E. Selmo, H. Oerter, H. Meyer, R. Rothlisberger, J. Jouzel, O. Cattani, S. Falourd, and H. Fischer (2010b), The deuterium excess records of EPICA Dome C and Dronning Maud Land ice cores (East Antarctica), *Quaternary Sci. Rev.*, *29*(1), 146–159.

Stohl, A., and H. Sodemann (2010), Characteristics of atmospheric transport into the Antarctic troposphere, *J. Geophys. Res.*, *115*, D02305, doi:10.1029/2009JD012536.

Uemura, R., Y. Matsui, N. Yoshida, O. Abe, and S. Mochizuki (2005), Isotopic fractionation of water during snow formation: Experimental evidence of kinetic effect, *Polar Meteorol. Glaciol.*, *19*, 1–14.

Uemura, R., E. Barkan, O. Abe, and B. Luz (2010), Triple isotope composition of oxygen in atmospheric water vapor, *Geophys. Res. Lett.*, *37*, L04402, doi:10.1029/2009GL041960.

Uemura, R., V. Masson-Delmotte, J. Jouzel, A. Landais, H. Motoyama, and B. Stenni (2012), Ranges of moisture-source temperature estimated from Antarctic ice cores stable isotope records over glacial–interglacial cycles, *Clim. Past*, *8*(3), 1109–1125, doi:10.5194/cp-8-1109-2012.

Vimeux, F., V. Masson, G. Delaygue, J. Jouzel, J. R. Petit, and M. Stievenard (2001), A 420,000 year deuterium excess record from East Antarctica: Information on past changes in the origin of precipitation at Vostok, *J. Geophys. Res.*, *106*(D23), 31,863–31,873, doi:10.1029/2001JD900076.

WAIS Divide Project Members (2013), Onset of deglacial warming in West Antarctica driven by local orbital forcing, *Nature*, *1–7*, doi:10.1038/nature12376.

Watanabe, O., J. Jouzel, S. Johnsen, F. Parrenin, H. Shoji, and N. Yoshida (2003), Homogeneous climate variability across East Antarctica over the past three glacial cycles, *Nature*, *422*(6931), 509–512, doi:10.1038/nature01525.

Werner, M., and M. Heimann (2002), Modeling interannual variability of water isotopes in Greenland and Antarctica, *J. Geophys. Res.*, *107*(D1), 4001, doi:10.1029/2001JD900253.

Werner, M., P. M. Langebroek, T. Carlsen, and M. Herold (2011), Stable water isotopes in the ECHAM5 general circulation model: Toward high-resolution isotope modeling on a global scale, *J. Geophys. Res.*, *116*, D15109, doi:10.1029/2011JD015681.

Winkler, R., A. Landais, H. Sodemann, L. Dümbgen, F. Prié, V. Masson-Delmotte, B. Stenni, J. Jouzel, and V. Rath (2012), Deglaciation records of ^{17}O-excess in East Antarctica: Reliable reconstruction of oceanic normalized relative humidity from coastal sites, *Clim. Past*, *8*(1), 1–16.

Winkler, R., A. Landais, C. Risi, and M. Baroni (2013), Interannual variation of water isotopologues at Vostok indicates a contribution from stratospheric water vapor, *Proc. Natl. Acad. Sci. U. S. A.*, *110*, 17,674–17,679.

Wolff, E. W., et al. (2006), Southern Ocean sea-ice extent, productivity and iron flux over the past eight glacial cycles, *Nature*, *440*(7083), 491–496, doi:10.1038/nature04614.

Zahn, A., P. Franz, C. Bechtel, J.-U. Grooß, and T. Röckmann (2006), Modelling the budget of middle atmospheric water vapour isotopes, *Atmos. Chem. Phys.*, *6*(8), 2073–2090.

©2014. American Geophysical Union. All Rights Reserved.

Chapter 4

Supporting Information to: Triple water-isotopologue record from WAIS Divide, Antarctica: controls on glacial-interglacial changes in $^{17}O_{excess}$ of precipitation

Originally Published in Journal of Geophysical Research: Atmospheres
http://onlinelibrary.wiley.com/doi/10.1002/2014JD021770/full

This supporting information was published as-is online with the supporting text, tables, and figures as individual components. The supporting information provides details on the correction for seawater isotopic composition, normalized relative humidity, VSMOW-SLAP normalization of published datasets, and data comparison of LGM to Early Holocene isotopic results. Here the supporting materials have been compiled into one single document.

Supplementary Information for

Triple water-isotopologue record from WAIS Divide, Antarctica: controls on glacial-interglacial changes in $^{17}O_{excess}$ of precipitation.

Spruce W. Schoenemann, Eric J. Steig, Qinghua Ding, Bradley R. Markle, Andrew J. Schauer

IsoLab, Department of Earth and Space Sciences, University of Washington, Seattle, WA 98195, USA

Journal of Geophysical Research, Atmospheres, 2014

Contents

1. Correction for seawater isotopic composition

In order to make comparisons of the isotopic records and model results, we must account for the change in oxygen-18 ($\delta^{18}O$) and deuterium (δD) composition of the ocean during the last glacial period, resulting from the build-up of the continental ice sheets. These isotopic seawater corrections have a considerable influence on the d_{excess} and d_{ln} records, and are therefore necessary for interpretation of the glacial-interglacial d_{excess} and d_{ln} changes [*Jouzel et al.*, 2003; *Stenni et al.*, 2010]. To do this we use the $\delta^{18}O_{sw}$ record [*Bintanja et al.*, 2005] reconstructed from the marine sediment benthic stacks of *Lisiecki and Raymo* [2005], which have been corrected for deep water temperature effects using an ocean GCM (FigureS4). The $\delta^{18}O_{sw}$ record provided by *Bintanja et al.* [2005] has a 100-year resolution; therefore we use this as the minimum time interval for the $\delta^{18}O_{corr}$ and δD_{corr} records. Implicit in these corrections is that the d_{excess} and d_{ln} of the ocean source water at present is zero. Following *Jouzel et al.* [2003] we apply the following corrections:

$$\delta^{18}O_{corr} = \delta^{18}O_{ice} - \delta^{18}O_{sw} \times (1 + \delta^{18}O_{ice}/10^3)/(1 + \delta^{18}O_{sw}/10^3) \quad \text{Eq. S1}$$

$$\delta D_{corr} = \delta D_{ice} - 8\delta^{18}O_{sw} \times (1 + \delta D_{ice}/10^3)/(1 + 8\delta^{18}O_{sw}/10^3) \quad \text{Eq. S2}$$

$$d_{xs\ corr} = \delta D_{corr} - 8\delta^{18}O_{corr} \quad \text{Eq. S3}$$

$$\delta^{18}O_{ln\ corr} = (\ln(1 + \delta^{18}O_{ice}/10^3))10^3 - (\ln(1 + \delta^{18}O_{sw}/10^3))10^3 \quad \text{Eq. S4}$$

$$\delta D_{ln\ sw} = -2.85 \times 10^{-2}\,[(\ln(1 + \delta^{18}O_{sw}/10^3))10^3]^2 + 8.47\,[(\ln(1 + \delta^{18}O_{sw}/10^3))10^3] \quad \text{Eq. S5}$$

$$\delta D_{ln\ corr} = [\ln(1 + \delta D_{ice}/10^3)]10^3 - \delta D_{ln\ sw} \quad \text{Eq. S6}$$

$$d_{ln\ corr} = \delta D_{ln\ corr} - (-2.85 \times 10^{-2}(\delta^{18}O_{ln\ corr})^2 + 8.47(\delta^{18}O_{ln\ corr}) \quad \text{Eq. S7}$$

Note that for d_{ln} (the natural log version of d_{excess}), we use the 2nd order polynomial fit from *Uemura et al.* [2012], with zero intercept. In Figure S2, we show the d_{excess} and $d_{xs\ corr}$ data compared to the d_{ln} and $d_{ln\ corr}$ data for six cores for which full δ^{18}O and δD records are published. WDC and EDML show 100-year averages; Siple Dome, Taylor Dome, and Dome Fuji 200-year averages, and Vostok 400-year averages. For the marine-influenced sites (WDC and Siple Dome) the correction is smaller than for East Antarctic interior sites, as the magnitude of the correction is dependent on the amount of distillation, determined to first order by the site temperature. Once d_{excess} has been corrected to $d_{xs\ corr}$, it is clear that the apparent LGM to EH d_{excess} increase seen in all cores is largely an artifact of the change in $\delta^{18}O_{sw}$, and furthermore, the $d_{xs\ corr}$ data show an inconsistent response between coastal and interior sites. On the other hand, $d_{ln\ corr}$ data show a more consistent response between ice cores sites during the LGM to EH transition. Note that the magnitude of scaling between d_{excess} and d_{ln} is different due to the different definitions. We find that the d_{ln} definition of d_{excess} reduces the large impact of the isotopic seawater correction on d_{excess}, providing more reliable spatial estimates of the glacial-interglacial change [*Stenni et al.*, 2010; *Uemura et al.*, 2012].

2. Normalized Relative Humidity

The normalized relative humidity directly above the ocean-air interface is the dominant factor controlling $^{17}O_{excess}$ in the marine boundary layer [*Landais et al.*, 2008]. The normalized relative humidity (rh_n) is defined as the ratio of water vapor concentration in the near-surface air divided by the saturated vapor concentration at the temperature of the ocean surface [*Gat*, 1996; *Barkan and Luz*, 2007; *Risi et al.*, 2010; *Uemura et al.*, 2010]:

$$rh_n = rh_a \times \frac{q_{sat}(T_a)}{q_{sat}(T_s)} = \frac{q(T_a)}{q_{sat}(T_a)} \times \frac{q_{sat}(T_a)}{q_{sat}(T_s)} = \frac{q(T_a)}{q_{sat}(T_s)} \quad \text{Eq. S8}$$

where rh_a is the relative humidity of the near-surface air, q = specific humidity, q_{sat} = saturated specific humidity, T_a = air temperature (K), and T_s = surface temperature (K).

To determine the rh_n in the ECHAM4.6 model simulations, we use the lowest level (2 m) specific humidity, $q(T_a)$, of the atmosphere and the standard calculation for relative humidity (e.g. *Large and Vertenstein,* 1995), but substitute the surface temperature (T_s) for air temperature in the denominator:

$$rh_n = q(T_a)/(640380/\exp(5107.4/T_s)) \quad \text{Eq. S9}$$

The importance of making such a calculation is that under conditions where the near-surface air is cooler than the ocean surface temperature, rh_n will be lower than rh_a. The difference is apparent in the ECHAM4.6 zonal annual averages shown in Fig. S5. Once the Antarctic continent is encountered, a temperature inversion begins where the surface temperature is colder than the overlying surface air, causing rh_n to become very large. Note that the surface moisture fluxes are very low over the continent, so that the large rh_n has little impact on $^{17}O_{excess}$.

3. VSMOW-SLAP Normalization of published datasets

For comparison of published $^{17}O_{excess}$ records from different laboratories, we normalize the $\delta^{17}O$ and $\delta^{18}O$ data to the VSMOW-SLAP scale, as in *Schoenemann et al*. [2013], where SLAP $\delta^{18}O$ = –55.5 ‰, SLAP $^{17}O_{excess}$ = 0, and VSMOW $\delta^{17}O = \delta^{18}O = 0$. The Vostok $^{17}O_{excess}$ record was produced at the Institute of Earth Sciences (IES), Hebrew University of Jerusalem, and therefore we use the SLAP $\delta^{18}O$ and $^{17}O_{excess}$ values reported in *Barkan and Luz*, [2005] to normalize the data to the VSMOW-SLAP scale. This normalization lowers the published Vostok $^{17}O_{excess}$ values by 7 per meg for data where the $\delta^{18}O$ values are at –55.5 ‰. The normalization results in LGM–EH change in $^{17}O_{excess}$ of 22 per meg, slightly larger than the 20 per meg given in [*Landais et al.*, 2008]. We apply an offset to the entire Vostok $^{17}O_{excess\ VSMOW\text{-}SLAP}$ record based on the present-day UW Isolab WAIS Water–Vostok Water difference of ~24 per meg (Figure 4), bringing the Vostok EH values into better agreement with present-day Vostok values measured at IES, LSCE and UW Isolab (Table 2).

The $^{17}O_{excess}$ records for EDC and Talos Dome were measured at Le Laboratoire des Sciences du Climat et l'Environnement (LSCE) [*Winkler et al.*, 2012]. The original $^{17}O_{excess}$ values were corrected by LSCE to be in agreement with the Dome F water standard measured at both IES and LSCE, which had a 22 per meg difference between labs [*Winkler et al.*, 2012]. This was done by applying a correction of –22 per meg for EDC and –15 per meg for Talos Dome to the original $^{17}O_{excess}$ data (*R. Winkler, personal communication*, 2013). After accounting for this offset to the original $^{17}O_{excess}$ data, we used the uncorrected SLAP and the VSMOW-corrected SLAP values reported in *Landais et al.* [2012] to normalize EDC and Talos Dome to the VSMOW-SLAP scale. The normalization lowers $^{17}O_{excess}$ values by ~26 per meg for data where the $\delta^{18}O$ values are –55.5 ‰. The result of this normalization on $^{17}O_{excess}$ is larger for EDC than for Talos Dome

because EDC $\delta^{18}O$ is further from VSMOW. These corrections result in a larger LGM–EH change in $^{17}O_{excess}$ at EDC of 12 per meg compared with the 9 per meg, and a LGM–EH change at Talos Dome of ~ –1.5 per meg compared with the value of 1 per meg in the published data file [*Winkler et al.*, 2012].

The data set "Normalized_17Oxs_LGM-EH_01.xlsx" contains the normalized VSMOW-SLAP values from this study for WDC, Siple Dome, Taylor Dome, along with the published $\delta^{17}O$, $\delta^{18}O$, and $^{17}O_{excess}$ values for Vostok, EDC, and Talos Dome, as shown in Figures 2, 3, and 4 in the main text. Deuterium excess and d_{ln} data are also included for each ice core.

4. Data Comparison of LGM to Early Holocene

To determine the significance of the LGM to EH $^{17}O_{excess}$ change for all ice cores we use a two-sample *t*-test with a 95 % confidence interval. We perform the test under the assumption that the population variances are approximately equal, as supported by the standard deviations for each period. In Table S1 we provide the VSMOW-SLAP normalized $^{17}O_{excess}$ values for the LGM and EH, the number of samples and the 1 sigma S.D. for each time period. The final two columns show the *p*-value and pooled sample standard deviation. The results of the statistical analysis show that the LGM to EH change for all cores is significant (at 95 % confidence), except for Siple Dome and Talos Dome.

REFERENCES

Barkan, E., and B. Luz (2005), High precision measurements of $^{17}O/^{16}O$ and $^{18}O/^{16}O$ ratios in H_2O, *Rapid Commun. Mass Spectrom.*, *19*(24), 3737–3742.

Barkan, E., and B. Luz (2007), Diffusivity fractionations of $H_2{}^{16}O/H_2{}^{17}O$ and $H_2{}^{16}O/H_2{}^{18}O$ in air and their implications for isotope hydrology, *Rapid Commun. Mass Spectrom.*, *21*, 2999–3005.

Bintanja, R., R. S. W. van de Wal, and J. Oerlemans (2005), Modelled atmospheric temperatures and global sea levels over the past million years, *Nature*, *437*(7055), 125–128, doi:10.1038/nature03975.

Gat, J. (1996), Oxygen and hydrogen isotopes in the hydrologic cycle, *Annu. Rev. Earth Planet. Sci.*, (24), 225–262.

Jouzel, J., F. Vimeux, N. Caillon, G. Delaygue, G. Hoffmann, V. Masson-Delmotte, and F. Parrenin (2003), Magnitude of isotope/temperature scaling for interpretation of central Antarctic ice cores, *J. Geophys. Res.*, *108*(D12), 4361, doi:10.1029/2002JD002677.

Landais, A., E. Barkan, and B. Luz (2008), Record of $\delta^{18}O$ and ^{17}O-excess in ice from Vostok Antarctica during the last 150,000 years, *Geophys. Res. Lett.*, *35*(L02709), 1–5, doi:10.1029/2007GL032096.

Landais, A., H. C. Steen-Larsen, M. Guillevic, V. Masson-Delmotte, B. Vinther, and R. Winkler (2012), Triple isotopic composition of oxygen in surface snow and water vapor at NEEM (Greenland), *Geochim. Cosmochim. Acta*, *77*(C), 304–316, doi:10.1016/j.gca.2011.11.022.

Lisiecki, L., and M. Raymo (2005), A Plio-Pleistocene stack of 57 globally distributed benthic $\delta^{18}O$ records, *Paleoceanography*, *20*, 522–533.

Risi, C., A. Landais, S. Bony, J. Jouzel, V. Masson-Delmotte, and F. Vimeux (2010), Understanding the ^{17}O-excess glacial-interglacial variations in Vostok precipitation, *J. Geophys. Res.*, *115*(D10112), 1–15, doi:10.1029/2008JD011535.

Schoenemann, S. W., A. J. Schauer, and E. Steig (2013), Measurement of SLAP2 and GISP $\delta^{17}O$ and proposed VSMOW-SLAP normalization for $\delta^{17}O$ and $^{17}O_{excess}$, *Rapid Commun. Mass Spectrom.*, (27), 582–590, doi:10.1002/rcm.6486.

Stenni, B., V. Masson-Delmotte, E. Selmo, H. Oerter, H. Meyer, R. Rothlisberger, J. Jouzel, O. Cattani, S. Falourd, and H. Fischer (2010), The deuterium excess records of EPICA Dome C and Dronning Maud Land ice cores (East Antarctica), *Quaternary Sci. Rev.*, *29*(1), 146–159.

Uemura, R., E. Barkan, O. Abe, and B. Luz (2010), Triple isotope composition of oxygen in atmospheric water vapor, *Geophys. Res. Lett.*, *37*(L04402), 1–4, doi:10.1029/2009GL041960.

Uemura, R., V. Masson-Delmotte, J. Jouzel, A. Landais, H. Motoyama, and B. Stenni (2012), Ranges of moisture-source temperature estimated from Antarctic ice cores stable isotope records over glacial–interglacial cycles, *Clim. Past*, *8*(3), 1109–1125, doi:10.5194/cp-8-1109-2012.

Winkler, R., A. Landais, H. Sodemann, L. Dümbgen, F. Prié, V. Masson-Delmotte, B. Stenni, J. Jouzel, and V. Rath (2012), Deglaciation records of ^{17}O-excess in East Antarctica: reliable reconstruction of oceanic normalized relative humidity from coastal sites, *Clim. Past*, *8*(1), 1–16, doi:10.5194/cp-8-1-2012.

Supplementary Figures and Tables

Table S1 Comparison of $^{17}O_{excess}$ ice core data for the Last Glacial Maximum (LGM) to Early Holocene (EH) and Present-Day (PD) change for WDC, Siple Dome, Taylor Dome, Vostok, EDC, and Talos Dome. The table includes the number of samples, the 1σ sample S.D, and results of a two tailed *t*-test that includes the 95 % confidence level (*p*-value) and pooled sample standard deviation.

Fig. S1 Model experiments for the LGM (21 ka) minus PD (0 ka) performed by ECHAM4.6 GCM to determine d_{excess} sensitivity to all three supersaturation values **(a)** S = 1–0.002T, **(b)** S = 1–0.004T, and **(c)** S = 1–0.007T, compared with the LGM to EH change in $d_{xs\ corr}$ ice core data (Table 3). All experiments were run at T42 (2.8˚ by 2.8˚) resolution.

Fig. S2 Comparison of d_{excess} (upper panel) and d_{ln} (lower panel) data corrected for seawater isotopic composition based on the $\delta^{18}O_{sw}$ record [*Bintanja et al.*, 2005] for all ice cores discussed in text, excluding Taylor Dome and Talos Dome (not published data). Original d_{excess} and d_{ln} data are shown in light grey with dark grey averages (WDC and EDML 100-yr; Siple Dome, EDC, Dome F, 200-yr; Vostok, no average). The $d_{xs\ corr}$ and $d_{ln\ corr}$ data are shown for the respective average in black, except for Vostok (original 400-yr resolution). Note the scale for all d_{excess} plots is (12 ‰) and for d_{ln} (20 ‰), due to the different definitions. Light blue bars show the LGM period (25-20 ka); red bars show the EH period (12–9 ka).

Fig. S3 Calculation of the zonal annual average slope in $^{17}O_{excess}$ for the temperature range between –20˚C to – 45˚C for each model simulation. Modern (red), Extend Ice (light blue), LGM (blue), LGM-cold (dark blue) and their respective slopes: –0.53, –0.63, –0.70, and –0.87 per meg/˚C. Note the increasing sensitivity of $^{17}O_{excess}$ to temperature as sea ice extent expands in each colder experiment.

Fig. S4 The $\delta^{18}O_{sw}$ (‰) record from *Bintanja et al.* [2005] used to correct the ice core records for seawater isotopic composition changes during the glacial period due to increased continental ice volume.

Fig. S5 **(a)** The zonal annual average relative humidity (rh_a (%), blue) and normalized relative humidity (rh_n (%), dashed blue) for the ECHAM4.6 GCM control simulation *vs*. latitude (20 to 75˚S), **(b)** the $rh_n - rh_a$ difference (%), and **(c)** the zonal annual average surface temperature (T_s) and near-surface air temperature at 2 meters (T_a) in ˚C.

Table S1: Ice core $^{17}O_{excess}$ data comparison of Last Glacial Maximum (LGM) to Early Holocene (EH) change

Ice Core Site	LGM $^{17}O_{excess}$ (per meg)	LGM # of samples	LGM ± 1σ (per meg)	EH $^{17}O_{excess}$ (per meg)	EH # of samples	EH ± 1σ (per meg)	LGM-EH $^{17}O_{excess}$ (per meg)	Two-tailed *t*-test, *p*-value	Two-tailed *t*-test, pooled S.D.
WDC	12	13	4.3	29	18	5.2	–17	<0.001	4.9
Siple Dome	18[c]	10	5.0	*21*	4	6.0	–3[d]	0.2577	5.0
Taylor Dome	6[c]	4	5.5	*17*	11	2.2	–11[d]	<0.001	3.3
Vostok[b]	–16	13	4.9	6	13	5.8	–22	<0.001	5.4
Dome C[a]	7	11	9.7	19	17	8.0	–12	0.002	8.7
Talos Dome[a]	–1.5	6	8.6	0	13	8.0	–1.5	0.745	8.1

[a] Measurements performed at LSCE
[b] Measurements performed at IES
[c] 25 to 19.5 ka
[d] Siple $^{17}O_{excess}$ PD = (2-1 ka), Taylor $^{17}O_{excess}$ EH = (~6-2ka)

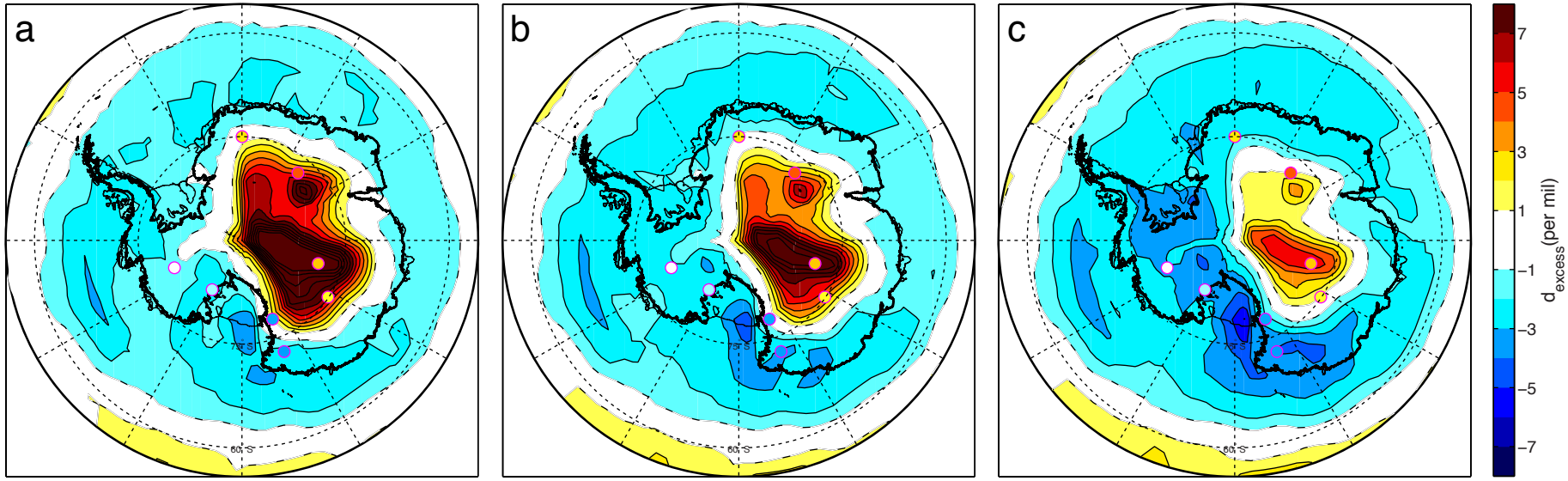

Fig. S1

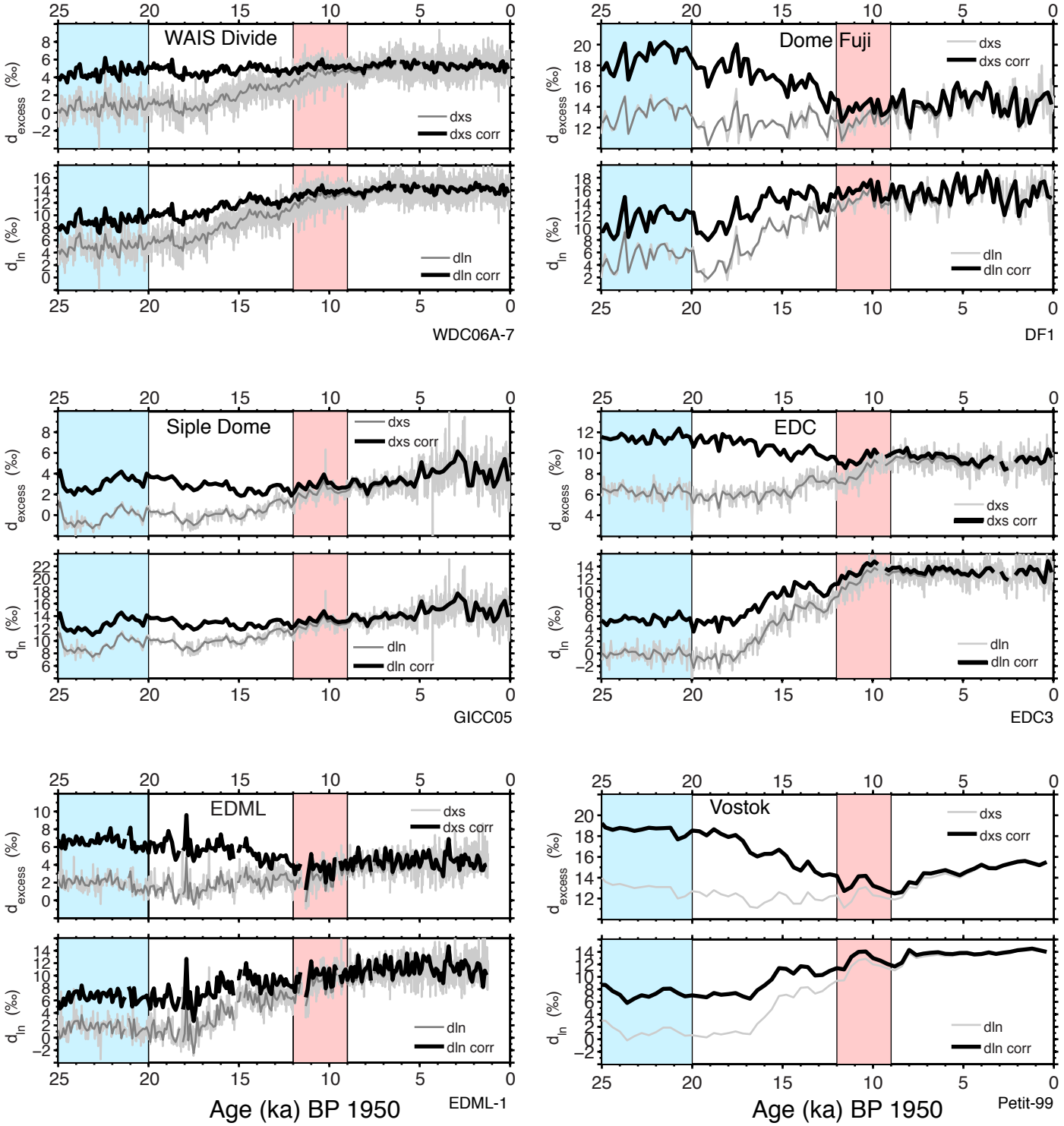
WAIS Divide
Dome Fuji
Siple Dome
EDC
EDML
Vostok
dxs
dxs corr
dln
dln corr
d_excess (‰)
d_ln (‰)
WDC06A-7
DF1
GICC05
EDC3
EDML-1
Petit-99
Age (ka) BP 1950

Fig. S2

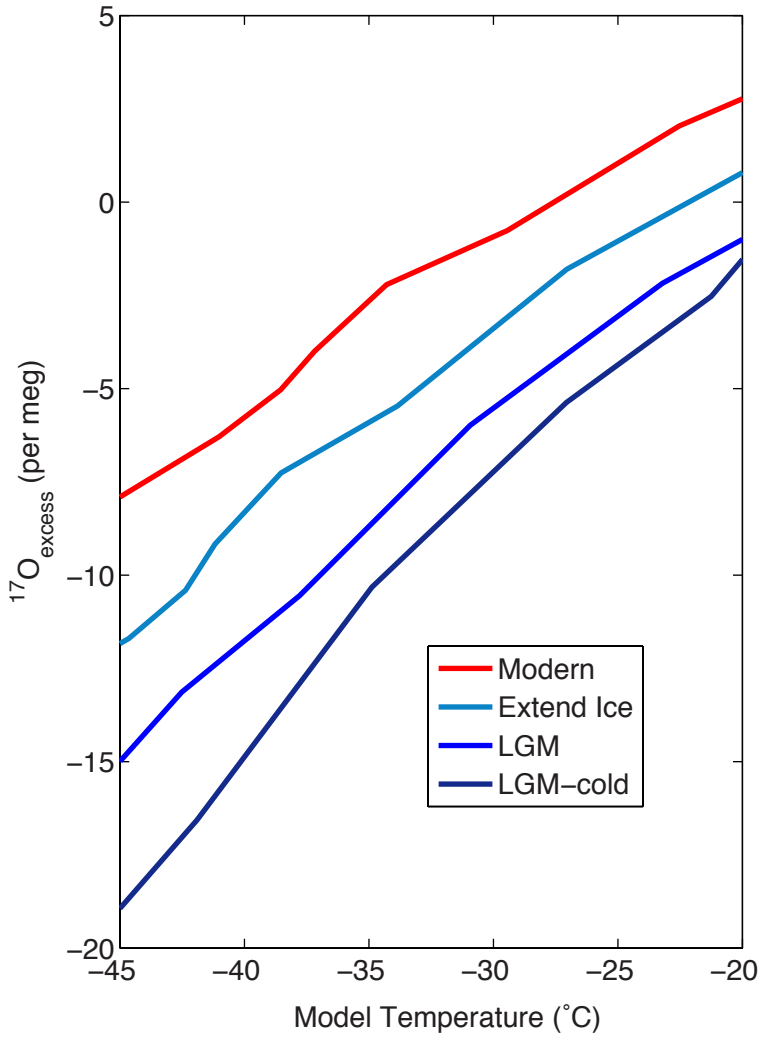
5
0
−5
−10
−15
−20
−45
−40
−35
−30
−25
−20
$^{17}O_{excess}$ (per meg)
Model Temperature (˚C)
Modern
Extend Ice
LGM
LGM−cold

Fig. S3

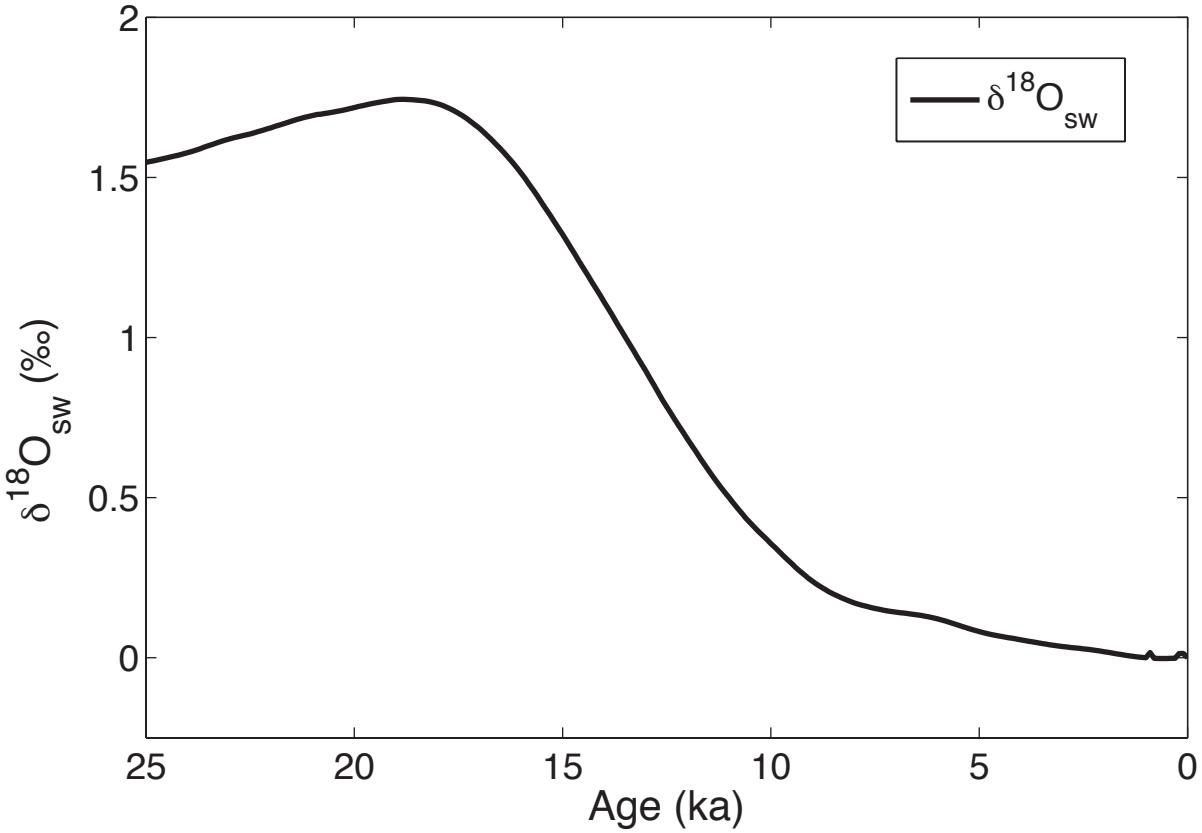

Fig. S4

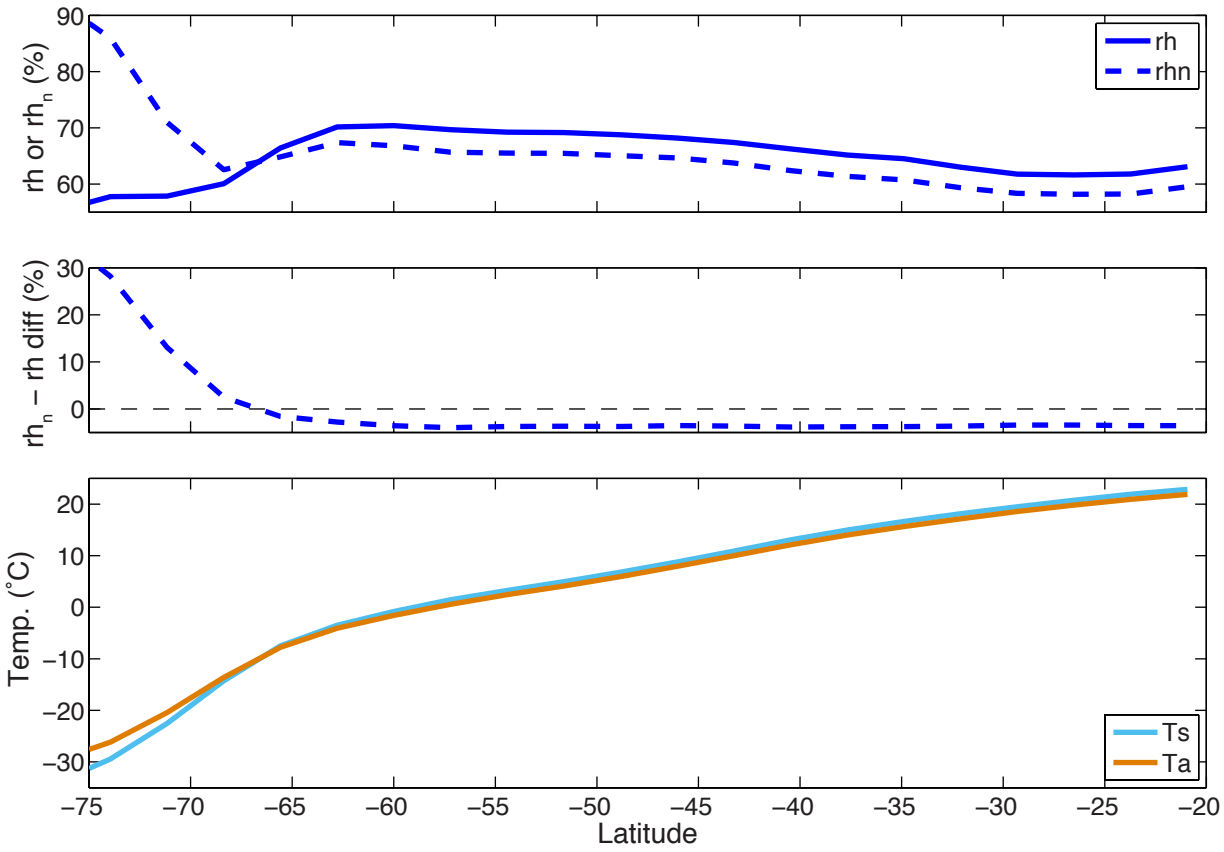

Fig. S5

Chapter 5

Calibrated high-precision $^{17}O_{excess}$ measurements using cavity ring-down spectroscopy with laser-current-tuned cavity resonance

Originally Published in Atmospheric Measurement Techniques
http://www.atmos-meas-tech.net/7/2421/2014/

The focus of this work was to develop a new laser spectroscopy instrument for making high-precision $^{17}O_{excess}$ measurements, and compare it with conventional IRMS techniques. This work originated out of collaboration between Vasileios Gkinis at the University of Copenhagen, Eric Steig at University of Washington, and Picarro Instruments of Santa Clara, CA. Early on, it was clear that evaluation of the prototype instrument would benefit from analyzing waters that had previously been measured by IRMS, and therefore my experience was solicited to develop methods for water sampling and to improve measurement precision of the prototype. Testing of various water sample introduction and measurement techniques led to multiple iterations of the prototype instrument over a three-year period. Furthermore, additional IRMS $^{17}O_{excess}$ measurements of new reference waters were required due to the large volumes of water needed by the Picarro sample introduction system and for long-term drift experiments.

The new triple water-isotope instrument uses cavity ring-down spectroscopy (CRDS) with laser-current-tuned cavity resonance which results in reduced measurement drift relative to previous versions. The advantage of laser absorption spectroscopy is the ability to make direct measurements of the water isotopologues in the water-vapor sample. We show that the instrument can achieve better than 8 per meg precision on water-vapor samples when integrated over a period of 30 minutes. Compared to the traditional water fluorination techniques that require 30 min or more per sample and the dual-inlet mass-spectrometric analysis time of ~3 h, this new laser-based approach is significantly less time-consuming and more consistent. The new laser-spectroscopic methods offer increased sample throughput with competitive precision and accuracy, provided that proper calibration methods are employed.

Calibrated CRDS measurements of the UW Δ*IsoLab and International Atomic Energy Agency (IAEA) reference waters show excellent agreement with the IRMS measurements by *Schoenemann et al*. [2013]. In particular, $^{17}O_{excess}$ measurements of GISP water by CRDS give a value of 27± 4 per meg, compared to the 28 ± 2 per meg by IRMS. Furthermore, concurrent work by *Berman et al*. [2013] using different laser-spectroscopic methods reported a GISP value somewhat lower than ours (23 ± 2), along with IRMS measurements from John Hopkins University (25 ± 3), and Le Laboratoire des Sciences du Climat et l'Environnement (32 ± 6), which were all normalized to the VSMOW-SLAP scale proposed by *Schoenemann et al*. [2013]. The mean VSMOW-SLAP normalized value for GISP for all recent measurements from the four different laboratories (*Berman et al*. [2013], *Schoenemann et al*. [2013], *Steig et al.* [2014]) is $^{17}O_{excess}$ = 28 ± 3 per meg, which attests to the reliability of the high-precision IRMS measurements produced here at UW, and that inter-laboratory agreement is improved when VSMOW-SLAP normalization methods are adopted.

My contribution to this work included method development for measuring samples on the CRDS prototype instrument, data analysis, additional IRMS $^{17}O_{excess}$ measurements, and

significant discussions with the lead authors on the sections referring to comparisons between IRMS and CRDS techniques. I reviewed multiple drafts of the paper, wrote a key section on the IRMS/CRDS comparison, and made substantive editorial comments and clarifications throughout.

Atmos. Meas. Tech., 7, 2421–2435, 2014
www.atmos-meas-tech.net/7/2421/2014/
doi:10.5194/amt-7-2421-2014
© Author(s) 2014. CC Attribution 3.0 License.

Atmospheric Measurement Techniques
Open Access

Calibrated high-precision ^{17}O-excess measurements using cavity ring-down spectroscopy with laser-current-tuned cavity resonance

E. J. Steig[1,2], V. Gkinis[2,3], A. J. Schauer[1], S. W. Schoenemann[1], K. Samek[1], J. Hoffnagle[4], K. J. Dennis[4], and S. M. Tan[4]

[1]Δ*IsoLab, Earth & Space Sciences, and Quaternary Research Center, University of Washington, Seattle, WA 98195, USA
[2]Centre for Ice and Climate, Niels Bohr Institute, University of Copenhagen, 2100 Copenhagen, Denmark
[3]Institute of Arctic and Alpine Research, University of Colorado, Boulder, CO 80309, USA
[4]Picarro Inc. Santa Clara, CA 95054, USA

Correspondence to: E. J. Steig (steig@uw.edu)

Received: 7 October 2013 – Published in Atmos. Meas. Tech. Discuss.: 29 November 2013
Revised: 27 June 2014 – Accepted: 30 June 2014 – Published: 8 August 2014

Abstract. High-precision analysis of the $^{17}O/^{16}O$ isotope ratio in water and water vapor is of interest in hydrological, paleoclimate, and atmospheric science applications. Of specific interest is the parameter ^{17}O excess ($\Delta^{17}O$), a measure of the deviation from a linear relationship between $^{17}O/^{16}O$ and $^{18}O/^{16}O$ ratios. Conventional analyses of $\Delta^{17}O$ of water are obtained by fluorination of H_2O to O_2 that is analyzed by dual-inlet isotope ratio mass spectrometry (IRMS). We describe a new laser spectroscopy instrument for high-precision $\Delta^{17}O$ measurements. The new instrument uses cavity ring-down spectroscopy (CRDS) with laser-current-tuned cavity resonance to achieve reduced measurement drift compared with previous-generation instruments. Liquid water and water-vapor samples can be analyzed with a better than 8 per meg precision for $\Delta^{17}O$ using integration times of less than 30 min. Calibration with respect to accepted water standards demonstrates that both the precision and the accuracy of $\Delta^{17}O$ are competitive with conventional IRMS methods. The new instrument also achieves simultaneous analysis of $\delta^{18}O$, $\delta^{17}O$ and δD with precision of < 0.03 ‰, < 0.02 and < 0.2 ‰, respectively, based on repeated calibrated measurements.

1 Introduction

Measurements of the stable isotope ratios of water are ubiquitous in studies of earth's hydrological cycle and in paleoclimatic applications (Dansgaard, 1964; Dansgaard et al., 1982; Johnsen et al., 1995; Jouzel et al., 2007). Isotopic abundances are reported as deviations of a sample's isotopic ratio relative to that of a reference water, and expressed in the δ notation as

$$\delta^i = \frac{{}^iR_{\text{sample}}}{{}^iR_{\text{reference}}} - 1, \quad (1)$$

where ${}^2R = n(^2H)/n(^1H)$, ${}^{18}R = n(^{18}O)/n(^{16}O)$, ${}^{17}R = n(^{17}O)/n(^{16}O)$, and n refers to isotope abundance.

One important innovation was the development by Merlivat and Jouzel (1979) of a theoretical understanding of "deuterium excess":

$$d = \delta D - 8(\delta^{18}O), \quad (2)$$

where δD is equivalent to δ^2H. The deuterium excess is commonly used as a measure of kinetic fractionation processes. For example, deuterium excess variations from ice cores have been used to infer variations in evaporative conditions over the ocean surface areas from which polar precipitation is derived (Johnsen et al., 1989; Petit et al., 1991; Vimeux et al., 2001; Masson-Delmotte et al., 2005).

The $\delta^{18}O$ and δD isotopic values can be experimentally determined via a number of isotope ratio mass spectrometry (IRMS) techniques. For $\delta^{18}O$, equilibration with CO_2 has been the standard method for many decades (Cohn and Urey, 1938; McKinney et al., 1950; Epstein, 1953). For δD, reduction of water to H_2 over hot U (Bigeleisen et al., 1952; Vaughn et al., 1998) or Cr (Gehre et al., 1996) has typically

been used. Simultaneous determination of δ^{18}O and δD was made possible via the development of continuous-flow mass-spectrometric techniques utilizing conversion of water to CO and H_2 in a pyrolysis furnace (Begley and Scrimgeour, 1997; Gehre et al., 2004).

A recent innovation is the measurement of the difference between δ^{18}O and δ^{17}O at sufficiently high precision to determine very small deviations from equilibrium. In general, the nuclei mass differences of $+1n^0$ and $+2n^0$ (n^0 denotes a neutron) imply that the fractionation factor for δ^{17}O between two different phases will be approximately the square root of the fractionation factor for δ^{18}O (Urey, 1947; Craig, 1957; Mook, 2000):

$$\frac{^{17}R_\mathrm{a}}{^{17}R_\mathrm{b}} = \left(\frac{^{18}R_\mathrm{a}}{^{18}R_\mathrm{b}}\right)^{\lambda}, \tag{3}$$

where $\lambda = 0.5010$–0.5305 (Kaiser, 2008) and the subscripts "a" and "b" refer to different phases or samples. For isotopic equilibrium, the value of λ will approach θ, given theoretically by the ratio of the partition functions (Q), which in the limit of high temperature approaches a constant value given as follows (Matsuhisa et al., 1978):

$$\theta = \frac{\ln(Q_{17}/Q_{16})}{\ln(Q_{18}/Q_{16})} = \frac{\frac{1}{m_{16}} - \frac{1}{m_{17}}}{\frac{1}{m_{16}} - \frac{1}{m_{18}}} = 0.5305\,, \tag{4}$$

where m_{16} is the atomic mass of ^{16}O, m_{17} is that of ^{17}O, etc.[1]

By analyzing a set of meteoric waters, Meijer and Li (1998) estimated the value of λ to be 0.528. Barkan and Luz (2005) used careful water equilibrium experiments to determine an equilibrium value for λ of 0.529, while Barkan and Luz (2007) showed that λ is 0.518 under purely diffusive conditions, in good agreement with theory (Young et al., 2002). Thus, the Meijer and Li (1998) value of 0.528 for meteoric waters reflects the combination of equilibrium and diffusive processes in the hydrological cycle.

Based on these observations, Barkan and Luz (2007) defined the ^{17}O excess parameter as the deviation from the meteoric water line with slope of 0.528 in $\ln(\delta + 1)$ space:

$$\Delta^{17}\mathrm{O} = \ln(\delta^{17}\mathrm{O} + 1) - 0.528\ln(\delta^{18}\mathrm{O} + 1). \tag{5}$$

Like deuterium excess, ^{17}O excess is sensitive to kinetic fractionation but, unlike deuterium excess, it is nearly insensitive to temperature and much less sensitive than δD and δ^{18}O to equilibrium fractionation during transport and precipitation. Natural variations of Δ^{17}O in precipitation are orders of magnitude smaller than variations in δ^{18}O and δD and are typically expressed in per meg (10^{-6}) rather than per mil (10^{-3}).

[1]Note that the precise atomic masses should be used. $m_{16} = 15.99491462230 \pm 0.00000000016$, $m_{17} = 16.9991317 \pm 0.0000012$, and $m_{18} = 17.9991610 \pm 0.0000070$ (Audi et al., 2003).

The potential of Δ^{17}O in hydrological research is significant because it provides independent information that may be used to disentangle the competing effects of fractionation during evaporation, in transport, and in the formation and deposition of precipitation (Landais et al., 2008; Risi et al., 2010; Schoenemann et al., 2014). It also has applications in atmospheric dynamics because of the importance of supersaturation conditions that, during the formation of cloud ice crystals, impart a distinctive isotope signature to water vapor (e.g., Blossey et al., 2010; Schoenemann et al., 2014).

Compared to the routine nature of δ^{18}O and δD analysis, isotopic ratio measurements of ^{17}O, the second heavy isotope of oxygen in terms of natural abundance, are challenging. The greater abundance of ^{13}C than ^{17}O makes the measurement of δ^{17}O in CO_2 equilibrated with water by IRMS at $m/z = 45$ impractical. As a result, the precise measurement of Δ^{17}O requires conversion of water to O_2 rather than equilibration with CO_2 or reduction to CO. Meijer and Li (1998) developed an electrolysis method using $CuSO_4$. More recently, Baker et al. (2002) used a fluorination method to convert water to O_2, which was analyzed by continuous-flow IRMS; this approach was updated by Barkan and Luz (2005) for dual-inlet IRMS.

The dual-inlet IRMS method can provide high-precision and high-accuracy Δ^{17}O measurements. However, the technique is time consuming, resulting in significantly lower sample throughput when compared to the standard and relatively routine analysis of δ^{18}O and δD. The fluorination procedure requires 30 min or more per sample, while the dual-inlet mass-spectrometric analysis requires 2–3 h. In practice, multiple samples must be processed because of memory effects in the cobalt-fluoride reagent and other issues that can arise in the vacuum line (e.g., fractionation during gas transfer) (Barkan and Luz, 2005). Moreover, while this method provides the most precise available measurements of Δ^{17}O, measurements of individual δ^{18}O values by this method are generally less precise than those obtained with other approaches.

In recent years, laser absorption spectroscopy in the near-infrared and mid-infrared regions has increasingly been used for isotope analysis. An overview of experimental schemes for different molecules and isotopologues can be found in Kerstel (2004). In the case of water, laser absorption spectroscopy constitutes an excellent alternative to mass spectrometry. The main advantage is the ability to perform essentially simultaneous measurements of the water isotopologues directly on a water-vapor sample. As a result, tedious sample preparation and conversion techniques are not necessary. Commercialization of laser absorption spectrometers has recently allowed measurements of water isotope ratios to be performed with high precision and competitive relative accuracy, provided that a valid calibration scheme is applied (Brand et al., 2009; Gupta et al., 2009; Gkinis et al., 2010, 2011; Schmidt et al., 2010; Aemisegger et al., 2012; Kurita et al., 2012; Wassenaar et al., 2012).

The measurement of $^{17}O/^{16}O$ ratios should in principle not pose any additional challenges when compared to the measurement of $^{18}O/^{16}O$ and D/H. Provided that the absorption lines of interest are accessible by the laser source with no additional interferences from other molecules, a triple isotope-ratio measurement can be performed, resulting in calibrated values for $\delta^{18}O$, $\delta^{17}O$ and δD. In fact, triple isotope-ratio measurements of water have been presented in the past via the use of various laser sources utilizing different optical and data analysis techniques (Kerstel et al., 1999, 2002, 2006; Van Trigt et al., 2002; Gianfrani et al., 2003; Wu et al., 2010). However, with the exception of results presented recently by Steig et al. (2013) and Berman et al. (2013), precision has not been sufficient to be useful for applications requiring the detection of the very small natural variations in $\Delta^{17}O$.

In this work we report on development of a new cavity ring-down laser absorption spectrometer that provides both high-precision and high-relative-accuracy measurements of $\Delta^{17}O$. The instrument we discuss here is a modification, first described by Hsiao et al. (2012) and Steig et al. (2013), of the Picarro Inc. water isotope analyzer model L2130-*i*. It is now commercially available as model L2140-*i*. Critical innovations we introduced include the use of two lasers that measure absorption in two different infrared (IR) wavelength regions, and modifications to the spectroscopic measurement technique. We also developed a sample introduction system that permits the continuous introduction of a stable stream of water vapor from a small liquid water sample into the optical cavity. In combination with precise control of the temperature and pressure in the optical cavity of the instrument, data averaging over long integration times results in precision of better than 8 per meg in $\Delta^{17}O$. We establish the relative accuracy of our results in comparison with IRMS measurements. This work can also be seen as a demonstration of state-of-the-art performance for laser absorption spectroscopy isotope ratio analysis for all four main isotopologues of water ($H_2{}^{16}O$, $H_2{}^{17}O$, $H_2{}^{18}O$ and HDO).

2 Methods

2.1 Reporting of water isotope ratios

Normalization to known standards is critical in the measurement of water isotope ratios. By convention, $\delta^{18}O$ of a sample is relative to $^{18}O/^{16}O$ of VSMOW (Vienna Standard Mean Ocean Water) and normalized to $\delta^{18}O$ of SLAP (Standard Light Antarctic Precipitation). "Measured" δ values with respect to VSMOW are determined from the difference of "raw" values calculated directly from the ratio of measured isotopologue abundances:

$$\delta^{18}O_{\text{sample}}^{\text{measured}} = \frac{\delta^{18}O_{\text{sample}}^{\text{raw}} - \delta^{18}O_{\text{VSMOW}}^{\text{raw}}}{\delta^{18}O_{\text{VSMOW}}^{\text{raw}} + 1}, \quad (6)$$

where the subscript refers to an arbitrary sample. Normalization to SLAP is by

$$\delta^{18}O_{\text{sample}}^{\text{normalized}} = \delta^{18}O_{\text{sample}}^{\text{measured}} \frac{\delta^{18}O_{\text{SLAP}}^{\text{assigned}}}{\delta^{18}O_{\text{SLAP}}^{\text{measured}}}, \quad (7)$$

where $\delta^{18}O_{\text{SLAP}}^{\text{assigned}} = -55.5‰$ is the value assigned by the International Atomic Energy Agency (Gonfiantini, 1978; Coplen, 1988). δD is normalized in the same manner, using $\delta D_{\text{SLAP}}^{\text{assigned}} = -428‰$.

We normalize $\delta^{17}O$ using

$$\delta^{17}O_{\text{sample}}^{\text{normalized}} = \delta^{17}O_{\text{sample}}^{\text{measured}} \frac{\delta^{17}O_{\text{SLAP}}^{\text{assigned}}}{\delta^{17}O_{\text{SLAP}}^{\text{measured}}}. \quad (8)$$

There is no IAEA (International Atomic Energy Agency)-defined value for $\delta^{17}O_{\text{SLAP}}^{\text{assigned}}$, but Schoenemann et al. (2013) recommended that it be defined such that SLAP $\Delta^{17}O$ is precisely zero. We follow that recommendation here; that is, we define

$$\delta^{17}O_{\text{SLAP}}^{\text{assigned}} = e^{(0.528\ln(-55.5\times10^{-3}+1))} - 1\,, \quad (9)$$

which yields $\delta^{17}O_{\text{SLAP}}^{\text{assigned}} = -29.6986‰$, well within the error of published measurements (Barkan and Luz, 2005; Kusakabe and Matsuhisa, 2008; Lin et al., 2010; Schoenemann et al., 2013) after normalization to the associated $\delta^{18}O$ values (Schoenemann et al., 2013).

Throughout this paper, reported values of $\delta^{18}O$, $\delta^{17}O$, δD and $\Delta^{17}O$ have been normalized as described above unless specifically noted otherwise. Superscripts and subscripts are omitted except where needed for clarity.

2.2 $\Delta^{17}O$ analysis with mass spectrometry

IRMS measurements provide the benchmark for comparison with results from analysis of $\Delta^{17}O$ by CRDS (cavity ring-down spectroscopy). We used IRMS to establish accurate measurements of $\Delta^{17}O$ of five laboratory working standards and the IAEA reference water GISP (Greenland Ice Sheet Precipitation), relative to VSMOW and SLAP. We also used both IRMS and CRDS measurements to determine the δD and $\delta^{18}O$ of the same standards; $\delta^{17}O$ is calculated from the $\Delta^{17}O$ and $\delta^{18}O$ data. Table 1 reports the values, updated from those in Schoenemann et al. (2013).

We used the method described in Schoenemann et al. (2013) to convert water to O_2 by fluorination, following procedures originally developed by Baker et al. (2002) and Barkan and Luz (2005). A total of 2 µL of water are injected into a nickel column containing CoF_3 heated to 370 °C, converting H_2O to O_2, with HF and CoF_2 as byproducts. The O_2 sample is collected in a stainless steel cold finger containing 5A molecular sieve following Abe (2008). To minimize memory effects, a minimum of three injections are made prior to collecting a final sample for measurement.

Table 1. VSMOW-SLAP-normalized isotopic ratios of reference waters analyzed at the University of Washington "Δ*IsoLab". $\Delta^{17}O$ values are from long-term average IRMS measurements, updated from Schoenemann et al. (2013) to reflect the inclusion of additional data. $\delta^{18}O$ and δD values are from long-term average laser spectroscopy measurements. $\delta^{17}O$ values are calculated from $\Delta^{17}O$ and $\delta^{18}O$ (Eq. 5). Precision (±) is the standard error ($\sigma/\sqrt{n}$). n is the sample size.

	$\Delta^{17}O$ (per meg)	$\delta^{18}O$ (‰)	$\delta^{17}O$[a] (‰)	δD (‰)	n
GISP[b]	28 ± 2	-24.80 ± 0.02	-13.1444	-189.67 ± 0.20	20
VW	3 ± 3	-56.61 ± 0.02	-30.2980	-438.79 ± 0.35	10
WW	27 ± 2	-33.82 ± 0.03	-17.9754	-268.30 ± 0.31	36
SW	33 ± 2	-10.55 ± 0.02	-5.5515	-75.63 ± 0.17	18
PW	30 ± 2	-6.88 ± 0.02	-3.6087	-42.12 ± 0.18	17
KD[c]	-0.8 ± 4	0.43 ± 0.01	0.2262	1.33 ± 0.13	5

[a] $\delta^{17}O$ calculated from $\delta^{18}O$ and $\Delta^{17}O$. See Schoenemann et al. (2013). [b] CIAAW values for GISP are $\delta D = -189.73$ ‰ and $\delta^{18}O = -24.78$ ‰ (Gonfiantini et al., 1995). [c] Provisional measurement. Long-term average data for KD (Kona Deep) are not yet available.

The O_2 sample is analyzed on a ThermoFinnigan MAT 253 dual-inlet mass spectrometer at $m/z = 32$, 33, and 34 for $\delta^{18}O$ and $\delta^{17}O$, using O_2 gas as a reference. Each mass-spectrometric measurement comprises 90 sample-to-reference comparisons. Precise adjustment of both sample and reference gas signals (10 V±100 mV) permits long-term averaging with no measurable drift, so that the analytical precision is given by simple counting statistics: $\sigma/\sqrt{90}$, where σ is the standard deviation of the individual sample/reference comparisons. The resulting precision of repeated measurements of O_2 gas is 0.002, 0.004, and 0.0037 ‰ (3.7 per meg) for $\delta^{17}O$, $\delta^{18}O$, and $\Delta^{17}O$, respectively. Reproducibility of the $\delta^{17}O$ and $\delta^{18}O$ ratios of water samples is in practice less precise than these numbers indicate, because fractionation can occur during the fluorination process or during the collection of O_2. However, because this fractionation closely follows the relationship $\ln(\delta^{17}O + 1) = 0.528 \ln(\delta^{18}O + 1)$, the errors largely cancel in the calculation of $\Delta^{17}O$ (Barkan and Luz, 2005; Schoenemann et al., 2013). The reproducibility of the calibrated $\Delta^{17}O$ of repeated water samples ranges from 4 to 8 per meg (Schoenemann et al., 2013).

2.3 $\Delta^{17}O$ analysis with cavity ring-down spectroscopy

2.3.1 Instrument design

We used modified versions of a CRDS analyzer designed for $\delta^{18}O$ and δD, commercially available as model L2130-*i*, manufactured by Picarro Inc. The L2130-*i* is an update to the water-isotope analyzers originally discussed in Crosson (2008). It uses an Invar (Ni–Fe) optical cavity coupled to a near-infrared laser. Optical resonance is achieved by piezoelectric modifications to the length of the cavity. When the intensity in the cavity reaches a predetermined value, the laser source is turned off and the intensity then decays exponentially. The time constant of this decay is the "ring-down time". The ring-down time depends on the reflectivity of the mirrors, the length of the cavity, the mixing ratio of the gas being measured, and the frequency-dependent absorption coefficient. The frequency is determined with a wavelength monitor constructed on the principle of a solid etalon (Crosson et al., 2006; Tan, 2008).

Determination of $\delta^{18}O$ and δD ratios on the model L2130-*i* is obtained by measurements of the amplitude of $H_2{}^{18}O$, $H_2{}^{16}O$ and HDO spectral lines from a laser operating in the area of 7200 cm^{-1} (wavelength 1389 nm). In a modified version, which we refer to as the L2130-*i*-C, we added a second laser that provides access to another wavelength region, centered on 7193 cm^{-1}, where there are strong $H_2{}^{17}O$ and $H_2{}^{18}O$ absorption lines (Fig. 1). Rapid switching between the two lasers allows the measurement of all three isotope ratios essentially simultaneously. About 200–400 ring-down measurements are made per second, and complete spectra covering all four isotopologues are acquired in 0.8 s intervals.

For isotope measurements with the L2130-*i* or L2130-*i*-C under normal operating conditions, water vapor in a dry air or N_2 carrier gas flows continuously through the cavity to maintain a cavity pressure of (66.7 ± 0.1) hPa at a temperature of (80 ± 0.01) °C, normally at a H_2O mixing ratio of 20 mmol mol^{-1}. The flow rate of 40 $cm^3 min^{-1}$ (290 K, 10^5 Pa) is maintained by two proportional valves in a feedback loop configuration up- and down-stream of the optical cavity. The spectral peak amplitudes are determined from the least-squares fit of discrete measurements of the absorption (calculated from measurements of the ring-down time) to a model of the continuous absorption spectrum.

The spectroscopic technique utilized for the acquisition and analysis of the spectral region relevant to the measurement of the isotopologues of interest is essentially the same as the one used in the earlier commercially available L2130-*i* analyzer. One of the main features of this technique is that optical resonance is obtained by dithering the length of the cavity. As discussed in Results (Sect. 3), we found that drift on timescales longer than a few minutes limited the achievable precision of $\Delta^{17}O$ measurements to about 20 per meg;

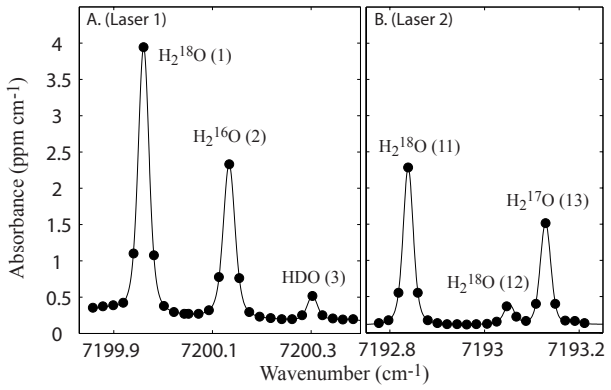

Figure 1. Measured absorption spectrum for water isotopologues in the two wavenumber regions used by the L2130-*i*-C and L2140-*i* CRDS analyzers. Filled circles: measured absorption for H_2O vapor 20 mmol mol^{-1} in dry air carrier, 66.7 hPa cavity pressure. The isotopologue associated with each peak is noted, with nominal peak numbers for reference (1–3 on laser 1, 11–13 on laser 2). Lines: least-squares fit to the data using Galatry profiles as discussed in the text.

this drift is ascribed to small but detectable drift in the wavelength monitor.

To improve measurement precision, we developed an updated version of the L2130-*i*-C, hereafter referred to as model L2140-*i*, which incorporates a different spectroscopic method. As in the L2130-*i*, a piezoelectric actuator is used to physically move one mirror of the cavity, and the wavelength monitor is used for feedback to the laser-frequency control electronics, thus allowing for rapid tuning to a target frequency. In the new method, though, the length of the optical cavity is kept constant during the acquisition of a spectrum, and resonance is obtained by dithering of the laser frequency by means of laser-current modulation. The frequency for each ring-down measurement is then determined directly from the resonance itself, based on the principle that resonance will occur only at frequencies spaced by integer multiples of the free spectral range (FSR) of the cavity (e.g., Morville et al., 2005).

The target frequency for each spectral region (e.g., that for $H_2{}^{17}O$) is determined in advance from measurements made at higher frequency resolution and used to tightly constrain the parameters in a spectral model (see below). The fine frequency spacing for a given narrow spectral region is determined only by the FSR. In this way, each ring-down measurement can be unambiguously assigned to a stable and equidistant frequency axis and the spectral line shape fit to a well-defined model; only a few data points are needed to precisely define each spectral peak. This new scheme also yields higher cavity excitation rates – typically 500 ring-downs per second.

The FSR is inversely proportional to the cavity length. The FSR of the L2130-*i* and L2140-*i* under normal operating conditions is 0.02 cm^{-1}, and varies by no more than 10^{-5} cm^{-1} owing to the precisely controlled temperature and pressure conditions. The cavity finesse is 44 000. The ring-down time constant for an empty cavity is 22 µs, corresponding to an effective optical path length of 6.7 km. Each ring-down measurement has a frequency resolution of 14 kHz (given by the FSR divided by the cavity finesse). The noise-equivalent absorption spectral density is 2.3×10^{-11} cm^{-1}Hz$^{-1/2}$ for both the L2130-*i* and L2130-*i*-C, and the L2140-*i* instruments. This corresponds to a noise-equivalent absorption of only 7×10^{-13} cm^{-1} for integration times of 10^3 s.

2.3.2 Spectroscopy

The use of laser-current tuning permits greater accuracy in the determination of the width of spectral lines than was achievable with the L2130-*i* or L2130-*i*-C instruments. This allows us, with the L2140-*i*, to use the integrated absorption under the spectral lines, rather than the height of spectral peaks, to determine isotopologue abundances (e.g., Kerstel, 2004; Kerstel et al., 2006; Hodges and Lisak, 2007).

The integrated absorption (cm^{-1}) is given by

$$A = u\int_0^\infty \kappa(\tilde{\nu})\mathrm{d}\tilde{\nu}, \tag{10}$$

where $\kappa(\tilde{\nu},T,P)$ is the molecular monochromatic absorption coefficient (cm^2), u is the column density of absorbers (cm^{-2}) and $\tilde{\nu}$ is the wavenumber (cm^{-1}) (Rothman et al., 1996).

The integrated absorption is directly related to the absorption strength, S, via

$$\kappa(\tilde{\nu},T,P) = S(T)\,f(\tilde{\nu},T,P), \tag{11}$$

where f is the line shape function due to Doppler and pressure spectral line broadening, T is temperature and P is pressure. The integral $\int_0^\infty f(\tilde{\nu},T,P)\mathrm{d}\tilde{\nu}=1$ and S is independent of pressure (Rothman et al., 1996). The ratios A_i/A_j for two different absorbing isotopologues i and j – and therefore in principle the isotope ratios – are also independent of pressure. This makes the integrated absorption superior to the spectral peak amplitude used in earlier-generation instruments. In practice, it is convenient to replace the wavenumber, $\tilde{\nu}$, in the integral with the dimensionless detuning $x = (\tilde{\nu}-\tilde{\nu}_0)/\sigma_D$, following Varghese and Hanson (1984), where $\tilde{\nu_0}$ is the center frequency of the absorption line, and σ_D is the Doppler width (half-width of the Gaussian Doppler-broadening profile at $1/e$ of the height).

Values of A are obtained by a least-squares fit of the measurements to an empirically determined spectral model. The spectral model describes the measured absorption as the sum of a baseline and molecular absorption lines. Free parameters in the baseline are an offset, slope and quadratic curvature term. The molecular absorption spectrum is modeled as the

superposition of Galatry profiles, which describe the shape function, f, for each spectral line. The Galatry profile, G, is given by the real part of the Fourier transform of the correlation function, Φ (Galatry, 1961):

$$G(x,y,z) = \frac{1}{\sqrt{\pi}}\mathrm{Re}\left\{\int_0^\infty \left[\Phi(y,z,\tau)e^{-ix\tau}\mathrm{d}\tau\right]\right\},$$
$$\Phi(y,z,\tau) = \exp\left(-y\tau + \frac{1}{2z^2}\left[1 - z\tau - e^{-z\tau}\right]\right), \quad (12)$$

where x is the frequency separation from the line center normalized by the Doppler width (as given above), y and z are collisional broadening and narrowing parameters, respectively, and τ is dimensionless time.

The parameters that determine the shape of the lines are obtained from spectra acquired by operating the analyzer in a fine-scan mode where ring-downs are acquired with a frequency spacing much smaller than the line width and using the wavelength monitor to determine the frequency axis. This determines the relationship between the collisional broadening and narrowing parameters, y and z, and the relationship between y for the "normal" water peak ($H_2{}^{16}O$) and the values of y for each of the isotopologues. The Doppler width is a known function of temperature (e.g., Galatry, 1961) and is therefore a fixed parameter. This leaves three or four free parameters needed to describe absorption for unknown samples in each spectral region: one y parameter and one value for the integrated absorption, A, for each independent isotopologue spectral line of interest (e.g., one each for the $H_2{}^{18}O$, $H_2{}^{16}O$ and HDO lines in the 7200 cm^{-1} wavenumber region).

2.3.3 Determination of isotope ratios

For the determination of δ^{18}O and δ^{17}O, the $^{18}O/^{16}O$ and $^{17}O/^{16}O$ ratios are obtained from the ratios of integrated absorptions of the rare isotopologues on the second laser to the integrated absorption of the common isotopologue on the first laser:

$$^{18}R = \frac{A(H_2{}^{18}O(11))}{A(H_2{}^{16}O(2))}, \quad (13)$$

$$^{17}R = \frac{A(H_2{}^{17}O(13))}{A(H_2{}^{16}O(2))}, \quad (14)$$

where $H_2{}^{18}O(11)$, $H_2{}^{16}O(2)$, etc. refer to the absorption lines shown in Fig. 1.

The raw (uncalibrated) δ^{18}O and δ^{17}O values are then obtained using the usual definition of δ:

$$\delta^{18}O^{\mathrm{raw}} = \frac{^{18}R}{^{18}R_{\mathrm{ref}}} - 1\,, \quad (15)$$

$$\delta^{17}O^{\mathrm{raw}} = \frac{^{17}R}{^{17}R_{\mathrm{ref}}} - 1\,, \quad (16)$$

where the value of R_{ref} is an instrument-specific estimate of the ratio of integrated absorption of $H_2{}^{17}O$ or $H_2{}^{18}O$ to that of $H_2{}^{16}O$ for the IAEA water standard, VSMOW. Values of δD are determined similarly using data from the first laser only:

$$^{2}R = \frac{A(\mathrm{HDO}(3))}{A(H_2{}^{16}O(2))}, \quad (17)$$

$$\delta D^{\mathrm{raw}} = \frac{^{2}R}{^{2}R_{\mathrm{ref}}} - 1\,. \quad (18)$$

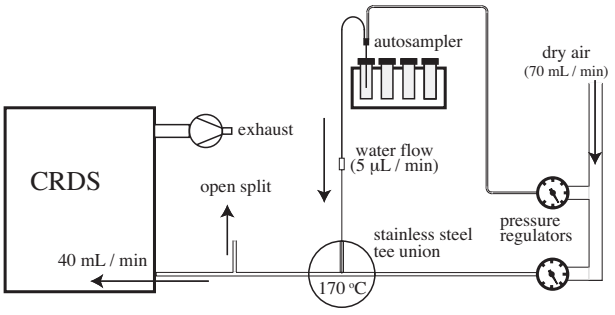

Figure 2. Schematic of custom vaporizer design used for isotope ratio measurements over long integration times. Double lines denote 1/16 inch and 1/32 inch stainless steel tubing (outside diameter). Single lines denote fused-silica capillary (0.3 mm inside diameter exiting the vials, reduced to 0.1 mm where the capillary enters the vaporizer).

2.4 Sample inlet system

We use two different inlet systems for the introduction of water into the CRDS optical cavity. To obtain measurements of the same water sample continuously over several hours, we use a "custom vaporizer". The custom vaporizer comprises a continuous-flow inlet system similar to that described by Gkinis et al. (2010, 2011) and used previously for δ^{18}O and δD. In this design, water is pumped continuously through a capillary and into a stainless steel tee union heated to 170 °C. In our application, the "pump" is a simple air pressure system, with a double needle that is used to puncture septum-sealed vials; air pressure introduced into the vial through a small steel tube pushes water through a fused-silica capillary and into the heated tee union. Within the tee union, the liquid water is mixed with dry air and exits the tee union as water vapor that is introduced into the CRDS optical cavity through an open split (Fig. 2). Water-vapor mixing ratios as measured by the CRDS analyzer are maintained at a target value (normally 20 mmol mol^{-1}) to within better than $\pm$0.1 mmol mol^{-1}.

For discrete injections of water into the CRDS we use a commercial vaporizer available from Picarro Inc. as model A0211 and described by Gupta et al. (2009). The vaporizer, operating at 110 °C, mixes dry carrier gas with 1.8 µL of water, which is injected through a septum. The resulting water vapor is introduced into the optical cavity via a three-way valve after a $\approx$ 60 s equilibration. Analysis of a single injection pulse takes approximately 120 s, excluding injection,

vaporizer purging and equilibration time. Automated sampling from 2 mL vials is accomplished with an autosampler (LEAP Technologies LC PAL). In our experiments, a complete vial analysis consists of 10 repeated injections from the same vial, for a total analysis time of about 1200 s.

3 Results

3.1 Measurement precision and drift

We use the custom vaporizer to obtain CRDS analyses of the isotope ratios of the same water over several hours. The Allan variance statistic provides a convenient way to assess the analytical precision and drift for the resulting long integrations. The Allan variance is defined as (Werle, 2011)

$$\sigma^2_{\mathrm{Allan}}(\tau_m) = \frac{1}{2\,\mathrm{m}} \sum_{j=1}^{m} \left(\overline{\delta}_{j+1} - \overline{\delta}_j\right)^2 , \qquad (19)$$

where τ_m is the integration time and $\overline{\delta}_{j+1}$, $\overline{\delta}_j$ are the mean values (e.g., $\delta = \delta^{18}\mathrm{O}$ or $\delta^{17}\mathrm{O}$) over neighboring time intervals. Here, we use the "Allan deviation" (σ_{Allan}, square root of the Allan variance) which can be interpreted as an estimate of the achievable reproducibility as a function of integration time.

Figure 3 shows σ_{Allan} for measurements made both with the L2130-*i*-C instrument using peak amplitudes, and with the L2140-*i* instrument using laser-current tuning and the integrated absorption measurement. In both cases, σ_{Allan} values for $\Delta^{17}\mathrm{O}$ of < 20 per meg are achieved after integration times of 5×10^2 s, and σ_{Allan} values for $\delta^{18}\mathrm{O}$, $\delta^{17}\mathrm{O}$ and $\delta\mathrm{D}$ are below 0.03, 0.03 and 0.04 ‰, respectively. However, these values represent the limits with the L2130-*i*-C; no additional improvements in precision were achieved with longer integration times, and in general σ_{Allan} begins to rise after 10^3 s. In contrast, with the L2140-*i*, σ_{Allan} values for $\delta^{18}\mathrm{O}$ and $\delta^{17}\mathrm{O}$ improve to < 0.015 ‰, and σ_{Allan} for $\Delta^{17}\mathrm{O}$ is better than 10 per meg after 1200 s (20 min). For $\delta\mathrm{D}$, the precision is < 0.07 ‰ at 10^3 s, and remains well below 0.1 ‰ for much longer integrations times ($> 10^4$ s). Both the measurements with the custom vaporizer, and those with the commercial vaporizer, show that long-term drift in $\Delta^{17}\mathrm{O}$ is greatly reduced in the L2140-*i*. Long-term drift for $\delta^{18}\mathrm{O}$ and $\delta^{17}\mathrm{O}$ is also improved, though not eliminated. We discuss the relationship between drift in $\delta^{18}\mathrm{O}$, $\delta^{17}\mathrm{O}$ and $\Delta^{17}\mathrm{O}$ in Sect. 4.

Repeated measurements of discrete water injections provide another way to assess measurement precision and drift. Results from running the same water from multiple vials (with 10 discrete 1.8 µL injections per vial), yield statistics comparable to those obtained with the custom vaporizer (Fig. 4). Typical injection-to-injection precision is 20 per meg for $\Delta^{17}\mathrm{O}$. Averages over 10 repeated injections from each vial result in a total analysis time per vial of 1200 s, corresponding to the integration time at which the Allan deviation data (Fig. 3) show $\Delta^{17}\mathrm{O}$ precision reaching < 10 per meg. Vial average reproducibility of $\Delta^{17}\mathrm{O}$ is 8 per meg. Typical vial-to-vial reproducibility is 0.03 ‰ for $\delta^{18}\mathrm{O}$, 0.015 ‰ for $\delta^{17}\mathrm{O}$, and 0.1 ‰ for $\delta\mathrm{D}$.

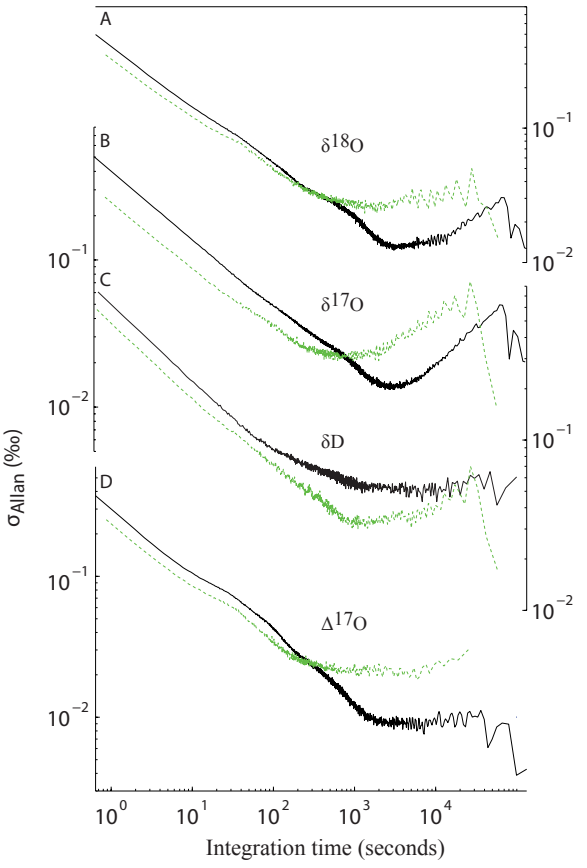

Figure 3. Comparison of Allan deviations for water isotope ratios with the L2130-*i*-C using a conventional wavelength monitor and spectral peak amplitude (green dashed lines), and with the L2140-*i* using laser-current-tuned cavity resonance and integrated absorption (solid lines). **(A)** $\delta^{18}\mathrm{O}$, **(B)** $\delta^{17}\mathrm{O}$, **(C)** $\delta\mathrm{D}$, **(D)** $\Delta^{17}\mathrm{O}$.

3.2 Sensitivity to water-vapor mixing ratio

Laser spectroscopy instruments used for water isotope measurements exhibit dependence of $\delta^{18}\mathrm{O}$ and $\delta\mathrm{D}$ values on the water-vapor mixing ratio (Gkinis et al., 2010), and similar dependence is expected for $\delta^{17}\mathrm{O}$ and $\Delta^{17}\mathrm{O}$. This dependence arises primarily from the effect of pressure broadening on peak shape. As noted in Sect. 2.3.2, use of the integrated absorption in place of peak amplitude in the calculation of isotope ratios with the L2140-*i* instrument should theoretically eliminate the water-vapor mixing-ratio dependence. We used the custom vaporizer to obtain measurements with the L2140-*i* over a wide range of water-vapor mixing ratios. Figure 5 shows that there is a significant reduction in the sensitivity of isotope ratios to mixing ratio when using the integrated absorption measurement, as

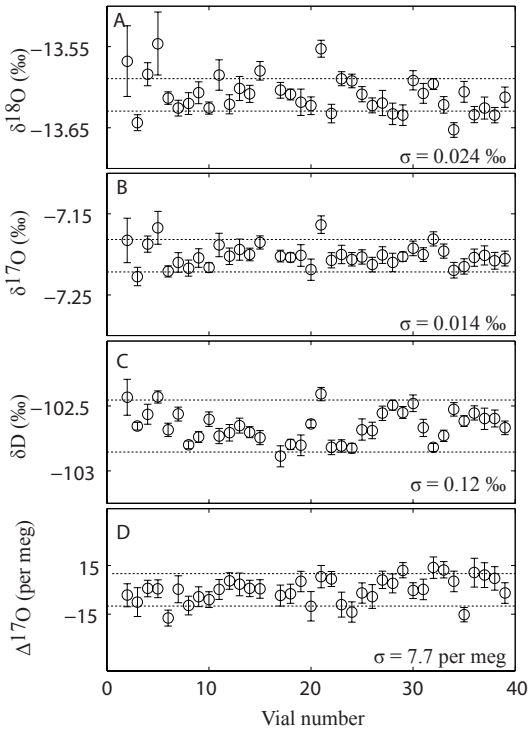

Figure 4. Isotope ratios from repeated measurements of 2 mL vials of identical water, using integrated absorption on the L2140-*i*. **(A)** δ^{18}O, **(B)** δ^{17}O, **(C)** δD, and **(D)** Δ^{17}O. Each dot represents the average of ten 1.8 µL injections from one vial; the vertical error bars show the standard error ($\sigma/\sqrt{n}$) of the $n = 10$ individual injections. The standard deviation of all vial means (σ) is given in each panel. Horizontal dashed lines are shown for reference at ±0.02 ‰ for δ^{18}O and δ^{17}O, at ±0.2 ‰ for δD, and at ±10 per meg for Δ^{17}O. The experiment shown took about 60 h. No drift corrections or other post-measurement adjustments were made to the raw data.

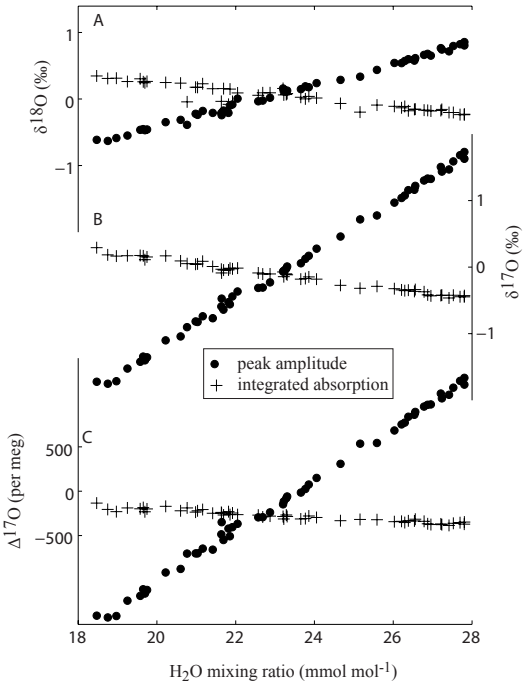

Figure 5. Comparison of the sensitivity of isotope ratio measurements on the L2140-*i* CRDS analyzer to the water-vapor mixing ratio using peak amplitude vs. integrated absorption. Note that a mixing ratio of 20 mmol mol^{-1} is reported by the instrument software as a concentration (20 000 ppm). **(A)** δ^{18}O, **(B)** δ^{17}O and **(C)** Δ^{17}O.

expected. For δ^{18}O, sensitivity is reduced from 0.2 ‰ for a 1 mmol mol^{-1} variation in water-vapor mixing ratio – comparable to that seen in the L2130-*i* and other earlier-generation instruments – to less than 0.04 ‰/(mmol mol^{-1}). Sensitivity for δ^{17}O is comparably reduced, from 0.4 ‰ to less than 0.08 ‰/(mmol mol^{-1}). Finally, the sensitivity of Δ^{17}O to the water-vapor mixing ratio is reduced from > 250 per meg to < 30 per meg/(mmol mol^{-1}). The mixing-ratio sensitivity of δD, however, at about 1 ‰/(mmol mol^{-1}) is not significantly changed between earlier models and the L2140-*i*. This may suggest an incomplete accounting for the structure of the mixing-ratio-dependent spectral baseline, or other aspects of the spectroscopy that are not yet fully characterized.

3.3 Calibration to VSMOW and SLAP

We performed two independent types of calibration experiments with the L2140-*i*. In the first experiment, we analyzed standard waters SLAP2 and VSMOW2, along with reference waters GISP, VW (Vostok Water), WW (West Antarctic Ice Sheet Water) and KD (Kona Deep), and used the two-point calibration lines defined by Eqs. (7) and (8) to determine the value of the references waters treated as "unknowns". The resulting calibrated δ^{18}O and δ^{17}O values are then used to calculate Δ^{17}O, using Eq. (5) (note that the δ^{18}O and δ^{17}O of VSMOW2 and SLAP2 are indistinguishable from those of VSMOW and SLAP (Lin et al., 2010)). In the second experiment, we analyzed lab reference waters SW (Seattle Water) and WW and used the IRMS δ^{18}O and δ^{17}O values of PW (Pennsylvania Water) and VW as calibration points.

In both types of calibration experiments, we used the commercial vaporizer and 2 mL vials, from which ten 1.8 µL injections were made. The measurement order was as follows, where the number gives the number of vials for each water sample in parentheses. First experiment: 5 (KD), 5 (VSMOW2), 4 (VW), 5 (SLAP2), 4 (WW), 5 (GISP), 5 (KD), 5 (VSMOW2), 4 (WW), 5 (GISP), 4 (VW), and 5 (SLAP2). Second experiment: 7 (VW), 7 (WW), 7 (SW), 7 (KD), 7 (PW), 7 (VW), 7 (WW), 7 (SW), 7 (KD), and

7 (PW). In the experiment with VSMOW2, SLAP2 and GISP, the use of lab reference waters with similar isotopic composition prior to the IAEA standards was done in order to reduced the potential for instrument memory effects influencing the results. We use data only from the last three vials for each standard or reference water in our calculations, using all 10 injections from each of those vials in the average. We find that the instrument response time for δ^{17}O is indistinguishable from that for δ^{18}O. This suggests that memory effects should be minimized for Δ^{17}O measurements compared with deuterium excess, which can be problematic because the response time for δD is greater than for δ^{18}O in most instruments (Aemisegger et al., 2012). Further work is needed, however, to fully characterize the influence of memory on Δ^{17}O with the L2140-*i*.

The results of the calibration experiments are tabulated in Table 2. Figure 6 shows the calibrated mean values and uncertainties in Δ^{17}O for the two different types of calibration experiment. The uncertainties are calculated as the standard deviation of the mean ($\sigma/\sqrt{n}$) based on n repeated measurements. This calculation may underestimate the true uncertainty because it assumes a Gaussian error distribution, which is not supported by the Allan deviation data for long integration times (Fig. 3). However, this is conservative with respect to the calibration experiments: the results show that the Δ^{17}O values of the "unknowns" in each experiment with the CRDS are indistinguishable from the values previously determined using IRMS. Note in particular that the CRDS value of the IAEA reference water, GISP (27 ± 4 per meg), calibrated independently, is nearly identical to the IRMS value of 28 ± 2 per meg (Schoenemann et al., 2013). Further, we find that both KD, which is fresh water derived by reverse osmosis from an ocean water sample, and VW, which is a meteoric water sample from the interior of East Antarctica, have indistinguishable Δ^{17}O values.

We emphasize that, as with IRMS measurements, data that are referenced to VSMOW but are not normalized on the VSMOW-SLAP scale can result in inconsistent results because of instrument-specific scale compression (or expansion) relative to the defined calibration (see e.g., Coplen, 1988; Schoenemann et al., 2013). In the context of Δ^{17}O measurements on water, such scale compression results in a slope differing from the defined value of 0.528 on a plot of $\ln(\delta^{17}\mathrm{O}+1)$ vs. $\ln(\delta^{18}\mathrm{O}+1)$. Also, if the slope is significantly different from 0.528, errors in Δ^{17}O will result even if a linear normalization to VSMOW-SLAP is applied. This problem can in principle be addressed using a nonlinear normalization method (Kaiser, 2008); i.e.,

$$\delta^{17}\mathrm{O}_{\mathrm{sample}}^{\mathrm{normalized}} = (\delta^{17}\mathrm{O}_{\mathrm{sample}}^{\mathrm{measured}}+1)^{\frac{\ln((\delta^{17}\mathrm{O}_{\mathrm{SLAP}}^{\mathrm{assigned}}+1))}{\ln((\delta^{17}\mathrm{O}_{\mathrm{SLAP}}^{\mathrm{measured}}+1)}} - 1\,, \quad (20)$$

and similarly for δ^{18}O, rather than our linear calculation (Eqs. 7–9). However, the nonlinear calibration method cannot effectively remove scale compression due to blank

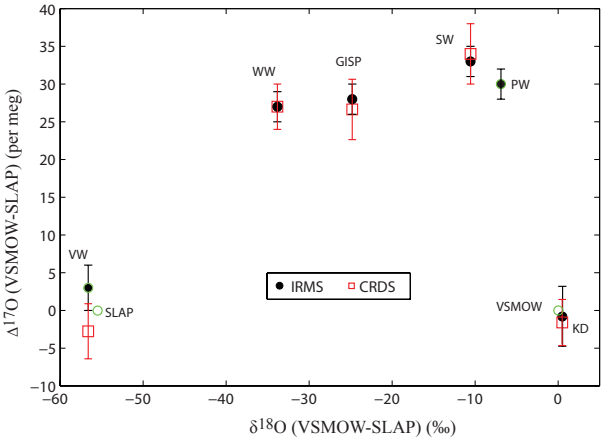

Figure 6. Comparison of Δ^{17}O data from two independent sets of calibrations of reference waters and standards measured by laser spectroscopy on the L2140-*i* (CRDS, open squares) with previously determined values from mass spectrometry (IRMS, filled circles). Δ^{17}O data are plotted vs. δ^{18}O. Error bars on the CRDS values are the standard deviation of the mean (see Table 2). Values and error bars (1 standard error) on the IRMS values are from Table 1, updated from Schoenemann et al. (2013). The calibration points VSMOW, SLAP, PW and VW are shown as open circles for reference.

effects. In our case, as shown in Fig. 7, the slope of $\ln(\delta^{17}\mathrm{O}+1)$ vs. $\ln(\delta^{18}\mathrm{O}+1)$ is 0.5254; the scale compression is therefore 0.995. Use of Eq. (20) would result in a difference for the GISP reference water of < 0.0006‰ for δ^{17}O, < 0.003‰ for δ^{18}O and < 1.6 per meg for Δ^{17}O, all well below measurement uncertainty. Use of the linear normalization from Schoenemann et al. (2013) is therefore preferred. Nevertheless, users of L2140-*i* instruments will need to verify any calibration strategy for their particular application, taking into account the instrument response time, the availability of reference waters of known composition, and the scale compression, which may be different for different instruments.

4 Discussion

Our results demonstrate that analysis of Δ^{17}O using cavity ring-down laser absorption spectroscopy, as implemented in the L2140-*i* instrument, can be competitive with analyses by mass spectrometry. The reproducibility of repeated individual measurements made over 30 min is better than 8 per meg, similar to the precision reported for IRMS (e.g., Luz and Barkan, 2010; Schoenemann et al., 2013), and calibrated values of reference waters are indistinguishable between the two methods. Achieving Δ^{17}O measurements at the < 10 per meg level with CRDS requires relatively long integration times when compared with the more common δ^{18}O or δD measurements, which for typical applications require lower

Table 2. VSMOW-SLAP-normalized Δ^{17}O, δ^{18}O, δ^{17}O and δD values for reference waters determined by CRDS using (a) IAEA standards VSMOW2 and SLAP2 as calibration points and (b) using University of Washington standards PW and VW as calibration points. IRMS-measured Δ^{17}O values are shown for comparison. Precision ($\pm$) is the standard deviation of the mean ($\sigma/\sqrt{n}$). n is the sample size.

	IRMS Δ^{17}O (per meg)	CRDS Δ^{17}O (per meg)	δ^{18}O (‰)	δ^{17}O (‰)	δD (‰)	n
GISP[a]	28 ± 2	27 ± 4	-24.77 ± 0.02	-13.13 ± 0.01	-190.19 ± 0.14	6
VW[a]	3 ± 3	-3 ± 3	-56.50 ± 0.03	-30.24 ± 0.02	-438.19 ± 0.35	6
WW[a]	27 ± 2	27 ± 4	-33.90 ± 0.03	-18.02 ± 0.02	-268.87 ± 0.40	6
WW[b]	27 ± 2	27 ± 2	-33.98 ± 0.03	-18.06 ± 0.03	-269.29 ± 0.26	6
SW[b]	33 ± 2	34 ± 4	-10.64 ± 0.04	-5.60 ± 0.03	-76.05 ± 0.24	6
KD[a]	-0.8 ± 4	-1.6 ± 3	0.43 ± 0.01	0.23 ± 0.01	1.33 ± 0.13	6
KD[b]	-0.8 ± 4	-1.6 ± 4	0.50 ± 0.03	0.26 ± 0.03	1.71 ± 0.22	6

[a] VSMOW2 and SLAP2 calibration. [b] PW and VW calibration. Errors take into account uncertainty in calibration points.

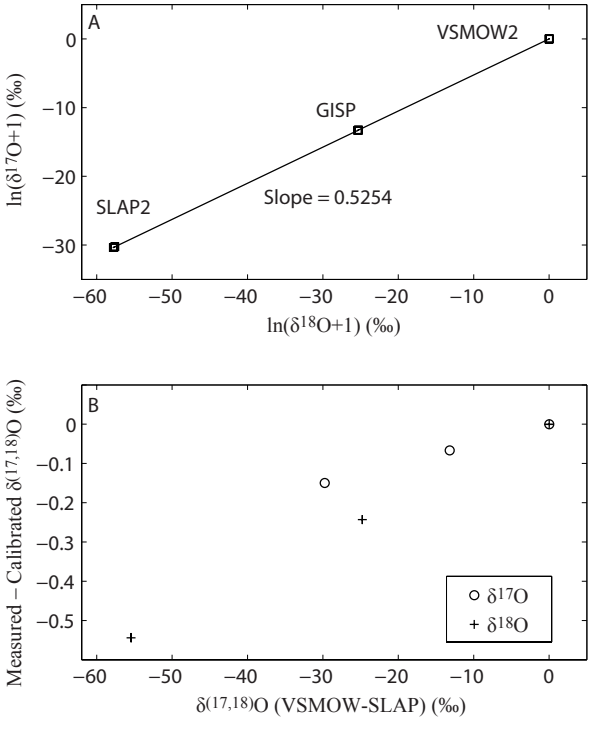

Figure 7. Characterization of scale compression on the L2140-*i*. **(A)** Measured (vs. VSMOW) $\ln(\delta^{17}\mathrm{O}+1)$ vs. $\ln(\delta^{18}\mathrm{O}+1)$ for VSMOW2, SLAP2 and GISP. **(B)** Difference between measured and calibrated δ^{17}O and δ^{18}O of VSMOW2, SLAP2 and GISP as a function of the calibrated value.

precision (< 0.1 and < 1‰, respectively). Nevertheless, the new method is less time consuming, less labor intensive, and safer than the IRMS method requiring the use of fluorination.

Measurements of Δ^{17}O with a laser spectroscopy instrument with a different design (off-axis integrated cavity output spectroscopy, or OA-ICOS) were reported recently by Berman et al. (2013). Measurements of the IAEA reference water GISP reported by Berman et al. (2013), when calibrated to VSMOW and SLAP, are somewhat lower than ours (23 ± 2 per meg, compared with our values of 27 ± 4 (CRDS) and 28 ± 2 (IRMS)), but both are compatible within 2σ of most reported IRMS values from the literature; e.g., the weighted average of the most precise previously reported measurements (IRMS only) was 22 ± 11 per meg (Schoenemann et al., 2013). The mean VSMOW-SLAP-normalized value for GISP for all recent measurements from four different laboratories (as reported here, and by Schoenemann et al., 2013 and Berman et al., 2013) is $\Delta^{17}\mathrm{O} = 28 \pm 3$ per meg.

High-precision Δ^{17}O measurements are achieved without drift correction on the L2140-*i*. Indeed, the precision and drift characteristics of the Δ^{17}O results are better than would be expected from the simple combination of noise in the δ^{18}O and δ^{17}O measurements, both of which show evidence of some drift in their Allan deviations (Fig. 3).

The relationship between δ^{18}O, δ^{17}O and Δ^{17}O errors can be understood as a combination of correlated and uncorrelated noise contributions (Schoenemann et al., 2013):

$$\sigma_{\mathrm{xs}} = (m - 0.528)\sigma_{18} + \eta_{17} \,, \tag{21}$$

where σ_{xs} is the precision of Δ^{17}O, σ_{18} is the precision of $\ln(\delta^{18}\mathrm{O}+1)$, and η_{17} is the residual in $\ln(\delta^{17}\mathrm{O}+1)$ from a best-fit line through the data having slope m. In general, the uncorrelated errors (η_{17}) are small. At higher frequencies, m tends towards higher values (Fig. 8).

We find that for the 0.8 s averages of ≈ 400 individual ring-down measurements, the slope is 0.82 ± 0.02, or 1.0 ± 0.1 if a "model 2" regression that accounts for variance in both the δ^{18}O and δ^{17}O measurements is used (e.g., York, 1969). A slope of precisely 1.0 would be expected if, for example, all measurement error were due to noise in the $H_2{}^{16}O$ spectral line, since this measurement is shared equally in the calculation of both δ^{18}O and δ^{17}O. The noise in the high-

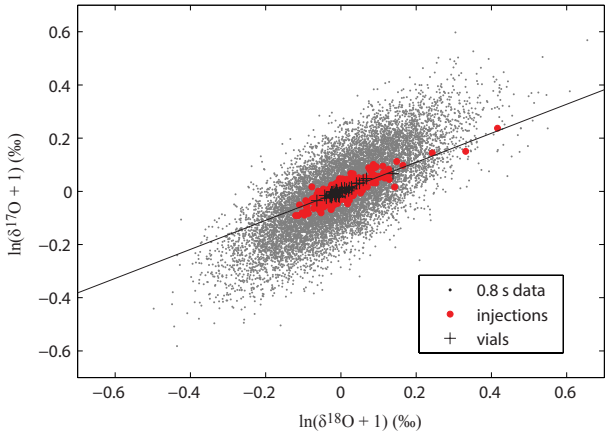

Figure 8. Relationship between $\ln(\delta^{17}\mathrm{O}+1)$ and $\ln(\delta^{18}\mathrm{O}+1)$ residuals for 40 vials of identical water, each injected 10 times in the L2140-*i* CRDS. Small gray dots show every 100th high-frequency 0.8 s measurement, large circles the individual injection means,"+"-signs the vial-mean values. The slopes of the 0.8 s and individual injection data are 0.82 ± 0.02 and 0.59 ± 0.02, respectively ($\pm = 2\sigma$). The slope of the vial-mean data is 0.54 ± 0.03, shown by the line.

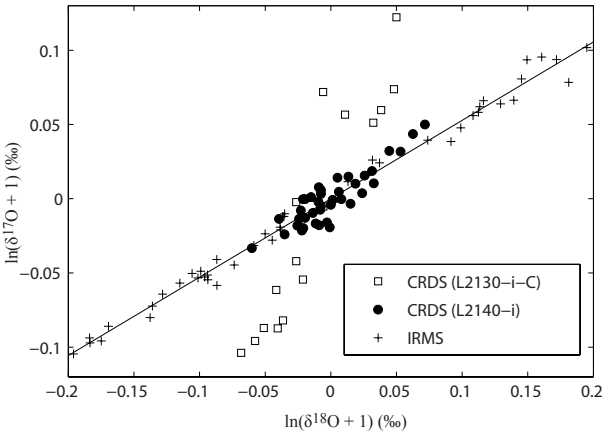

Figure 9. Comparison of the $\ln(\delta^{17}\mathrm{O}+1)$ vs. $\ln(\delta^{18}\mathrm{O}+1)$ relationship for residuals (difference of individual analyses from the mean) of measurements of water samples with the L2130-*i*-C and the L2140-*i* CRDS instruments, and with IRMS. The slope of 0.528 that defines $\Delta^{17}\mathrm{O}$ is shown for reference.

frequency data is indistinguishable from Gaussian, and is consequently reduced as a function of the square root of the integration time. For longer measurement times (integrations of 10^3 s or longer), m is ≈ 0.5, so that the term $(m-0.528)\sigma_{18}$ is small. As for IRMS measurements, it is the combination of the very small magnitude of uncorrelated noise, η_{17}, combined with $m \approx 0.5$ that leads to the very high precision for $\Delta^{17}\mathrm{O}$ measurements, even where the $\delta^{18}\mathrm{O}$ and $\delta^{17}\mathrm{O}$ measurements are comparatively imprecise.

Frequency dependence of the error slope, m, is not observed in IRMS measurements. As discussed in Schoenemann et al. (2013), in both the H_2O fluorination procedure and in the mass-spectrometer source, likely sources of error will involve some combination of diffusive and equilibrium fractionation processes, both of which will lead to values of m close to 0.5 (e.g., Miller, 2002). That the relationship between $\delta^{18}\mathrm{O}$ and $\delta^{17}\mathrm{O}$ errors in the CRDS also tends towards $m \approx 0.5$ at longer integration times suggests that low-frequency drift in these measurements is similarly attributable to fractionation effects, rather than, for example, drift in the optical cavity temperature or other aspects of the CRDS instrument itself. Fractionation of the $\delta^{18}\mathrm{O}$ and $\delta^{17}\mathrm{O}$ values could be associated with diffusion of water vapor, incomplete evaporation, or condensation and re-evaporation during the vaporization process, or possibly in the optical cavity.

These observations suggest that the current practical limit of precision for isotope measurements on the L2140-*i* is set by the sample introduction system, rather than the CRDS analysis itself. As illustrated in Fig. 9, which compares IRMS and CRDS measurements, the magnitude of η_{17} is very small – similar to that obtained with high-precision IRMS – while the magnitude of σ_{18} is much smaller than that obtained with IRMS measurements of O_2 prepared by fluorination.

This was not the case with our original prototype instrument (L2130-*i*-C), for which analyzer noise was dominant even for long integration times (Fig. 9). Because the term $(m-0.528)\sigma_{18}$ is very small, < 1 per meg, for vial-average measurements, changes to the sample introduction system that would significantly improve $\Delta^{17}\mathrm{O}$ precision will be challenging. These comparisons attest to the significant improvement in the spectroscopic measurements achieved in the L2140-*i*, as well as to the stability of the water-vapor delivery and minimal amount of fractionation occurring both in the commercial vaporizer and in our custom vaporizer design.

The L2140-*i* should be useful in a variety of applications, such as the high-resolution analysis of ice core samples using in-line continuous melting systems (Gkinis et al., 2011), or in the measurement of ambient water-vapor mixing ratios in the atmosphere, currently done with laser spectroscopy instruments for $\delta^{18}\mathrm{O}$ and $\delta\mathrm{D}$ (e.g., Noone et al., 2011; Sayres et al., 2009), though such applications have not yet been fully tested. The low sensitivity to water-vapor mixing ratio achieved with the integrated-absorption measurement would be an advantage in such applications, though there is still some sensitivity that may become important for mixing-ratio variability greater than $\pm 0.1\,\mathrm{mmol\,mol^{-1}}$. In the current commercial version of the L2140-*i* instrument, a water-vapor mixing-ratio correction is available in the instrument software that uses a bilinear relationship of the form

$$A(1)_{\mathrm{corrected}} = A(1) + a_0 + a_1 A(1) A(2), \qquad (22)$$

where $A(1)$ and $A(2)$ refer to the integrated absorption for peaks 1 and 2 (Fig. 1), and a_0 and a_1 are empirically determined coefficients. The coefficients are determined by

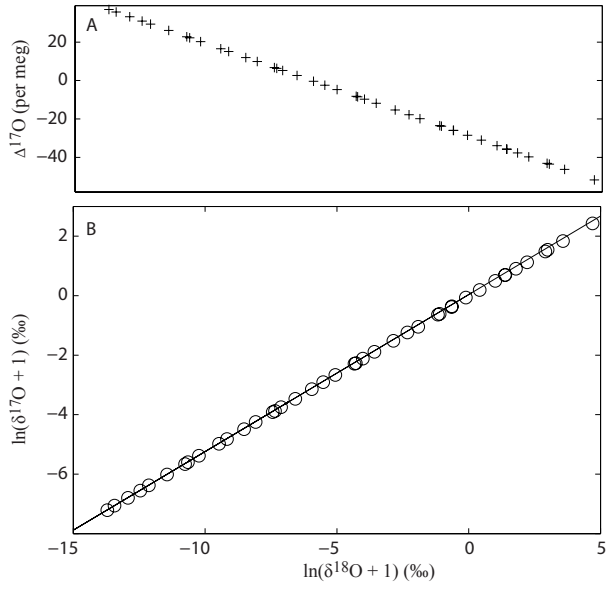

Figure 10. Results of an evaporation experiment in which 2 mL sample vials are left open to the ambient air and are progressively sampled (ten 1.8 µL injections for each vial) over a ≈ 60 h period. **(A)** δ^{17}O vs. $\ln(\delta^{18}\mathrm{O}+1)$, **(B)** $\ln(\delta^{17}\mathrm{O}+1)$ vs. $\ln(\delta^{18}\mathrm{O}+1)$. Time progress to the right in both panels. Note the gradual deviation of the measurements (open circles) from a slope of 0.528 (line).

varying the water mixing ratio over a large range and then applied to each measurement. A similar correction is applied to $A(3)$, $A(11)$, and $A(13)$. A simple linear correction following instrument-specific empirical measurements such as illustrated in Fig. 5 could be used as an alternative. We note, however, that we have not evaluated the performance of the instrument at low water-vapor mixing ratios (< 18 mmol mol^{-1}).

As an example of an application of the L2140-*i*, we performed a simple experiment in which 42 vials containing identical water, open to the air, were measured sequentially using 10 injections each. Because the vials were open to a relatively low-humidity laboratory atmosphere, evaporation of the vials would be expected to raise the δ^{18}O values through time, and the Δ^{17}O value should decrease; furthermore, the relationship between $\ln(\delta^{17}\mathrm{O}+1)$ and $\ln(\delta^{18}\mathrm{O}+1)$ would be expected to evolve along a slope intermediate between the equilibrium value (0.529) (Barkan and Luz, 2005) and the value for diffusion into dry air (0.518) (Barkan and Luz, 2007). These features are indeed observed in the experiment: Δ^{17}O decreases by 90 per meg (Fig. 10).

The slope of $\ln(\delta^{17}\mathrm{O}+1)$ vs. $\ln(\delta^{18}\mathrm{O}+1)$ is 0.5232 ± 0.0005, distinguishable at $> 99\%$ confidence from the "meteoric water line" slope, accounting for scale compression. A simple experiment like this, which was run fully automated over ≈ 60 h, would take many hours of sample preparation time and > 100 h of analysis time using the traditional fluorination and IRMS method. Note also that the progressive lowering of the Δ^{17}O value is clearly detectable from vial to vial at the 1–2 per meg level; this would probably not be possible to observe using the IRMS method. We suggest that the laser spectroscopy method for Δ^{17}O could be used in a number of hydrological and atmospheric sciences applications that were previously impractical.

5 Conclusions

CRDS is commonly used for measurements of the ^{18}O / ^{16}O and D / H isotope ratios of water and water vapor, reported as δ^{18}O and δD deviations from VSMOW. We have developed a new CRDS instrument that makes possible the additional measurement of the ^{17}O/^{16}O isotope ratio, and of the small difference, Δ^{17}O, between $\ln(\delta^{17}\mathrm{O}+1)$ and $0.528\ln(\delta^{18}\mathrm{O}+1)$, known as the "^{17}O excess". The new instrument uses a novel laser-current-tuned cavity resonance method to achieve precision of < 8 per meg for Δ^{17}O while simultaneously providing measurements of δ^{18}O and δD with a precision competitive with previous-generation instruments. Liquid samples are introduced into the optical cavity using an automated vaporization system that requires no prior sample preparation. Direct analysis of ambient water vapor in air is also possible. Calibration against the IAEA standard waters VSMOW2 and SLAP2 yields calibrated values for the reference water GISP of 27 ± 4 per meg, indistinguishable from the value of 28 ± 2 obtained by Schoenemann et al. (2013) using IRMS. Our results establish CRDS measurements of Δ^{17}O of H_2O as a viable alternative to conventional IRMS methods that require the use of fluorination to convert H_2O samples to O_2 prior to analysis.

Acknowledgements. We thank B. Vanden Heuvel, B. H. Vaughn, J. W. C. White, B. Vinther, G. Hsiao and E. Crosson. Reviews by E. Kerstel, J. Kaiser and E. Berman led to improvements in the manuscript. We also thank the editor for his handling of the manuscript. This work was supported by the US National Science Foundation Division of Polar Programs (Antarctic Glaciology Program), Division of Atmospheric and Geospace Sciences (Paleoclimate Program; Climate and Large Scale Dynamics Program) and Division of Industrial Innovation & Partnerships (Academic Liaison with Industry Program) (NSF award numbers DPP-1341360 and OPP-0806387). It was also supported by the Quaternary Research Center at the University of Washington, the Centre for Ice and Climate at the University of Copenhagen, and the Lundbeck Foundation, Copenhagen, Denmark.

Edited by: D. Heard

References

Abe, O.: Isotope fractionation of molecular oxygen during adsorption/desorption by molecular sieve zeolite, Rapid Commun. Mass Spec., 22, 2510–2514, 2008.

Aemisegger, F., Sturm, P., Graf, P., Sodemann, H., Pfahl, S., Knohl, A., and Wernli, H.: Measuring variations of δ^{18}O and δ^{2}H in atmospheric water vapour using two commercial laser-based spectrometers: an instrument characterisation study, Atmos. Meas. Tech., 5, 1491–1511, doi:10.5194/amt-5-1491-2012, 2012.

Audi, G., Wapstra, A. H., and Thibault, C.: The 2003 atomic mass evaluation. II: Tables, graphs and references, Nucl. Phys. A, 729, 337–676, 2003.

Baker, L., Franchi, I. A., Maynard, J., Wright, I. P., and Pillinger, C. T.: A technique for the determination of ^{18}O/^{16}O and ^{17}O/^{16}O isotopic ratios in water from small liquid and solid samples, Anal. Chem., 74, 1665–1673, 2002.

Barkan, E. and Luz, B.: High precision measurements of ^{18}O/^{16}O and ^{17}O/^{16}O ratios in H_2O, Rapid Commun. Mass Sp., 19, 3737–3742, 2005.

Barkan, E. and Luz, B.: Diffusivity fractionations of $H_2{}^{16}O/H_2{}^{17}O$ and $H_2{}^{16}O/H_2{}^{18}O$ in air and their implications for isotope hydrology, Rapid Commun. Mass Spec., 21, 2999–3005, 2007.

Begley, I. S. and Scrimgeour, C. M.: High-precision δ^{2}H and δ^{18}O measurement for water and volatile organic compounds by continuous-flow pyrolysis isotope ratio mass spectrometry, Anal. Chem., 69, 1530–1535, 1997.

Berman, E. S. F., Levin, N., Landais, A., Li, S., and Thomas Owano, T.: Measurement of δ^{18}O, δ^{17}O, and ^{17}O-excess in water by off-axis integrated cavity output spectroscopy and isotope ratio mass spectrometry, Anal. Chem., 85, 10392–10398, 2013.

Bigeleisen, J., Perlman, M. L., and Prosser, H. C.: Conversion Of hydrogenic materials to hydrogen for isotopic analysis, Anal. Chem., 24, 1356–1357, 1952.

Blossey, P. N., Kuang, Z., and Romps, D. M.: Isotopic composition of water in the tropical tropopause layer in cloud-resolving simulations of an idealized tropical circulation, J. Geophys. Res.-Atmos., 115, D24309, doi:10.1029/2010JD014554, 2010.

Brand, W. A., Geilmann, H., Crosson, E. R., and Rella, C. W.: Cavity ring-down spectroscopy versus high-temperature conversion isotope ratio mass spectrometry; a case study on δ^{2}H and δ^{18}O of pure water samples and alcohol/water mixtures, Rapid Commun. Mass Spec., 23, 1879–1884, 2009.

Cohn, M. and Urey, H.: Oxygen exchange reactions of organic compounds and water, J. Am. Chem. Soc., 60, 679–687, 1938.

Coplen, T.: Normalization of oxygen and hydrogen isotope data, Chem. Geol., 72, 293–297, 1988.

Craig, H. H.: Isotopic standards for carbon and oxygen and correction factors for mass-spectrometric analysis of carbon dioxide, Geochim. Cosmochim. Acta, 12, 133–149, 1957.

Crosson, E. R.: A cavity ring-down analyzer for measuring atmospheric levels of methane, carbon dioxide, and water vapor, Appl. Phys. B, 92, 403–408, 2008.

Crosson, E., Fidric, B., Paldus, B., and Tan, S.: Wavelength control for cavity ringdown spectrometer, Patent US7106763 B2, Picarro, Inc., 2006.

Dansgaard, W.: Stable isotopes in precipitation, Tellus, 16, 436–468, 1964.

Dansgaard, W., Clausen, H., Gundestrup, N., Hammer, C., Johnsen, S., Kristinsdottir, P., and Reeh, N.: A new Greenland deep ice core, Science, 218, 1273–1277, 1982.

Epstein, S. and Mayeda, T.: Variations of ^{18}O content of waters from natural sources, Geochim. Cosmochim. Acta, 4, 213–224, 1953.

Galatry, L.: Simultaneous effect of Doppler and foreign gas broadening on spectral lines, Phys. Rev., 122, 1218–1223, 1961.

Gehre, M., Hoefling, R., Kowski, P., and Strauch, G.: Sample preparation device for quantitative hydrogen isotope analysis using chromium metal, Anal. Chem., 68, 4414–4417, 1996.

Gehre, M., Geilmann, H., Richter, J., Werner, R. A., and Brand, W. A.: Continuous flow ^{2}H/^{1}H and ^{18}O/^{16}O analysis of water samples with dual inlet precision, Rapid Commun. Mass Spec., 18, 2650–2660, 2004.

Gianfrani, L., Gagliardi, G., van Burgel, M., and Kerstel, E. R. T.: Isotope analysis of water by means of near-infrared dual-wavelength diode laser spectroscopy, Opt. Express, 11, 1566–1576, 2003.

Gkinis, V., Popp, T. J., Johnsen, S. J., and Blunier, T.: A continuous stream flash evaporator for the calibration of an IR cavity ring-down spectrometer for the isotopic analysis of water, Isotop. Environ. Health Stud., 46, 463–475, 2010.

Gkinis, V., Popp, T. J., Blunier, T., Bigler, M., Schüpbach, S., Kettner, E., and Johnsen, S. J.: Water isotopic ratios from a continuously melted ice core sample, Atmos. Meas. Tech., 4, 2531–2542, doi:10.5194/amt-4-2531-2011, 2011.

Gonfiantini, R.: Standards for stable isotope measurements in natural compounds, Nature, 271, 534–536, 1978.

Gonfiantini, R., Stichler, W., and Rozanski, K.: Standards and Intercomparison Materials Distributed by the International Atomic Energy Agency for Stable Isotope Measurements, Vol. 825 of IAEA-TECDOC, 13–29, International Atomic Energy Agency, Vienna, 1995.

Gupta, P., Noone, D., Galewsky, J., Sweeney, C., and Vaughn, B. H.: Demonstration of high-precision continuous measurements of water vapor isotopologues in laboratory and remote field deployments using wavelength-scanned cavity ring-down spectroscopy (WS-CRDS) technology, Rapid Commun. Mass Spec., 23, 2534–2542, 2009.

Hsiao, G. Hoffnagle, J. Gkinis, V., Steig, E. J., Vaughn, B., Schoenemann, S. and Schauer, A: $^{17}O_{excess}$ measurements of water without fluorination using optical spectroscopy, Geophysical Research Abstracts, 14, EGU2012-6565, 2012.

Hodges, J. T. and Lisak, D.: Frequency-stabilized cavity ring-down spectrometer for high-sensitivity measurements of water vapor concentration, Appl. Phys. B., 85, 375–382, 2007.

Johnsen, S. J., Dansgaard, W., and White, J. W. C.: The origin of Arctic precipitation under present and glacial conditions, Tellus B, 41, 452–468, 1989.

Johnsen, S. J., Clausen, H. B., Dansgaard, W., Gundestrup, N. S., Hammer, C. U., and Tauber, H.: The Eem stable-isotope record along the GRIP ice core and its interpretation, Quaternary Res., 43, 117–124, 1995.

Jouzel, J., Masson-Delmotte, V., Cattani, O., Dreyfus, G., Falourd, S., Hoffmann, G., Minster, B., Nouet, J., Barnola, J. M., Chappellaz, J., Fischer, H., Gallet, J. C., Johnsen, S., Leuenberger, M., Loulergue, L., Luethi, D., Oerter, H., Parrenin, F., Raisbeck, G., Raynaud, D., Schilt, A., Schwander, J., Selmo, E., Souchez, R., Spahni, R., Stauffer, B., Steffensen, J. P., Stenni, B., Stocker, T. F., Tison, J. L., Werner, M., and Wolff, E. W.: Orbital and millennial Antarctic climate variability over the past 800 000 years, Science, 317, 793–796, 2007.

Kaiser, J.: Reformulated ^{17}O correction of mass spectrometric stable isotope measurements in carbon dioxide and a critical appraisal of historic "absolute" carbon and oxygen isotope ratios, Geochim. Cosmochim. Acta, 72, 1312–1334, 2008.

Kerstel, E. R. T.: Isotope ratio infrared spectrometry, Vol. 1 of Handbook of Stable Isotope Analytical Techniques, 759–787, Elsevier B. V., Amsterdam, 2004.

Kerstel, E. R. T., van Trigt, R., Dam, N., Reuss, J., and Meijer, H. A. J.: Simultaneous determination of the ^{2}H/^{1}H, ^{17}O/^{16}O and ^{18}O/^{16}O isotope abundance ratios in water by means of laser spectrometry, Anal. Chem., 71, 5297–5303, 1999.

Kerstel, E. R. T., Gagliardi, G., Gianfrani, L., Meijer, H. A. J., van Trigt, R., and Ramaker, R.: Determination of the ^{2}H/^{1}H, ^{17}O/^{16}O, and ^{18}O/^{16}O isotope ratios in water by means of tunable diode laser spectroscopy at 1.39 µm, Spectrochim. Ac. A, 58, 2389–2396, 2002.

Kerstel, E. R. T., Iannone, R. Q., Chenevier, M., Kassi, S., Jost, H. J., and Romanini, D.: A water isotope (^{2}H, ^{17}O, ^{18}O) spectrometer based on optical feedback cavity-enhanced absorption for in situ airborne applications, Appl. Phys. B, 85, 397–406, 2006.

Kurita, N., Newman, B. D., Araguas-Araguas, L. J., and Aggarwal, P.: Evaluation of continuous water vapor δD and δ^{18}O measurements by off-axis integrated cavity output spectroscopy, Atmos. Meas. Tech., 5, 2069–2080, doi:10.5194/amt-5-2069-2012, 2012.

Kusakabe, M. and Matsuhisa, Y.: Oxygen three-isotope ratios of silicate reference materials determined by direct comparison with VSMOW-oxygen, Geochem. J., 42, 309–317, 2008.

Landais, A., Barkan, E., and Luz, B.: Record of delta O-18 and O-17-excess in ice from Vostok Antarctica during the last 150 000 years, Geophys. Res. Lett., 35, L02709, doi:10.1029/2007GL032096 2008.

Lin, Y., Clayton, R. N., and Groening, M.: Calibration of δ^{17}O and δ^{18}O of international measurement standards – VSMOW, VSMOW2, SLAP, and SLAP2, Rapid Comm. Mass Spec., 24, 773–776, 2010.

Luz, B. and Barkan, E.: Variations of ^{17}O/^{16}O and ^{18}O/^{16}O in meteoric waters, Geochim. Cosmochim. Acta, 74, 6276–6286, 2010.

Masson-Delmotte, V., Jouzel, J., Landais, A., Stievenard, M., Johnsen, S. J., White, J. W. C., Werner, M., Sveinbjornsdottir, A., and Fuhrer, K.: GRIP deuterium excess reveals rapid and orbital-scale changes in Greenland moisture origin, Science, 309, 118–121, 2005.

Matsuhisa, Y., Goldsmith, J. R., and Clayton, R. N.: Mechanisms of hydrothermal crystallization of quartz at 250 °C and 15 kbar, Geochim. Cosmochim. Acta, 42, 173–182, 1978.

McKinney, C. R., McCreal, J. M., Epstein, S., Allen, H. A., and Urey, H. C.: Improvements in mass spectrometers for the measurement of small differences in isotope abundance ratios, Rev. Sci. Instrum., 21, 724–730, 1950.

Meijer, H. A. J. and Li, W. J.: The use of electrolysis for accurate δ^{17}O and δ^{18}O isotope measurements in water, Isotop. Environ. Health Stud., 34, 349–369, 1998.

Merlivat, L. and Jouzel, J.: Global Climatic Interpretation of the Deuterium-Oxygen 18 Relationship for Precipitation, J. Geophys. Res., 84, 5029–5033, 1979.

Miller, M. F.: Isotopic fractionation and the quantification of ^{17}O anomalies in the oxygen three-isotope system: an appraisal and geochemical significance, Geochim. Cosmochim. Acta, 66, 1881–1889, 2002.

Mook, W.: Environmental Isotopes in the Hydrological Cycle: Principles and Applications, Vol. I, IAEA, Unesco and IAEA, 2000.

Morville, J., Kassi, S., Chenevier, M., and Romanini, D.: Fast, low-noise, mode-by-mode, cavity-enhanced absorption spectroscopy by diode-laser self-locking, Appl. Phys. B, 80, 1027–1038., 2005.

Noone, D., Galewsky, J., Sharp, Z. D., Worden, J., Barnes, J., Baer, D., Bailey, A., Brown, D. P., Christensen, L., Crosson, E., Dong, F., Hurley, J. V., Johnson, L. R., Strong, M., Toohey, D., Van Pelt, A., and Wright, J. S.: Properties of air mass mixing and humidity in the subtropics from measurements of the D/H isotope ratio of water vapor at the Mauna Loa Observatory, J. Geophys. Res., 116, D22113, doi:10.1029/2011JD015773, 2011.

Petit, J. R., White, J. W. C., Young, N. W., Jouzel, J., and Korotkevich, Y. S.: Deuterium excess in recent Antarctic snow, J. Geophys. Res., 96, 5113–5122, 1991.

Risi, C., Landais, A., Bony, S., Jouzel, J., Masson-Delmotte, V., and Vimeux, F.: Understanding the ^{17}O excess glacial-interglacial variations in Vostok precipitation, J. Geophys. Res., 115, D10112, doi:10.1029/2008JD011535, 2010.

Rothman, L. S., Rinsland, C. P., Goldman, A., Massie, S. T., Edwards, D. P., Flaud, J.-M., Perrin, A., Camy-Peyret, C., Dana, V., Mandin, J.-Y., Schroeder, J., McCann, A., Gamache, R. R., Wattson, R. B., Yoshino, K., Chance, K. V., Jucks, K. W., Brown, L. R., Nemtchinov, V., and Varanasi, P.: The HITRAN spectroscopic database and HAWKS (HITRAN Atmospheric Workstation): 1996 edition, J. Quant. Spectrosc. Ra., 60, 665–710, 1996.

Sayres, D. S., Moyer, E. J., Hanisco, T. F., St Clair, J. M., Keutsch, F. N., O'Brien, A., Allen, N. T., Lapson, L., Demusz, J. N., Rivero, M., Martin, T., Greenberg, M., Tuozzolo, C., Engel, G. S., Kroll, J. H., Paul, J. B., and Anderson, J. G.: A new cavity based absorption instrument for detection of water isotopologues in the upper troposphere and lower stratosphere, Rev. Sci. Instrum., 80, 044102, doi:10.1063/1.3117349, 2009.

Schmidt, M., Maseyk, K., Lett, C., Biron, P., Richard, P., Bariac, T., and Seibt, U.: Concentration effects on laser-based δ^{18}O and δ^{2}H measurements and implications for the calibration of vapour measurements with liquid standards, Rapid Comm. Mass Spec., 24, 3553–3561, 2010.

Schoenemann, S. W., Schauer, A. J., and Steig, E. J.: Measurement of SLAP and GISP δ^{17}O and proposed VSMOW-SLAP normalization for ^{17}O$_{excess}$, Rapid Commun. Mass Spec., 27, 582–590, 2013.

Schoenemann, S. W., Steig, E. J., Ding, Q., Markle, B. R., and Schauer, A. J.: Triple water-isotopologue record from WAIS Divide Antarctica: controls on glacial-interglacial changes in $^{17}O_{excess}$ of precipitation, J. Geophys. Res., 119, doi:10.1002/2014JD021770, in press, 2014.

Steig, E.J., Gkinis, V, Schauer A.J., Hoffnagle, J., Tan, S., and Schoenemann, S.: Cavity ring-down spectroscopy for the high-precision analysis of the triple oxygen isotope composition of water and water vapor, Mineral. Magazine, 77, 2257, 2013.

Tan, S. M.: Wavelength measurement method based on combination of two signals in quadrature, Patent US7420686 B2, Picarro, Inc., 2008.

Urey, H. C.: The thermodynamic poperties of isotopic substances, J. Chem. Soc., 562–581, 1947.

Van Trigt, R., Meijer, H. A. J., Sveinbjornsdottir, A. E., Johnson, S. J., and Kerstel, E. R. T.: Measuring stable isotopes of hydrogen and oxygen in ice by means of laser spectrometry: the Bølling transition in the Dye-3 (south Greenland) ice core, Ann. Glaciol., 35, 125–130, 2002.

Varghese, P. L. and Hanson, R. K.: Collisional narrowing effects on spectral lines shapes measured at high resolution, Appl. Opt., 23, 2376–2385, 1984.

Vaughn, B. H., White, J. W. C., Delmotte, M., Trolier, M., Cattani, O., and Stievenard, M.: An automated system for hydrogen isotope analysis of water, Chem. Geol., 152, 309–319, 1998.

Vimeux, F., Masson, V., Jouzel, J., Petit, J. R., Steig, E. J., Stievenard, M., Vaikmae, R., and White J. W. C.: Holocene hydrological cycle changes in the Southern Hemisphere documented in East Antarctic deuterium excess records, Clim. Dynam., 17, 503–513, 2001.

Wassenaar, L. I., Ahmad, M., Aggarwal, P., van Duren, M., Poltenstein, L., Araguas, L., and Kurttas, T.: Worldwide proficiency test for routine analysis of δ^2H and δ^{18}O in water by isotope-ratio mass spectrometry and laser absorption spectroscopy, Rapid Commun. Mass Spec., 26, 1641–1648, 2012.

Werle, P.: Accuracy and precision of laser spectrometers for trace gas sensing in the presence of optical fringes and atmospheric turbulence, Appl. Phys. B, 102, 313–329, 2011.

Wu, T., Chen, W. D., Kerstel, E., Fertein, E., Gao, X. M., Koeth, J., Rossner, K., and Bruckner, D.: Kalman filtering real-time measurements of H_2O isotopologue ratios by laser absorption spectroscopy at 2.73 µm, Opt. Lett., 35, 634–636, 2010.

York, D.: Least squares fitting of a straight line with correlated errors, Earth Planet. Sci. Lett., 5, 320–324, 1969.

Young, E. D., Galy, A., and Nagahara, H.: Kinetic and equilibrium mass-dependent isotope fractionation laws in nature and their geochemical and cosmochemical significance, Geochim. Cosmochim. Acta, 66, 1095–1104, 2002.

Chapter 6

Seasonal and spatial variation of $^{17}O_{excess}$ and d_{excess} in Antarctic precipitation: insights from an intermediate complexity isotope model

In-preparation for the Journal of Geophysical Research

In this fourth paper, we use an intermediate complexity isotope model (ICM) to investigate the sensitivity of water isotope ratios in precipitation to climate variations in the Southern Hemisphere. Model improvements include the addition of $\delta^{17}O$, $^{17}O_{excess}$, and d_{ln}, and updates to the equilibrium fractionation factors for temperatures below zero and kinetic fractionation factors for evaporation over the ocean and condensation during snow formation. The ICM is forced with seasonal NCEP/DOE II reanalysis data for model boundary conditions. Experiments with perturbations to the surface temperature and humidity fields are used to investigate the isotopic sensitivity. We find that the response of $^{17}O_{excess}$ to a uniform temperature change is insignificant over the ocean, while there is a large magnitude response over the ice sheet, particularly in East Antarctica. A decrease of ocean surface relative humidity produces increased $^{17}O_{excess}$ and d_{excess}, with a coherent response over both the ocean and Antarctica. For interior East Antarctica, the model simulates a seasonal cycle in $^{17}O_{excess}$ that is positively correlated with $\delta^{18}O$ and of large magnitude (~50 per meg), consistent with the observations from Vostok. The seasonal cycle in $^{17}O_{excess}$ for West Antarctica is predicted to be considerably smaller in magnitude (~12 per meg), and is negatively correlated with $\delta^{18}O$. Over the ocean, the model predicts a seasonal cycle in $^{17}O_{excess}$ of ~8 per meg for the East Antarctic sector and only ~3 per meg for the West Antarctic sector, due in part to seasonal changes in ocean surface relative humidity and sea-surface temperatures. These changes are insufficient to explain the full amplitude of the simulated seasonal cycle over the continent or that observed in modern precipitation. The spatial differences in the response of $^{17}O_{excess}$ to local temperature reflect the balance of equilibrium and kinetic fractionation during snow formation en route. To capture the modern spatial distribution and seasonal variability of $^{17}O_{excess}$ and d_{excess} over the ice sheet, a higher sensitivity to temperature for supersaturated conditions (i.e., stronger kinetic effects) is required. We find that evaporative recharge is an important climatic process that moderates the variability of $^{17}O_{excess}$ and d_{excess} over the ocean. Evidence is provided that the process of kinetic fractionation during snow formation may not occur under purely molecular diffusive conditions, requiring a term that accounts for turbulence.

For this work, I modified the ICM to include $\delta^{17}O$, $^{17}O_{excess}$ and d_{ln}, updated the model fractionation factors, processed the NCEP reanalysis data for compatibility with the ICM, performed all the model simulations and sensitivity analyses, converted d_{excess} snow sample data to d_{ln} and normalized $^{17}O_{excess}$ ice core data to the VSMOW-SLAP scale, performed the model-data comparison, wrote the manuscript and interpreted the results, and made all the tables and figures. Eric Steig contributed valuable comments and overall improvements to the manuscript.

Seasonal and spatial variation of $^{17}O_{excess}$ and d_{excess} in Antarctic precipitation: insights from an intermediate complexity isotope model

Spruce W. Schoenemann and Eric J. Steig
IsoLab, Department of Earth and Space Sciences, University of Washington, Seattle, WA 98195, USA

Corresponding author: S. Schoenemann (schoes@uw.edu)

Abstract

The sensitivity of water isotope ratios ($^{17}O_{excess}$ and d_{excess}) in precipitation to climate variations in the Southern Hemisphere is investigated with an intermediate complexity isotope model (ICM) that incorporates updated equilibrium and kinetic fractionation factors for temperatures below zero. NCEP/DOE II reanalysis data, with permutations to the surface temperature and humidity fields, are used as model boundary conditions. Decreases in ocean surface relative humidity result in increased $^{17}O_{excess}$ and d_{excess}, with a uniform response over the ocean and Antarctic continent. The response of $^{17}O_{excess}$ to a global temperature change is insignificant over the ocean, but there is a significant $^{17}O_{excess}$ response to temperature change over the ice sheet, particularly in East Antarctica. The simulated seasonal cycle in $^{17}O_{excess}$ for interior East Antarctica is positively correlated with $\delta^{18}O$ and of large magnitude (~50 per meg), in agreement with observations at Vostok. The seasonal cycle in $^{17}O_{excess}$ for West Antarctica is predicted to be smaller in magnitude (~12 per meg) and of opposite sign. The $^{17}O_{excess}$ seasonal cycle over the ocean is only ~3 per meg for the West Antarctic sector and ~8 per meg for the East Antarctic sector, neither of which are large enough to explain the full seasonal changes over the ice sheet produced by the ICM or observed in ice cores. The sensitivity of $^{17}O_{excess}$ to local site temperature, and both the modern spatial distribution and seasonal variability of $^{17}O_{excess}$ and d_{excess} over the ice sheet, reflect the balance of equilibrium and kinetic fractionation during the formation of solid precipitation. To simulate the present-day $^{17}O_{excess}$ observations requires that the sensitivity of supersaturation to temperature to be relatively high. Evaporative recharge is also found to be an important process that moderates the variability of $^{17}O_{excess}$ and d_{excess} over the ocean. Evidence is provided that the simulation of kinetic fractionation during snow formation may require the inclusion of a term that accounts for turbulence.

1. Introduction

The stable water isotopic ratios in precipitation, as obtained from ice cores, ($\delta^{18}O$ and δD, collectively as δ), and the second order parameter d_{excess}, have provided useful tools for investigating paleoclimatic conditions. δ is expressed as

$$\delta^i = ({}^iR_{sample}/{}^iR_{reference}) - 1, \qquad \text{Eq. 1}$$

where ${}^2R = n({}^2H)/n({}^1H)$, ${}^{18}R = n({}^{18}O)/n({}^{16}O)$, ${}^{17}R = n({}^{17}O)/n({}^{16}O)$, and n refers to isotope abundance.

Deuterium excess as defined by *Dansgaard* [1964], is given by:

$$d_{excess} = \delta D - 8(\delta^{18}O) \quad \text{Eq. 2}$$

Measurements of d_{excess} from ice cores have been used to infer the vapor source-region temperature and humidity history and to correct the δ history for such source region effects, thereby isolating the local site conditions [*Cuffey and Vimeux*, 2001; *Vimeux et al.*, 2001a]. However, interpretation of d_{excess} as a source indicator is complicated by its strong sensitivity to both equilibrium and kinetic fractionation during transport, precipitation, and snow formation. The recent addition of $\delta^{17}O$ and accompanying ^{17}O excess,

$$^{17}O_{excess} = \ln(\delta^{17}O+1) - 0.528 \ln(\delta^{18}O+1) \quad \text{Eq. 3}$$

further complement the existing suite of isotopic indicators, permitting a more comprehensive investigation into characteristics of the global hydrological cycle. Although the use of $^{17}O_{excess}$ has become more prevalent, the factors that control its spatial and temporal variability are not fully understood, as evidenced by the evolving interpretation of $^{17}O_{excess}$ in polar climates [*Landais et al.*, 2008; *Risi et al.*, 2010; *Winkler et al.*, 2012; *Risi et al.*, 2013; *Winkler et al.*, 2013; *Schoenemann et al.*, 2014].

Most investigations into the climatic factors that control $^{17}O_{excess}$ have relied on Rayleigh distillation models with isolated air parcels or general circulation models (GCMs) enabled with isotopes [*Landais et al.*, 2008; *Risi et al.*, 2010; *Winkler et al.*, 2012; *Schoenemann et al.*, 2014]. While both approaches have aided in the interpretation of $^{17}O_{excess}$ variations, both have disadvantages. Rayleigh models lack important processes like evaporative recharge and atmospheric transport characteristics. GCMs incorporate important physical mechanisms and relevant climatological boundary conditions, which make them exceptional instruments for determining the response of isotopes to climatic changes. However, the complexity and coupled-nature of GCMs makes difficult the investigation of individual components of the isotopic distillation system. Intermediate complexity models (ICMs) are useful in providing a means to conduct simple experiments to gain both conceptual and quantitative understanding of the connections between large scale climate variations and the isotopic response of precipitation.

In this study we use an intermediate complexity model (ICM) of atmospheric water vapor transport and isotopic distillation initially developed by *Hendricks et al.* [2000] based upon work by *Fisher* [1991; 1992], and improved upon by *Kavanaugh and Cuffey* [2003] to investigate the influence of temporal and spatial variations of climate conditions over the annual cycle on $^{17}O_{excess}$ and d_{excess}. A study of this type has yet to be performed for $^{17}O_{excess}$. We evaluate the performance of the ICM by comparing model results to available measurements of $^{17}O_{excess}$ and d_{excess}.

1.2 Model Description

The ICM used here is that of *Kavanaugh and Cuffey* [2003] (hereafter KC03), which incorporates surface and atmospheric conditions to simulate water vapor transport and calculates the δ values of the ensuing precipitation. For a full description of the model, the reader is directed to *Hendricks et al.* [2000] , and *Kavanaugh and Cuffey* [2002; 2003]. The model calculates variations of δ to zonally averaged climate variables (temperature (T), precipitation (P), evaporation (E), water content (w), and surface relative humidity (rh)). An important aspect of the ICM is that it includes evaporative recharge of the low and middle latitude atmosphere with isotopically enriched vapor, which was found by *Hendricks et al.* [2000] to reduce the variability of isotopic values over the Antarctic ice sheet

compared to predictions by Rayleigh-type models. Model improvements by KC03 included kinetic effects for isotopic fractionation factors during evaporation and condensation, which are fundamental to the accurate depiction of d_{excess} behavior in cold regions. KC03 further modified the ICM to include both advective and diffusive transport mechanisms, with the partitioning controlled by a tuning parameter (f_k), determined by using values of diffusive (D_k) and advective (D_v) divergences over the subtropics from *Hartmann* [1994], and model tuning to match Antarctic isotope data [*Dahe et al.*, 1994].

1.3 Model Updates

We updated the KC03 ICM by incorporating the $H_2{}^{17}O$ isotopologue, allowing calculation of $\delta^{17}O$ and $^{17}O_{excess}$, and by using improved equilibrium and kinetic fractionation factors. The implementation of $\delta^{17}O$ into the ICM was accomplished by creating a second version of the ICM where all variables, parameters, and functions pertaining to δD were replaced by those for $\delta^{17}O$, including the associated fractionation factors. We revised the isotopic fractionation factors during evaporation and condensation based on studies by *Uemura et al.* [2005; 2010] and *Ellehøj et al.* [2013]. The most important of these are the kinetic fractionation factors of oxygen-18 and deuterium for solid precipitation, the kinetic fractionation factor during ocean evaporation, and equilibrium fractionation factors for δD and $\delta^{18}O$ at temperatures below freezing.

Isotopic fractionation during evaporation and condensation are given as follows. The isotopic composition of vapor evaporated from the ocean surface is determined by the total fractionation factor for each isotopic species, calculated as the product of an equilibrium fractionation factor, α_{eq}, and a kinetic fractionation parameter that accounts for the boundary-layer process of vapor transport (i.e., molecular diffusion and turbulence). For the non-equilibrium fractionation, we use the term k for the kinetic fractionation parameter for evaporation over the ocean and α_{kin} for the kinetic process of snow formation. Note that terms α_{kin} and $k + 1$ are sometimes used interchangeably, but their values may be different. The total fractionation factors for each process are then given by $\alpha_{tot} = (k+1)\alpha_{eq}$ (ocean evaporation) or $\alpha_{tot} = \alpha_{kin}\alpha_{eq}$ (snow formation).

As in KC03, we use the liquid-vapor equilibrium fractionation factors for deuterium ($^2\alpha_{eq} = n(HD^{16}O)_l / n(H_2{}^{16}O)_v$) and oxygen-18 ($^{18}\alpha_{eq} = n(H_2{}^{18}O)_l / n(H_2{}^{16}O)_v$) from *Horita and Wesolowski* [1994], for ocean surface temperatures above freezing, where l = liquid, v = vapor:

$$^{18}\alpha_{eq} = \exp[(-7.685 + (6.7123(10^3/T)) - (1.6664(10^6/T^2)) + (0.3504(10^9/T^3)))/10^3] \quad \text{Eq. 4}$$

$$^{2}\alpha_{eq} = \exp[(1158.8(T^3/10^9) - 1620.1(T^2/10^6) + 794.84(T/10^3) - 161.04+2.9992(10^9/T^3))/10^3] \quad \text{Eq. 5}$$

The value of k, for evaporation at the ocean surface, is poorly constrained, as it depends both on the molecular diffusivities D of the different water isotopologues in air, and on turbulence in the boundary layer at the ocean surface. The usage of k is inconsistent in the literature: it is often referred to in terms of a pure theoretical diffusivity fractionation factor, α_{diff}, following *Merlivat and Jouzel* [1979]: with $k = \alpha_{diff} - 1 = D/D^*$ where D and D^* refer to the molecular diffusivity in air of the light and heavy isotopologues, respectively. However, α_{diff} is also used to describe the combination of diffusion and turbulence (e.g., [*Cappa et al.*, 2003; *Barkan and Luz*, 2007; *Uemura et al.*, 2008; *Luz and Barkan*, 2010; *Uemura et al.*, 2010], in which case $\alpha_{diff} = [D/D^*]^n$, where n is a parameter that ranges from 0 (complete turbulent diffusion) to 1 (pure molecular diffusion). To avoid confusion, we use $^{18}\alpha_{diff}$ and

$^{2}\alpha_{diff}$ to refer to the theoretical values for oxygen-18 and deuterium fractionation for pure molecular diffusion, and $^{18}\alpha^{*}_{diff}$ and $^{2}\alpha^{*}_{diff}$ to refer to observed, *effective* diffusivity fractionation factors that account for both diffusion and turbulence. Thus $k_{18} = {}^{18}\alpha^{*}_{diff} - 1$ and $k_D = {}^{2}\alpha^{*}_{diff} - 1$.

In GCMs, k is normally parameterized following *Merlivat and Jouzel* [1979] (hereafter MJ79), who determined k as function of 10 meter wind speed (u_{10m}) based on wind tunnel experiments by *Merlivat* [1978b] and on the theoretical evaporation model of *Brutsaert* [1975]. In simpler isotope models, the value of k is generally held constant, since changes in wind speed cannot be explicitly accounted for [*Gat*, 1996; *Cappa et al.*, 2003]. Here, we also assume that k is constant, following KC03. We use values based on recent isotopic measurements from water vapor samples collected over the Southern Ocean by *Uemura et al.* [2008; 2010]. The initial value of $^{18}\alpha^{*}_{diff}$ reported by *Uemura et al.* [2010] was 1.0083 ± 0.18 (1σ), determined by minimizing the root mean square error (RMSE) between calculated and observed $\delta^{18}O$ and $\delta^{17}O$ data. Later, the $^{18}\alpha^{*}_{diff}$ value was updated to 1.0096 by *Luz and Barkan* [2010], to account for the difference of $^{17}O_{excess}$ in seawater with respect to VSMOW of –5 per meg. This value provides the current best estimate of kinetic fractionation during evaporation over the open ocean, where the influences of turbulence are inherent in the measured value. To calculate k_D, we use the relationship of the diffusivities ϕ_{diff} (for δD and $\delta^{18}O$) $= \ln(^{2}\alpha_{diff})/\ln(^{18}\alpha_{diff}) = 0.88$ from *Merlivat* [1978a]. Note that our values for k_{18} (0.0096) and k_D (0.0084) are considerably greater than those used by KC03 ($k_{18} = 0.006$ and $k_D = 0.00528$). To determine k_{17} we use the ratio of the experimentally derived molecular diffusivities ϕ_{diff} (for $\delta^{17}O$ and $\delta^{18}O$) $= \ln(^{17}\alpha_{diff})/\ln(^{18}\alpha_{diff}) = 0.518$ from *Barkan and Luz* [2007], which gives $k_{17} = (k_{18}+1)^{0.518} - 1 = 0.00496$.

For the condensation of precipitation, the isotopic fractionation of rain droplets is assumed to occur under equilibrium conditions and is calculated using the equilibrium fractionation factors from *Horita and Wesolowski* [1994] (see Eq. 5 above). For the fractionation of water vapor during condensation below freezing (the ice-vapor equilibrium fractionation values for $^{2}\alpha_{eq}$ and $^{18}\alpha_{eq}$), we use values obtained recently by *Ellehøj et al.* [2013] rather than the values of *Majoube* [1971] as used in KC03. The choice of equilibrium fractionation factors between *Majoube* [1971] and *Ellehøj et al.* [2013] significantly influences d_{excess}, but has little influence on the sensitivity of $^{17}O_{excess}$, for which the equilibrium fractionation factors are given by the power law relationship of $^{17}\alpha_{eq} = (^{18}\alpha_{eq})^{0.529}$.

Kinetic fractionation between vapor and ice during snow formation is calculated as:

$$\alpha_{kin} = S_i/(1 + \alpha_{eq}(\alpha^{*}_{diff})(S_i - 1)) \qquad \text{Eq. 6}$$

where S_i is the supersaturation ratio over ice within the condensing air mass. The supersaturation ratio with respect to ice is defined as $(e/e_{si} - 1)$, where the water vapor pressure in the air is e, and e_{si} is the saturation vapor pressure over ice at the temperature of the air. We use the formulation of *Jouzel and Merlivat* [1984] where the supersaturation ratio is linearly related to the cloud condensation temperature T_{cond} such that $S_i = c - FT_{cond}$ (T_{cond} in degrees Celsius). The coefficient c represents the initial supersaturation (e.g., 1.00 for 100 %) and F represents the temperature dependence of the supersaturation ratio between total water (supercooled water droplets and vapor) and saturated vapor pressure over ice. In the polar regions, the presence of ice particles in a cloud produce an environment where vapor deposition occurs in supersaturated conditions with respect to ice (i.e., $(e/e_{si} - 1)\times 100 >$ 100 % ice saturation, which often occurs largely below water saturation (100 % RH)). For the same temperature, the saturation vapor pressure over ice is less than over water, which results in the preferential growth of ice crystals at the expense of supercooled water droplets. Due to extremely low temperatures in Antarctica, droplet formation and subsequent freezing are unlikely, and thus the snow is formed primarily through the mechanism of vapor deposition [*Jouzel and Merlivat*, 1984]. As

temperatures decrease, both the supersaturation with respect to ice and the ice nuclei concentrations increase, providing more abundant deposition nuclei for ice to form directly from the vapor phase [*Wallace and Hobbs*, 2006]. This diffusive process favors the preferential deposition of $H_2{}^{17}O$ onto the ice particle, leaving the remaining vapor enriched in $H_2{}^{18}O$ relative to the global meteoric water line (GMWL = 0.528). As ice deposition proceeds into the Antarctic interior, the $^{17}O_{excess}$ of the vapor is progressively lowered, eventually resulting in lower $^{17}O_{excess}$ of the snow/ice particles. Once these particles are deposited on the ice sheet surface, the process of sublimation is not thought to fractionate isotopes [*Neumann and Waddington*, 2005].

As for k, the values for effective diffusion fractionation factors (α^*_{diff}) during snow formation are not well constrained. *Jouzel and Merlivat* [1984] assumed that the process of water vapor diffusing to the ice crystal surface to form snow occurs under conditions of pure molecular diffusion. This assumption was based on results from frost grown onto a cooling plate (–20˚C) from room temperature (20˚C). However, this study was performed under conditions that did not control for the supersaturation ratio and did not take into account the possible influence of turbulence during frost formation. Recent work by *Uemura et al.* [2005] produced experimental conditions that are thought to more accurately represent those of mixed clouds in which both vapor and supercooled water droplets coexist. They also accounted for turbulence during snow formation. Their experiment produced lower supersaturation ratios and suggested weaker kinetic fractionation than observed by *Jouzel and Merlivat* [1984]. The supersaturation ratios determined by *Uemura et al.* [2005] for cloud condensation temperatures of –13˚C (S_i = 1.165) and –18˚C (S_i = 1.221) are significantly lower than the estimated value of *Jouzel and Merlivat* [1984] (S_i = 2.00). Matching the supersaturation ratios determined by *Uemura et al.*[2005] with the linear relation $S_i = c - FT$ requires F = 0.011 (given c = 1). This is a significantly greater value for F than is than is commonly cited in the literature [*Petit et al.*, 1991; *Hoffmann et al.*, 1998; *Schmidt et al.*, 2005; *Landais et al.*, 2008; 2012b].

In the parameterization of α_{kin}, greater supersaturation (S_i) values require a commensurate reduction in the α^*_{diff} value to produce reasonable values of α_{kin} and still match isotopic data. The results of *Uemura et al.* [2005] thus provide reason to question the assumption that the process of snow formation occurs under purely molecular diffusive conditions, and implies that the effective diffusion fractionation factors are lower than is usually assumed. Previous modeling studies, including KC03, have used the pure molecular diffusion values ($^{18}\alpha_{diff}$ = 1.0285) and ($^{2}\alpha_{diff}$ = 1.0251) from *Merlivat* [1978a].

To determine an optimal model value for $^{18}\alpha^*_{diff}$, we evaluated the effect of different values of $^{18}\alpha^*_{diff}$ and S_i on the spatial gradient in $^{17}O_{excess}$, as observed in Antarctic snowfall [*Schoenemann et al.*, 2014]. Note that the coefficient F controls the temperature-dependence of S_i, and therefore is most relevant to the following sensitivity analysis, while c is assumed to be at saturation (i.e., c =1). For calculating α_{kin} during snow formation in the ICM, we tested a range of $^{18}\alpha^*_{diff}$ values from 1.0096 (molecular diffusion with turbulence) to 1.0285 (pure molecular diffusion) with a range of F values used in previous studies (F = 0.002 to 0.008), and then determined the corresponding change in $^{17}O_{excess}$ between –30 and –55˚C (Table 1). The lower $^{18}\alpha^*_{diff}$ value is identical to the effective diffusion fractionation value used over the ocean during evaporation (k_{18} +1 = 1.0096), and was chosen as a plausible low-end estimate of turbulent processes within a cloud. Although any range of diffusion fractionation factors between pure molecular diffusion and pure turbulence are possible in principle, we found that the combination of low $^{18}\alpha^*_{diff}$ values (e.g., 1.0096) and a high sensitivity of supersaturation to temperature (e.g., F = 0.008) produced more realistic $^{17}O_{excess}$ gradients that were also less sensitive to small adjustments in F (Table 1). Compared to the pure molecular diffusion value ($^{18}\alpha_{diff}$ = 1.0285) used previously by KC03, our value ($^{18}\alpha^*_{diff}$ = 1.0096) represents a process that is

approximately 35% diffusive, or in terms of the turbulence parameter *n,* a value of $n = 0.34$. As for k, to calculate values of ${}^{2}\alpha^{*}_{diff}$ we use the relationship of the kinetic fractionation factors given by $\phi_{diff} = 0.88$ from *Merlivat* [1978a] and confirmed by *Luz et al.* [2009], where ${}^{2}\alpha^{*}_{diff} = ({}^{18}\alpha^{*}_{diff})^{0.88}$. We note that the choice of ϕ_{diff} of 0.88 from *Merlivat* [1978a] or 0.52 from that of *Cappa et al.* [2003] has only a minor effect on the results, lowering d_{excess} and d_{ln} by only about 1 ‰ for even the most depleted $\delta^{18}O$ values.

2. Observational Data Sets

KC03 examined two hypothetical water-vapor transport paths that both approach central East Antarctica. The term "path" refers to a specified spatial distribution of climate variables, zonally averaged over a particular geographic zone and timeframe, and is expressed as a function of latitude. The first path (Path 1) is that used by *Hendricks et al.* [2000] which begins in the southern Pacific Ocean, travels along the Antarctic Peninsula and crosses Antarctica from the west to the central East Antarctic Plateau. The second path (Path 2) originates over the southeastern Indian Ocean and reaches East Antarctica directly from the north, following the path taken during the 1990 International Trans-Antarctica Expedition [*Dahe et al.*, 1994]. We include Path 1 (not shown) and Path 2 in order to ensure that our calculations are consistent with those of KC03.

We define two additional transport paths that include a more representative spatial area for the moisture source regions contributing to precipitation at Vostok (78.47˚S, 106.87˚E) and WAIS Divide (79.47˚S, 112.09˚W). We use the reanalysis products from National Center for Environmental Prediction/Department of Energy (NCEP/DOE) II ([*Kanamitsu et al.*, 2002], hereafter referred to as NCEP2) covering the period from 1979 to 2011 to investigate how the spatial and temporal variations in the climate fields influence the seasonal cycle of modeled water isotopes. For the East and West Antarctica sectors, the longitudinal ranges are based on the back trajectories derived from the Lagrangian particle transport model FLEXPART results of [*Sodemann and Stohl*, 2009]. The East Antarctic sector is similar to Path 2 used by KC03, but rather than a single longitude, the "path" comprises a broader longitudinal range from 0˚E to 120˚E. The West Antarctica sector spans longitudes between 70˚W and 150˚W. These longitude ranges are slightly narrower than the 1σ range given in *Sodemann and Stohl* [2009], but centered on the same mean moisture source longitudes determined in that study for Vostok (~60˚E) and Byrd (~105˚W). The reduced longitude ranges should not have significant consequences, since most climate parameters of the mid-latitude and polar oceans are zonally fairly uniform. Both paths originate in the low-latitudes (27˚S) and end at the latitude of their respective ice core site (Figure 1). The low-latitude limit is identical to that used in KC03, and represents the average peak evaporation latitude band where moisture divergence is directed poleward.

The climate parameters required as inputs for the ICM are sea-surface/skin temperature (SST, in ˚C), entire atmospheric column water content (mm), precipitation rate (mm a^{-1}), evaporation rate (mm a^{-1}), and relative humidity (%). As no surface evaporation rate data are available for NCEP2, the latent heat flux is used instead, converted to an evaporation rate using the latent heat of vaporization (2.26×10^{6} J/kg) over the oceans and the latent heat of sublimation (2.838×10^{6} J/kg, [*Bromwich et al.*, 2011]) over the Antarctic continent. For simplicity of calculation we set the latitudinal boundary between the latent heat of vaporization and sublimation at 73˚S and 66˚S, for the West and East path, respectively. This simplification has little impact on the resulting evaporation rate calculations, and provides results that are consistent with ECMWF ERA-Interim evaporation rates for the Southern Hemisphere. The NCEP2 data are calculated as monthly averages for each parameter and then zonally averaged over latitude and longitude for each respective path. Note that the zonal averaging tends to reduce the meridional temperature gradients compared to that for a single longitude like that used for Path 2. In

Figure 2 we show a seasonal average for austral winter (JAS) and summer (DJF), based on the monthly reanalysis data, as an example of the range of climate variables with respect to latitude.

To evaluate the performance of the ICM, we compared the mean annual paths to a number of Antarctic isotopic data sets that include mean annual d_{excess} and $^{17}O_{excess}$ measurements. As in KC03, we used the $\delta^{18}O$, δD and d_{excess} data obtained from the 1990 International Trans-Antarctica Expedition traverse that spans both West and East Antarctica [*Dahe et al.*, 1994]. To obtain the d_{ln} values, the same $\delta^{18}O$ and δD data are converted into the logarithmic form as proposed by *Uemura et al*. [2012] and described in detail by *Schoenemann et al.* [2014] . To make direct comparisons with the West and East Antarctic paths, we used select isotopic measurements from the Antarctic-wide compilation of *Masson-Delmotte et al.* [2008] that were located within the respective West and East Antarctic sectors. We only included the isotopic data (for $\delta^{18}O$, δD, and d_{excess}) that had latitude, longitude, and temperature information associated with them. For $^{17}O_{excess}$, we used the compilation of present-day measurements from Antarctic ice core sites from *Schoenemann et al.* [2014]. West Antarctic sites include $^{17}O_{excess}$ from Siple Dome and WAIS Divide; coastal East Antarctic sites include D57 and Taylor Dome, and interior East Antarctic sites include Dome F, Dome C, and Vostok (Figures 2 and 3). We use the difference in the $^{17}O_{excess}$ between the marine-influenced sites and the East Antarctic plateau to define the spatial gradient in $^{17}O_{excess}$. The decrease in $^{17}O_{excess}$ is 24 to 33 per meg, for a change in $\delta^{18}O$ from –33.8 ‰ (WAIS Divide) to –56.5 ‰ (Vostok) [*Schoenemann et al.*, 2014]. For ICM comparisons with the seasonal d_{excess} and $^{17}O_{excess}$ variability at Vostok we use the event-based precipitation data from the study of *Landais et al.* [2012a], and for WAIS Divide we use $^{17}O_{excess}$ data we obtained from water samples provided by S. Rupper, from the Satellite Era Accumulation Traverse (SEAT) 2011–3 firn core (latitude: 78˚43.7`S, longitude: 114˚43.9`W), using methods described in *Steig et al.*[2014]. All $^{17}O_{excess}$ values are normalized to the VSMOW-SLAP scale as in *Schoenemann et al.* [2014]. Note that some earlier studies did not normalize to VSMOW-SLAP and therefore the values presented here will be different from the previously published data.

3. Model Calibration and Application

Here, we use the same climate paths as in *Kavanaugh and Cuffey* [2003] to calibrate the updated ICM and to compare with results from the annual-averaged East and West paths. To aid in the interpretation of d_{excess} and provide an additional isotope constraint, we include the natural log definition of d_{excess}, denoted d_{ln}, defined by *Uemura et al.* [2012] as:

$$d_{ln} = \ln(\delta D+1) - (-2.85 \times 10^{-2} (\ln(\delta^{18}O+1))^2 + 8.47(\ln(\delta^{18}O +1)) \quad \text{Eq. 7}$$

To calibrate the ICM to the isotopic data there are five tunable parameters that can be adjusted, for each isotope ratio of interest. These are: the ocean surface water isotopic composition at the low-latitude limit, the initial $\delta^{18}O$, $\delta^{17}O$ and δD composition of atmospheric vapor (calculated in the ICM from assigned values of the average isotopic composition of precipitation), the fraction of high-latitude eddy diffusive transport (f_k), and the cloud supersaturation coefficients c and F. We keep the oceanic surface water isotopic composition at 0 ‰ with respect to VSMOW for all the isotope ratios, but this can be varied to reflect glacial-interglacial changes or localized source conditions. The atmospheric $\delta^{18}O$, $\delta^{17}O$, and δD for the low-latitude limit are calculated (accounting for surface *rh* and SST) from the $\delta^{18}O$, d_{excess}, and $^{17}O_{excess}$ from prescribed values of precipitation. The values used here for the precipitate composition are the same as in KC03 for $\delta^{18}O = -3.0$ ‰, $\delta D = -14.0$ ‰, and $d_{excess} = +10.0$ ‰, and we use the value of $^{17}O_{excess} = 33$ per meg from the compilation of meteoric waters by [*Luz and Barkan*, 2010]. We back-calculated the $\delta^{17}O = -1.552$ ‰ based on the $^{17}O_{excess}$ and $\delta^{18}O$ precipitation

values above. We set the ratio of high-latitude eddy-turbulence to advective transport (f_k) to be 0.65 following KC03.

The coefficients of cloud supersaturation (c = 1.04 and F = 0.003) determined by KC03 were based on tuning to match Antarctic isotopic data using the older fractionation factors and therefore are no longer consistent with the updated equilibrium and kinetic fractionation factors described in the Model Updates section. To determine new best-fit supersaturation values of c and F, we use the Path 2 climate inputs and observational data. We emphasize that the supersaturation fit is dependent on the choice of molecular diffusivities during snow formation (discussed earlier); however, any combination of diffusivities and supersaturation coefficients chosen must reproduce the present-day spatial gradient of $^{17}O_{excess}$ and still be consistent with d_{excess} and d_{ln}. Because KC03 did not include $^{17}O_{excess}$, we first compare the updated Path 2 d_{excess} and d_{ln} with the isotopic measurements of *Dahe et al.* [1994] and the original KC03 results. In order to improve the agreement between the ICM and data, the coefficients for the supersaturation function (c and F) are tuned to visually fit both the d_{ln} and d_{excess} data. Recall that the value of c controls the magnitude of the initial supersaturation (i.e., the intercept) and therefore adjustment of c is typically set at 1.00 (i.e., 100% saturated) [*Landais et al.*, 2008; *Luz and Barkan*, 2010; *Steen-Larsen et al.*, 2011; *Landais et al.*, 2012a; 2012b]. As recommended by *Kavanaugh and Cuffey* [2003], to evaluate the goodness-of-fit of the ICM, we compare the water isotope parameter of interest (d_{excess}, $d_{ln,}$ $^{17}O_{excess}$) to the total distillation (for which $\delta^{18}O$ is a proxy), rather than to external variables like T or latitude (Figures 3 and 4). The best model-data agreement for both d_{excess} and d_{ln} occurs when using a high sensitivity of supersaturation to temperature where F = 0.01, when c = 1.0

We then use c = 1.0 and F = 0.01 determined from above to calibrate $^{17}O_{excess}$. When we use such a value of F for $^{17}O_{excess}$ in Path 2, the spatial gradient for $^{17}O_{excess}$ is greatly overestimated. Next we tried progressively lower values of F to improve the $^{17}O_{excess}$–data fit. We found that a lower sensitivity (still relatively high) of F = 0.007 better fits the $^{17}O_{excess}$ data. To reconcile the difference between the two possible values of F an average could be taken; however, because the slope of $^{17}O_{excess}$ is considerably more sensitive to F than that for d_{excess}, we choose to use $^{17}O_{excess}$ as the primary benchmark for the tuning of supersaturation.

While the use of $S_i = 1.00–0.007T$ does not produce a sufficient depletion of $\delta^{18}O$ relative to d_{excess} and d_{ln}, the mean annual d_{excess} (d_{ln}) value at the end of the Path 2 remains within the upper bound of the measured isotopic values (Figures 3 and 4). The somewhat different best-fit value of F for $^{17}O_{excess}$ and d_{excess} (or d_{ln}) is not ideal, and suggests an incomplete understanding of the relationship among supersaturation, temperature, and isotope fractionation. However, these results also highlight the added benefit of having $^{17}O_{excess}$ as an extra constraint on the ICM that was not available to KC03. To our knowledge, this is the first time that $^{17}O_{excess}$ has been used in tandem with d_{excess} and d_{ln} to constrain the supersaturation coefficients and the relationship between supersaturation and molecular diffusivities.

The ICM results acquired by using the NCEP2 reanalysis data for the mean annual East path using the same model tuning parameters of c = 1.0 and F = 0.007 are then compared to the calibrated Path 2. To better evaluate the model-data fit for the East and West path d_{excess} and d_{ln}, we include additional isotopic observations from *Masson-Delmotte et al.* [2008] specific to each path that provide much greater spatial coverage in $\delta^{18}O$–d_{excess} space than the data set for Path 2 used previously from *Dahe et al*. [1994] (Figure 4). Compared to the *Masson-Delmotte et al.* [2008] data, the East path d_{excess} and d_{ln} are more enriched relative to the depletion of $\delta^{18}O$ than for Path 2. Both the East path and Path 2 mean $^{17}O_{excess}$ values in coastal Antarctica are higher than observations, but the East path produces a lower spatial gradient in $^{17}O_{excess}$ that better matches the coastal-to-interior change in $^{17}O_{excess}$ data (Figures 3 and 4). Adjustment of the initial $^{17}O_{excess}$ precipitation value at the low-latitude limit could improve the

model-data offset, but the $^{17}O_{excess}$ value must also be consistent with the surface relative humidity. Here we have offset the entire NCEP2 relative humidity field (*rh* + 10%) to be in agreement with the relative humidity values as used in KC03, which also produces closer equilibrium between the model $^{17}O_{excess}$ and surface *rh*. Comparison of the West path with $^{17}O_{excess}$ measurements in coastal/West Antarctica confirms a similar positive $^{17}O_{excess}$ offset between the ICM and data as found for the East path (Figure 4).

4. Results: Numerical Experiments

We use perturbation experiments to investigate the sensitivity of $^{17}O_{excess}$, d_{excess} and d_{ln} to relative humidity and sea surface temperature changes. The results obtained by adjusting relative humidity or surface temperatures (ocean and ice sheet) are compared to the results for the mean annual climate of the West and East paths. We employ the insights gained from these model perturbation experiments to evaluate results from seasonal cycle experiments.

4.1 Relative humidity

The relative humidity in the boundary layer at the ocean surface controls the moisture gradient between the ocean surface and the overlying unsaturated vapor, which determines the molecular diffusive transport of water isotopes from the saturated surface layer to drier atmospheric air. Increases in *rh* will reduce the importance of kinetic fractionation, lowering $d_{excess,}$ d_{ln} and $^{17}O_{excess}$ ([*Merlivat and Jouzel*, 1979; *Barkan and Luz*, 2007]. Additionally, d_{excess} and d_{ln} in marine vapor is controlled by the SST through the temperature dependence of α_{eq} (which should not to be confused with the temperature dependence of *rh* on SST). Based on a global-scale closure assumption, the isotopic model of *Merlivat and Jouzel* [1979] predicts a relationship between d_{excess} in vapor with *rh* of –0.43‰/% and SST of 0.35 ‰/˚C. While this estimation is useful for understanding the relationship between d_{excess} and ocean surface conditions, the effects of wind speed on evaporation and the subsequent process of precipitation and snow formation in the polar regions complicates the interpretation of d_{excess} in ice cores as a source region proxy [*Petit et al.*, 1991; *Vimeux et al.*, 2001a].

To investigate the effect of relative humidity changes on $^{17}O_{excess}$, d_{excess}, and d_{ln}, we apply both a global reduction and a global increase of 5 and 10% in relative humidity. No other changes are imposed in the model. We perform the experiments for both the East and West path to determine if spatial differences in ocean surface conditions influence the sensitivity of the isotope parameters. In KC03, the relative humidity field was linearly related to the SST field, where $rh = 0.9 - 0.005T$ with T in ˚C. Here, we use the relative humidity field derived from the monthly mean annual NCEP2 reanalysis data for each respective path. Note that in the ICM the relative humidity field is considered only during evaporation (i.e., only over the ocean with a SST cutoff of –3.6˚C). For the East path the 5 and 10% reductions in relative humidity result in uniform increases of $^{17}O_{excess}$ over the ice sheet of 8 and 15 per meg, respectively, while an increase in relative humidity has an equal and opposite effect (Figure 5). Over the ocean, the $^{17}O_{excess}$ response increases moderately with latitude from the initial source region for both the East and West path, reaching "equilibrium" in the mid-latitudes (45 to 60˚S) (Figure 5). Our calculations for the East path produce a sensitivity of $^{17}O_{excess}$ to relative humidity of –1.4 per meg/% over the mid-latitude region, which increases slightly to –1.5 per meg/% over the ice sheet. For the West path, reductions in relative humidity of 5 and 10% produce $^{17}O_{excess}$ values that increase by 7 and 14 per meg over the ice sheet. The sensitivity of $^{17}O_{excess}$ to relative humidity is therefore only slightly lower than for the East path; –1.2 per meg/% and –1.4 per meg/% for the ocean and the ice sheet, respectively. These values are somewhat higher but reasonably consistent with previous (Single Column Model-based) estimates of –1.0 per meg/% from *Risi et al.* [2010].

The global 5 and 10% reductions in relative humidity produce similar patterns of response for d_{excess} and d_{ln}, with mostly spatially uniform increases in both parameters. As for $^{17}O_{excess}$, the response in d_{excess} and d_{ln} is slightly greater for the East path than West path. Calculations for the East path give a sensitivity of d_{excess} to relative humidity change of –0.50 ‰/% over the ocean and –0.53 ‰/% over the ice sheet. For the West path, the d_{excess} sensitivity is lower over the ocean (–0.42 ‰/%) and ice sheet (–0.49 ‰/%). Contrary to d_{excess}, the response of d_{ln} to the change in relative humidity gradually increases between the mid-latitude ocean and ice sheet. This is true for both the East and West path. The d_{ln} sensitivity is –0.58 ‰/% over the ocean (45 to 60˚S) and –0.77 ‰/% over the ice sheet (78˚S) for the East path, and –0.49 ‰/% and –0.63 ‰/% for the West path (80˚S). The isotopic sensitivity of d_{excess} to the prescribed relative humidity changes is similar to the results of KC03 who obtained an average value of –0.4 ‰/% despite using different relative humidity fields.

4.2 Surface Temperature

Spatial Variation of Isotopic Sensitivity

We use the ICM to examine the isotopic response $\Delta(^{17}O_{excess}$, d_{excess} and $d_{ln})$ to local climatic temperature change ΔT at the site of interest (i.e., the ice core sites: Vostok and WAIS Divide) on the ice sheet. The isotopic response to temperature has been shown to depend on geographic location, with smaller responses at the continental margin and larger responses in the interior [*Hendricks et al.*, 2000; *Kavanaugh and Cuffey*, 2003]. We designed four simple experiments. The first two experiments applied a global ± 5˚C change to the surface temperature field; hereafter referred to as experiments Minus5 and Plus5. For these experiments a ± 5˚C change was applied to the high-latitude core site (78˚S and 80˚S for the East and West path, respectively) with a magnitude that diminished to 0˚C at the low-latitude limit as shown in Figures 6a and 6b. We refer to these experiments as Minus5-0 and Plus5-0. This design mimics the effects of polar amplification, where the high latitude sites warm or cool considerably more than the mid to low-latitude regions. To isolate the effect of surface temperature we hold the relative humidity field constant, and P and E are unchanged. Note that if the rh is constant, then the water content w must be allowed to adjust to the temperature change.

The results for the East and West path are shown in Figure 6. The top panel shows the prescribed change in temperature for each path, the solid lines represent the cooling or warming over the entire model domain (Minus5 and Plus5 experiments), and the short-dashed lines for the Minus5-0 and Plus5-0 experiments. We calculate the temporal (i.e., not spatial isotopic gradients) isotopic sensitivity, defined as $\gamma = \partial\delta/\partial T$ (as in KC03), for $\gamma\delta^{18}O$, $\gamma^{17}O$, γd_{xs} and γd_{ln} over the entire model domain for both paths. Note that in Figure 6 we truncate the latitudes, displaying only 40˚S to 80˚S to focus on changes in the mid-latitude source regions and Antarctic continent.

The isotopic sensitivity, $\gamma\delta^{18}O$, displays the characteristic response of increasing sensitivity toward high latitudes for both the East and West paths, with a stronger sensitivity for the East path. In general, the Plus5 and Minus5 experiments produce a nearly identical γ over the ocean regions for each isotopic parameter, with the main differences in sensitivity occurring over the ice sheets. For the East and West path, the response of $\gamma\delta^{18}O$ is higher when the equator-to-pole temperature gradient is altered (dashed lines), producing similar isotopic sensitivity for both increases (Minus5-0) and decreases (Plus5-0) in the temperature gradient. The major differences in isotopic sensitivity between the East and West path occur for $^{17}O_{excess}$ and d_{excess}. For $^{17}O_{excess}$, the response of $\gamma^{17}O$ is anticorrelated with $\gamma\delta^{18}O$ for the West path throughout the model domain, while for the East path $\gamma^{17}O$ switches from anticorrelated to positively correlated southward of ~75˚S. In Figure 6e, the near overlap of the solid and short-dashed lines for both sets of experiments indicates the dominance of site temperature (through the temperature-dependent parameterization of supersaturation, S_i) in controlling the response of $^{17}O_{excess}$

for the East Path. This is not the case for the West Path, which suggest that ice-vapor kinetic fractionation plays a weaker role in West Antarctica, where temperatures are generally higher. The larger $\gamma^{17}O$ for the colder experiments (Minus5, Minus5-0) for the East path is also indicative of the strong effect of kinetic fractionation on $^{17}O_{excess}$ in extremely cold conditions. At Vostok, $\gamma^{17}O$ reaches values of 4.5 per meg/˚C for the cooling experiments, while at WD the average $\gamma^{17}O$ is about –1 per meg/˚C. The relatively constant and minimal mean $\gamma^{17}O_{excess}$ (–0.44 and –0.28 per meg/˚C) for both the East and West paths over the oceans indicates that $^{17}O_{excess}$ is less sensitive to changes in ocean surface temperatures than relative humidity, as expected from the very low theoretical sensitivity of $^{17}O_{excess}$ to temperature during evaporation [*Barkan and Luz*, 2007; *Landais et al.*, 2008].

In the case of d_{excess} and d_{ln}, the isotopic response to a given change in temperature over the ocean is opposite in sign to that of $^{17}O_{excess}$. That is, colder sea surface temperatures cause lower d_{excess} and d_{ln}. The magnitude of the response of d_{excess} and d_{ln} to a given change in temperature for the Plus5 and Minus5 is ~0.38 ‰/˚C over the ocean. The sensitivity to temperature is lower for both the Plus5-0 and Minus5-0 experiments (dashed lines), with average values of 0.21 ‰/˚C for γd_{xs} and 0.11 ‰/˚C for γd_{ln}. Despite the differences in surface temperature gradients between the Minus5-0 and Plus5-0 experiments, γd_{xs} and γd_{ln} do not begin to diverge from one another until ~60˚S for the West path and ~55˚S for the East path. The γd_{xs} and γd_{ln} remains positive for the entire West path, while for the East path γd_{xs} becomes anticorrelated midway into the interior (~75˚S), and more strongly so for the colder experiments (Minus5 and Minus5-0) (Figure 6g). In Figure 6i and 6j, the dashed lines demonstrate that the d_{ln} response is small if only the poles are cooled, and that only when changes to SST occur across the entire domain is there a consistent and large response. Figure 6 shows that for all the isotopic parameters, the isotopic sensitivity increases toward the interior of the continent, with an opposite sign of sensitivity for $^{17}O_{excess}$ and d_{excess} between the East and West Antarctic interiors. The sensitivity increases by approximately a factor of two for $\delta^{18}O$, d_{excess} and d_{ln}, and by a factor of three to four for $^{17}O_{excess}$, in going from the mid latitudes towards the interior of the continent. For most of the temperature perturbation experiments, the isotopic sensitivity is comparable to the present-day isotopic spatial gradients for East and West Antarctica. This differs from the results of KC03, who found isotopic sensitivities that were significantly larger in the interior of the continent than the isotopic spatial gradient.

4.3 Annual Cycle at WAIS Divide and Vostok

The aim of this section is to estimate the magnitude of the seasonal cycle in $^{17}O_{excess}$, d_{excess}, and d_{ln} for both Vostok and WAIS Divide using the ICM. We examine the temporal and spatial variation of isotopic sensitivity by using the monthly averaged reanalysis data for the West and East Antarctic sectors. In KC03, the location of a given ice core site in the model was determined by matching the modeled $\delta^{18}O$ composition to the observed mean annual $\delta^{18}O$, and any changes at the "site" were relative to the original model $\delta^{18}O$ site composition. To examine the seasonal cycle at Vostok and WAIS Divide, we choose instead to use the actual model latitude of the ice core site rather than the model $\delta^{18}O$ site composition. This is done in order to directly compare the model latitudes with the identical latitudes of the NCEP2 reanalysis climate variables. While this results in mean isotope values slightly lower than actually observed at the real WAIS Divide and Vostok sites, it does not affect interpretation of the results. For the East path and West path, the maximum model latitude is ~78˚S and ~80˚S respectively. When we refer to "Vostok" and "WD," the site locations represent the final trajectory of each path in the ICM.

In the following sections we compare the model isotope results to surface temperature for direct comparison with observational data sets. It should be noted that the condensation temperature

determines the degree of isotopic distillation in the model, which is derived from the surface temperature field. The condensation temperature is given by a static atmospheric lapse rate of 6˚C/km, for a height of 1 km, which was chosen by KC03 as representative of the average height of precipitate formation, and is approximately equal to the 850 hPa temperature height used by other Antarctic precipitation studies [*Schlosser et al.*, 2008]. Adjustments to the atmospheric lapse rate are not explored in this work, but are worth considering in future experiments. The ICM is parameterized to produce an inversion layer for both East and West Antarctica, the magnitude of which linearly depends on the surface temperature and is designed to generally match inversion temperature observations from East Antarctica (Figure 7g and 7h). Note that for both paths, the ICM monthly surface temperatures are slightly elevated with respect to the NCEP2 reanalysis 2.5 x 2.5˚ grid cell enclosing the site location due to the zonal sector averaging (Figures 1 and 8). This may cause an underestimation of the actual isotopic seasonal cycle for the investigated sites.

Seasonal Cycle of $\delta^{18}O$ and Temperature at Vostok (East Path)

Results for the East path indicate a strong seasonal cycle in $\delta^{18}O$ with a peak-to-trough range of ~25 ‰ for Vostok. The amplitude of the $\delta^{18}O$ cycle is comparable to seasonal measurements from Vostok station that range from –50 ‰ to –67 ‰ during the months of March through October [*Landais et al.*, 2012a]. The ICM also reproduces the amplitude of annual variability of $\delta^{18}O$ (±8.2 ‰, 1σ) reasonably well compared to Vostok seasonal measurements (±5.2 ‰, 1σ). The $\delta^{18}O$ seasonal cycle produced by the ICM generally follows the monthly NCEP2 prescribed temperatures. The ICM predicts the lowest $\delta^{18}O$ values during the months of September and October, rather than during the conventional "peak" winter season (JAS) (Figure 8). An important aspect of these results is that the $\delta^{18}O$ in the ICM does not solely track temperature as would occur in a simple Rayleigh-type distillation model. Rather, the ICM is influenced by moisture availability from evaporative recharge along the transport path. The lowest $\delta^{18}O$ values during the months of September and October correspond to a minimum in water content and precipitation, and maximum in sea ice concentration, which in tandem with the cold temperatures produces the more depleted $\delta^{18}O$.

Figure 9 shows a plot of the relationship of the model $\delta^{18}O$ and model surface temperature, indicating a significant linear relationship ($R^2 = 0.91$) between $\delta^{18}O$ and surface temperature ($\Delta\delta^{18}O/\Delta T$ = 0.89 ‰/˚C). The ICM temporal slope is more than double that estimated from seasonal data at Vostok (0.35 ‰/˚C) for a similar range of temperatures. This may suggest that the ICM is overly sensitive to temperature for colder locations; note however that the Vostok seasonal slope is based on less than a complete year of event-based precipitation measurements ([*Landais et al.*, 2012a]) that do not span a full seasonal temperature range, and therefore probably underestimates the full magnitude of the seasonal cycle.

Seasonal Cycle of $^{17}O_{excess}$ for Vostok

Results from the ICM for Vostok produce a seasonal cycle in $^{17}O_{excess}$ that closely resembles the $\delta^{18}O$ seasonal cycle. The $^{17}O_{excess}$ seasonal cycle has a large amplitude, from low values of –10 per meg in September to peak values of 39 per meg in January, and a step-like profile with abrupt fall and spring transitions (Figure 8). The strong intra-annual variability predicted by the ICM (±18 per meg, 1σ) is in excellent agreement with the observed variability of Vostok seasonal $^{17}O_{excess}$ (±18 per meg, 1σ), although the mean annual ICM value of 10 per meg overestimates the average seasonal Vostok $^{17}O_{excess}$ measurement of –6 per meg [*Landais et al.*, 2012a]. Previous work by *Landais et al.* [2012a] showed that $^{17}O_{excess}$ measurements at Vostok had a positive but insignificant relationship with

temperature of 0.92 per meg/˚C, $R^2 = 0.25$, which they attributed to variability in the source regions for the event-based samples. Over a similar temperature range, the ICM results show a positive correlation between $^{17}O_{excess}$ and temperature (2.1 per meg/˚C) with much greater significance ($R^2 = 0.96$) (Figure 9a). The strong positive correlation between $^{17}O_{excess}$ and surface temperature should be expected, as the primary control on $^{17}O_{excess}$ at very low temperatures (at least in the model) is the temperature-dependent supersaturation parameterization during snow formation.

Note that we overestimate both the $\delta^{18}O$ and $^{17}O_{excess}$ temporal isotope slopes by approximately the same amount – a factor of two – compared with observations. However, as already noted, the observations are limited and likely underestimate the full seasonal cycle. Additional field data from Vostok and elsewhere in the East Antarctic interior would be useful. The model results suggest a similar relationship between $\delta^{18}O$ and $^{17}O_{excess}$ to that observed. For Vostok, a strong positive correlation is observed between the model $^{17}O_{excess}$ and $\delta^{18}O$ (2.1 per meg/‰, $R^2 = 0.94$) (Figure 9c). *Landais et al.* [2012a] also found the relationship between $^{17}O_{excess}$ and $\delta^{18}O$ data to be more significant than that observed with temperature, with a similar sensitivity of (2.96 per meg/‰, $R^2 = 0.78$). The relationship between $^{17}O_{excess}$ and $\delta^{18}O$ is also in good agreement with the interannual measurements from *Winkler et al.* [2013].

The evolution of the $^{17}O_{excess}$ seasonal cycle for the East path displays some notable features. Low $^{17}O_{excess}$ values occur from April to October, tracking the long "coreless" East Antarctic winter, interrupted by a small peak during the months of JJA (Figure 8). The $^{17}O_{excess}$ increase during JJA coincides with the annual peak in local precipitation rate, and minor rises in water content and temperature (Figure 7e and 7g, water content not shown). The same climatological conditions also produce decreases in d_{excess} and d_{ln}, and enrichment of $\delta^{18}O$. The lowest $^{17}O_{excess}$ value occurs in September despite equally cold temperatures during the prior four months. During this interval, sea ice concentration in the East path sector steadily increases to its peak concentration in September (Figure 10e) while precipitation at Vostok reaches a local minimum (Figure 7e). These results suggest that the model $^{17}O_{excess}$ for the East path is primarily sensitive to site temperature, but with additional sensitivity to changes in precipitation rate and sea ice concentration, consistent with the earlier GCM-based results of *Schoenemann et al.* [2014].

In Figure 11, the monthly $^{17}O_{excess}$ model results are shown as a function of latitude for the East path. In the annual average, the East path $^{17}O_{excess}$ shows no latitudinal trend with the SST or relative humidity over the ocean. The maximum seasonal range in $^{17}O_{excess}$ over the mid-latitude source region (37 to 52˚S for Vostok, [*Sodemann and Stohl*, 2009]) is ~8 per meg, with the lowest values occurring in austral summer and fall, and the highest values during austral winter and spring. The high $^{17}O_{excess}$ values during fall and winter coincide with lower relative humidity and cooler sea surface temperatures (Figure 10a and 10e), which both contribute to raising $^{17}O_{excess}$. Based on the modeled sensitivity of $^{17}O_{excess}$ to relative humidity and SST, the 2.5% maximum annual range in *rh* can account for 3.5 per meg of the annual variation, while the 3˚C change in SST can produce no more than 1.5 per meg. Over the East Antarctic sea ice region (~54 to 66˚S), the greatest spatial variation in $^{17}O_{excess}$ values occurs for the winter and spring months, with decreases of 2 to 4 per meg, while summer and fall months show no response. These results show that $^{17}O_{excess}$ is sensitive to the presence of sea ice, particularly in the winter months during the greatest concentration. This supports the results of *Schoenemann et al.* [2014], who examined the sensitivity of $^{17}O_{excess}$ to imposed changes in sea ice boundary conditions in a GCM.

Seasonal cycle of d_{excess} and d_{ln} for Vostok

The d_{excess} and d_{ln} seasonal cycle for the East path are nearly identical to one another, albeit with slightly different magnitudes. Both have low values during the austral summer and peak values during austral winter. The amplitude of the model d_{excess} seasonal cycle is approximately 30 ‰. This is in reasonable agreement with the seasonal d_{excess} data from Vostok which range from 5 to 27 ‰ [*Landais et al.*, 2012a]. Comparison of the mean annual d_{excess} from the ICM (23 ‰) with the seasonal Vostok measurements (18 ‰) shows reasonable agreement, although the ICM values are higher than mean annual d_{excess} values from earlier Vostok ice core and snow pit (~15 ‰) measurements [*Vimeux et al.*, 2001b; *Masson-Delmotte et al.*, 2008].

To characterize the temporal sensitivity of d_{excess} to both temperature and $\delta^{18}O$, we plot them in Figure 9. Over the temperature range of –35 to –60˚C the d_{excess} sensitivity to temperature is –0.92‰/˚C ($R^2 = 0.77$) and for $\delta^{18}O$ the negative correlation is even stronger (–1.17‰/‰, $R^2 = 0.96$). In comparison, the seasonal d_{excess} measurements at Vostok showed a negative but insignificant correlation between d_{excess} and site temperature (–0.22‰/˚C, $R^2 = 0.09$). *Landais et al.* [2012a] noted that despite the weak relationship with temperature, the lowest d_{excess} value (5 ‰) was obtained during a warm period in October, and the highest d_{excess} values (24 and 27 ‰) occurred during the coldest periods of precipitation (May and August). Closer inspection of the Vostok seasonal d_{excess} data show that the event-based precipitation samples appear much more correlated with $\delta^{18}O$ than local precipitation temperature, which *Landais et al.* [2012a] suggested was due to other non-local climate parameters controlling the isotopic composition at Vostok [*Landais et al.*, 2012a]. The relationship between d_{excess} and $\delta^{18}O$ samples (–0.91‰/‰) at Vostok is well captured by the climate-data driven ICM, indicating that variations in the monthly climatologies produce concomitant anti-correlated changes in d_{excess} and $\delta^{18}O$. However, our analysis of the controls on d_{excess} sensitivity differs from that of *Landais et al.* [2012a]; see Discussion.

Based on field measurements of water vapor over the ocean, evaporation of d_{excess} and d_{ln} are expected to be sensitive to sea surface temperature and relative humidity, with colder SSTs producing lower d_{excess} (or d_{ln}) and lower relative humidity resulting in higher d_{excess} (or d_{ln}) [*Gat*, 1996; *Uemura et al.*, 2008; *Risi et al.*, 2010]. These relationships can be examined in the spatial (e.g., latitude, *T*, *rh*) mean annual response and then used to compare the seasonal response of d_{excess} and d_{ln} in the ICM. We compare the East path results to water vapor measurements taken over a one-month (January) transect of the Southern Indian Ocean by *Uemura et al.* [2008], who determined the spatial relationship between d_{excess} and SST to be 0.85 ‰/˚C ($R^2 = 0.55$) over the latitudes of 35 to 65˚S (~21 to 0˚C). The ICM mean annual d_{excess} shows a dependency on SST of 0.24 ‰/˚C for roughly the same latitude and temperature range (35 to 56˚S, 18 to 0˚C). The mean annual slope between *rh* and SST for 35˚S (22.5˚C) to 56˚S (0˚C) in the NCEP2 data is –0.25%/˚C, which can be converted to a d_{excess}/rh slope of –0.96‰/%. In comparison, the sensitivity of d_{excess} vapor to relative humidity from the study of *Uemura et al.* [2008] is lower by a third (–0.61 ‰/%, $R^2 = 0.63$). Based on the mean annual East path, the ICM produces results that are generally similar to the evaporative closure assumption model of *Merlivat and Jouzel*, [1979], where the simple Rayleigh model predicts d_{excess}/rh relationship of –0.43‰/% and d_{excess}/SST relationship of 0.35‰ /°C). The $\Delta(d_{excess})/\Delta(rh)$ value also compares well with the –0.38‰/% value from the study of *Risi et al.* [2010]. These spatially derived relationships between mean annual d_{excess}-SST and d_{excess}-*rh* provide context for the expected magnitude of seasonal d_{excess} changes.

In Figure 12, the seasonal d_{excess} and d_{ln} model results are shown as a function of latitude for the East path. The seasonal spread in d_{excess} and d_{ln} over the mid-latitude source region for the East path is quite small (of order 1 ‰), with higher values during austral winter (June and July) and lower values

during the austral spring (September, October and November), and average values during austral summer and fall. For the East path, the largest variability in seasonal d_{excess} and d_{ln} occurs over the sea ice zone (54 to 66˚S), where most d_{excess} and d_{ln} values are highest during the months of greatest sea ice concentration (June through October), but the magnitude of change relative to the mean annual East path is a nominal 1.5 ‰ for both d_{excess} and d_{ln}. In Figure 12, it is apparent that by the time d_{excess} and d_{ln} precipitation reaches the edge of the East Antarctic continent (~66˚S), the seasonal variability in SST, relative humidity, and evaporation have had a minimal impact on the isotopic composition, where the annual range in d_{excess} and d_{ln} is 1.5 to 3.3 ‰ and 9.8 to 11.8 ‰, respectively. These minor seasonal variations in d_{excess} and d_{ln} at the coastal margin of Antarctica indicate that the effect of annual variability in source region climate parameters is relatively negligible, suggesting that coastal locations should have a damped seasonal cycle compared to interior sites.

Seasonal Cycle of $\delta^{18}O$ and Temperature at WAIS Divide

In Figure 7, we show the annual cycle in surface temperature, evaporation rate, precipitation rate, and relative humidity for the 2.5˚ x 2.5˚ grid cell that includes the location of WAIS Divide from the NCEP2 reanalysis. The monthly values in surface temperature, $\delta^{18}O$, $^{17}O_{excess}$, d_{excess}, and d_{ln} determined from the ICM for the West path are shown in Figure 8b. For the West path, the ICM produces a seasonal cycle in $\delta^{18}O$ with a peak-to-trough amplitude of 7.0 ‰, which underestimates the observed seasonal cycle at WAIS Divide by about 25%. The standard deviation of the seasonal variation in $\delta^{18}O$ (2.3 ‰, ±1σ) for the West path is roughly half that of the East path, despite the similar standard deviations in temperature (West Path, 8.1 ˚C, ±1σ) and (East Path, 10.5˚C, ±1σ). For WD, the ICM predicts a mean annual $\delta^{18}O$ value of –33.46 ‰ which is an excellent agreement with measurements of surface snow from WD (–33.8 ‰) [*Schoenemann et al.*, 2013; *Steig et al.*, 2014]. Based on the NCEP2 reanalysis, the West path mean annual surface temperature is –26.8˚C of WD, which agrees reasonably well with the mean annual temperature of –28.5˚C for the ice core site [*Orsi et al.*, 2012]. The results displayed in Figure 9b show that over an annual cycle, the West path $\delta^{18}O$ is significantly correlated with surface temperature ($\Delta\delta^{18}O/\Delta T$ = 0.27 ‰/˚C, R^2 = 0.94). The sensitivity of $\delta^{18}O$ to temperature for the West path is considerably lower than for the East path, which is likely the result of the very different climatologies between West and East Antarctica (e.g., higher precipitation rate, water content, and surface and condensation temperatures).

Seasonal Cycle of $^{17}O_{excess}$ for WAIS Divide

The ICM seasonal cycle in $^{17}O_{excess}$ for WD displays a step-like behavior, unlike the more sinusoidal shape of temperature and $\delta^{18}O$ (Figure 8). Low $^{17}O_{excess}$ values are predicted during December and January, and then during the months of February and March a rapid transition to higher values occurs, which remains fairly constant from April to October before decreasing abruptly in November back to summertime levels. The peak-to-trough amplitude of the seasonal changes in $^{17}O_{excess}$ is 12 per meg. The relatively constant $^{17}O_{excess}$ during AMJJASO despite the progressively colder temperatures and more depleted $\delta^{18}O$ is noteworthy because it indicates that $^{17}O_{excess}$ at WD might be more sensitive to shifts in the onset/termination of sea ice rather than to changes in site temperature alone, as suggested by *Schoenemann et al.* [2014]. An unexpected finding is that the model $\delta^{18}O$ and $^{17}O_{excess}$ are negatively correlated for WD (–1.7 per meg/‰, R^2 = 0.85), with high $^{17}O_{excess}$ values during austral winter when $\delta^{18}O$ is more depleted (Figure 9b and 9d). This is contrary to the positive correlation between $\delta^{18}O$ and $^{17}O_{excess}$ observed at Vostok [*Landais et al.*, 2012a]. The seasonal $^{17}O_{excess}$-$\delta^{18}O$ relationship simulated for WD is more similar to measurements from NEEM,

Greenland. Firn core measurements of $\delta^{18}O$, d_{excess} and $^{17}O_{excess}$ spanning three annual cycles at NEEM gave a temporal $^{17}O_{excess}$-$\delta^{18}O$ slope of –1.44 per meg/‰ (R^2 = 0.28) [*Landais et al.*, 2012b].

The monthly $^{17}O_{excess}$ results for the West path are plotted as a function of latitude in Figure 11b and 11c. Like the East path, the West path mean annual $^{17}O_{excess}$ shows no obvious latitudinal trend with SST or relative humidity over the ocean. Over the mid-latitude source region (45˚ to 54˚S for WD/Byrd [*Sodemann and Stohl*, 2009]), the maximum seasonal variation in $^{17}O_{excess}$ is ~3 per meg, less than half that of the East path, yet the response of higher $^{17}O_{excess}$ during austral winter/spring remains. The greatest variability in $^{17}O_{excess}$ over the ocean occurs in the sea ice zone, where wintertime $^{17}O_{excess}$ values drop sharply by ~4 to 5 per meg coincident with relative humidity increases (Figure 11c and 13c).

Annual Cycle of d_{excess} and d_{ln} for WAIS Divide

The modeled monthly mean d_{excess} values for precipitation for WD are plotted in Figure 8. In contrast to Vostok, the peak-to-trough amplitude of the d_{excess} seasonal cycle for WD is considerably smaller, only 3 ‰ (note the scale differences between East and West path in Figure 8). The standard deviation of the seasonal cycle is 1 ‰ for WD, which is lower than other model simulations for marine-influenced sites [*Helsen et al.*, 2007; *Schlosser et al.*, 2008]. Despite the low seasonal amplitude, the mean annual d_{excess} value for WD is 2.6 ‰, which agrees well with the surface snow value (2.6 ‰) and the past 2 kyr average of the WD ice core (3.3 ‰) [*Schoenemann et al.*, 2014].

The course of the seasonal cycle for WD exhibits a different character than Vostok. The ICM results give a broad peak in March that lags the maximum peak in $\delta^{18}O$ and a second local maximum during October. The WD d_{excess} values decrease steadily from March, reaching a minimum during JAS, which coincides with the coldest source region SSTs and the peak in sea ice concentration. The strong sensitivity of d_{excess} to temperature-dependent equilibrium fractionation is well expressed in the plot of monthly d_{excess} versus latitude, where d_{excess} values track the latitudinal gradient of colder SST (Figure 13a). Over the ocean, particularly in the mid-latitudes, the monthly d_{excess} values also appear to reflect warmer and cooler sea surface temperatures, with more positive d_{excess} values during the summer and fall than during the winter and spring.

The modeled annual cycle and amplitude for d_{ln} is nearly identical to that of d_{excess}, except with an offset in the mean values (due to the logarithmic definition). Comparisons of d_{ln} with d_{excess} show that both definitions produce a double-peaked annual cycle, which is not apparent in the $^{17}O_{excess}$ annual cycle. Review of the latitudinal structure of d_{ln} compared to d_{excess} demonstrates the reduced sensitivity of d_{ln} to equilibrium fractionation. Although they both show a negative trend over the ocean the sensitivity of mean annual d_{excess} to temperature (0.32 ‰/˚C) is three times greater than for d_{ln} (0.10 ‰/˚C) (Figure 13). Comparison of the d_{excess}-$\delta^{18}O$ and d_{ln}-$\delta^{18}O$ relationships at WD show no significant correlation between d_{excess} (or d_{ln}) and $\delta^{18}O$ (Figure 9). In fact, the temporal slope of $\Delta(d_{excess})/\Delta(\delta^{18}O)$ is only slightly negative (–0.07 ‰/‰, R^2 = 0.16), while the temporal slope of $\Delta(d_{ln})/\Delta(\delta^{18}O)$ is nearly zero (0.02 ‰/‰ R^2 = 0.03). The lack of a strong response of d_{excess} and d_{ln} to $\delta^{18}O$ at WD is comparable to seasonal measurements from Greenland where no relationship between d_{excess} and $\delta^{18}O$ was observed (0.015, R^2 = 0.00) [*Landais et al.*, 2012b].

5. Discussion

The results of the revised intermediate complexity model confirm the strong positive correlation between $^{17}O_{excess}$ and $\delta^{18}O$ observed in the seasonal precipitation samples from Vostok. The reasonably good agreement between the ICM results and measurements at Vostok show that this novel modeling approach can capture the annual isotope evolution and amplitude, and therefore can be

applied to other ice core sites. In this case, we have applied the model to study the isotopic response for moisture transport to the WAIS Divide site. Without tuning the ICM to match West Antarctica mean annual $\delta^{18}O$ or $^{17}O_{excess}$ data, the ICM produced a typical $\delta^{18}O$ annual cycle for WD, but an opposite seasonal cycle in $^{17}O_{excess}$ than for Vostok, and of considerably smaller magnitude (~12 per meg). The anticorrelated relationship predicted by the ICM between $^{17}O_{excess}$ and $\delta^{18}O$ for WD is similar to the relationship for seasonal measurements from NEEM, Greenland, which has similar climate conditions to WD, but the seasonal amplitude simulated for WD is much lower than at NEEM [*Landais et al.*, 2012b]. In the following paragraphs we discuss the possible mechanisms for the similarities and differences between Vostok and WD in the modeled isotopic response with a focus on: annual variability, effects of kinetic fractionation during snow formation, evolution of the seasonal cycle, sea ice concentration, and spatio-temporal isotope sensitivity.

Annual Amplitudes and Isotopic Variability

Comparison of the modeled $^{17}O_{excess}$ seasonal cycle to direct measurements has been possible for Vostok; however, there are no published seasonally resolved measurements of $^{17}O_{excess}$ from West Antarctica to date. Here we include preliminary, unpublished $^{17}O_{excess}$ measurements from a shallow firn core (SEAT 2011-3) from the WAIS Divide region (78˚43.7`S, 114˚43.9`W). The data include ~350 individual samples (not replicated) from the upper ~7 m of the core measured on a Picarro 2140*i* water vapor analyzer using laser spectroscopy (see [*Steig et al.*, 2014] for methods and measurement precision). We use these data in order to make comparisons with the West path ICM results. It is important to note that additional replicates and data quality control are pending which may affect the following results. The mean of the seasonal firn core $^{17}O_{excess}$ data is 31 per meg and is in excellent agreement with the annual average WAIS reference water value of 28 per meg (via IRMS), both of which are lower than the mean ICM value of 44 per meg. Despite the close model-data agreement for seasonal variability at Vostok, the standard deviation of annual cycle amplitude simulated by the ICM for WD (4.7 per meg, ±1σ) underestimates the variability observed in the West Antarctic firn core (11.6 per meg, ±1σ). We identify a similar model underestimation of the d_{excess} and $\delta^{18}O$ annual amplitude (1.01 ‰ and 2.28 ‰, ±1σ) compared to the firn core (1.97 ‰ and 3.19 ‰, ±1σ, respectively). The effects of isotopic diffusion on damping the annual amplitudes have not been accounted for in the above firn core values, but such effects will bias the estimates of variability low. The annual amplitudes of $^{17}O_{excess}$ and d_{excess} are strongly linked to the magnitude of variability between $\delta^{18}O$, $\delta^{17}O$, and δD, which in turn are dependent on the model boundary conditions (i.e., the NCEP2 reanalysis). The model underestimation of the observed amplitude in $^{17}O_{excess}$ and d_{excess} is due to several smoothing effects due to temporal (monthly values) and spatial averaging (moisture source area) of the NCEP2 reanalysis climate parameters. For West Antarctica, this smoothing effect may be more significant since much of its precipitation is delivered by eddy-driven, cyclonic storms [*Connolley*, 1997; *Noone and Simmonds*, 2002]. A further consideration is that the isotopic source values used to initialize the model atmospheric vapor are held constant throughout the monthly simulations. This effect appears to be important only at the low-latitude limit, where the model d_{excess} and d_{ln} rapidly adjust to equilibrate with the monthly surface boundary conditions (Figures 12 and 13). However, the explanations above should apply equally to the isotopic variability for both the West and East path, therefore either spatial biases exist in the NCEP2 reanalysis between West and East Antarctica or model parameterizations tuned for East Antarctica are inappropriate for West Antarctica (see discussion below).

Ice-Vapor Fractionation and Site Temperature effects on $^{17}O_{excess}$

Examining the East and West trajectories of $^{17}O_{excess}$ with respect to surface temperature provides insight into the differences between the behaviors of $^{17}O_{excess}$ for the two sites (Figure 14). The large amplitude $^{17}O_{excess}$ seasonal cycle at Vostok is driven by the strong sensitivity of $^{17}O_{excess}$ to ice-vapor kinetic fractionation effects at extremely cold temperatures. This is apparent in the steep decrease of $^{17}O_{excess}$ values during the colder months (March – October) that commence around –35˚C, where the relative proportion of liquid-vapor equilibrium diminishes and the ice-vapor kinetic fractionation begins to dominate (Figure 14). In the ICM the onset of the presence of ice vapor is given by the critical temperature (T_{crit}). The fraction of ice to liquid vapor is determined by a linear mixing where ice vapor is initiated at the critical temperature, in this case at –10˚C, and the fraction of liquid vapor diminishes until only ice vapor exists below –40˚C. In most isotopic models, the range of critical temperatures is between 0 and –10˚C. Sensitivity experiments of adjusting T_{crit} from 0˚C to –10˚C result in delaying the onset of the kinetic effects, allowing equilibrium fractionation to continue over a colder temperature range; further increasing $^{17}O_{excess}$ until the amount of ice-vapor and kinetic fractionation dominate and abruptly lower the $^{17}O_{excess}$. Compared to T_{crit} = 0˚C, setting T_{crit} = –5˚C or –10˚C results in an increase at Vostok of ~4 and ~9 per meg, respectively. Note that the sensitivity of $^{17}O_{excess}$ to T_{crit} is dependent on the model coefficients of supersaturation and choice of kinetic fractionation factors, but in general, decreasing the temperature of T_{crit} (i.e., more negative) has a positive effect on the final site $^{17}O_{excess}$.

In contrast to Vostok, the amplitude of the $^{17}O_{excess}$ seasonal cycle at WD is considerably reduced, likely owing to the warmer condensation temperatures and limited degree of supersaturation influences. For WD, despite the onset of kinetic fractionation at –10˚C, the relative proportion of equilibrium fractionation outweighs the effects of kinetic fractionation, thus producing the increase in $^{17}O_{excess}$ values with colder temperatures. Comparison of the West and East path $^{17}O_{excess}$ with respect to surface temperature in Figure 14 shows that at WD the magnitude of seasonal change in $^{17}O_{excess}$ is approximately equal to that of the East path for the same surface temperature (~ –30˚C), suggesting that lower elevation East Antarctic sites with similar precipitation/moisture regimes would experience seasonal cycles of comparable magnitudes to WD.

Comparison of Seasonal Isotope Signals between Vostok and WAIS Divide

The conventional view of the seasonality of d_{excess} in Antarctic precipitation is that d_{excess} is greatest in winter, due to increased sea ice cover and more distant moisture source regions with relatively lower *rh* and warmer SSTs [*Delmotte et al.*, 2000; *Masson-Delmotte et al.*, 2003; *Schlosser et al.*, 2008]. In the summer when the high-latitude oceans are ice free, it is thought that moisture contributions from more proximal sources with relatively higher relative humidity and cooler SSTs lower d_{excess} values in marine vapor. The assumption has been that source region changes in the d_{excess} of vapor are preserved in the precipitation falling over the ice sheet, and therefore d_{excess} could be used as a source indicator of both SST and relative humidity. The monthly ICM isotopic results provide evidence suggesting that seasonal source region changes only partially contribute to the d_{excess} and d_{ln} signal, and that the entire moisture transport path must be considered if one is to generalize about the seasonality of d_{excess} (d_{ln}) at the final ice core site.

The timing of the modeled $\delta^{18}O$, $^{17}O_{excess}$ and d_{excess} (d_{ln}) annual cycles are entirely dependent on the NCEP2 reanalysis climate data, and therefore any interpretation of the specific signals can only be broadly applied to other climate and ice core data. For example, the use of ERA-Interim reanalysis may alter any given seasonal isotope peak by ± a month, but typically only the magnitudes, not seasonality, of the specific climate variables differ between reanalysis products [*Bromwich et al.*, 2011;

Lindsay et al., 2014]. Within this context, we compare the modeled isotopic cycles for Vostok and WD to each other, and to other seasonally resolved isotopic measurements, back-trajectory model results, and climate reanalysis studies for the Antarctic region to evaluate the overall performance of the ICM seasonal simulations.

Overall, the modeled seasonal cycles in $^{17}O_{excess}$ produced for Vostok and WD closely track local site temperature, but variations in precipitation rate and total atmospheric water content also appear to play an important role in the amount of isotopic distillation for each path. This is most apparent in the timing of the precipitation rate and the wintertime local peak (trough) in $^{17}O_{excess}$ (d_{excess} and d_{ln}) for the East path, as well as the timing of the double-peaked structure of d_{excess} and d_{ln} for the West path.

Precipitation, Surface Temperature, and Relative Humidity Effects

At Vostok, a local peak in $\delta^{18}O$ and $^{17}O_{excess}$ during JJA occurs in the midst of the extended cold period (AMJJAS) where temperatures are mostly constant (Figure 8a). During the same interval, d_{excess} and d_{ln} exhibit a significant local minimum. The timing of this peak in $^{17}O_{excess}$ (trough in d_{excess} and d_{ln}) coincides with the maximum in monthly averaged precipitation rate at Vostok (Figure 7e), along with small increases in total column water content (not shown). The peak in winter precipitation rate is known to be a consistent feature of East Antarctic climate from back-trajectory modeling [*Sodemann and Stohl*, 2009; *Scarchilli et al.*, 2010; *Winkler et al.*, 2012] (see Figure 4 in *Winkler et al.* [2012]). In the NCEP2 reanalysis the peak Vostok precipitation rate occurs immediately prior to the maximum in sea ice concentration when evaporation over the source region is greatest due to strong ocean-air temperature gradients (Figure 10c and 10e). The responses of $\delta^{18}O$, $^{17}O_{excess}$ and d_{excess} (d_{ln}) during this interval are all consistent with weaker kinetic fractionation effects due to the relative increase in water availability associated with the peak winter precipitation rate increases.

The course of d_{excess} over the season at WAIS Divide is not as straightforward as the traditional interpretation presented above. At WD, d_{excess} values are lowest during summer (DJF) but are also low during the peak winter months (JAS) (Figure 8b). Source region SSTs are warmest during January – March, which should lead to higher summer d_{excess} values, and this effect is apparent in Figure 13 where d_{excess} (d_{ln}) in precipitation is greatest during summer months over the mid-latitude source region. Despite the high summer d_{excess} values over the mid-latitude source region, summer d_{excess} is lowest over the high-latitude ocean where evaporative recharge of vapor from cooler SSTs and higher relative humidity contributes to lowering d_{excess}. The low summer d_{excess} values simulated at WD are consistent with the traditional interpretation of d_{excess} if there is indeed an increase in the relative contribution of moisture from high latitudes during the summer. Timing of moisture delivery at WD is ambiguous; back-trajectory simulations show that West Antarctica receives a greater contribution of its precipitation during the winter months [*Sodemann and Stohl*, 2009]. On the other hand, the NCEP2 reanalysis for WD suggests that the precipitation rate is highest in austral fall and spring. The first maximum in d_{excess} and d_{ln} occurs in fall (MAM), even while site temperatures and $\delta^{18}O$ steadily decrease toward peak winter (JAS). The second d_{excess} and d_{ln} local maximum occurs during October and November. The bi-modal peak in the monthly averaged NCEP2 precipitation rate during March–June and November has been observed in other reanalysis products and back-trajectory modeling for Antarctica (*Markle et al.* [2012]), and has been ascribed to the half-yearly mode of pressure variability of the Semiannual Oscillation (SAO) which is strongest in the Amundsen-Ross Sea sectors [*Simmonds and Jones*, 1998; *Simmonds et al.*, 2003]. The SAO is expressed as two separate average low pressure states between 55˚S and 75˚S that occur from February to April and from September to November due to the differing annual cycles of temperature in the mid-latitude ocean regions and in the Antarctic [*Van Loon*, 1967; *Simmonds et al.*, 2003]. The poleward shift and intensification of the circumpolar

trough during the equinox periods is associated with high latitude cyclonic activity and increased precipitation in coastal Antarctica stations [*Turner et al.*, 1997]. The coeval double peaks in precipitation and d_{excess} (d_{ln}) for WD during fall and spring suggest that source region changes, particularly increased evaporation rates from relatively warmer ocean SSTs and lower humidity during March–May, combined with the local precipitation rate increase are responsible.

The lower d_{excess} and d_{ln} values at WD during winter (JAS) are also contrary to the conventional expectation of higher d_{excess}, and unlike the high d_{excess} and d_{ln} values at Vostok, the low WD d_{excess} and d_{ln} wintertime signals imply a more local ocean source region influence rather than site temperature-driven fractionation effects or the transport of low-latitude moisture carrying high d_{excess}. Deuterium excess measurements from an array of West Antarctic ice cores give similarly low wintertime values [*Küttel et al.*, 2012]. One weakness of our calculation of the mean annual source region is that it does not account for latitudinal shifts of the moisture source, though it does span the 1σ winter and summer source limits ([*Sodemann and Stohl*, 2009]). Seasonally adjusting the latitudes of the defined moisture source region has no effect on the modeled isotopes since the ICM is sampling ocean surface moisture along its entire path; however, it can slightly alter the timing of the source region changes displayed in Figure 10.

Kinetic Fractionation Effects on d_{excess} and d_{ln} at Vostok

In general, the model d_{excess} seasonal cycle for Vostok matches the conventional interpretation [*Delmotte et al.*, 2000; *Masson-Delmotte et al.*, 2003; *Schlosser et al.*, 2008], with lower d_{excess} values during summer (DJF) and higher d_{excess} values during the extended cold period (AMJJAS). Although model d_{excess} values over the ocean are lower in the summer from higher relative humidity and are higher in the winter when relative humidity is lower, the annual range in d_{excess} and d_{ln} is less than 2 ‰. The low isotopic variability is not surprising, considering the relatively low seasonal peak-to-trough amplitude of SST (~9 to 12˚C) and *rh* (78.5 to 81%) for the East path source region (Figure 10). Furthermore, the seasonal phasing of the two parameters is such that they work against one another, thereby reducing the seasonal d_{excess} (d_{ln}) amplitude over the ocean. In fact, the magnitude of seasonal changes in d_{excess} and d_{ln} at Vostok are much larger than that predicted by the magnitude of ocean source region seasonal changes and the respective model dependencies of d_{excess} and d_{ln} on SST (max ~ 0.40 ‰/˚C) and *rh* (–0.51 ‰/%) (Figures 5, 6, 12a and 12b). For instance, in the winter months (JAS) the highest mid-latitude oceanic d_{excess} values do not result in the highest d_{excess} values at the Vostok site. Instead, the large d_{excess} seasonal cycle (30 ‰) at Vostok is driven by the balance of equilibrium and kinetic effects during snow precipitation. *Jouzel and Merlivat*, [1984] showed that pure equilibrium fractionation (i.e., supersaturation of 1) between liquid vapor and ice vapor results in very high d_{excess} (60 ‰) in the East Antarctic regions like Vostok. This is because at very low temperatures the ratio of the equilibrium fractionation factors $({}^2\alpha_{eq}-1)/({}^{18}\alpha_{eq}-1)$ for δD (${}^2\alpha_{eq}$) and δ^{18}O (${}^{18}\alpha_{eq}$) is considerably different from the GMWL slope of 8. To simulate the mean annual d_{excess} value (~15 ‰) at Vostok, an additional contribution of kinetic fractionation (i.e., $S_i > 1$) to the equilibrium process of snow formation is needed to lower d_{excess}. Despite the contribution of the kinetic effect lowering d_{excess}, the anticorrelation between δ^{18}O and d_{excess} remains, whereas for ${}^{17}O_{excess}$ the correlation between δ^{18}O and ${}^{17}O_{excess}$ switches from positive to negative depending on the degree of supersaturation. As for ${}^{17}O_{excess}$, increasing supersaturation leads to a decrease of the $\Delta(d_{excess})/\Delta(\delta^{18}O)$ slope. Separating the combination of equilibrium and kinetic effects on the Vostok d_{excess} is difficult for the above reasons. The d_{ln} parameter more directly reflects the magnitude of kinetic isotope effects, as the logarithmic definition accounts for the deviation of the ratio of equilibrium fractionation factors from a slope of 8.

This is observed in Figures 8a and 12, where the amplitude of the d_{ln} annual cycle is only 18.6 ‰ compared to 30.5 ‰ for d_{excess}.

It is important to note that the seasonal cycle amplitudes and mean annual values for d_{excess} and d_{ln} simulated by the ICM are strongly sensitive to the choice of supersaturation coefficients. As mentioned in the model calibration section, we chose a value of $F = 0.007$ to best capture the $^{17}O_{excess}$, even though a value of $F = 0.010$ better fits the d_{excess} and d_{ln} data, highlighting that the simple linear definition of S_i as a function of T or that the parameterization of α_{kin}, or both, are insufficient. Results from seasonal simulations for the East path using $F = 0.010$ give a peak-to-trough amplitude of ~20 ‰ for d_{excess} and ~13 ‰ for d_{ln}, and lower mean values that are in better agreement with Vostok data. The structure of the seasonal cycle remains the same for d_{excess}, and for d_{ln} only the summer months are somewhat elevated with respect to the rest of annual cycle indicating that the ICM seasonal simulations are rather robust.

Sea Ice Concentration and $^{17}O_{excess}$ at WAIS Divide

The ICM does not explicitly account for sea ice concentration but the monthly averaged NCEP2 surface temperature, evaporation rate, precipitation rate, water content and relative humidity fields all reflect the influences of sea ice changes throughout the year. This is most evident in the winter (JAS) evaporation field for both the West and East path, where the evaporation rate suddenly drops at the sea ice margin (Figure 2). From the ICM simulations we can indirectly infer sea ice concentration effects on the seasonal cycle of stable isotopes. The challenge of teasing apart the effects of source or site changes is due to the integrated nature of the transport paths, but it is done more easily for the West path where the site temperature and kinetic fractionation effects are less dominant than the East path. Based on an analysis of $\delta^{18}O$ from seasonally resolved ice cores in West Antarctica, *Küttel et al.* [2012] found that the seasonal correlation of the dominant modes of $\delta^{18}O$ with West Antarctic sea ice concentrations was significant during the fall and winter season (March through August). Other modeling studies have also shown that sea ice concentrations play a contributing role in modulating the seasonal cycle of isotopes, particularly for West Antarctica [*Noone and Simmonds*, 2004]. Of all the isotope parameters that possibly reflect changes in sea ice concentration and the associated ocean surface changes in relative humidity and evaporation, $^{17}O_{excess}$ provides the best chance of identifying such changes, as it is the least sensitive to source SSTs and equilibrium fractionation during transport (see Figures 11a and 11b). As discussed previously, the seasonal cycle of $^{17}O_{excess}$ at WD exhibits a step-like pattern with a steep transition from low summer values to peak values beginning in April and extending until October. The onset of the sharp transition in $^{17}O_{excess}$ coincides with the onset of increasing sea ice concentration and source evaporation rate during March and April. The plateau of stable high $^{17}O_{excess}$ overlaps with the steady evaporation rate and consistent low relative humidity over the source regions during austral fall and winter (MAMJJA) (Figure 8 and 10). Although the general character of the $^{17}O_{excess}$ response mimics the pattern of the source relative humidity, the magnitude of *rh* change (~2%) is too small to fully account for the magnitude of the $^{17}O_{excess}$ change at WD. In Figure 11b and 11c, the path of $^{17}O_{excess}$ versus latitude shows that the $^{17}O_{excess}$ response at the WD site reflects multiple processes, including seasonal variability of *rh* at the mid-latitude source region and wintertime reduction of $^{17}O_{excess}$ over the sea ice region due to evaporative recharge of higher *rh* moisture (Figure 13c). The increased evaporative recharge during the winter months over the high-latitude ocean is evident in Figure 2, where the evaporation rate is ~2–3x greater than during the summer months. The high evaporation rate is driven by the strong ocean-air temperature gradients, while the increased winter precipitation rate over the sea ice region reflects both the strong evaporation rate and the effect of a stronger equator-to-pole temperature gradient during winter (Figure 2). These

climatological patterns combined with the sharp increase in the relative humidity over the sea ice region highlight the importance of moisture recharge on the $^{17}O_{excess}$. In the ICM, the influence of moisture recharge on $^{17}O_{excess}$ over the sea ice region during the winter and spring months is apparent for both the West and East path, and therefore seems to be a common feature in the high-latitude ocean region. In the final portion of the West path trajectory, the equilibrium fractionation effects for ice crystal growth over the ice sheet result in increased $^{17}O_{excess}$.

Temporal vs. Spatial $\delta^{18}O$-T slope for Vostok and WAIS Divide

The $\delta^{18}O$ of polar precipitation has long been used as a proxy for the temperature of the cloud at the time of condensation [*Jouzel and Merlivat*, 1984; *Jouzel et al.*, 1997]. Unlike a simple Rayleigh fractionation model, the ICM $\delta^{18}O$ value represents an integration of the sea surface temperature, condensation temperature, evaporation rate, precipitation rate, water content and relative humidity during its entire model trajectory. Therefore we can use the ICM to examine the relationship between the isotopic signal in precipitation and the temperature at the precipitation site (for both the surface and condensation temperature). We can estimate the spatial isotope-temperature relationship for East Antarctica from the mean annual $\delta^{18}O$ and mean annual surface temperature over the East path from the coastal latitude (~66˚S) to the site location. The spatial $\delta^{18}O$-T relationship for the East Path is 0.91 ‰/˚C which is similar to the spatial isotopic gradient (0.84 ‰/˚C) calculated with data from Antarctic snow and ice core measurements spanning the East path longitudes (0˚E to 120˚E) [*Masson-Delmotte et al.*, 2008]. For some ice core sites the temporal and spatial isotope-temperature relationships significantly differ, for instance, the event-based precipitation samples from Vostok gave a temporal slope of 0.35‰/˚C. The modeled temporal slope for Vostok gives a linear relationship between the seasonal $\delta^{18}O$ and surface temperature of 0.89 ‰/˚C, which is in better agreement with the temporal slope observed at Dome F (0.78 ‰/˚C, [*Fujita and Abe*, 2006]), suggesting that the Vostok precipitation measurements from a partial year may be not be completely representative of East Antarctic temporal $\delta^{18}O$-T slopes. The analysis of the relationship of seasonal $\delta^{18}O$ and condensation temperature gives a slope of 1.41 ‰/˚C for Vostok. The magnitude of the $\delta^{18}O$–T_{cond} slope is indicative of the ICM prescribed inversion temperature that is assumed to be directly related to surface temperature by the classical slope of 0.67 suggested by *Jouzel and Merlivat,* [1984]. The 0.67 slope relating variations of near-surface and condensation (or inversion) temperatures from *Jouzel and Merlivat* [1984] is similar to other linear relationships between inversion and surface temperature (0.6 to 0.65) estimated by *Helsen et al.* [2007] and *Ekaykin and Lipenkov* [2009]. Moreover, comparison of the prescribed ICM T_{cond} with the NCEP2 air temperature from 850 hPa height (~1 km a.g.l.) show good agreement and that the model inversion temperature produces reasonable isotope-temperature relationships for Vostok. Seasonal variations in the inversion strength are not modeled here, but such variations may account for the some of the differences between observations and ICM results.

When we examine the spatial isotope-temperature relationship between mean annual $\delta^{18}O$ and mean annual surface temperature for the West path (from Antarctic margin to site) the linear relationship is 0.91‰/˚C, which compares well with the spatial isotope gradient (0.82 ‰/˚C) derived from snow and ice core transects in the West Antarctic region [*Masson-Delmotte et al.*, 2008]. In contrast to the spatial gradient, the seasonal $\delta^{18}O$ and surface temperatures for WD result in a temporal slope of 0.27 ‰/˚C, which is considerably lower than that modeled for Vostok. For West Antarctica, the low temporal slope may be due to warm temperature biases in the NCEP2 reanalysis data that originate from the low model grid-resolution (2.5˚ x 2.5˚), which are further enhanced by the zonal sector averaging to create the path. The differences between the temporal and spatial slope for WD are intriguing because most estimates of West Antarctic accumulation indicate year-round precipitation

without much seasonal bias [*Banta et al.*, 2008; *Nicolas and Bromwich*, 2011]. The model-data disagreement suggests that either the assumption of a year-round temperature inversion for condensation temperatures may not be appropriate for modeling West Antarctica, or that the "classical" slope of 0.67 observed in East Antarctica is not sufficient. Comparison of the NCEP2 850 hPa air temperature versus NCEP2 surface temperature for the West path give a slope of 0.85, supporting the notion of a steeper condensation-surface temperature relationship.

6. Implications and Future Work

The monthly results from the updated ICM qualitatively and quantitatively reproduce the observed variability of $\delta^{18}O$, $^{17}O_{excess}$ and d_{excess} for East Antarctica (Vostok). The monthly mean $^{17}O_{excess}$ values for both the East and West path are overestimated compared to measurements, but the gradient between the continental margin and interior is of the correct magnitude. It is worth noting here, that using only the mean annual climatological path (i.e., the average of the monthly NCEP2 climatological input data) produces a bias of the mean annual $^{17}O_{excess}$ value, which for the East path is +16 per meg compared to the mean annual value of 10 per meg determined from the twelve monthly simulations. This indicates that model studies that attempt to use mean annual conditions to estimate mean annual $^{17}O_{excess}$ values for East Antarctica may produce biased results. The bias likely results from not capturing the combined effect of extreme cold, minimal water content, and lower precipitation rates that produce a non-linear response in the kinetic fractionation of $^{17}O_{excess}$. Inconsistencies in capturing the isotopic variability for the West path simulation highlights a number of factors that should be considered in improving simulations of the annual cycle of $^{17}O_{excess}$, d_{excess}, and d_{ln}. Addressing these factors in future work will help improve the functionality of intermediate complexity models and our understanding of the spatio-temporal isotopic response of precipitation in Antarctica.

First, we have shown that the effective diffusion fractionation factors during snow formation are not very well known, and as a result, we cannot constrain the supersaturation values of c and F all that well. Although multiple combinations of diffusion fractionation factors and supersaturation values of F are possible, they must reproduce the spatial gradient of decreasing $^{17}O_{excess}$ into the interior and be consistent with d_{excess} and d_{ln}. Properly characterizing the sensitivity of water isotopologues to kinetic fractionation during snow formation is paramount to accurately modeling water isotopes, and therefore we strongly recommend further experimental work along the lines of that carried out by *Uemura et al.* [2005], where isotopic measurements are made on the source water, water vapor, ice vapor, and snow at very low temperatures to determine molecular diffusivities and degree of supersaturation.

Second, in order to better capture the spatial gradient of isotopes in both East and West Antarctica, improvements in estimating or measuring the condensation temperature (and the strength of inversion) are needed. The classical T_{cond}/T_{surf} ratio of 0.67 from measurements in East Antarctica may be inappropriate for coastal or marine-influenced sites where the condensation temperature is more similar to the surface temperatures. Furthermore, the warm bias of surface temperatures in both reanalysis data and in GCMs needs to be more realistic to begin with; otherwise the degree of kinetic fractionation effects will be overestimated when calibrating the model to observations.

Finally, there are a number of approaches for more accurately simulating the seasonal cycle within the ICM. These include adjusting the initial atmospheric isotopic values, the initial moisture source latitude, the longitudinal moisture source origin, the zonal sector over which the model path is averaged, and the type of reanalysis product used. Varying the initial isotopic water vapor values could be accomplished with monthly observations of $\delta^{18}O$, δD, d_{excess} and $^{17}O_{excess}$ in precipitation from the GNIP network and shipboard measurements. The latitude of the moisture origin could be varied depending on the location of the peak evaporation rate determined from reanalysis or GCM output.

Longitudinal variations in the moisture source region can be ascertained by using back-trajectory modeling or GCM water tagging experiments. The selection of the model transport path could then incorporate both the dominant moisture source latitude and the range of longitudes to zonally average. Lastly, multiple reanalysis products are available for climatological boundary conditions, each with their own advantages depending on the focus of the isotopic study (e.g., accurate accumulation versus condensation temperatures). Inclusion of the suggested modeling approaches should further improve simulations of the annual isotopic cycles in Antarctic precipitation and will expand the usefulness of the ICM for application to other ice core locations.

7. Summary and Conclusion

The motivation to investigate the affects of seasonality on the stable isotopes of water arises from the current uncertainty about the relationship between $^{17}O_{excess}$ and $\delta^{18}O$ on both seasonal and interannual timescales. Differences between hemispheres show opposing $^{17}O_{excess}$-$\delta^{18}O$ relationships for Greenland and Antarctica, requiring location specific interpretations dependent on source changes in relative humidity, strong kinetic effects at cold temperatures, and/or stratospheric water vapor inputs. These discrepancies and uncertainties require further investigation. Our work attempts to identify the relative importance of source and site changes for temperature and relative humidity, changes in sea ice concentration, and kinetic fractionation effects, with the aim to clarify the current understanding of $^{17}O_{excess}$ in polar regions. Here, we have used the Intermediate Complexity Model to simulate the annual cycle for two distinct moisture transport pathways with different climatological conditions, one for West Antarctica (similar climatology as Greenland) and one for East Antarctica. Results from the simulated annual cycles have been used to investigate the isotopic response of $\delta^{18}O$, $^{17}O_{excess}$, and d_{excess} in Antarctic precipitation.

We have used the improved ICM to investigate the climatic influences on the complete suite of stable isotopes ($\delta^{18}O$, δD, $\delta^{17}O$, d_{excess}, d_{ln}, and $^{17}O_{excess}$) in Antarctic precipitation. Inclusion of $^{17}O_{excess}$ and d_{ln} expand the utility of the ICM, and provide new constraints for calibrating the model against modern isotopic data. The model of KC03 now includes updates to the equilibrium fractionations during ice condensation and kinetic fractionation factors for evaporation over the ocean and during ice crystal growth. We have created two additional transport paths for East and West Antarctic sectors that incorporate seasonal climate inputs, including a direct measure of relative humidity, to examine the spatial and temporal sensitivity of stable isotopes to the annual cycle.

To match both the Antarctic deuterium excess and $^{17}O_{excess}$ spatial gradients in East Antarctica strong kinetic fractionation effects are necessary. Based on experimental results from *Uemura et al.* [2005], we incorporated lower effective molecular diffusivities for solid precipitation than those proposed by *Jouzel and Merlivat* [1984], which reduces the very sensitive nature of d_{excess} and $^{17}O_{excess}$ to minor changes in the coefficients of supersaturation. This adjustment requires a stronger sensitivity of supersaturation to temperature, which is in better alignment with experimental results. Small discrepancies between the choice of tuning parameters c and F for d_{excess} (d_{ln}) and $^{17}O_{excess}$ remain, but due to the greater sensitivity of the $^{17}O_{excess}$ gradient to kinetic effects, and its reduced sensitivity to equilibrium fractionation and transport, we use it as the calibration benchmark for tuning supersaturation.

Following calibration of the model to modern $^{17}O_{excess}$, d_{excess} and d_{ln} for multiple transport paths, we used the ICM to examine the sensitivity of $^{17}O_{excess}$, d_{excess}, and d_{ln} to source region perturbations in relative humidity and surface temperature. Previous studies on the $^{17}O_{excess}$ of Antarctica have focused on variations in the source regions for driving the changes observed in $^{17}O_{excess}$ on seasonal and interannual timescales. The results from the intermediate complexity model driven by monthly

averaged NCEP2 reanalysis show that seasonal changes in the source regions have a limited contribution on the final $^{17}O_{excess}$ site values. The $^{17}O_{excess}$ seasonal cycle over the ocean is only ~3 per meg for the West path and ~8 per meg for the East path, neither of which are large enough to explain the full seasonal changes produced by the ICM over the ice sheet (~50 per meg) or observed in ice cores (~60 per meg). In the ICM, the ocean surface relative humidity change affects West and East Antarctic $^{17}O_{excess}$ by an average of –1.3 per meg/%, and the magnitude of this effect remains fairly constant even in the interior of the continent. The magnitude of the d_{excess} response over the ice sheet is nearly identical for the West and East path, with an average sensitivity of 0.51 ‰/%. In contrast to results from *Petit et al.*[1991], we find evidence that the relative humidity effect on d_{excess} (and d_{ln}) slightly increases into the interior, rather than diminishes. There is a clear signature of relative humidity affecting the monthly $^{17}O_{excess}$ and d_{excess} values over the ocean regions, but the full seasonal magnitude of $^{17}O_{excess}$ and d_{excess} over the ocean can only partially be explained by source region *rh* and SST changes.

We investigated the temporal sensitivity of d_{excess} (d_{ln}) and $^{17}O_{excess}$ to surface temperature with source and site temperature perturbations. Results from the ICM showed that changes in $^{17}O_{excess}$ over the ocean are anticorrelated with changes in sea surface temperature, while d_{excess} and d_{ln} are positively correlated. The magnitude of sensitivity to surface temperature is low for $^{17}O_{excess}$ over the ocean, except for in the East Antarctic interior where the magnitude reaches ~4 per meg/°C and becomes positively correlated. Over the ocean the isotopic response of d_{excess} and d_{ln} to a given change in temperature is opposite in sign to that of $^{17}O_{excess}$, with a magnitude of ~ 0.40 ‰/°C that increases to ~0.50 – 0.70 %/°C in the interior of the ice sheet.

Our model simulations of $^{17}O_{excess}$ produced a large amplitude seasonal cycle (~50 per meg) at Vostok dominated by strong kinetic fractionation effects and without requiring stratospheric water inputs. The positive correlation between $^{17}O_{excess}$ and $\delta^{18}O$ for Vostok matches observations, as does the model intra-annual variability. At WAIS Divide, the model predicts an anticorrelation between $^{17}O_{excess}$ and $\delta^{18}O$ and a much weaker annual cycle (~12 per meg). Analysis of the NCEP2 data over the mean oceanic moisture source region and at the ice core site shows that the isotopic variability within the annual cycle is predominantly controlled by surface temperature and precipitation rate (and the associated change in water content). Relative humidity and surface temperature over the mid-latitude oceans partially contribute to the isotopic seasonal signal but cannot account for the full seasonal amplitude. In the high-latitude ocean region, variation in sea ice concentration indirectly affects $^{17}O_{excess}$ and, to a lesser extent, d_{excess}, through increases in ocean surface relative humidity and lower sea surface temperatures.

Acknowledgements
We thank J. Kavanaugh for providing the Intermediate Complexity Isotope Model code and his advice on its use. We also thank A. Schauer, R. Smith, and M. Shusterman for assistance with the $^{17}O_{excess}$ CRDS measurements. This work was supported by the US National Science Foundation grants 0837990, 1043092, and OPP-0806387.

References

Banta, J. R., J. R. McConnell, M. M. Frey, R. C. Bales, and K. Taylor (2008), Spatial and temporal variability in snow accumulation at the West Antarctic Ice Sheet Divide over recent centuries, *J. Geophys. Res.*, *113*(D23), D23102, doi:10.1029/2008JD010235.

Barkan, E., and B. Luz (2007), Diffusivity fractionations of $H_2{}^{16}O/H_2{}^{17}O$ and $H_2{}^{16}O/H_2{}^{18}O$ in air and their implications for isotope hydrology, *Rapid Commun. Mass Spectrom.*, *21*, 2999–3005.

Bromwich, D. H., J. P. Nicolas, and A. J. Monaghan (2011), An Assessment of Precipitation Changes over Antarctica and the Southern Ocean since 1989 in Contemporary Global Reanalyses *, *J. Climate*, *24*(16), 4189–4209, doi:10.1175/2011JCLI4074.1.

Brutsaert, W. (1975), A theory for local evaporation (or heat transfer) from rough and smooth surfaces at ground level, *Water Resources Research*, *11*(4), 543–550, doi:10.1029/WR011i004p00543.

Cappa, C. D., M. B. Hendricks, D. J. DePaolo, and R. C. Cohen (2003), Isotopic fractionation of water during evaporation, *J. Geophys. Res.*, *108*(D16), 4525, doi:10.1029/2003JD003597.

Connolley, W. M. (1997), Variability in annual mean circulation in southern high latitudes, *Clim. Dyn.*, *13*(10), 745–756.

Cuffey, K. M., and F. Vimeux (2001), Covariation of carbon dioxide and temperature from the Vostok ice core after deuterium-excess correction, *Nature*, *412*(6846), 523–527.

Dahe, Q., J. R. Petit, J. Jouzel, and M. Stievenard (1994), Distribution of Stable Isotopes in Surface Snow Along the Route of the 1990 International Trans-Antarctica Expedition, *J. Glaciol.*, *40*(134), 107–118.

Dansgaard, W. (1964), Stable isotopes in precipitation, *Tellus*, *16*, 436–468.

Delmotte, M., V. Masson, J. Jouzel, and V. I. Morgan (2000), A seasonal deuterium excess signal at Law Dome, coastal eastern Antarctica: A southern ocean signature, *J. Geophys. Res.*, *105*(D6), 7187–7197, doi:10.1029/1999JD901085.

Ekaykin, A., and V. Y. Lipenkov (2009), *Formation of the Ice Core Isotopic Composition*, In Hondoh T ed. Physics of ice core records II., Hokkaido University Press, Sapporo.

Ellehøj, M. D., H. C. Steen-Larsen, S. J. Johnsen, and M. B. Madsen (2013), Ice-vapor equilibrium fractionation factor of hydrogen and oxygen isotopes: Experimental investigations and implications for stable water isotope studies, *Rapid Commun. Mass Spectrom.*, *27*(19), 2149–2158, doi:10.1002/rcm.6668.

Fisher, D. A. (1991), Remarks on the deuterium excess in precipitation in cold regions, *Tellus B*, *43*(5), 401–407.

Fisher, D. A. (1992), Stable isotope simulations using a regional stable isotope model coupled to a zonally averaged global model, *Cold Regions Science and Technology*, *21*(1), 61–77.

Fujita, K., and O. Abe (2006), Stable isotopes in daily precipitation at Dome Fuji, East Antarctica, *Geophys. Res. Lett.*, *33*(L18503), 1–4.

Gat, J. (1996), Oxygen and hydrogen isotopes in the hydrologic cycle, *Annu. Rev. Earth Planet. Sci.*, (24), 225–262.

Hartmann, D. L. (1994), *Global Physical Climatology*, Academic press.

Helsen, M. M., R. S. W. van de Wal, and M. R. van den Broeke (2007), The Isotopic Composition of Present-Day Antarctic Snow in a Lagrangian Atmospheric Simulation*, *J. Climate*, *20*(4), 739–756, doi:10.1175/JCLI4027.1.

Hendricks, M. B., D. J. DePaolo, and R. C. Cohen (2000), Space and time variation of $\delta^{18}O$ and δD in precipitation: Can Paleotemperature be estimated from ice cores? *Global Biogeochem. Cy.*, *14*(3), 851–861.

Hoffmann, G., M. Werner, and M. Heimann (1998), Water isotope module of the ECHAM atmospheric general circulation model: A study on timescales from days to several years, *J. Geophys. Res.*, *103*(D14), 16871–16896.

Horita, J., and D. Wesolowski (1994), Liquid-vapor fractionation of oxygen and hydrogen isotopes of water from the freezing to the critical temperature, *Geochim. Cosmochim. Acta*, *58*(16), 3425–3437, doi:10.1016/0016-7037(94)90096-5.

Jouzel, J., and L. Merlivat (1984), Deuterium and oxygen 18 in precipitation: modeling of the isotopic effects during snow formation, *J. Geophys. Res.*, *89*, 11749–11757.

Jouzel, J., R. Alley, K. M. Cuffey, W. Dansgaard, P. Grootes, G. Hoffmann, S. Johnsen, R. Koster, D. Peel, and C. Shuman (1997), Validity of the temperature reconstruction from water isotopes in ice cores, *J. Geophys. Res: Oceans*, *102*(C12), 26–471–26–487.

Kanamitsu, M., W. Ebisuzaki, J. Woollen, S.-K. Yang, J. J. Hnilo, M. Fiorino, and G. L. Potter (2002), NCEP–DOE AMIP-II Reanalysis (R-2), *Bull. Amer. Meteor. Soc.*, (83), 1631–1643, doi:10.1175/BAMS-83-11-1631.

Kavanaugh, J. L., and K. M. Cuffey (2002), Generalized view of source-region effects on δD and deuterium excess of ice-sheet precipitation, *Ann. Glaciol.*, *35*(1), 111–117.

Kavanaugh, J. L., and K. M. Cuffey (2003), Space and time variation of $\delta^{18}O$ and δD in Antarctic precipitation revisited, *Global Biogeochem. Cy.*, *17*(1), 1017–1031, doi:10.1029/2002GB001910.

Küttel, M., E. J. Steig, Q. Ding, A. J. Monaghan, and D. S. Battisti (2012), Seasonal climate information preserved in West Antarctic ice core water isotopes: relationships to temperature, large-scale circulation, and sea ice, *Clim. Dyn.*, *39*(7-8), 1841–1857, doi:10.1007/s00382-012-1460-7.

Landais, A., A. Ekaykin, E. Barkan, R. Winkler, and B. Luz (2012a), Seasonal variations of ^{17}O-excess and d-excess in snow precipitation at Vostok station, East Antarctica, *J. Glaciol.*, *58*(210), 725–733, doi:10.3189/2012JoG11J237.

Landais, A., E. Barkan, and B. Luz (2008), Record of δ^{18}O and ^{17}O-excess in ice from Vostok Antarctica during the last 150,000 years, *Geophys. Res. Lett.*, *35*(L02709), 1–5, doi:10.1029/2007GL032096.

Landais, A., H. C. Steen-Larsen, M. Guillevic, V. Masson-Delmotte, B. Vinther, and R. Winkler (2012b), Triple isotopic composition of oxygen in surface snow and water vapor at NEEM (Greenland), *Geochim. Cosmochim. Acta*, *77*(C), 304–316, doi:10.1016/j.gca.2011.11.022.

Lindsay, R., M. Wensnahan, A. Schweiger, and J. Zhang (2014), Evaluation of Seven Different Atmospheric Reanalysis Products in the Arctic*, *J. Climate*, *27*(7), 2588–2606, doi:10.1175/JCLI-D-13.

Luz, B., and E. Barkan (2010), Variations of ^{17}O/^{16}O and ^{18}O/^{16}O in meteoric waters, *Geochim. Cosmochim. Acta*, *74*(22), 6276–6286, doi:10.1016/j.gca.2010.08.016.

Luz, B., E. Barkan, R. Yam, and A. Shemesh (2009), Fractionation of oxygen and hydrogen isotopes in evaporating water, *Geochim. Cosmochim. Acta*, *73*(22), 6697–6703, doi:10.1016/j.gca.2009.08.008.

Majoube, M. (1971), Fractionnement en oxygene 18 et en deuterium entre l'eau et sa vapeur, *J. Chem. Phys.*, *68*(10), 1423–1436.

Markle, B. R., N. Bertler, K. E. Sinclair, and S. B. Sneed (2012), Synoptic variability in the Ross Sea region, Antarctica, as seen from back-trajectory modeling and ice core analysis, *J. Geophys. Res.*, *117*(D02113), 1–17, doi:10.1029/2011JD016437.

Masson-Delmotte, V. et al. (2008), A review of Antarctic surface snow isotopic composition: Observations, atmospheric circulation, and isotopic modeling, *J. Climate*, *21*(13), 3359–3387, doi:10.1175/2007JCLI2139.1.

Masson-Delmotte, V., M. Delmotte, V. Morgan, D. Etheridge, T. van Ommen, S. Tartarin, and G. Hoffmann (2003), Recent southern Indian Ocean climate variability inferred from a Law Dome ice core: new insights for the interpretation of coastal Antarctic isotopic records, *Clim. Dyn.*, *21*(2), 153–166, doi:10.1007/s00382-003-0321-9.

Merlivat, L. (1978a), Molecular diffusivities of $H_2{}^{16}O$, $HD^{16}O$, and $H_2{}^{18}O$ in gases, *J. Chem. Phys.*, *69*(6), 2864–2871, doi:10.1063/1.436884.

Merlivat, L. (1978b), The dependence of bulk evaporation coefficients on air-water interfacial conditions as determined by the isotopic method, *J. Geophys. Res.*, *83*(C6), 2977–2980.

Merlivat, L., and J. Jouzel (1979), Global Climatic Interpretation of the Deuterium-Oxygen-18 Relationship for Precipitation, *J. Geophys. Res.*, *84*(C8), 5029–5033.

Neumann, T. A., and E. D. Waddington (2005), Effects of firn ventilation on isotopic exchange, *J. Glaciol.*, *50*(169), 183–194.

Nicolas, J. P., and D. H. Bromwich (2011), Climate of West Antarctica and Influence of Marine Air Intrusions*, *J. Climate*, *24*(1), 49–67, doi:10.1175/2010JCLI3522.1.

Noone, D., and I. Simmonds (2002), Annular variations in moisture transport mechanisms and the abundance of $\delta^{18}O$ in Antarctic snow, *J. Geophys. Res.*, *107*(D24), 4742, doi:10.1029/2002JD002262.

Noone, D., and I. Simmonds (2004), Sea ice control of water isotope transport to Antarctica and implications for ice core interpretation, *J. Geophys. Res.*, *109*(D07105), 1–13, doi:doi:10.1029/2003JD004228.

Orsi, A. J., B. D. Cornuelle, and J. P. Severinghaus (2012), Little Ice Age cold interval in West Antarctica: Evidence from borehole temperature at the West Antarctic Ice Sheet (WAIS) Divide, *Geophys. Res. Lett.*, *39*(L09710), 1–7, doi:10.1029/2012GL051260.

Petit, J. R., J. White, N. W. Young, J. Jouzel, and Y. S. Korotkevich (1991), Deuterium excess in recent Antarctic Snow, *J. Geophys. Res.*, *96*(D3), 5113–5122.

Risi, C., A. Landais, R. Winkler, and F. Vimeux (2013), Can we determine what controls the spatio-temporal distribution of d-excess and ^{17}O-excess in precipitation using the LMDZ general circulation model? *Clim. Past*, *9*(5), 2173–2193, doi:10.5194/cp-9-2173-2013.

Risi, C., A. Landais, S. Bony, J. Jouzel, V. Masson-Delmotte, and F. Vimeux (2010), Understanding the ^{17}O-excess glacial-interglacial variations in Vostok precipitation, *J. Geophys. Res.*, *115*(D10112), 1–15, doi:10.1029/2008JD011535.

Scarchilli, C., M. Frezzotti, and P. M. Ruti (2010), Snow precipitation at four ice core sites in East Antarctica: provenance, seasonality and blocking factors, *Clim. Dyn.*, *37*(9-10), 2107–2125, doi:10.1007/s00382-010-0946-4.

Schlosser, E., H. Oerter, V. Masson-Delmotte, and C. Reijmer (2008), Atmospheric influence on the deuterium excess signal in polar firn: implications for ice-core interpretation, *J. Glaciol.*, *54*(184), 117–124, doi:10.3189/002214308784408991.

Schmidt, G. A., G. Hoffmann, D. T. Shindell, and Y. Hu (2005), Modeling atmospheric stable water isotopes and the potential for constraining cloud processes and stratosphere-troposphere water exchange, *J. Geophys. Res.*, *110*(D21314), 1–15, doi:10.1029/2005JD005790.

Schoenemann, S. W., A. J. Schauer, and E. Steig (2013), Measurement of SLAP2 and GISP $\delta^{17}O$ and proposed VSMOW-SLAP normalization for $\delta^{17}O$ and $^{17}O_{excess}$, *Rapid Commun. Mass Spectrom.*, (27), 582–590, doi:10.1002/rcm.6486.

Schoenemann, S. W., E. J. Steig, Q. Ding, B. R. Markle, and A. J. Schauer (2014), Triple water-isotopologue record from WAIS Divide, Antarctica: Controls on glacial-interglacial changes in $^{17}O_{excess}$ of precipitation, *Journal of Geophysical Research: Atmospheres*, *119*, 1–23,

doi:10.1002/2014JD021770.

Simmonds, I., and D. A. Jones (1998), The Mean Structure and Temporal Variability of the Semiannual Oscillation in the Southern Extratropics, *Int. J. Climatol.*, *18*, 473–504.

Simmonds, I., K. Keay, and E.-P. Lim (2003), Synoptic Activity in the Seas around Antarctica, *Monthly Weather Review*, *131*, 272–288.

Sodemann, H., and A. Stohl (2009), Asymmetries in the moisture origin of Antarctic precipitation, *Geophys. Res. Lett.*, *36*(L22803), 1–5, doi:10.1029/2009GL040242.

Steen-Larsen, H. C. et al. (2011), Understanding the climatic signal in the water stable isotope records from the NEEM shallow firn/ice cores in northwest Greenland, *J. Geophys. Res.*, *116*(D6), doi:10.1029/2010JD014311.

Steig, E. J., V. Gkinis, A. J. Schauer, S. W. Schoenemann, K. Samek, J. Hoffnagle, K. J. Dennis, and S. M. Tan (2014), Calibrated high-precision ^{17}O-excess measurements using cavity ring-down spectroscopy with laser-current-tuned cavity resonance, *Atmos. Meas. Tech.*, *7*(8), 2421–2435, doi:10.5194/amt-7-2421-2014.

Turner, J., S. R. Colwell, and S. Harangozo (1997), Variability of precipitation over the coastal western Antarctic Peninsula from synoptic observations, *J. Geophys. Res: Atmos*, *102*(D12), 13999–14007.

Uemura, R., E. Barkan, O. Abe, and B. Luz (2010), Triple isotope composition of oxygen in atmospheric water vapor, *Geophys. Res. Lett.*, *37*(L04402), 1–4, doi:10.1029/2009GL041960.

Uemura, R., V. Masson-Delmotte, J. Jouzel, A. Landais, H. Motoyama, and B. Stenni (2012), Ranges of moisture-source temperature estimated from Antarctic ice cores stable isotope records over glacial–interglacial cycles, *Clim. Past*, *8*(3), 1109–1125, doi:10.5194/cp-8-1109-2012.

Uemura, R., Y. Matsui, K. Yoshimura, H. Motoyama, and N. Yoshida (2008), Evidence of deuterium excess in water vapor as an indicator of ocean surface conditions, *J. Geophys. Res.*, *113*(D19114), 1–10, doi:10.1029/2008JD010209.

Uemura, R., Y. Matsui, N. Yoshida, O. Abe, and S. Mochizuki (2005), Isotopic fractionation of water during snow formation: Experimental evidence of kinetic effect, *Polar Meteorol. Glaciol.*, *19*, 1–14.

Van Loon, H. (1967), The half-yearly oscillations in middle and high southern latitudes and the coreless winter, *Journal of the Atmospheric Sciences*, *24*(5), 472–486.

Vimeux, F., V. Masson, G. Delaygue, J. Jouzel, J. R. Petit, and M. Stievenard (2001a), A 420,000 year deuterium excess record from East Antarctica: Information on past changes in the origin of precipitation at Vostok, *J. Geophys. Res.*, *106*(D23), 31–863–31–873.

Vimeux, F., V. Masson, J. Jouzel, J. R. Petit, E. J. Steig, M. Stievenard, R. Vaikmae, and J. White (2001b), Holocene hydrological cycle changes in the Southern Hemisphere documented in East Antarctic deuterium excess records, *Clim. Dyn.*, *17*(7), 503–513.

Wallace, J. M., and P. V. Hobbs (2006), *Atmospheric science: an introductory survey*, Academic press.

Winkler, R., A. Landais, C. Risi, M. Baroni, A. Ekaykin, J. Jouzel, J.-R. Petit, F. Prie, B. Minster, and S. Falourd (2013), Interannual variation of water isotopologues at Vostok indicates a contribution from stratospheric water vapor, *Proc. Natl. Acad. Sci. U.S.A*, *110*(44), 17674–17679, doi:10.1073/pnas.1215209110.

Winkler, R., A. Landais, H. Sodemann, L. Dümbgen, F. Prié, V. Masson-Delmotte, B. Stenni, J. Jouzel, and V. Rath (2012), Deglaciation records of ^{17}O-excess in East Antarctica: reliable reconstruction of oceanic normalized relative humidity from coastal sites, *Clim. Past*, *8*(1), 1–16, doi:10.5194/cp-8-1-2012.

Figure 1. Map of Antarctica showing the East and West path sectors used for modeling isotopes at the Vostok (orange circle) and West Antarctic Ice Sheet Divide (WD, red star) ice core sites. The East Antarctic path spans from 0˚E to 120˚E and the West Antarctic path spans from 70˚W to 150˚W. Both paths originate at ~25˚S and end at the latitude of the respective ice core site (78˚S for Vostok and 80˚S for WD).

Figure 2. Example of East and West path model inputs of surface temperature (˚C), water content (mm), evaporation rate (mm a^{-1}), precipitation rate (mm a^{-1}), relative humidity (%), and sea ice concentration as functions of latitude for summer (DJF) and winter (JAS) seasons. Climatological data are monthly mean NCEP2 reanalysis from 1979–2011 that have been seasonally averaged for purposes of comparison between the two paths. Note that the scales are the same for both plots.

Figure 3. Modeled $\delta^{18}O$ (a and b), $^{17}O_{excess}$ (c and d), d_{ln} (e and f), and d_{excess} (g and h) values of precipitation for Path 2 (black) and East path (orange) as functions of latitude (˚S) and surface temperature (˚C). Supersaturation coefficients used for tuning the ICM were $c = 1.00$, and $F = 0.007$. The circles and triangles represent field measurements by [*Dahe et al.*, 1994]. The stars represent present-day mean annual $^{17}O_{excess}$ values for East Antarctic sites (Dome F, Vostok, and Dome C) compiled in [*Schoenemann et al.*, 2014], and the diamonds represent seasonal $^{17}O_{excess}$ measurements for Vostok by [*Landais et al.*, 2012a].

Figure 4. Modeled $^{17}O_{excess}$ (a and b), d_{ln} (c and d), and d_{excess} (e and f) values of precipitation for Path 2 (black), East path (orange), and West path (red) as functions of $\delta^{18}O$. The circles and triangles represent field measurements by [*Dahe et al.*, 1994]. Supersaturation coefficients identical to values used to obtain the results for Path 2 (Figure 3). The stars represent present-day mean annual $^{17}O_{excess}$ values for East Antarctic sites (Dome F, Vostok, and Dome C) and West Antarctic/coastal sites (WAIS Divide, Siple Dome, Taylor Dome, and D57) compiled in [*Schoenemann et al.*, 2014], and the diamond represents the mean of seasonal $^{17}O_{excess}$ measurements for Vostok by [*Landais et al.*, 2012a]. The triangles (d_{ln}) and squares (d_{excess}) represent field measurements by [*Masson-Delmotte et al.*, 2008] from the respective longitudinal sectors defined for the East and West path.

Figure 5. Relative humidity (*rh*) perturbation experiments for East (left) and West (right) paths. Global reduction of 5% (light blue) and 10% (dark blue) *rh*, and global increase of 5% (yellow) and 10% (orange) *rh*. Mean annual values for the control model of both paths are shown for comparison in all plots (grey). Note that all the initial isotopic source values are kept the same as the mean annual values, and therefore, the isotopic response to global changes in *rh* exhibit a period of model isotope–*rh* re-equilibrium reached by the mid-latitudes.

Figure 6. Global and polar amplification climate change scenarios for the East path (a, c, e, g, and i) and West path (b, d, f, h, and j), vertical dashed lines represent the edge of the Antarctic continent. Surface temperature change experiments (a and b). +5˚C warming (red). 0˚C to +5˚C warming (red dashes). –5˚C cooling (blue). 0˚C to –5˚C cooling (blue dashes). Isotopic sensitivity (γ) for $\delta^{18}O$ (c and d), $^{17}O_{excess}$ (e and f), d_{excess} (g and h), and d_{ln} (i and j), for all four temperature experiments. Water content *w* scaled with temperature (*T*), *P* and *E* unchanged.

Figure 7. The mean annual cycle (1979–2011) of average monthly relative humidity (a and b), sublimation rate (c and d), precipitation rate (e and f), surface temperature (T_{surf}) and condensation temperature (T_{cond}) at the 850 hPa pressure level (g and h) for the 2.5˚ by 2.5˚ grid cell surrounding the Vostok (a, c, e, and g) and WD (b, d, f, and h) ice core sites from the NCEP2 reanalysis. The 1σ range on the mean monthly values for the NCEP2 data are shown by dashed lines.

Figure 8. Seasonal cycle of modeled stable water isotopes for Vostok (top) and WD (bottom) for $\delta^{18}O$, $^{17}O_{excess}$, d_{excess}, and d_{ln} determined from final latitude on the East (78˚S) and West (80˚S) path. The model surface temperature (T_{surf}) is shown for comparison for each path. Note that the model surface temperature is slightly warmer than the NCEP2 T_{surf} in Figure 7 due to the zonal averaging to create the West and East paths. Dashed line in East Path indicates "estimated" values for Dec. due to model failure to converge on a value.

Figure 9. Model isotopic variation of $\delta^{18}O$ (blue), $^{17}O_{excess}$ (red), and d_{excess} (green) versus surface temperature (T_{surf}) for Vostok (a) and WAIS Divide (b) over the seasonal cycle. $^{17}O_{excess}$ (red), d_{excess} (green), and d_{ln} (dark green) versus $\delta^{18}O$ for Vostok (c) and WAIS Divide (b). Linear regression of the isotope slope plotted for each isotope parameter in its respective color.

Figure 10. The mean annual cycle (1979–2011) of average monthly relative humidity (a and b), evaporation rate (c and d), sea ice concentration (e and f), and sea surface temperature (g and h) for East (37˚S to 53˚S, 0˚E to 120˚E) (a, c, e, and g) and West (45˚S to 54˚S, 70˚W to 150˚W) (b, d, f, and h) path source regions from the NCEP2 reanalysis. The 1σ range of the mean monthly values for the NCEP2 data are shown by dashed lines. Source region latitudes determined from back-trajectory results of [*Sodemann and Stohl*, 2009] for Byrd/WD and Vostok.

Figure 11. ICM results of $^{17}O_{excess}$ as a function of latitude for the East (top) and West (bottom) path from January through December using monthly-averaged NCEP2 reanalysis. Middle panel shows West path on the same scale as East path. Each month is shown as an individual color. Due to model integration difficulties there is no Dec. month for East Path and the * represents months determined from seasonal mean (DJF for Jan. and OND for Nov.). Path 2 (red long-short dashes) and the annual-average path (based on the annual mean of the monthly averaged NCEP2 reanalysis) are shown for comparison (gray dashes). Gray band represents mean annual moisture source region for WD (~45˚S to ~54˚S) and Vostok (~37˚S to ~52˚S) based on air-parcel back-trajectory simulations from [*Sodemann and Stohl*, 2009].

Figure 12. ICM results of d_{excess} (a) and d_{ln} (b), and NCEP2 input of relative humidity (c), as a function of latitude (˚S) for the East path from Jan. through Nov. Each month is shown as an individual color and the annual-average path (based on an annual mean of the monthly averaged NCEP2 climatology) is shown for comparison (gray dashes).

Figure 13. ICM results of d_{excess} (a) and d_{ln} (b), and NCEP2 input of relative humidity (c) and surface temperature (d), as a function of latitude for the West path from Jan. through Dec. Each month is shown as an individual color and the annual-average path is shown for comparison (gray dashes).

Figure 14. ICM results of $^{17}O_{excess}$ as a function of surface temperature for the East (top) and West (bottom) path from Jan. through Dec. using monthly-averaged NCEP2 reanalysis. Due to model

integration difficulties there is no Dec. month for East Path, and the * represents months determined from seasonal mean (DJF for Jan. and OND for Nov.). Each month is shown as an individual color. The annual-average paths (based on the annual mean of the monthly averaged NCEP2 reanalysis) are shown for comparison (gray line).

Figure 15. Laser spectroscopy measurements of $^{17}O_{excess}$ and $\delta^{18}O$ from the SEAT 2011-3 firn core from West Antarctica over nine annual cycles. The mean (31 per meg) and 1σ standard deviation (11.6 per meg) are shown in red solid and dashed lines, respectively. Data have been normalized to the VSMOW-SLAP scale.

Table 1.

	Molecular Diffusivity of $^{18}\alpha_{diff}$, (Ratio of turbulent/pure molecular diffusion)			
	1.0285, (100%)	**1.0214**, (75%)	**1.0143**, (50%)	**1.0096**, (34%)
Sensitivity to Temperature	Change in $^{17}O_{excess}$ (per meg) between –30˚C and –55˚C for Path 2			
$F = 0.002$	32	18	4	–5
$F = 0.004$	84.5	58	34	18
$F = 0.006$	127	91.5	58	37
$F = 0.008$	162	120	79	52.5
$F = 0.010$	190	142	95	66

Figure 1

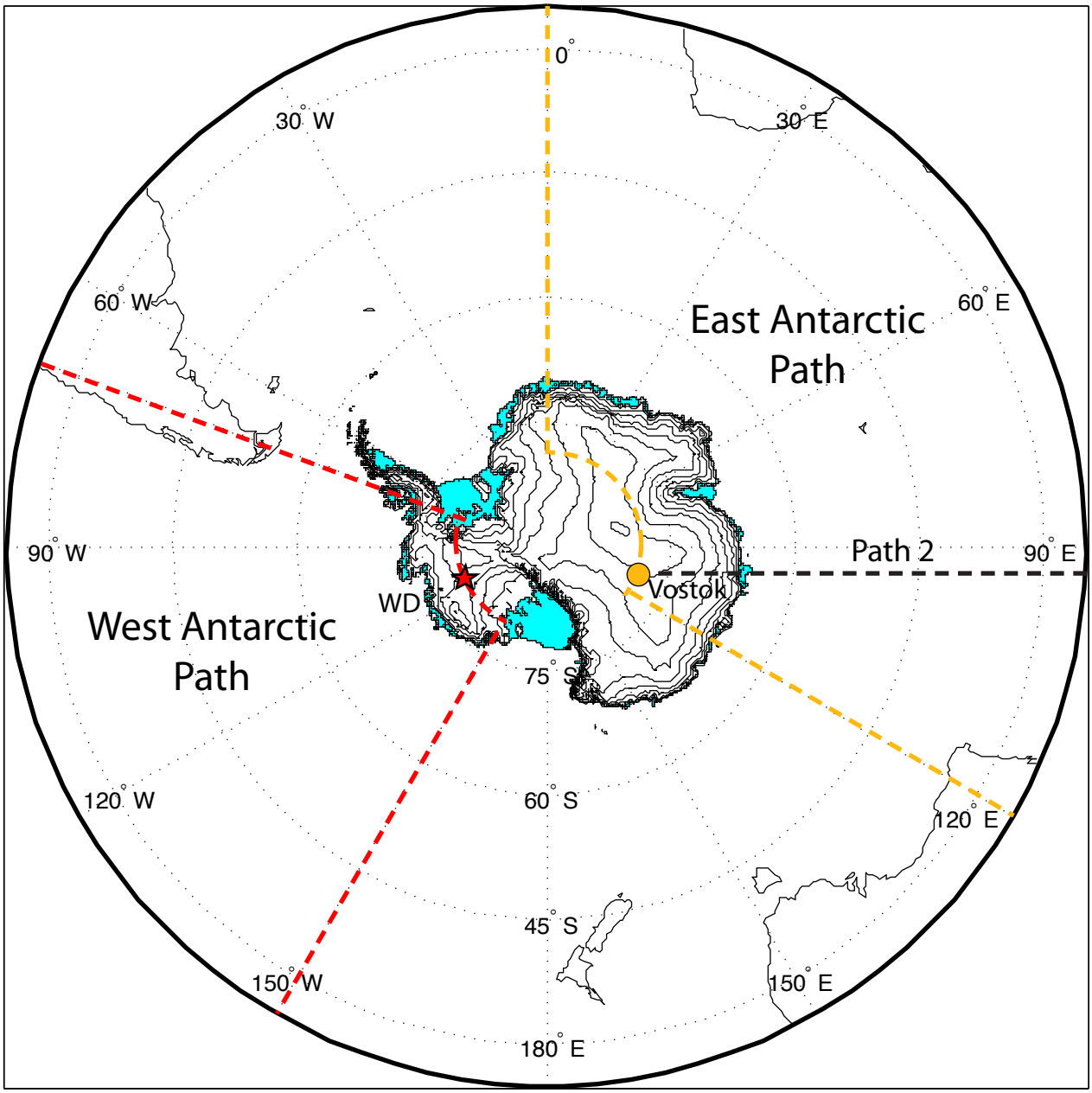
0°
30° W
30° E
60° W
60° E
East Antarctic
Path
90° W
Path 2
90° E
WD
Vostok
West Antarctic
Path
75° S
120° W
60° S
120° E
45° S
150° W
150° E
180° E

Figure 2

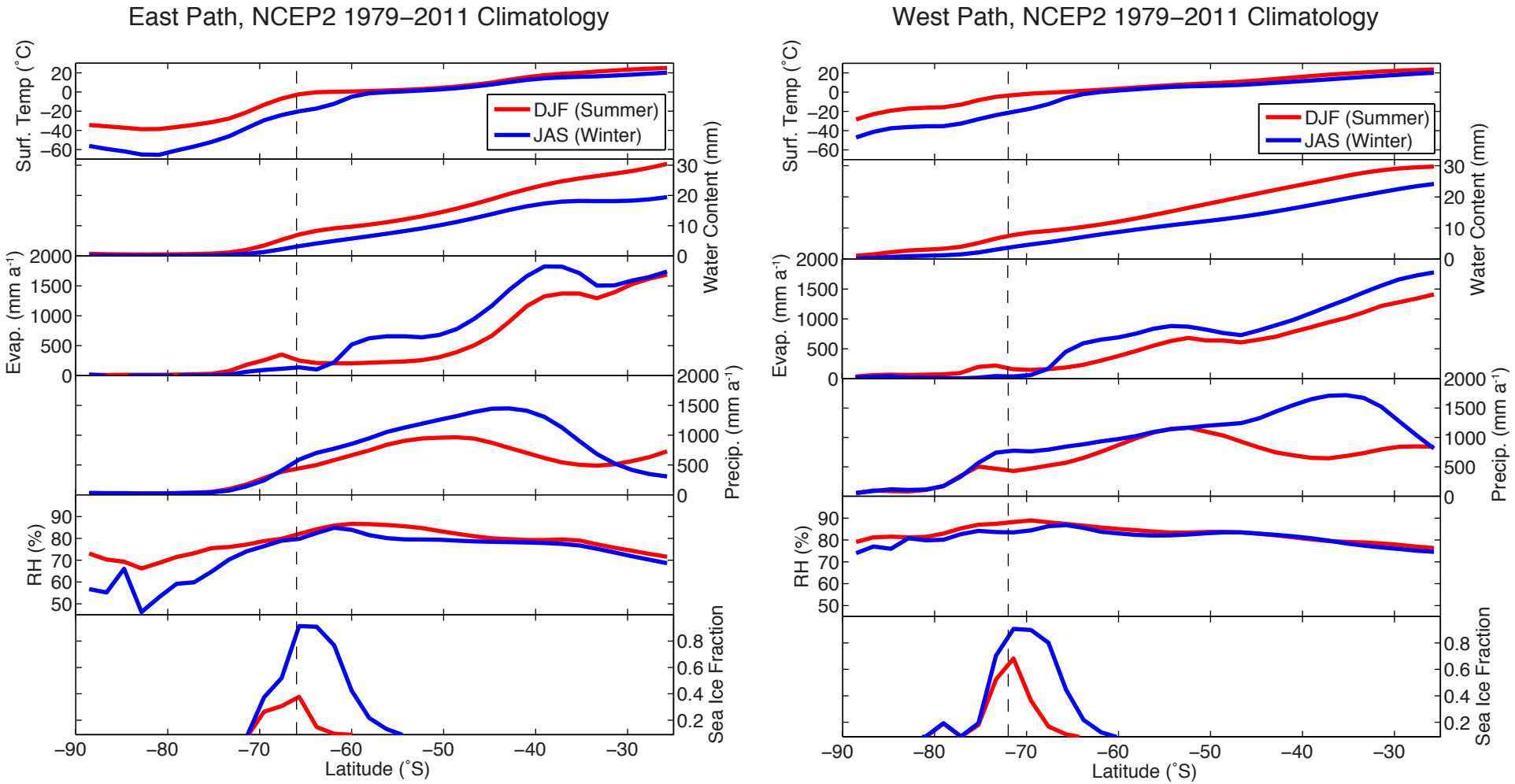
East Path, NCEP2 1979–2011 Climatology
West Path, NCEP2 1979–2011 Climatology
Surf. Temp (˚C)
Water Content (mm)
Evap. (mm a-1)
Precip. (mm a-1)
RH (%)
Sea Ice Fraction
DJF (Summer)
JAS (Winter)
Latitude (˚S)

Figure 3

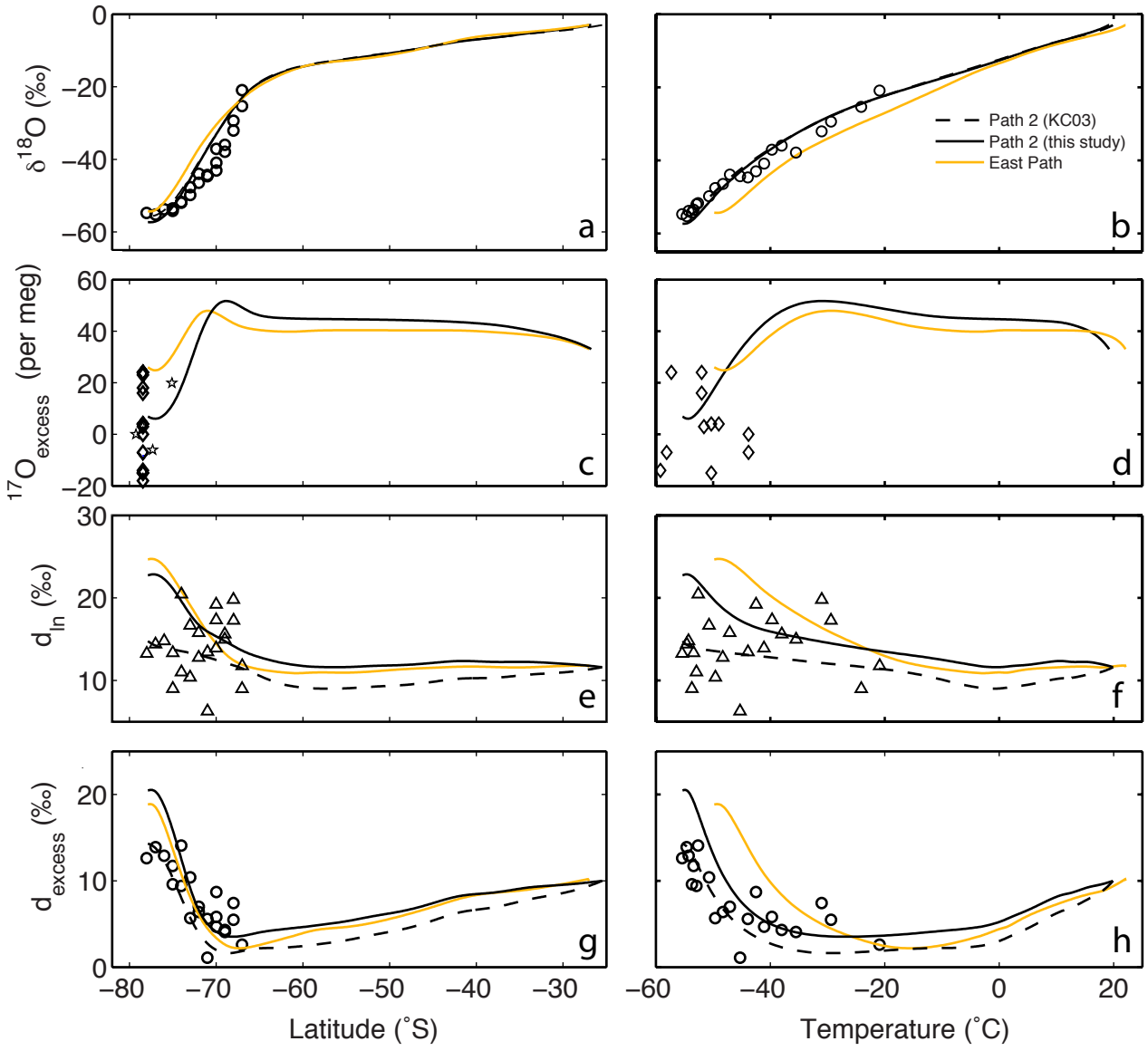
δ18O (‰)
17Oexcess (per meg)
dln (‰)
dexcess (‰)
Path 2 (KC03)
Path 2 (this study)
East Path
a
b
c
d
e
f
g
h
Latitude (˚S)
Temperature (˚C)

Figure 4

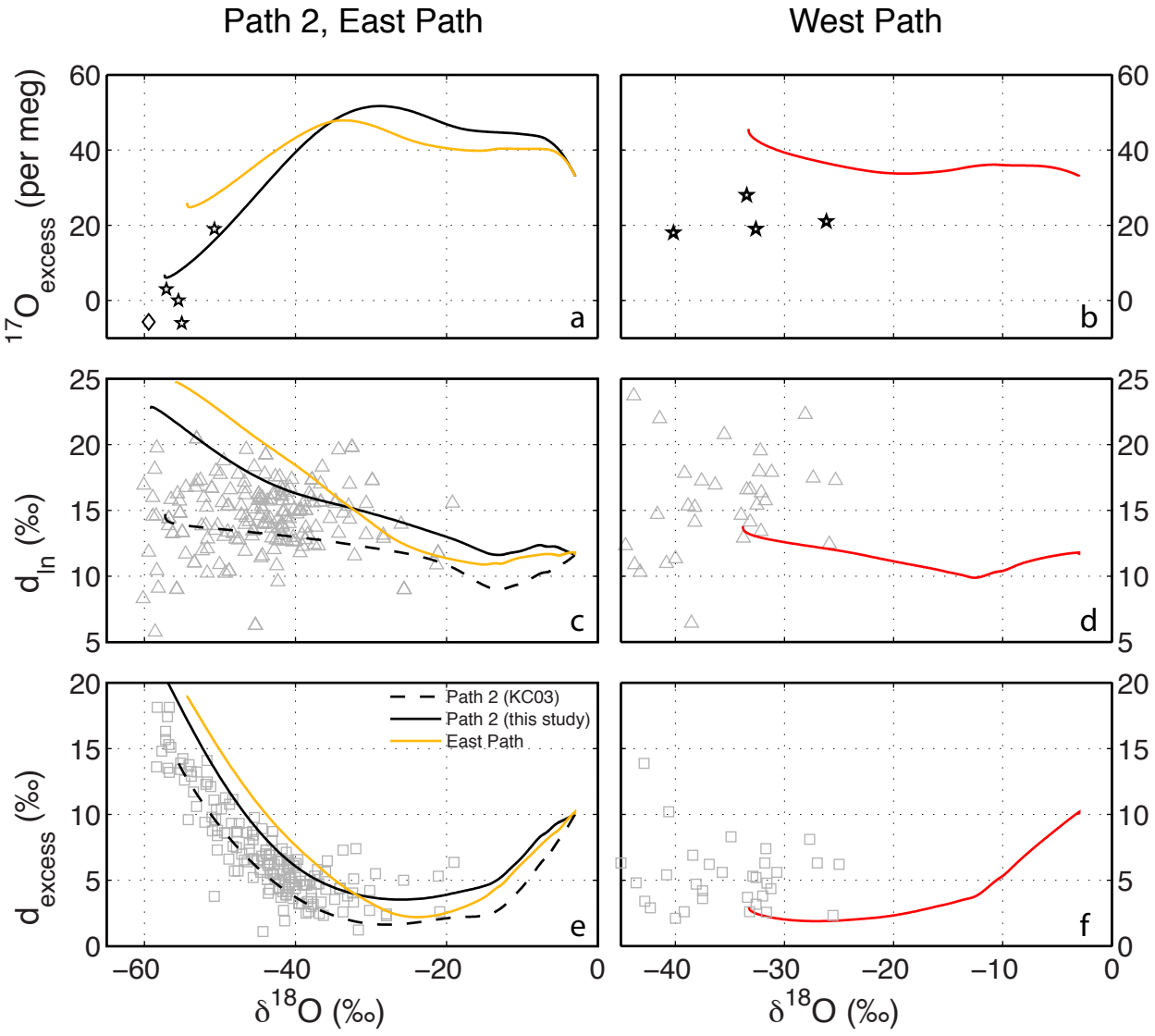
Path 2, East Path
West Path
$^{17}O_{excess}$ (per meg)
d_{ln} (‰)
d_{excess} (‰)
$\delta^{18}O$ (‰)
$\delta^{18}O$ (‰)
a
b
c
d
e
f
Path 2 (KC03)
Path 2 (this study)
East Path

Figure 5

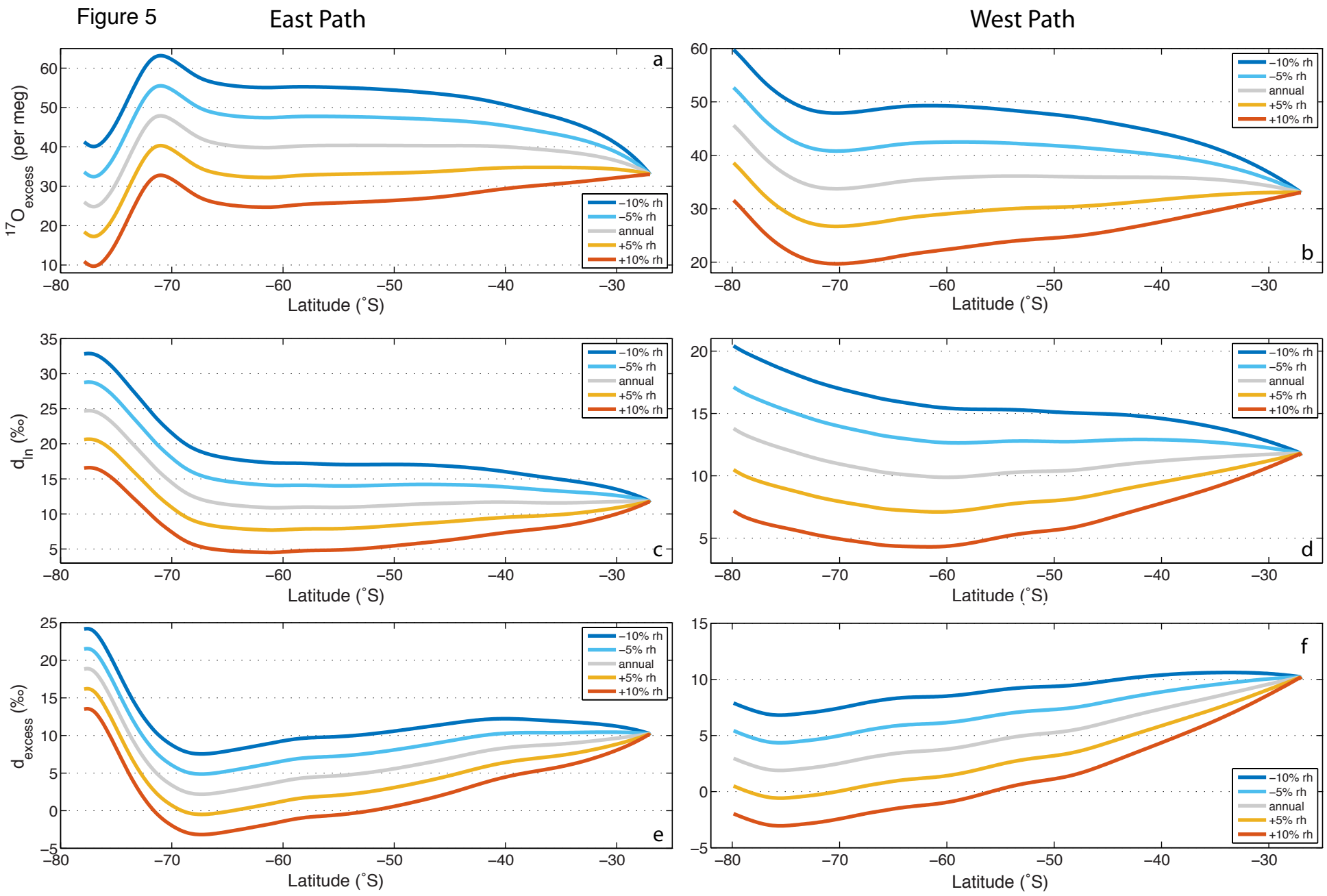
East Path
West Path
a
b
c
d
e
f
$^{17}O_{excess}$ (per meg)
d_{ln} (‰)
d_{excess} (‰)
Latitude (˚S)
−10% rh
−5% rh
annual
+5% rh
+10% rh

Figure 6

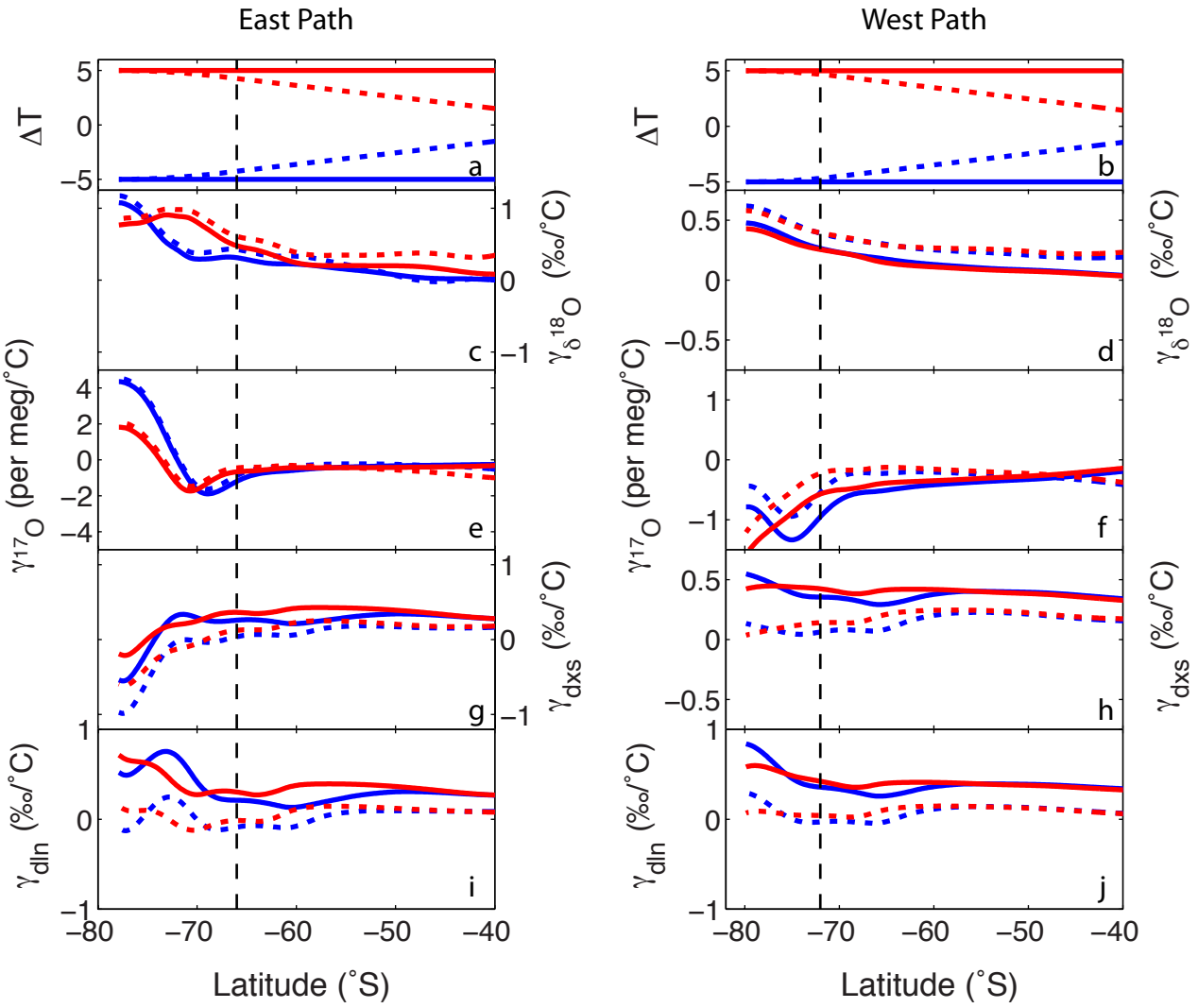
East Path
West Path
ΔT
$\gamma_{^{17}O}$ (per meg/°C)
$\gamma_{\delta^{18}O}$ (‰/°C)
γ_{dxs} (‰/°C)
γ_{dln} (‰/°C)
a
b
c
d
e
f
g
h
i
j
Latitude (°S)
Latitude (°S)

Figure 7

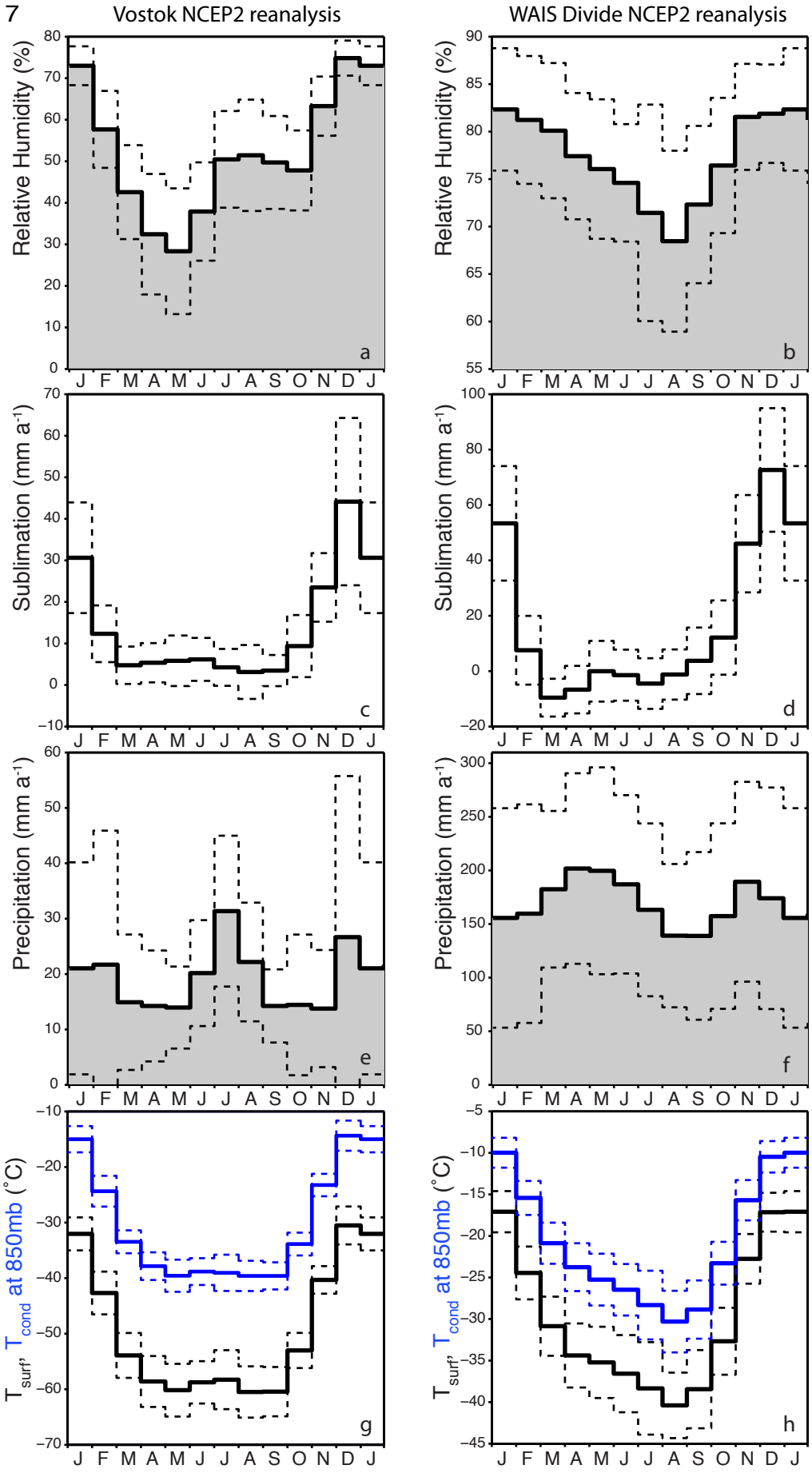
Vostok NCEP2 reanalysis
WAIS Divide NCEP2 reanalysis
Relative Humidity (%)
Sublimation (mm a-1)
Precipitation (mm a-1)
Tsurf, Tcond at 850mb (˚C)
a
b
c
d
e
f
g
h
J F M A M J J A S O N D J

Figure 8

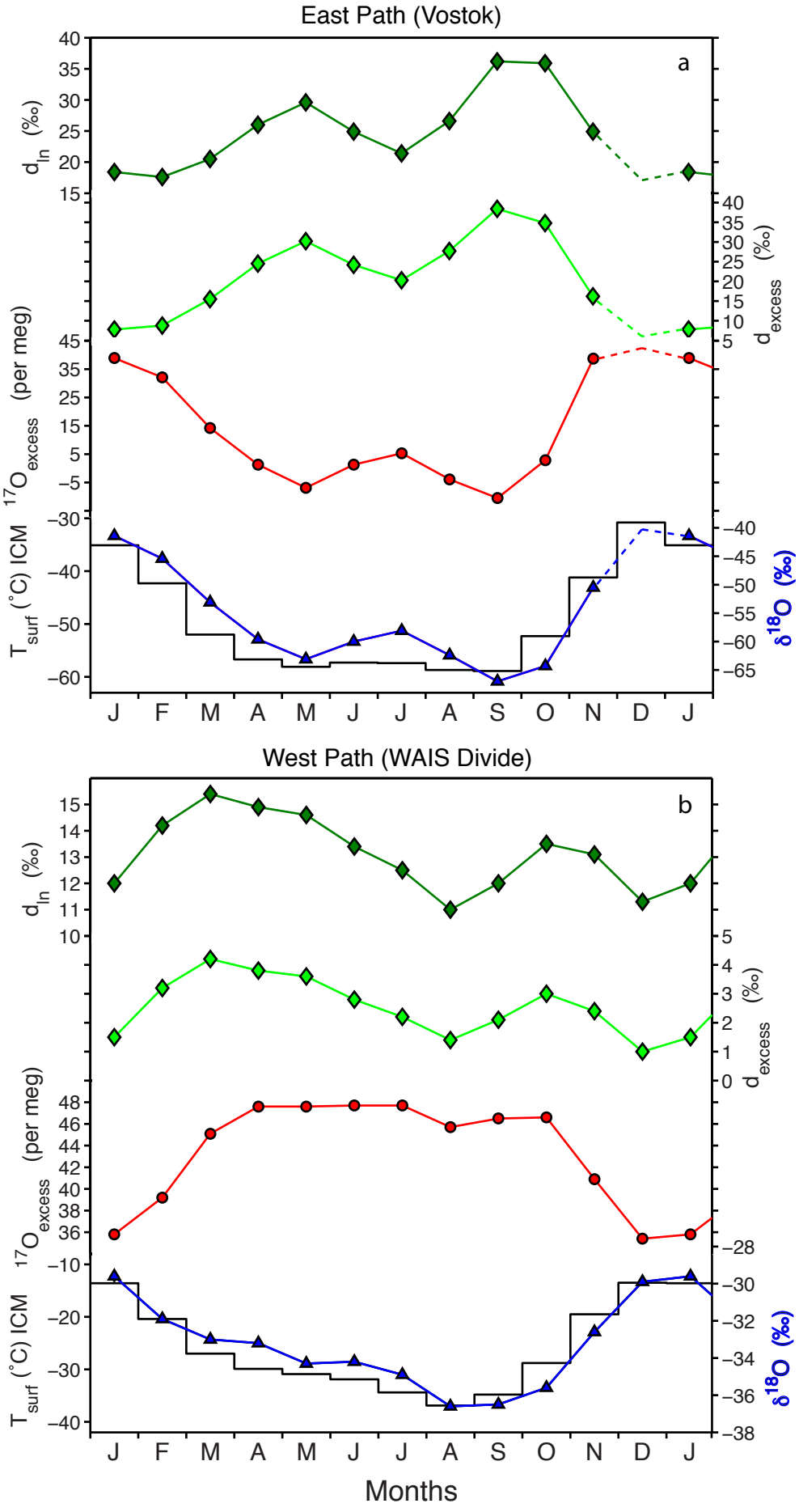
East Path (Vostok)
a
d_{ln} (‰)
d_{excess} (‰)
$^{17}O_{excess}$ (per meg)
T_{surf} (°C) ICM
$\delta^{18}O$ (‰)
J F M A M J J A S O N D J
West Path (WAIS Divide)
b
d_{ln} (‰)
d_{excess} (‰)
$^{17}O_{excess}$ (per meg)
T_{surf} (°C) ICM
$\delta^{18}O$ (‰)
J F M A M J J A S O N D J
Months

Figure 9

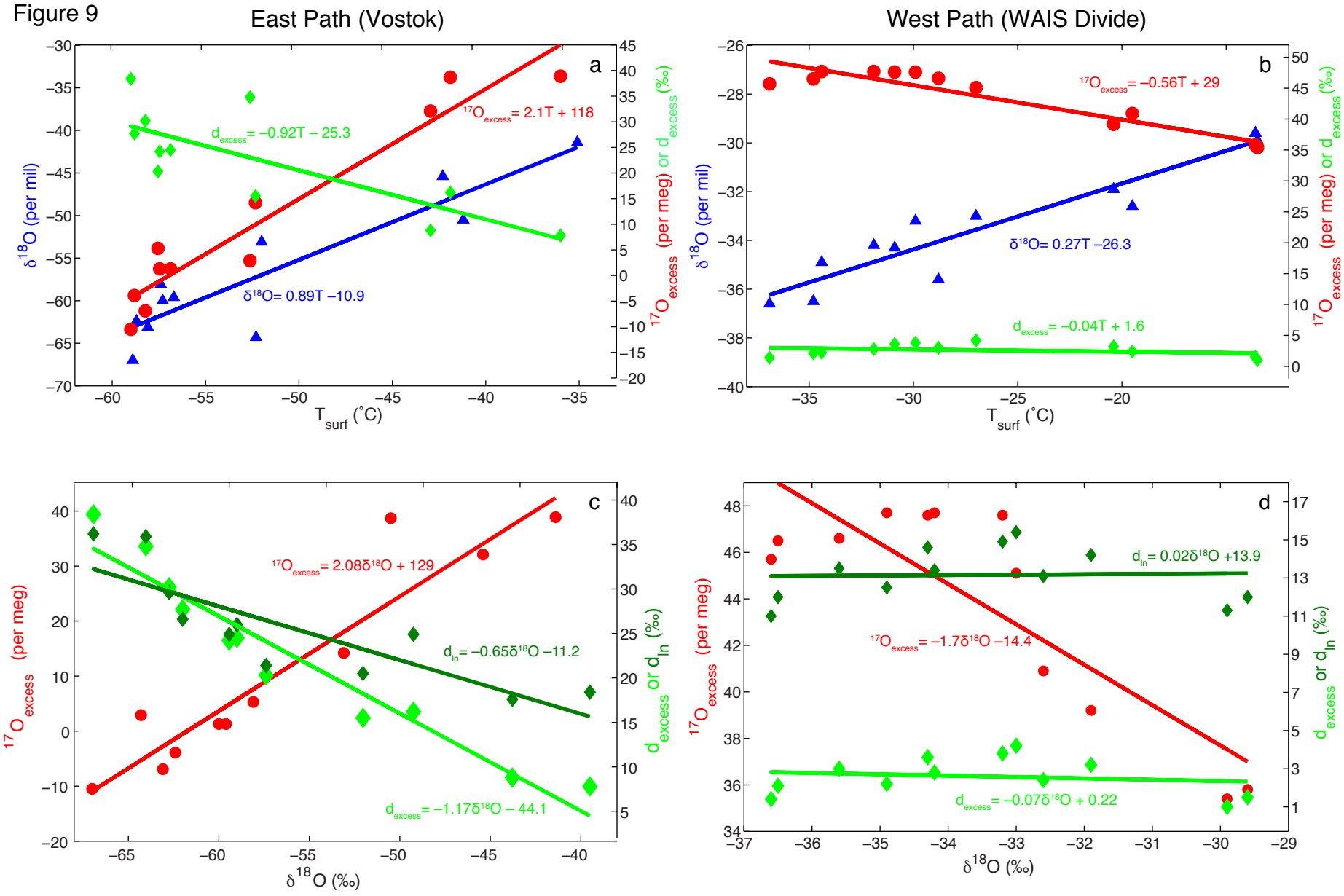
East Path (Vostok)
West Path (WAIS Divide)
a
b
c
d
δ18O (per mil)
17Oexcess (per meg) or dexcess (‰)
Tsurf (˚C)
17Oexcess= 2.1T + 118
dexcess= −0.92T − 25.3
δ18O= 0.89T −10.9
17Oexcess= −0.56T + 29
δ18O= 0.27T −26.3
dexcess= −0.04T + 1.6
17Oexcess (per meg)
dexcess or dln (‰)
δ18O (‰)
17Oexcess= 2.08δ18O + 129
dln= −0.65δ18O −11.2
dexcess= −1.17δ18O − 44.1
dln= 0.02δ18O +13.9
17Oexcess= −1.7δ18O −14.4
dexcess= −0.07δ18O + 0.22

Figure 10

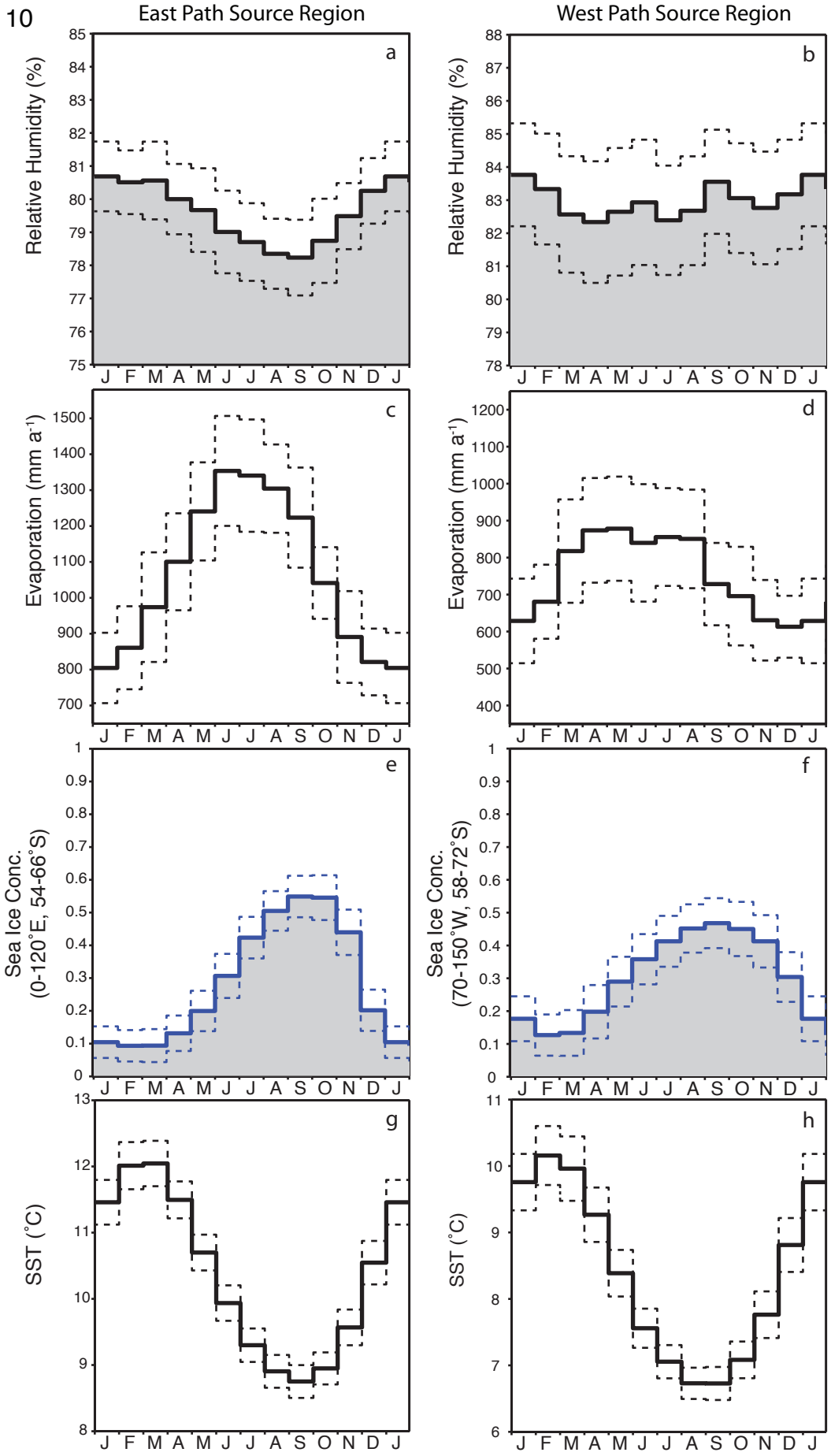
East Path Source Region
West Path Source Region
a
b
c
d
e
f
g
h
Relative Humidity (%)
Evaporation (mm a-1)
Sea Ice Conc. (0-120˚E, 54-66˚S)
Sea Ice Conc. (70-150˚W, 58-72˚S)
SST (˚C)
J F M A M J J A S O N D J

Figure 11

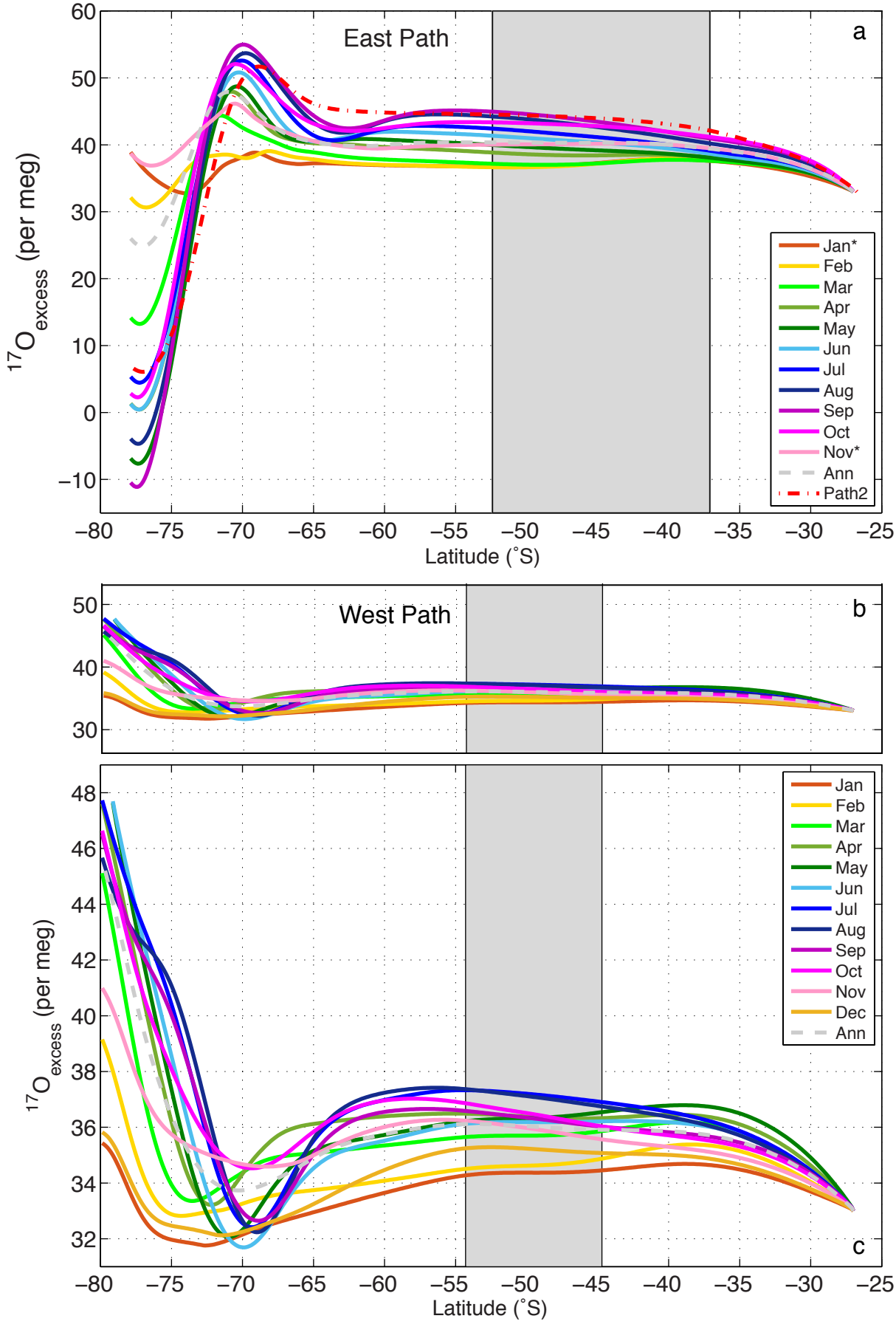
East Path
a
$^{17}O_{excess}$ (per meg)
Latitude (˚S)
Jan*
Feb
Mar
Apr
May
Jun
Jul
Aug
Sep
Oct
Nov*
Ann
Path2
West Path
b
Jan
Feb
Mar
Apr
May
Jun
Jul
Aug
Sep
Oct
Nov
Dec
Ann
c

Figure 12

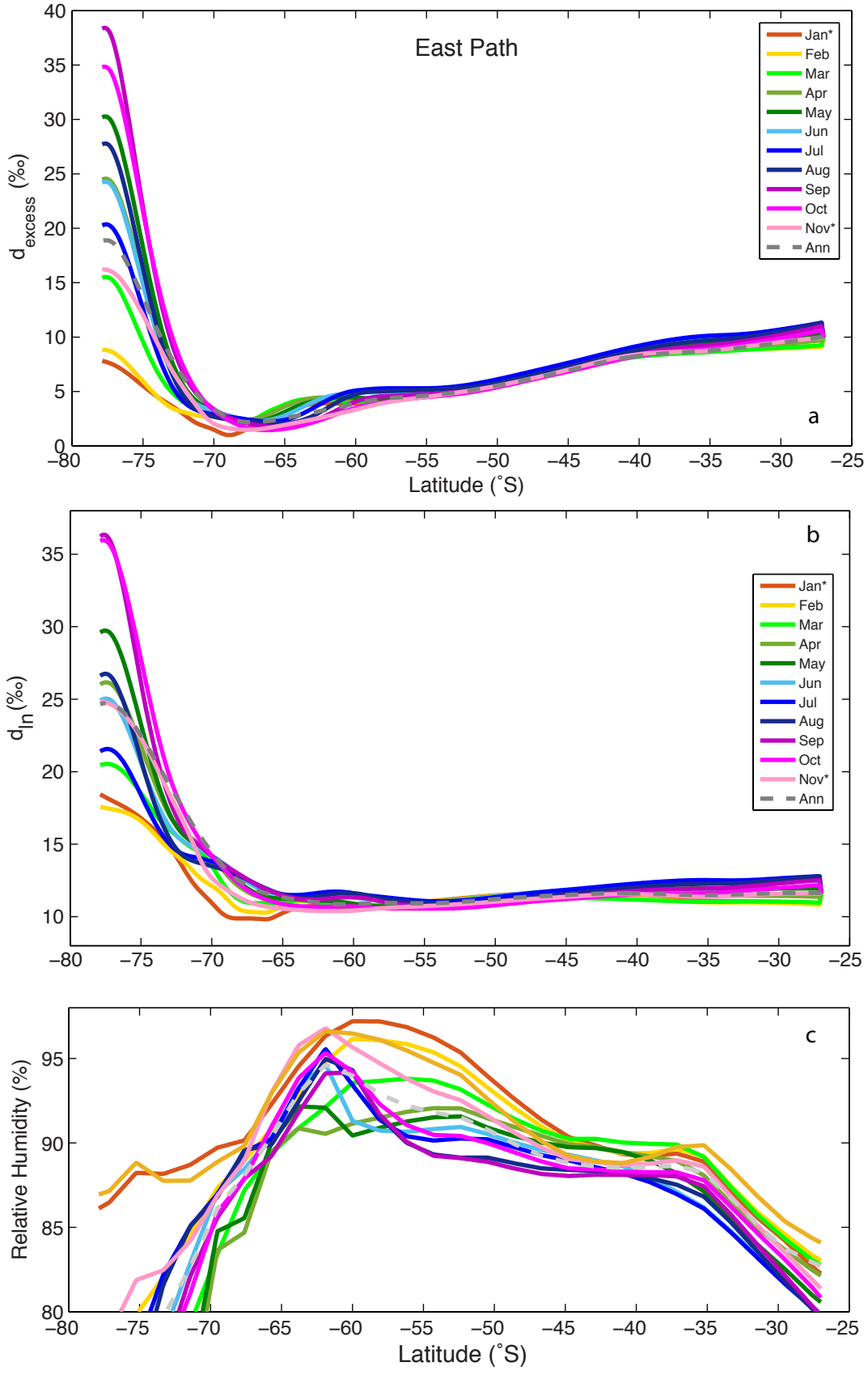
East Path
Jan*
Feb
Mar
Apr
May
Jun
Jul
Aug
Sep
Oct
Nov*
Ann
a
b
c
d_{excess} (‰)
d_{ln} (‰)
Relative Humidity (%)
Latitude (˚S)
Latitude (˚S)

Figure 13

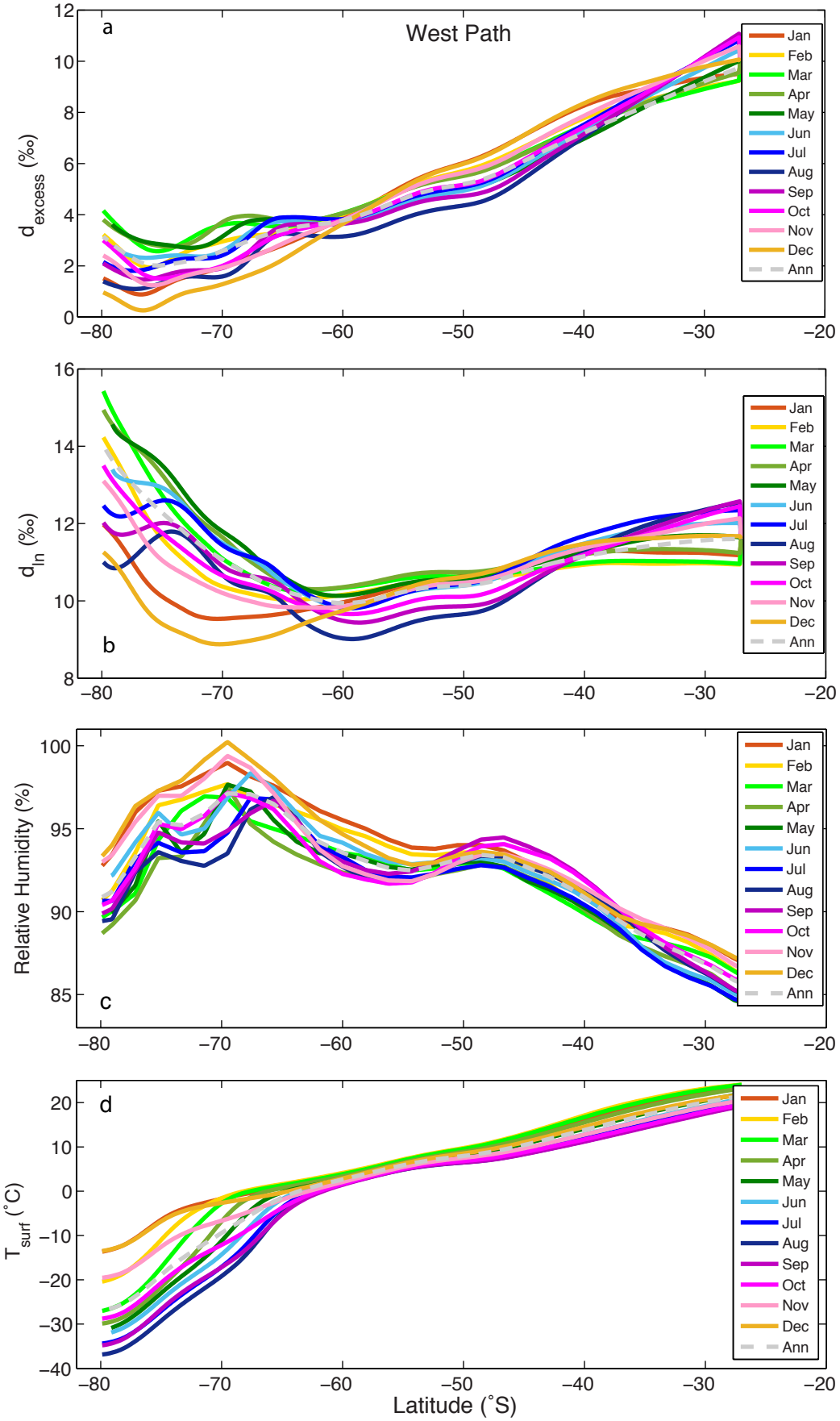
a
West Path
d_{excess} (‰)
b
d_{ln} (‰)
c
Relative Humidity (%)
d
T_{surf} (˚C)
Latitude (˚S)
Jan
Feb
Mar
Apr
May
Jun
Jul
Aug
Sep
Oct
Nov
Dec
Ann

Figure 14

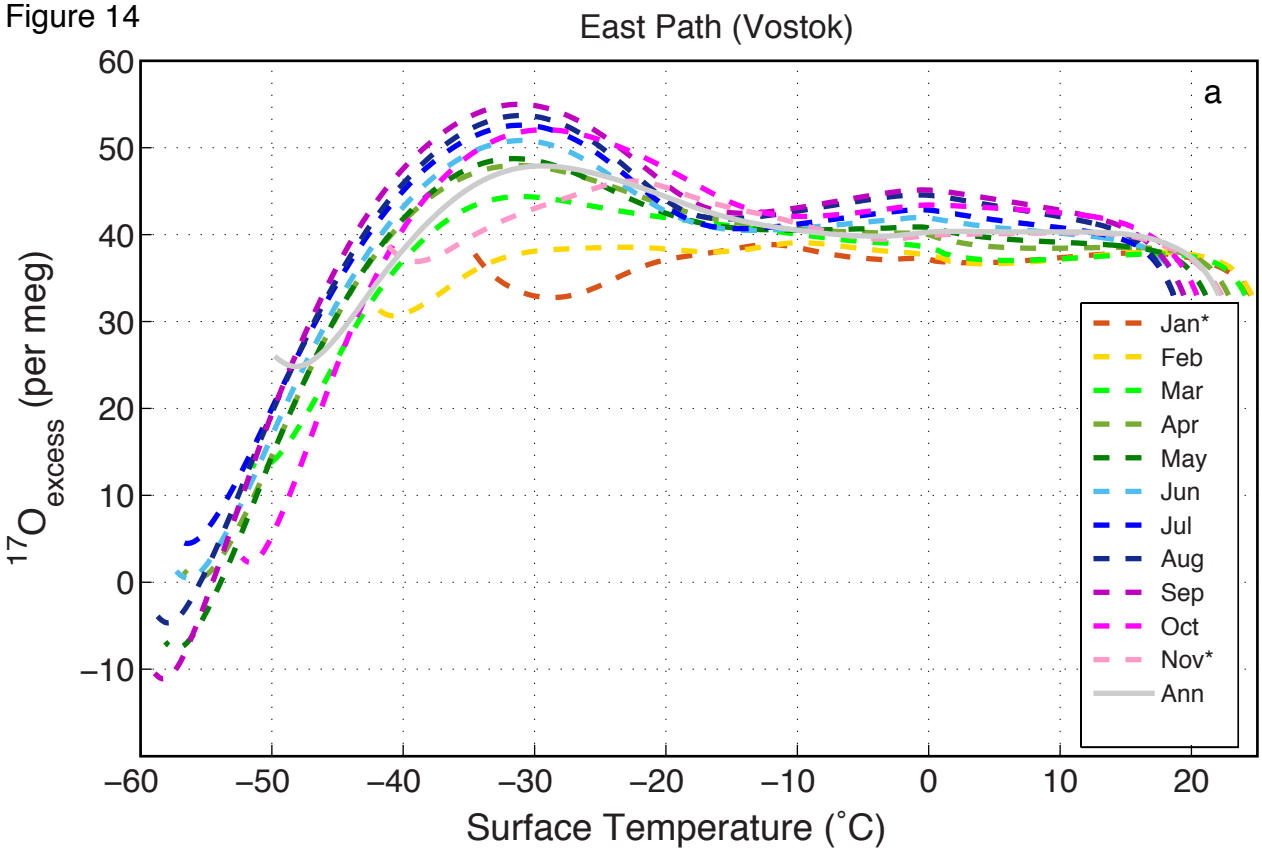
East Path (Vostok)
a
$^{17}O_{excess}$ (per meg)
Surface Temperature (˚C)
Jan*
Feb
Mar
Apr
May
Jun
Jul
Aug
Sep
Oct
Nov*
Ann

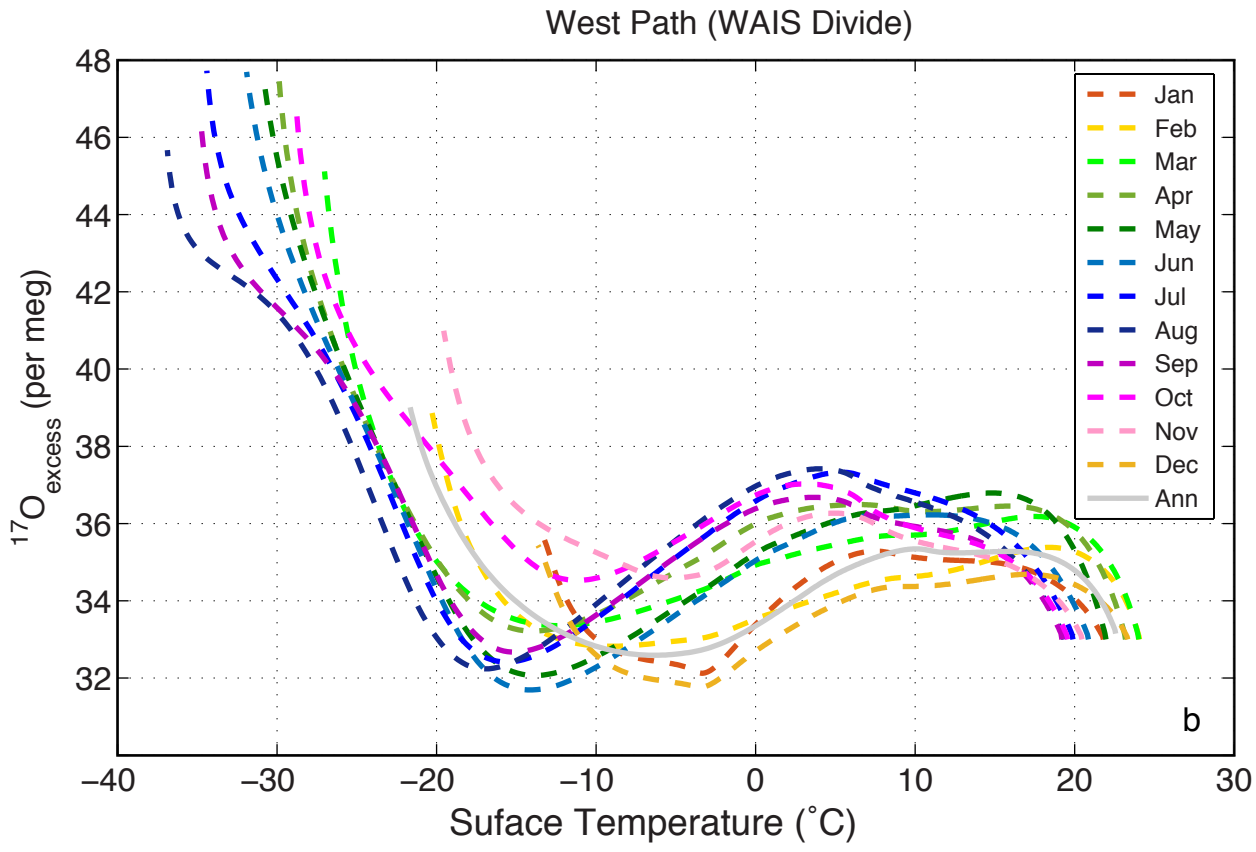
West Path (WAIS Divide)
b
$^{17}O_{excess}$ (per meg)
Suface Temperature (˚C)
Jan
Feb
Mar
Apr
May
Jun
Jul
Aug
Sep
Oct
Nov
Dec
Ann

Figure 15

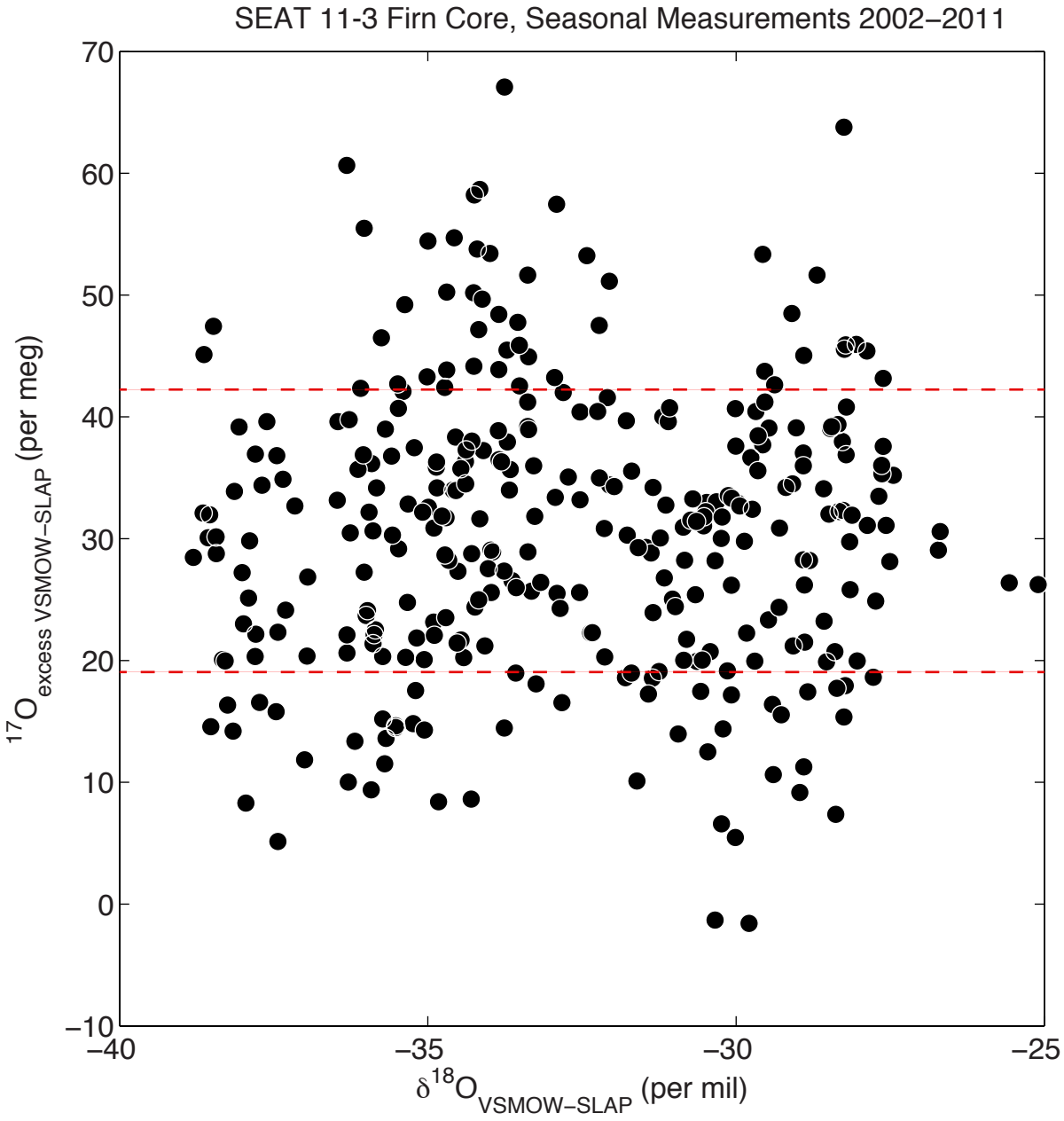
SEAT 11-3 Firn Core, Seasonal Measurements 2002–2011
70
60
50
40
30
20
10
0
−10
−40
−35
−30
−25
$^{17}O_{excess\ VSMOW-SLAP}$ (per meg)
$\delta^{18}O_{VSMOW-SLAP}$ (per mil)

Chapter 7

Future Research and Outlook

This dissertation has focused on interpreting glacial-interglacial and seasonal variations of the triple oxygen isotopes in Antarctic precipitation. Efforts have been made to improve $^{17}O_{excess}$ measurement techniques for both IRMS and laser-spectroscopy, and to use consistent normalization techniques for the reporting of $\delta^{17}O$, $\delta^{18}O$ and $^{17}O_{excess}$ values for interlaboratory comparison. Although much progress has been made, $^{17}O_{excess}$ data are still sparse and most areas of the globe remain essentially un-sampled. The depth of our understanding of $^{17}O_{excess}$ in polar ice cores has evolved considerably since the pioneering work of *Landais et al.* [2008]. Through the work presented here, we have shown that $^{17}O_{excess}$ provides additional information about the fractionation of isotopes in the hydrologic processes of evaporation over the ocean, moisture transport, and precipitation as snow over the ice sheets. As with any paleoenvironmental proxy, we must have a strong understanding of the present-day mechanisms that control $^{17}O_{excess}$ in order to confidently apply it to understanding past conditions. We would be equally remiss if we did not take advantage of past variations in Earth's climate, which provides a natural experiment that can facilitate investigation of the response of water isotopes to large changes in boundary conditions. In this chapter, ongoing work and future research possibilities are discussed, with a focus on understanding the response of $^{17}O_{excess}$ to variations in climate through additional isotopic measurements and modeling.

Climate Variations On Multiple Time Scales

Antarctic Cold Reversal

Comparison with the $\delta^{18}O$ and d_{excess} measurements shows that variations in $^{17}O_{excess}$ from the WAIS Divide core may have changed significantly at specific time intervals where important climatic shifts are known to have occurred. These include the Antarctic Cold Reversal (ACR) at 14.7 ka and the "~4.2 ka" event during the Holocene. However, the low temporal resolution of the $^{17}O_{excess}$ measurements precludes confident (i.e., statistically significant) interpretation of these $^{17}O_{excess}$ variations during these periods. There are other apparently-abrupt changes exhibited in the WAIS Divide $^{17}O_{excess}$ record, and it is only because of the *a priori* expectation based on other geochemical (e.g., methane, carbon dioxide, sea salt, and dust) and isotopic data from ice and ocean cores that we are interested in these specific time intervals. Furthermore, due to the current measurement precision of $^{17}O_{excess}$ (~6 per meg, 1σ), discerning significant variations in $^{17}O_{excess}$ smaller than this magnitude is challenging. Therefore, investigating periods that exhibit the greatest isotopic and geochemical changes offer the best opportunity to assess the response of $^{17}O_{excess}$ to such changes. In this context, we have begun measuring the entire ACR period (14.5 to 11.7 ka) at a much higher temporal resolution than in *Schoenemann et al.* [2014], using the new Picarro CRDS instrument to determine if we can detect a significant signal in the $^{17}O_{excess}$. If such a signal is observed, we intend to validate the magnitude of change from the Picarro data with a more limited set of carefully-chosen IRMS measurements. On the other hand, if no isotopic signal were observed, this would imply that $^{17}O_{excess}$ is relatively insensitive to these climatic changes. Even a lack of discernible signal in $^{17}O_{excess}$ would provide useful information for interpreting the changes observed in $\delta^{18}O$ and d_{excess}, and other paleoclimate proxies.

Although we expect there to be some sort of response in $^{17}O_{excess}$ based on the $\delta^{18}O$ data, investigating the ACR interval in a GCM could also provide an estimate of the $^{17}O_{excess}$ response at WAIS Divide to prescribed ACR climate forcings. With this in mind, we have included $^{17}O_{excess}$ in a number of ECHAM4.6 GCM simulations that used surface boundary fields from a transient simulation of the deglaciation from the ocean-atmospheric coupled CCSM3 GCM (TRACE experiments by *He et al.* [2013]). These model simulations still need to be analyzed, and then compared with the isotopic data from the new Picarro instrument, providing the first ever in-depth study of $^{17}O_{excess}$ over this important millennial-scale climate change event.

Last Glacial Maximum to Early Holocene

In the study of *Schoenemann et al.* [2014], we included a number of measurements from both Siple Dome and Taylor Dome over the last deglaciation and mid-Holocene period. Due to the limited availability of samples and other priorities, we were unable to measure the full magnitude of LGM to EH change for these ice cores. Previous work has shown that Siple Dome experienced significant elevation change over the Holocene period [*Steig et al.*, 2001; *Waddington et al.*, 2005], and therefore $^{17}O_{excess}$ measurement from the mid to late Holocene may not be representative of the full LGM to EH $^{17}O_{excess}$ change at this site; Taylor Dome is also somewhat enigmatic in showing much larger $\delta^{18}O$ change through the Holocene than other Antarctic ice cores [*Steig et al.*, 1998]. To provide a more accurate measure of the LGM to EH change in $^{17}O_{excess}$ at these coastal sites, we have obtained additional samples from the National Ice Core Lab (NICL) for the LGM, EH and present-day time intervals. We will analyze these samples both on the CRDS instrument, and a limited data set, for confirmation, on the IRMS. The updated measurements from Siple Dome and Taylor Dome are not expected to significantly alter the spatial pattern of LGM to EH $^{17}O_{excess}$ change discussed in *Schoenemann et al.* [2014]; however, the new measurements will allow for more accurate comparison with the other LGM to EH ice core records. This work will be the first work to compare the magnitudes of LGM to EH change between IRMS and CRDS measurement techniques.

Dansgaard-Oeschger Events

In Greenland ice cores, large and abrupt climatic changes have been inferred from the sharp transitions in both $\delta^{18}O$ and methane concentrations. These were first identified by Willi Dansgaard and Hans Oeschger, and are called Dansgaard-Oeschger (DO) events [*Dansgaard et al.*, 1993]. In Antarctic ice core records, smaller, but corresponding changes in $\delta^{18}O$ have been identified and are referred to as Antarctic Isotope Maximum (AIM) events [*EPICA Members et al.*, 2006; *Steig*, 2006]. Towards understanding the response of $^{17}O_{excess}$ to climate variations, DO events are prime candidates for further study as they offer periods of substantial change in climatic conditions. The WAIS Divide ice core has provided the highest temporal resolution record for studying the Antarctic counterparts to the Greenland DO events, making it an ideal core for such investigations. Recently, high-resolution measurements of methane and CO_2 for the entire WD record have been published [*Members*, 2013; *Marcott et al.*, 2014], which are essential for linking the timing of the Greenland DO events to the equivalent AIM events in the WD record.

With the new WD chronology available, we can precisely identify the specific DO events with substantial changes in methane and CO_2, and target these for $^{17}O_{excess}$ measurements. The aim of this work would be to determine whether or not Antarctic $^{17}O_{excess}$ changes over these intervals, which are likely to have involved large variations in ocean and atmospheric circulation,

ocean temperatures, and sea ice concentration. Sea ice concentration, in particular, should have affected $^{17}O_{excess}$, as discussed in Chapter 3 and 5 of this dissertation. *Guillevic et al.* [2014] has recently investigated the response of $^{17}O_{excess}$ during DO-8 and DO-12 in the Greenland NGRIP ice core, and found that $^{17}O_{excess}$ responded ~300-500 years prior to the abrupt changes in $\delta^{18}O$ and methane; the interpretation of the $^{17}O_{excess}$ changes, however, is ambiguous in the light of our work from Antarctica. High-resolution measurements of $^{17}O_{excess}$ on the WD record over DO-8 and the preceding one to two thousands years could provide additional constraints on ocean surface humidity, sea ice extent, and local temperature changes that are indicative of oceanic processes. The $^{17}O_{excess}$ measurements would complement our existing $\delta^{18}O$ and d_{excess} measurements, along with the high-resolution CH_4 and CO_2 data. By combining $^{17}O_{excess}$ with other multiple high-resolution proxies available from the WD record, there exists significant potential to improve our understanding of the inter-hemispheric mechanisms operating during abrupt climate change.

Seasonal Measurements from West Antarctica

As discussed in the final paper of this dissertation, use of the CRDS method to make $^{17}O_{excess}$ measurements allows for unprecedented temporal resolution from snow-pit, firn, and ice cores. The goal of ongoing measurements of available firn cores will help to determine if there is a clear seasonal cycle in $^{17}O_{excess}$ at WAIS Divide as predicted from the ICM and GCM work. Determining the magnitude and phasing of $^{17}O_{excess}$ with respect to temperature, $\delta^{18}O$ and d_{excess} will be valuable for gaining insight into which processes (e.g., evaporation, vapor transport, and condensation during snow formation) are most relevant to the variability of $^{17}O_{excess}$, d_{excess} and $\delta^{18}O$ over the annual cycle.

The SEAT 2011-3 firn core was selected for its high annual accumulation rate (~30–50 cm a^{-1}) and its proximity to the WD site. The firn core reaches a depth of ~17 m offering ~35 years of possible climate history. The core was sampled at 2 cm resolution by the Satellite Era Accumulation Traverse (SEAT) research group at Brigham Young University (BYU) and measured for $\delta^{18}O$ and d_{excess}. The firn core measurements exhibit a strong $\delta^{18}O$ seasonal cycle confirming its utility for investigating seasonal variability. The combination of the high annual accumulation rate and high-sampling rate of this firn core makes it an ideal core to study seasonal isotope variations, as the temporal resolution is ~12 to 25 samples per year, more than sufficient to characterize seasonal variability. The analysis of these high-resolution isotopic data will be compared with seasonal simulations from the Intermediate Complexity Model (ICM) of KC03 and the ECHAM4.6 GCM. This work will be part of a follow-up paper to the: *Seasonal and spatial variation of $^{17}O_{excess}$ and d_{excess} in Antarctic precipitation: insights from an intermediate complexity isotope model*, in which the isotopic data from the SEAT core will be used to help evaluate the model simulations.

Future research projects

In this section, I propose two examples of future research projects that would expand the spatial coverage of $^{17}O_{excess}$ measurements and address gaps in our understanding of specific hydrologic processes. The first of these involves isotopic measurements of water vapor over the sea ice regions of the Southern Ocean. The second focuses on understanding the water isotope variations recorded in alpine snowpack and possible links to storm systems.

Isotopic Composition of Water Vapor over Sea Ice

The first proposed project would investigate the effects of evaporation and relative humidity, in the presence of sea ice, on the isotopic composition of water vapor originating from the high-latitude oceans surrounding Antarctica. The proposed research is motivated by the results of *Uemura et al*. [2010], from water vapor measurements taken on a transect over the Southern Indian Ocean. The responses of $^{17}O_{excess}$ and d_{excess} to variations in normalized relative humidity, particularly along the Antarctic coast, are intriguing. In general, the $^{17}O_{excess}$ and d_{excess} measurements in the coastal sea ice zone give relatively low values compared to the mid-latitude sections of the transect, and they closely track the normalized relative humidity; however, during certain days the $^{17}O_{excess}$ and d_{excess} significantly increase, accompanied by depleted values of $\delta^{18}O$ and δD. Back-trajectory analyses on these days show offshore katabatic winds originating from the Antarctic interior. In these events, it is unclear whether the increases in $^{17}O_{excess}$ and d_{excess} are due to the strong evaporation into under-saturated air (i.e., low normalized relative humidity), or from the advection of continental-based vapor potentially carrying elevated d_{excess} and $^{17}O_{excess}$. These unusual results, together with our GCM and ICM simulations that show $^{17}O_{excess}$ in sea ice regions is strongly affected by evaporative recharge, motivates investigation into coastal Antarctic water vapor and the processes driving the isotopic composition.

The proposed project would use our new Picarro cavity ring-down spectroscopy (CRDS) instrument designed for precise measurement of $^{17}O_{excess}$, including the simultaneous measurement of $\delta^{18}O$, δD, d_{excess} and water vapor concentration. The primary objective is to determine how evaporation of moisture from sea ice leads/polynyas in coastal Antarctica influences the isotopic composition of the water vapor in the atmospheric boundary layer. Seasonal changes in the sea ice concentration (and extent) play an important role in controlling the amount of local moisture contribution to Antarctic precipitation [*Noone and Simmonds*, 2004]. In addition, seasonal patterns in wind direction could play an important role in the conditions under which moisture is evaporated, especially in regions of strong katabatic winds compared to locales with persistent onshore winds. Despite ample study on the correlations between sea ice and the seasonal variability of isotopic values recorded in ice cores, the contribution of local moisture from sea ice leads, and its effect on the $^{17}O_{excess}$ and d_{excess} composition of water vapor, is poorly understood.

Our ability to link the concentration of sea ice, and inversely the amount of interstitial open water, to the actual contribution of Antarctic precipitation and its associated isotopic composition has been limited by a lack of direct observational measurements and inability to resolve such small scale physical processes in isotope-enabled GCMs. To address these issues, this project will provide new measurements of water vapor over sea ice leads to 1) estimate the water vapor flux at different ocean/air temperatures throughout the season, 2) determine the isotopic composition of the evaporated water vapor from the leads and surrounding sea ice, 3) calculate the normalized relative humidity and supersaturation of moisture over the open water sources; 4) incorporate these results into isotope-enabled GCMs running re-analysis data (NCEP/DOE) in order to correctly simulate evaporative contributions from over the sea ice region, local precipitation amounts, and isotopic composition recorded in nearby ice cores.

$^{17}O_{excess}$ Applications to Alpine Ice Core Records

The second proposed project would investigate the isotopic composition of seasonal snowpack in alpine regions. Although many ice cores have been retrieved from alpine regions,

there has been no attempt thus far to understand how $^{17}O_{excess}$ measurements might be useful for interpretation of alpine ice-core isotope records. The goal of such a project would be to assess whether variations in $^{17}O_{excess}$ exist in alpine snowfall, and if so, whether the $^{17}O_{excess}$ variations reflect storm trajectories originating over marine or continental sources, local site temperatures, or post depositional effects like re-evaporation and equilibration with overlying water vapor. This work is motivated by two similar research projects. The first of which focused on continuous surface water vapor isotopic measurements and sampling snowfall over a summer at NEEM, Greenland, where they observed diurnal and intra-seasonal variations of d_{excess} with local water vapor, and with local and synoptic weather conditions [*Steen-Larsen et al.*, 2013]. The second example is based on the long-term monitoring project of the intra-seasonal and interannual isotopic composition of snowpack from an array of Sno-tel sites in the Rocky Mountains (referred to as: Isotopes in Rocky Mountain Snowpack, IRMS) and the observed isotopic relationships with temperature, precipitation amounts, and meteorological conditions (L. Anderson, AGU Science Meeting, 2012). An ideal location for such a study would be near previously drilled ice core sites, so that insights gained from the project could be applied to interpreting past isotopic variations within the ice cores. Two potential alpine locations include Alaska (Mt. Logan or Mt. Hunter ice cores) or British Columbia (Mt. Waddington/Combatant Col ice core). The proposed project would use the new Picarro CRDS to continuously measure the $^{17}O_{excess}$ and d_{excess} of surface water vapor and the relative humidity. Collections of snowfall during storm events and samples from snow pits at the end of the winter season will be compared with the water vapor analyzer measurements to determine if post depositional effects have occurred. Air mass back-trajectory calculations of reanalysis data will be used to investigate the relationships between local and synoptic weather conditions and the isotopic variations in the water vapor and snow pack. Although such a field campaign would incur challenges due to harsh weather, a preliminary test of the systems and concept could be carried out over a winter in the North Cascades.

Outlook

The potential of the triple oxygen isotopes (^{16}O, ^{17}O, ^{18}O) for hydrologic, biologic, and geologic process-based studies is significant. As demonstrated in this thesis and previous work, the use of $^{17}O_{excess}$ in ice core research provides additional, independent information to investigate both the fundamental processes controlling isotopic fractionation in the hydrologic cycle and to interpret climatic variations on broad spatial and temporal scales. Over the past five years, important developments in $^{17}O_{excess}$ measurement techniques, for both isotope-ratio mass spectrometry and laser-spectroscopy methods, has expanded the possible applications of $^{17}O_{excess}$. In particular, the new laser spectroscopic techniques offer unprecedented temporal resolution and mobility, which are revolutionizing our ability to examine environmental processes in real-time, and in-situ ([*Steen-Larsen et al.*, 2013]. Moreover, continuous flow measurements coupled with laser spectroscopy offers exceptionally high temporal-resolution measurement of water isotope-ratios in firn and ice cores, which has permitted the development of a new technique to directly infer temperature based on measured $\delta^{18}O$ (or δD) diffusion lengths [*Gkinis et al.*, 2011; 2014], which can now be applied to $\delta^{17}O$. One of the most critical functions of the new laser-based instruments will be to re-measure the isotope fractionation factors for both equilibrium and kinetic processes below freezing, which are necessary to improve the parameterizations and implementation of water isotopes in general circulation models. This type of work is paramount for the interpretation of past environmental conditions in the fields of ice core research and

beyond. The proposed VSMOW-SLAP calibration method for consistent $\delta^{17}O$ and $^{17}O_{excess}$ reporting is indispensible for the burgeoning field of triple oxygen isotopes, and has recently been applied to cutting-edge $^{17}O_{excess}$ measurements of atmospheric O_2 ([*Young et al.*, 2014]) and biogenic and sedimentary carbonates ([*Passey et al.*, 2014]). In summary, the work presented in this thesis provides substantial evidence supporting the use of the triple oxygen-isotope ratios of water as a tool for investigating the processes of evaporation, moisture transport, and condensation in the global hydrologic cycle.

REFERENCES

Angert, A., C. D. Cappa, and D. J. DePaolo (2004), Kinetic 17O effects in the hydrologic cycle: Indirect evidence and implications, *Geochim. Cosmochim. Acta*, *68*(17), 3487–3495, doi:10.1016/j.gca.2004.02.010.

Baker, L., I. Franchi, J. Maynard, I. Wright, and C. Pillinger (2002), A technique for the determination of $^{18}O/^{16}O$ and $^{17}O/^{16}O$ isotopic ratios in water from small liquid and solid samples, *Anal. Chem*, *74*(7), 1665–1673.

Barkan, E., and B. Luz (2005), High precision measurements of $^{17}O/^{16}O$ and $^{18}O/^{16}O$ ratios in H_2O, *Rapid Commun. Mass Spectrom.*, *19*(24), 3737–3742.

Barkan, E., and B. Luz (2007), Diffusivity fractionations of $H_2{}^{16}O/H_2{}^{17}O$ and $H_2{}^{16}O/H_2{}^{18}O$ in air and their implications for isotope hydrology, *Rapid Commun. Mass Spectrom.*, *21*, 2999–3005.

Berman, E. S. F., N. E. Levin, A. Landais, S. Li, and T. Owano (2013), Measurement of $\delta^{18}O$, $\delta^{17}O$, and ^{17}O-excess in Water by Off-Axis Integrated Cavity Output Spectroscopy and Isotope Ratio Mass Spectrometry, *Anal. Chem*, *85*(21), 10392–10398, doi:10.1021/ac402366t.

Ciais, P., and J. Jouzel (1994), Deuterium and oxygen 18 in precipitation: Isotopic model, including mixed cloud processes, *J. Geophys. Res.*, *99*(D8), 16–793–16–803.

Cuffey, K. M., and F. Vimeux (2001), Covariation of carbon dioxide and temperature from the Vostok ice core after deuterium-excess correction, *Nature*, *412*(6846), 523–527.

Dansgaard, W. (1964), Stable isotopes in precipitation, *Tellus*, *16*, 436–468.

Dansgaard, W., S. J. Johnsen, H. B. Clausen, D. Dahl-Jensen, N. S. Gundestrup, C. U. Hammer, C. S. Hvidberg, J. P. Steffensen, A. E. Sveinbjörnsdóttir, and J. Jouzel (1993), Evidence for general instability of past climate from a 250-kyr ice-core record, *Nature*, *364*(6434), 218–220.

EPICA Members et al. (2006), One-to-one coupling of glacial climate variability in Greenland and Antarctica, *Nature*, *444*(7116), 195–198, doi:10.1038/nature05301.

Gat, J. (1996), Oxygen and hydrogen isotopes in the hydrologic cycle, *Annu. Rev. Earth Planet. Sci.*, (24), 225–262.

Gkinis, V., S. B. Simonsen, S. L. Buchardt, J. W. C. White, and B. M. Vinther (2014), Water isotope diffusion rates from the NorthGRIP ice core for the last 16,000 years - Glaciological and paleoclimatic implications, *Earth Planet. Sci. Lett.*, *405*, 132–141, doi:10.1016/j.epsl.2014.08.022.

Gkinis, V., T. J. Popp, T. Blunier, M. Bigler, S. Schüpbach, E. Kettner, and S. J. Johnsen (2011), Water isotopic ratios from a continuously melted ice core sample, *Atmos. Meas. Tech.*,

4(11), 2531–2542, doi:10.5194/amt-4-2531-2011.

Guillevic, M. et al. (2014), Multi-proxy fingerprint of Heinrich event 4 in Greenland ice core records, *Clim. Past Discuss.*, *10*(2), 1179–1222, doi:10.5194/cpd-10-1179-2014.

He, F., J. D. Shakun, P. U. Clark, A. E. Carlson, Z. Liu, B. L. Otto-Bliesner, and J. E. Kutzbach (2013), Northern Hemisphere forcing of Southern Hemisphere climate during the last deglaciation, *Nature*, *494*(7435), 81–85, doi:10.1038/nature11822.

Jouzel, J., and L. Merlivat (1982), Deuterium excess in an East Antarctic ice core suggests higher relative humidity at the oceanic surface during the last glacial maximum, *Nature*, *299*, 688–691.

Jouzel, J., and L. Merlivat (1984), Deuterium and oxygen 18 in precipitation: modeling of the isotopic effects during snow formation, *J. Geophys. Res.*, *89*, 11749–11757.

Jouzel, J., F. Vimeux, N. Caillon, G. Delaygue, G. Hoffmann, V. Masson-Delmotte, and F. Parrenin (2003), Magnitude of isotope/temperature scaling for interpretation of central Antarctic ice cores, *J. Geophys. Res.*, *108*(D12), 4361, doi:10.1029/2002JD002677.

Kavanaugh, J. L., and K. M. Cuffey (2002), Generalized view of source-region effects on δD and deuterium excess of ice-sheet precipitation, *Ann. Glaciol.*, *35*(1), 111–117.

Kavanaugh, J. L., and K. M. Cuffey (2003), Space and time variation of $\delta^{18}O$ and δD in Antarctic precipitation revisited, *Global Biogeochem. Cy.*, *17*(1), 1017–1031, doi:10.1029/2002GB001910.

Kusakabe, M., and Y. Matsuhisa (2008), Oxygen three-isotope ratios of silicate reference materials determined by direct comparison with VSMOW-oxygen, *Geochem. J.*, *42*(4), 309–317, doi:10.2343/geochemj.42.309.

Landais, A., A. Ekaykin, E. Barkan, R. Winkler, and B. Luz (2012a), Seasonal variations of ^{17}O-excess and d-excess in snow precipitation at Vostok station, East Antarctica, *J. Glaciol.*, *58*(210), 725–733, doi:10.3189/2012JoG11J237.

Landais, A., E. Barkan, and B. Luz (2008), Record of $\delta^{18}O$ and ^{17}O-excess in ice from Vostok Antarctica during the last 150,000 years, *Geophys. Res. Lett.*, *35*(L02709), 1–5, doi:10.1029/2007GL032096.

Landais, A., H. C. Steen-Larsen, M. Guillevic, V. Masson-Delmotte, B. Vinther, and R. Winkler (2012b), Triple isotopic composition of oxygen in surface snow and water vapor at NEEM (Greenland), *Geochim. Cosmochim. Acta*, *77*(C), 304–316, doi:10.1016/j.gca.2011.11.022.

Luz, B., and E. Barkan (2010), Variations of $^{17}O/^{16}O$ and $^{18}O/^{16}O$ in meteoric waters, *Geochim. Cosmochim. Acta*, *74*(22), 6276–6286, doi:10.1016/j.gca.2010.08.016.

Marcott, S. A. et al. (2014), Centennial-scale changes in the global carbon cycle during the last deglaciation, *Nature*, *514*(7524), 616–619, doi:10.1038/nature13799.

Masson-Delmotte, V., B. Stenni, and J. Jouzel (2004), Common millennial-scale variability of Antarctic and Southern Ocean temperatures during the past 5000 years reconstructed from the EPICA Dome C ice core, *Holocene*, *14*(2), 145–151, doi:10.1191/0959683604hl697ft.

Members, W. D. P. (2013), Onset of deglacial warming in West Antarctica driven by local orbital forcing, *Nature*, *500*(7463), 440–444, doi:10.1038/nature12376.

Merlivat, L., and J. Jouzel (1979), Global Climatic Interpretation of the Deuterium-Oxygen-18 Relationship for Precipitation, *J. Geophys. Res.*, *84*(C8), 5029–5033.

Noone, D., and I. Simmonds (2004), Sea ice control of water isotope transport to Antarctica and implications for ice core interpretation, *J. Geophys. Res.*, *109*(D07105), 1–13, doi:doi:10.1029/2003JD004228.

Passey, B. H., H. Hu, H. Ji, S. Montanari, S. Li, G. A. Henkes, and N. E. Levin (2014), Triple oxygen isotopes in biogenic and sedimentary carbonates, *Geochim. Cosmochim. Acta*, *141*, 1–25, doi:10.1016/j.gca.2014.06.006.

Risi, C., A. Landais, R. Winkler, and F. Vimeux (2013), Can we determine what controls the spatio-temporal distribution of d-excess and ^{17}O-excess in precipitation using the LMDZ general circulation model? *Clim. Past*, *9*(5), 2173–2193, doi:10.5194/cp-9-2173-2013.

Risi, C., A. Landais, S. Bony, J. Jouzel, V. Masson-Delmotte, and F. Vimeux (2010), Understanding the ^{17}O-excess glacial-interglacial variations in Vostok precipitation, *J. Geophys. Res.*, *115*(D10112), 1–15, doi:10.1029/2008JD011535.

Schoenemann, S. W., A. J. Schauer, and E. Steig (2013), Measurement of SLAP2 and GISP δ^{17}O and proposed VSMOW-SLAP normalization for δ^{17}O and $^{17}O_{excess}$, *Rapid Commun. Mass Spectrom.*, (27), 582–590, doi:10.1002/rcm.6486.

Schoenemann, S. W., E. J. Steig, Q. Ding, B. R. Markle, and A. J. Schauer (2014), Triple water-isotopologue record from WAIS Divide, Antarctica: Controls on glacial-interglacial changes in $^{17}O_{excess}$ of precipitation, *Journal of Geophysical Research: Atmospheres*, *119*, 1–23, doi:10.1002/2014JD021770.

Steen-Larsen, H. C. et al. (2013), Continuous monitoring of summer surface water vapour isotopic composition above the Greenland Ice Sheet, *Atmos. Chem. Phys. Discuss.*, *13*(1), 1399–1433, doi:10.5194/acpd-13-1399-2013.

Steig, E. J. (2006), Climate change - The south-north connection, *Nature*, *444*(7116), 152–153, doi:10.1038/444152a.

Steig, E. J., C. P. Hart, J. W. C. White, W. L. Cunningham, M. D. Davis, and E. S. Saltzman (1998), Changes in climate, ocean and ice-sheet conditions in the Ross embayment, Antarctica, at 6 ka, *Ann. Glaciol.*, *27*, 305–310.

Steig, E. J., J. L. Fastook, C. Zweck, I. D. Goodwin, K. J. Licht, J. W. C. White, and R. P. Ackert (2001), West Antarctic Ice Sheet Elevation Changes, in *The West Antarctic Ice Sheet:*

Behavior and Environment, pp. 75–90, American Geophysical Union.

Steig, E. J., V. Gkinis, A. J. Schauer, S. W. Schoenemann, K. Samek, J. Hoffnagle, K. J. Dennis, and S. M. Tan (2014), Calibrated high-precision ^{17}O-excess measurements using cavity ring-down spectroscopy with laser-current-tuned cavity resonance, *Atmos. Meas. Tech.*, *7*(8), 2421–2435, doi:10.5194/amt-7-2421-2014.

Uemura, R., E. Barkan, O. Abe, and B. Luz (2010), Triple isotope composition of oxygen in atmospheric water vapor, *Geophys. Res. Lett.*, *37*(L04402), 1–4, doi:10.1029/2009GL041960.

Vimeux, F., V. Masson, G. Delaygue, J. Jouzel, J. R. Petit, and M. Stievenard (2001), A 420,000 year deuterium excess record from East Antarctica: Information on past changes in the origin of precipitation at Vostok, *J. Geophys. Res.*, *106*(D23), 31–863–31–873.

Waddington, E., H. Conway, E. Steig, R. Alley, E. J. Brook, K. Taylor, and J. White (2005), Decoding the dipstick: Thickness of Siple Dome, West Antarctica, at the Last Glacial Maximum, *Geology*, *33*(4), 281–284.

Winkler, R., A. Landais, H. Sodemann, L. Dümbgen, F. Prié, V. Masson-Delmotte, B. Stenni, J. Jouzel, and V. Rath (2012), Deglaciation records of ^{17}O-excess in East Antarctica: reliable reconstruction of oceanic normalized relative humidity from coastal sites, *Clim. Past*, *8*(1), 1–16, doi:10.5194/cp-8-1-2012.

Young, E. D., L. Y. Yeung, and I. E. Kohl (2014), On the $\Delta^{17}O$ budget of atmospheric O_2, *Geochim. Cosmochim. Acta*, *135*(C), 102–125, doi:10.1016/j.gca.2014.03.026.